

Lecture 1: The QFT framework—A broadbrush perspective

Aninda Sinha^{1,2}

¹Centre for High Energy Physics, Indian Institute of Science, India.

²Department of Physics and Astronomy, University of Calgary, Canada.

August 8, 2025

Contents

1 The biggest embarrassment and an opportunity	2
2 Where QM fails	3
3 Why the Quantum Field	6

I am going to assume that everyone reading these lectures/taking this course has done special relativity and two courses in quantum mechanics (perturbation theory). For students familiar with at least one course in quantum field theory, this will mainly be a revision of concepts¹.

Books (I will specify which chapters) and refs (I will keep adding refs in suitable places):

1. Quantum Field Theory and the Standard Model, M. Schwartz, CUP–(MS)
2. Quantum Computation and Quantum Information, M. Nielsen and I. Chuang, CUP–(NC)
3. Simulating Quantum Field Theory with a Quantum Computer, J. Preskill, arXiv:1811.10085–(P18)

¹I have used AI in writing portions of this lecture; especially, when you see overly itemized (bullet point) items. Be careful of those sections! I will attempt to indicate these sections with a *. After I have critically examined them, I will remove the *.

1 The biggest embarrassment and an opportunity

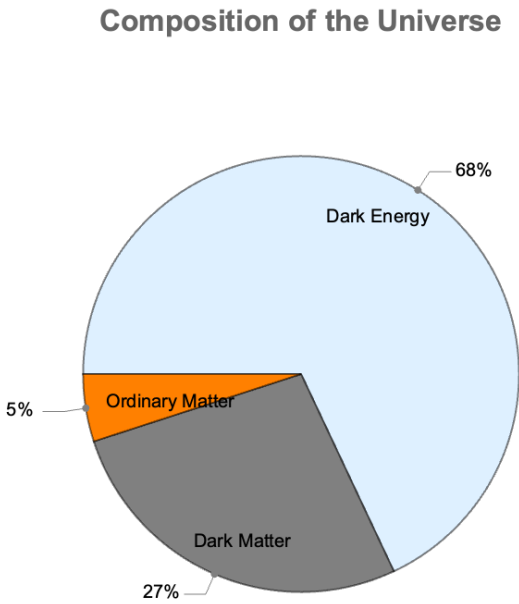


Figure 1: The cosmological pie-chart

Fig. (1) represents the biggest embarrassment at present in theoretical physics as well as a fantastic opportunity for young (and old!) researchers. In a quantifiable way, the figure shows that we do not understand 95% of what makes up the universe. The frameworks that enable us to study this question involve general relativity and quantum field theory. The figure demonstrates that something major is missing in our understanding. It could need a paradigm shift to solve.

In the history of physics, progress has sometimes happened when physicists have tried to recast (at that point of time) known physics in new language. For instance, before Maxwell, electricity and magnetism were thought of as separate phenomena. Maxwell's equations changed all that. Quantum field theory and general relativity are also thought to be different frameworks. However, the AdS/CFT correspondence or the holographic principle suggests that these may be two sides of the same coin, although in different spacetime dimensions. Closer in spirit to this course, we can talk about Kenneth Wilson's work on the renormalization group. This deep conceptual Nobel prize winning insight was obtained by thinking about quantum field theory on a classical computer.

Talking more about the last example, Wilson's work did not wait for powerful classical computers to emerge. He came up with deep conceptual insights by imagining how to do things on a classical computer. See table 1 for a comparison of what existed during his times. Despite the limited computing resources, Kenneth Wilson's development of the renormalization group approach revolutionized our understanding of phase transitions and critical phenomena. His work earned him the Nobel Prize in Physics in 1982 and laid the foundation for many areas of modern physics, including condensed matter physics, quantum field theory, and statistical mechanics.

Somewhat coincidentally, the year before Wilson got his Nobel prize, Richard Feynman proposed the idea of a quantum computer in 1981. This groundbreaking idea was presented in his famous lecture titled "Simulating Physics with Computers", which he delivered at the First Con-

Resource	1960s–1970s	Modern Equivalent
Processor Speed	~2.2 MHz (e.g., IBM 7090)	~3 GHz (modern CPU)
Memory	~32 KB	~16 GB (modern computer)
Storage	~MB (magnetic tape, disk drives)	~TB (modern SSD/HDD)
Programming Language	Fortran	Python, C++, Julia, etc.
Computational Power	~100,000 FLOPS	~ 10^{12} FLOPS (modern GPU)

Table 1: Comparison of Computing Resources: 1960s–1970s vs. Modern

ference on the Physics of Computation held at MIT. His take was that nature is fundamentally quantum and to simulate phenomena governed by quantum principles like entanglement, it would be desirable to develop a quantum computer. Curiously, Feynman, John Hopfield (Nobel Prize 24, AI/ML) and Carver Mead signed up to give a course in CalTech called "The Physics of Computation" in 1981.

At present, especially since the last two decades, there is a major endeavour in pushing the frontiers of quantum computing and technology. Can we hope to solve some of the major unsolved mysteries such as the one shown in fig. (1)? Many physicists believe that quantum field theory will be eventually replaced by a more useful framework—something like string theory but perhaps a different version of it. Can thinking about quantum field theory on a quantum computer enable us to probe such grand questions?

In any event, the goal of this course is to motivate some of you to take up these grand-challenge questions. Hopefully, we will learn together over the next 3 months.

2 Where QM fails

The non-relativistic Schrodinger equation is studied in great depth in any introductory course in quantum mechanics. It has had great success in describing physics, where relativistic effects can be ignored. The spacetime symmetries that leave the Schrodinger equation invariant are the so-called Galilean symmetries. Specifically consider the free particle Schrodinger equation in 1-space dimension:

$$-\frac{\hbar^2}{2m}\partial_x^2\psi = i\hbar\partial_t\psi. \quad (1)$$

The Galilean symmetries act on the partial derivatives to leave them invariant as follows:

$$t \rightarrow t, \quad x \rightarrow x + vt \quad (2)$$

where v is the velocity of the new frame of reference. Unlike special-relativistic transformations, clearly time and space are treated on different footings. The non-relativistic wave equation is usually "beaten to death" in any introductory course on quantum mechanics. Many body generalizations of this equation have also been enormously successful in explaining many observations in the micro-cosmos, for instance, how various elements exist. After two courses on quantum mechanics, many students plunge into quantum field theory.

There are many reasons to believe that there are several important gaps in our understanding at this stage:

1. Special relativity

The first logical step to overcome this shortcoming is to write a wave-equation that is consistent with **special relativity**. The simplest wave-equation is the **Klein-Gordon equation** ($c = 1$).

$$(\partial_t^2 - \partial_x^2 + m^2)\phi = 0. \quad (3)$$

To check the correctness of signs for a usual positive m^2 situation, we substitute $\phi = \exp(iEt - ikx)$. This leads to $-E^2 + k^2 + m^2 = 0$, which is the correct relativistic dispersion relation. Note: "dispersion relation" is used in at least 2 different contexts in modern QFT. This is one of them.

This is the famous Klein-Gordon equation discovered by Klein and Gordon in 1926. Schrodinger had initially considered this as a contender for the wave equation in 1925. Schrodinger had found that this relativistic wave equation gives the wrong fine-structure and discarded it, favouring his non-relativistic wave equation. When one tries to interpret the KG equation as a wave equation, there are other problems, including negative probability densities. The correct way of using the Klein-Gordon equation is to interpret ϕ (which implicitly depends on x, t) as a quantum field (more on this later). For now, it is sufficient to point out that this field corresponds to a "scalar" object of spin-0. We will elaborate on what these words mean in a bit.

2. How wave function collapse happens

This is an unsolved problem and a cause of great agony amongst all physicists. There are various schools of interpretation. Historically, a well-known school of thought was the Copenhagen interpretation. We will not go into the philosophical issues. We can rephrase the problem as asking:

Can we not use quantum mechanics to describe everything? Why do we resort to a classical picture?

This is a subtle issue. A typical experimental situation will consist of an observable and an observer. We usually think of these as distinct entities. In beginning courses, we also ignore any entanglement between the observer and the observable.

We typically teach students to "shut-up and calculate". Most often we get away with this. For instance, if you open PDG (Particle Data Group) handbook which is freely available, you will see millions of experimental results which are well explained using this approach. We also typically invoke the Ehrenfest theorem which enables us to derive classical equations when considering expectation values w.r.t. wave functions with large quantum numbers. In the next point of discussion, we will consider a situation where this appears to fail.

However, we encounter all kinds of conceptual questions—Einstein famously asked "Is the moon there when no one is looking?" We will not attempt to answer such (important) questions. But I encourage you to think of them.

Can we observe the wave function? To avoid talking about such "auxiliary" constructs in our description of nature, our founding fathers (eg Heisenberg) wanted to come up with a framework which directly dealt with observables, avoiding the wave function or the quantum field, and find equations for these observables based on various consistency conditions. This point of view is called the "**Bootstrap**" approach and forms a major theoretical effort in modern times. Keep this in mind. Here, we usually do not have a Hamiltonian (we don't assume a fundamental Lagrangian) approach. It will lead to interesting philosophical ramifications later on.

3. Quantum/classical chaos

Chaos theory has long been a cornerstone of classical mechanics, describing systems where small changes in initial conditions lead to exponentially diverging outcomes—a phenomenon famously encapsulated in the “butterfly effect.” In classical mechanics, chaos is well-understood and can be quantified using tools like **Lyapunov exponents**, which measure the rate of divergence of nearby trajectories. However, when we transition to the quantum realm, the concept of chaos becomes much more subtle and less straightforward.

Quantum systems are governed by the **Schrödinger equation**, which is linear and does not exhibit the same sensitivity to initial conditions. However, quantum systems can still exhibit behavior analogous to classical chaos, known as **quantum chaos**. This is often studied through the statistical properties of the **energy spectrum** and the **eigenfunctions** of the quantum system.

One of the key phenomena in quantum chaos is the **quantum scar**, where certain eigenstates exhibit enhanced probability density along unstable classical periodic orbits. While this provides a link between classical and quantum chaos, it also highlights the conceptual gap between the two regimes: in classical mechanics, chaos is about trajectories, while in quantum mechanics, it is about the statistical properties of the wavefunctions.

A situation that is discussed in the popular media (see Sabine Hossenfelder’s video on this) pertains to Hyperion, a satellite of Saturn, which exhibits chaotic trajectory. There is an interesting argument in the literature that suggests if **Hyperion** were treated as an **isolated quantum system**, quantum mechanics would predict that it would **fall out of chaos** within a finite time. This argument is based on the idea that quantum systems cannot exhibit true chaos in the same way classical systems do, due to the **linearity of the Schrödinger equation** and the **discrete nature of quantum states**. For Hyperion, this timescale has been estimated to be on the order of **20 years**, though the exact number depends on the system’s parameters and the assumptions made in the calculation.

This prediction highlights a fundamental tension between classical and quantum descriptions of chaotic systems: while classical mechanics predicts that Hyperion’s chaotic rotation will persist indefinitely, quantum mechanics suggests that the system will eventually **decohere** and settle into a more regular, non-chaotic state. This raises important questions about the **quantum-classical correspondence** and how classical chaos emerges from the underlying quantum dynamics. Zurek and Paz (1996) claim that decoherence is crucial to explain this discrepancy. The decoherence picture typically instructs us to consider a tensor product of the object of interest with its environment. In effect, Hyperion is interacting with the dust and photons that surround it. The correct description of Hyperion is a massive state which tensors all the constituents of Hyperion with whatever it is interacting with. This is something that will be worth simulating and getting to the bottom of. Simulating such dynamics classically appears quite hard and one has to go beyond the realm of classical computing. This does create something of a conundrum though. Will this classical-quantum correspondence always need us to think of an environment; if so, how big should this environment be? How do we think of the interactions, in what framework?

Including this argument in the discussion motivates the use of **quantum computers** to simulate such systems and explore the transition from quantum to classical behavior. By simulating Hyperion’s dynamics on a quantum computer, we can test whether the system

indeed falls out of chaos on the predicted timescale and gain insights into the mechanisms by which classical chaos emerges from quantum mechanics.

4. Pair creation

One of the most compelling reasons to study **Quantum Field Theory (QFT)** is its ability to explain phenomena that are completely inaccessible to **non-relativistic quantum mechanics (NRQM)**. A prime example of this is **pair creation**, the process by which a particle and its antiparticle are spontaneously produced from the vacuum. This phenomenon is a direct consequence of the **relativistic energy-momentum relation**,

$$E^2 = p^2 c^2 + m^2 c^4,$$

which allows for the conversion of energy into mass. In NRQM, the energy of a system is always positive, and the concept of negative energy states does not arise. However, in QFT, the **Dirac equation** predicts the existence of negative energy solutions, leading to the idea of a **Dirac sea** of filled negative energy states. When sufficient energy is provided, an electron can be excited from this sea, leaving behind a **positron** (the electron's antiparticle). This process is described by the **creation and annihilation operators** in QFT, which allow for the dynamic creation and destruction of particles.

The inability of NRQM to explain pair creation is particularly evident in the context of **strong external fields**. For example, in the presence of a strong electric field, the vacuum can become unstable, leading to the production of electron-positron pairs. This phenomenon, known as the **Schwinger effect**, is described by the rate of pair production per unit volume **Schwinger, 1951**:

$$\Gamma \sim \exp\left(-\frac{\pi m^2 c^3}{e \hbar E}\right),$$

where E is the electric field strength, m is the electron mass, and e is the electron charge. This result cannot be derived from NRQM, which lacks the framework to describe particle creation and annihilation. Furthermore, NRQM cannot account for the **relativistic invariance** of physical laws, which is crucial for understanding processes like pair creation that occur at high energies.

The study of pair creation in QFT not only provides a deeper understanding of fundamental physical processes but also has practical implications in fields such as **particle physics** and **cosmology**. For instance, pair creation plays a key role in the **early universe** and in the vicinity of **black holes**, where strong gravitational fields can lead to the production of particle-antiparticle pairs. By studying QFT, we gain the tools to explore these phenomena and push the boundaries of our understanding of the quantum world.

3 Why the Quantum Field

The discussions on special relativity and pair creation will motivate us toward thinking in the language of a quantum field. Let us briefly discuss why.

As I mentioned, when we try to think of the Klein-Gordon equation as the appropriate relativistic wave-equation, it gives negative probability densities. The same problem happens with the

Dirac equation. In quantum mechanics, we thought of the position x and its conjugate momentum p_x as operators satisfying the usual commutation relation. Time here is a parameter (label). This is another instance where we treat time on a different footing, unlike what special relativity teaches us. So there are two avenues forward: 1) demote position to be a parameter 2) Promote time to be an operator. The former approach is what we do in quantum field theory while the latter is what we do in the world-line or world-sheet formalism (for instance in string theory). In the former case, ϕ (what we wanted to think of as the relativistic wave-function) gets promoted to be an operator. This is sometimes referred to as second-quantization (we will refrain from this ancient terminology).

The $\hat{\phi}$ operator is made of creation and annihilation operators (more on this in the next section). These creation and annihilation operators enable us to talk about the pair creation example.

It is not that we will now forget about the wave-function! We can recover the single-particle wave function from the framework of quantum field theory. Depending on the physics we want to describe, it is preferable to talk in the language of probability amplitudes of various processes happening. For instance, Compton scattering. Quantum field theory is a framework that enables us to do this.

In fact, it is worth pointing out that the techniques in QFT are not restricted to the special relativistic situation alone. For instance, cosmologists are interested in calculating expectation values of primordial fluctuations. Their signatures are imprinted on the cosmic microwave background and in temperature correlations that can be measured. One would like to know the microscopic origins of these observables. Quantum field theory, accounting for the background, provides a framework for addressing such questions.

Lecture 2: Field quantization

Aninda Sinha^{1,2}

¹Centre for High Energy Physics, Indian Institute of Science, India.

²Department of Physics and Astronomy, University of Calgary, Canada.

August 8, 2025

Contents

1 Some classical fields that we know	1
2 Solutions to the classical equation	3
3 Heuristic quantization	4

This lecture is based on chapter 2 of MS.

1 Some classical fields that we know

In the last lecture, we briefly saw the Klein-Gordon equation, which is the simplest relativistic wave equation. Let's examine that a bit more. In 3+1 dimensional Minkowski space (the generalization to arbitrary dimensions is obvious), the Minkowski metric reads:

$$\eta_{\mu\nu} = \begin{pmatrix} 1 & 0 & 0 & 0 \\ 0 & -1 & 0 & 0 \\ 0 & 0 & -1 & 0 \\ 0 & 0 & 0 & -1 \end{pmatrix}. \quad (1)$$

Here, we made a choice for the signature of the metric. For obvious reasons, this is called the metric in the mostly negative signature. This is the usual convention in most particle physics textbooks. GR textbooks follow the mostly positive signature. The d'Alembertian operator is defined as:

$$\partial^2 = \eta^{\mu\nu} \partial_\mu \partial_\nu, \quad (2)$$

where $\eta^{\mu\nu}$ is the inverse metric (here the matrix form is the same as $\eta_{\mu\nu}$). We raise and lower indices using η . The positioning of the indices (up or down) may lead to different signs, so it is worth being careful about this (and any way, relativists will get annoyed if you are not careful!).

The Klein-Gordon equation for a massive scalar in the mostly negative signature (which is the conventions we will adopt) reads:

$$(\partial^2 + m^2)\phi = 0. \quad (3)$$

We are tacitly assuming m to be a real parameter (else we would get a tachyonic field—a discussion, we will avoid). ϕ depends on x^μ and we will sometimes just drop this dependence for simplicity.

Where do we encounter ϕ in physics? The most famous place is undoubtedly the case of the Higgs' boson, which is thought to be a scalar field. We have not yet defined what we mean by scalar, vector etc when it comes to fields—we will do that in the next lecture.

Another famous field that you have encountered in your coursework is the electromagnetic field. It is represented by an antisymmetric tensor:

$$F_{\mu\nu}(x^\alpha). \quad (4)$$

There are 6 components that this tensor has, corresponding to the 3 components of the electric field \vec{E} and the 3 components of the magnetic field \vec{B} . As you may recall, we write the electric and magnetic fields in terms of the scalar and 3-vector potential:

$$\vec{E} = -\vec{\nabla}\phi - \partial_t\vec{A}, \quad \vec{B} = \vec{\nabla} \times \vec{A}. \quad (5)$$

In terms of a 4-vector potential $A_\mu = (\phi, -\vec{A})$, defining

$$F_{\mu\nu} = \partial_\mu A_\nu - \partial_\nu A_\mu, \quad (6)$$

we can compute:

$$F_{\mu\nu} = \begin{pmatrix} 0 & E_x & E_y & E_z \\ -E_x & 0 & -B_z & B_y \\ -E_y & B_z & 0 & -B_x \\ -E_z & -B_y & B_x & 0 \end{pmatrix}. \quad (7)$$

Maxwell equations read:

$$\partial_\mu F^{\mu\nu} = J^\nu, \quad \partial_{[\mu} F_{\nu\rho]} = 0. \quad (8)$$

The notation $B_{[abc]}$ means totally antisymmetric in a, b, c . The first equation gives the Maxwell equations with sources and the second one is an identity called the Bianchi identity. This identity gives the equations $\vec{\nabla} \cdot \vec{B} = 0$, $\vec{\nabla} \times \vec{E} + \partial_t \vec{B} = 0$.

A_μ is called a vector field and the particle associated with it is the photon. It has spin-1 and 2 independent polarizations. It is worth reviewing how this conclusion is reached.

As we will soon see more carefully, particles can be thought of as excitations of fields in empty spacetime. We start with the equation:

$$\partial_\mu F^{\mu\nu} = 0, \implies \partial_\mu(\partial^\mu A^\nu - \partial^\nu A^\mu) = 0. \quad (9)$$

Now as you may know $F_{\mu\nu}$ remains invariant under the gauge transformation:

$$A_\mu \rightarrow A_\mu + \partial_\mu \chi. \quad (10)$$

This symmetry enables us to choose a gauge. For instance suppose we start with a solution A_μ such that $\partial_\mu A^\mu \neq 0$. Then gauge transforming to \hat{A}_μ enables us to consider:

$$\hat{\partial}_\mu A^\mu = \partial_\mu A^\mu + \partial^2 \chi. \quad (11)$$

Now we can choose χ such that $\partial_\mu A^\mu + \partial^2 \chi = 0$. So we can choose what is called the Lorentz gauge:

$$\partial_\mu A^\mu = 0, \quad (12)$$

because of this gauge freedom. This leads to a simplified equation from eq.(9):

$$\partial^2 A^\mu = 0. \quad (13)$$

(I am using obvious re-labelling of indices). Now note that this equation is similar to the massless scalar Klein-Gordon equation! At the classical level, this enables us to analyse both equations using similar (but not identical due to the vector index) tools.

There is another field that you may encounter which is called the spinor. There are various kinds of spinors (Dirac, Weyl, Majorana). They are denoted by

$$\psi_a(x^\mu) \quad (14)$$

where a is called a spinor-index. We will see what this means in the next lecture.

2 Solutions to the classical equation

Now let us consider solutions to the classical equations. Let us start with the massless KG equation. Explicitly this reads:

$$(\partial_t^2 - \partial_x^2 - \partial_y^2 - \partial_z^2 + m^2)\phi = 0. \quad (15)$$

It is easy to show that $\phi(x^\mu) = \exp(iEt - i\vec{p}.\vec{x})$ solves the above equation provided

$$E^2 = \vec{p}^2 + m^2, \quad (16)$$

holds. This, of course, means that choosing $E = +\sqrt{\vec{p}^2 + m^2}$, we will get 2 solutions $\exp(iEt - i\vec{p}.\vec{x})$ and $\exp(-iEt + i\vec{p}.\vec{x})$. These are written compactly using the 4-vector dot product as $\exp(\pm i\vec{p}.\vec{x})$. These are called "plane-wave" solutions. We will omit the dot sign for notational simplicity. Hopefully, this will not cause any confusion. Note that it is also clear that for any \vec{p} obeying eq.(16), we can superpose these plane-wave solutions giving the most general solution to be:

$$\phi(x) = \int \frac{d^3 \vec{p}}{(2\pi)^3} (a(p) \exp(-ipx) + a^*(p) \exp(ipx)). \quad (17)$$

a, a^* are complex conjugates of each other if ϕ is real. Since $p_0^2 = E^2 = \vec{p}^2 + m^2$, the p dependence on a, a^* is on \vec{p} . In other words, we can use either $a(p)$ or $a(\vec{p})$.

What about A_μ ? In Lorentz gauge it satisfies $\partial^2 A_\mu = 0$ and hence we should have a solution that looks like:

$$A_\mu(x) = \int \frac{d^3 \vec{p}}{(2\pi)^3} [a_\mu(p) \exp(-ipx) + a_\mu^*(p) \exp(ipx)]. \quad (18)$$

Further, since $\partial^2 A_\mu = 0$, we must have $p^2 = 0$, which is what we expect from a massless particle. This, however, misses a key fact which we know. There should be a polarization vector associated with A_μ . Thus, we should write:

$$a_\mu(p) \rightarrow \epsilon_\mu^{(s)}(p) a_{(s)}(p). \quad (19)$$

Why did we introduce this additional complication in (s) ? The reason is because there are multiple independent polarization vectors (for the photon in 3+1 d, it is 2 as we will shortly see). Thus we should allow for these possibilities and sum over them. Thus, we have:

$$A_\mu(x) = \sum_s \int \frac{d^3 \vec{p}}{(2\pi)^3} [\epsilon_\mu^{(s)} a_{(s)}(p) \exp(-ipx) + \epsilon_\mu^{*(s)} a_{(s)}^*(p) \exp(ipx)] . \quad (20)$$

Since $A_\mu = (a, b, c, d) = a(1, 0, 0, 0) + b(0, 1, 0, 0) + c(0, 0, 1, 0) + d(0, 0, 0, 1)$, a 4-vector, we may have expected that we have 4 independent polarization vectors: $(1, 0, 0, 0), (0, 1, 0, 0), (0, 0, 1, 0), (0, 0, 0, 1)$. However, recall the following. To reach this point, we need to ensure that $\partial_\mu A^\mu = 0$ holds. Further, since In momentum space, this condition reads:

$$p \cdot \epsilon = 0 . \quad (21)$$

Instead of choosing a general p_μ , let us choose

$$p = (E, 0, 0, E)$$

which obeys $p^2 = 0$. To satisfy $p \cdot \epsilon = 0$ for $\epsilon = (a, b, c, d)$, we must have $a = d$. Hence, it would seem at this stage that $\epsilon = a(1, 0, 0, 1) + b(0, 1, 0, 0) + c(0, 0, 1, 0)$ giving 3 independent polarization vectors. But there is a key point here. We could have also used:

$$\epsilon = (a, b, c, a) + \alpha p = (a, b, c, a) + \alpha(E, 0, 0, E) = (a + \alpha E, b, c, a + \alpha E)$$

for any α and using $p^2 = 0$, we would be able to satisfy $p \cdot E = 0$. This additional freedom to shift $\epsilon \rightarrow \epsilon + \alpha p$ is called a **residual gauge transformation**. Using this we can write $\epsilon = (0, b, c, 0) = b(0, 1, 0, 0) + c(0, 0, 1, 0)$ giving the correct count of 2 independent polarizations. Thus (s) in the sum in A_μ above takes values $s = 1, 2$.

The form in eq.(20) is same for other tensor fields, with ϵ_μ replaced by the corresponding polarization tensor.

3 Heuristic quantization

I will not go into explicit details about canonical quantization, which you can find in standard QFT textbooks. Here, I will present some heuristic arguments, which are shortcuts to remember how the field quantization works. Let us consider the scalar field (the argument for the vector case or any other case is similar). First, we want to promote ϕ to be an operator. For historical reasons, this is called "second quantization". We can write:

$$\hat{\phi}(x) = \int \frac{d^3 \vec{p}}{(2\pi)^3} [\hat{a}(p) \exp(-ipx) + \hat{a}^\dagger(p) \exp(ipx)] . \quad (22)$$

On the rhs, we have promoted a, a^* to be operators. Let us define them in the following way. First let us define the free or non-interacting vacuum $|0\rangle$ so that

$$a(p)|0\rangle = 0 . \quad (23)$$

$a(p)$ is called an annihilation operator. Further, let us define the action of $a^\dagger(p)$ such that

$$a^\dagger(p)|0\rangle = |\vec{p}\rangle . \quad (24)$$

In other words, $a^\dagger(p)$ creates from the vacuum a single particle momentum state $|\vec{p}\rangle$. The conjugate of this condition is:

$$\langle 0|a(p) = \langle \vec{p}|. \quad (25)$$

Now as in usual quantum mechanics we want

$$\langle \vec{k}|\vec{p}\rangle = (2\pi)^3\delta^{(3)}(\vec{p} - \vec{k}). \quad (26)$$

The lhs can be written as

$$\langle 0|a(k)a^\dagger(p)|0\rangle.$$

If we have

$$[a(k), a^\dagger(p)] = (2\pi)^3\delta^{(3)}(\vec{p} - \vec{k}), \quad (27)$$

then the condition in eq.(26) will be satisfied. The last commutation relation should remind you of the simple harmonic oscillator (you have to choose $p = k$ and imagine $\delta^{(3)}(0)$ to be a constant! This last bizarre fact is in fact something we use in QFT. We can regularize the infinite volume of spacetime by considering a box of volume V in which case $\delta^{(3)}(\vec{p}) = \int d^3x \exp(i\vec{p}\cdot\vec{x})$ so that putting $\vec{p} = 0$ we have $\delta^{(3)}(0) = \int d^3x = V.$

Now let me heuristically motivate why what we have done is a sensible thing to do. First, let us ask what do we expect from the operator $\hat{\phi}(x)$. Let us consider $t = 0$. We expect that $\hat{\phi}(0, \vec{x})|0\rangle$ should create a particle at position \vec{x} , in other words,

$$\hat{\phi}(0, \vec{x})|0\rangle = |\vec{x}\rangle. \quad (28)$$

To see that indeed this is the case, we compute

$$\langle \vec{k}|\hat{\phi}(0, \vec{x})|0\rangle = \langle \vec{k}|\vec{x}\rangle. \quad (29)$$

The rhs is the conjugate of $\langle \vec{x}|\vec{k}\rangle$ which is nothing but the position space wave function for $|\vec{k}\rangle$. We have

$$\langle \vec{x}|\vec{k}\rangle = e^{i\vec{k}\cdot\vec{x}} \implies \langle \vec{k}|\vec{x}\rangle = e^{-i\vec{k}\cdot\vec{x}}. \quad (30)$$

You should be able to readily verify (this was done in the lecture, but I would encourage you to practice independently) using eqs. (22)(23)(24)(26) that

$$\langle \vec{k}|\hat{\phi}(0, \vec{x})|0\rangle = \langle \vec{k}|\vec{x}\rangle = e^{-i\vec{k}\cdot\vec{x}}, \quad (31)$$

indeed holds.

The key quantization elements we have introduced are the conditions in eqs.(23)(24) to define the vacuum and a single particle state and the commutation relation in eq.(27).

Now unlike the harmonic oscillator case in quantum mechanics, we can create multiparticle states using:

$$|p_1, p_2, p_3, \dots, p_n\rangle = a^\dagger(p_1)a^\dagger(p_2)a^\dagger(p_3)\cdots a^\dagger(p_n)|0\rangle, \quad (32)$$

which defines an n -particle state. Thus instead of talking about a Hilbert space associated with a single particle, we talk about a Fock space associated with multiparticles.

In the case of A_μ , the single particle (single photon) state is

$$a_{(s)}^\dagger(p)|0\rangle = |p, s\rangle \quad (33)$$

where s now is an additional label for the polarization that the creation operator has created.

One of the main goals in QFT is to calculate the probability that particular scattering has happened. For instance let us consider $|in\rangle = |p_1, p_2\rangle$ as the 2 scalar particle states having momenta p_1, p_2 . Let us define $|out\rangle = |p_3, p_4\rangle$ as the 2 scalar particle state having momenta p_3, p_4 . Let us imagine that the $|in\rangle$ state is time-evolved by some Hamiltonian (which includes interactions) to the $|out\rangle$ state. Then we will be interested in calculating the scattering amplitude:

$$S = \langle out|in\rangle. \quad (34)$$

The whole machinery of Feynman diagrams was invented to calculate these quantities in perturbation theory. We will not consider a perturbative expansion in this course (except for carrying out some sanity checks, perhaps). A main objective will be to simulate the time-evolution of the in-state to the out-state on a quantum computer. But before we go there, we still need to build some more understanding of QFT, both from the point of view of what will come next in the course as well as for some background knowledge.

Lecture 3: Particles from Fields

Aninda Sinha^{1,2}

¹Centre for High Energy Physics, Indian Institute of Science, India.

²Department of Physics and Astronomy, University of Calgary, Canada.

August 13, 2025

Contents

1 How to think about the Quantum field	1
1.1 Wigner's classification theorem	1
1.2 The background geometry	3
1.3 Unitary IRREPs	5
1.4 Scalar example in Minkowski, dS and AdS	7

This lecture is based on chapter 2,8,10 of MS.

1 How to think about the Quantum field

In this section, I hope to convey to you how to think about the quantum field in many situations that physicists are interested in. For this, we will need some basic background material. First, we need to define what we mean by a particle: A particle is a unitary irreducible representation of the symmetry group; in flat space the symmetry group is the Poincaré group. To understand all this a bit more, I will ask you to bear with me as I take you on a brief detour. From MS, we will need chapters 2,6,7,8,10 and what follows below is a lightning review of these chapters. **Note: we will only try to focus on the logical flow of the arguments, rather than get lost in the details.**

1.1 Wigner's classification theorem

If you want a proof of Wigner's classification theorem, then I urge you to read Weinberg's treatment in his Quantum Fields book, chapter 2, vol I. Here, we will just quote the theorem and focus on the representations of the Poincare group.

Remember: Particles come from Wigner's classification. Fields come from the irreps of the Poincare group.

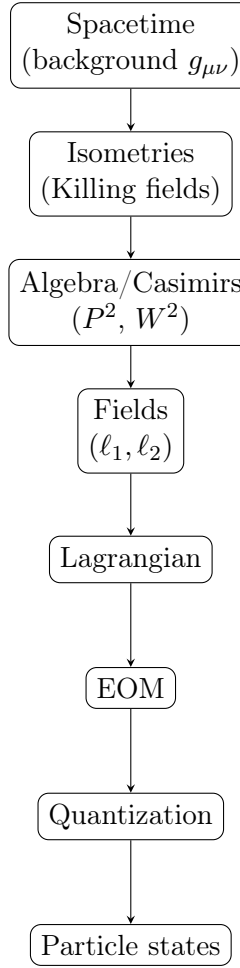


Figure 1: Logical flow in the lecture: from geometry to particle content.

What do we mean by this? In quantum mechanics, we would like to label a particle by the quantum numbers associated with a complete set of commuting observables. We further would like the state vector in the Hilbert space, to correspond to a unitary representation (to admit the probability interpretation). So we need some object, that in momentum space looks like:

$$|p, \sigma\rangle$$

where p is the 4-momentum satisfying $p^2 = m^2$ and σ are the other possible quantum numbers. Wigner showed 2 important things:

1. There are NO finite dimensional unitary irreducible representations of the Poincare group.
2. Wigner showed that particles in 3+1 dimensions are labeled by their masses m (already introduced above) and a spin quantum number J which can take values $0, 1/2, 1, \dots$. The label $p^2 = m^2 = E^2 - \vec{p}^2$ assumes $E > 0$ and because there are infinitely many ways to satisfy this constraint, it would mean the representations are infinite dimensional.

Our job then is to figure out the (non-unitary) irreducible representations of the Poincare group and how $|p, \sigma\rangle$ fits into them.

To talk about the irreps of the Poincare group, it is useful to introduce the notion of a spacetime metric. This will enable us to think about quantum field theory more generally. I hope to convey the flavour of the arguments.

1.2 The background geometry

To set the stage, let us consider the line element on a 2d plane. This just follows from Pythagoras' theorem and its infinitesimal form is given by

$$ds^2 = dx^2 + dy^2.$$

You can think of $dx = x_1 - x_2$ where x_1, x_2 are two nearby points. A general line element can be written as

$$ds^2 = g_{\mu\nu} dx^\mu dx^\nu. \quad (1)$$

$g_{\mu\nu}$ is called the spacetime metric tensor (you can think of this as a symmetric matrix). Here μ, ν run from $0, 1, 2 \dots d$, where we are in d space and 1 time dimension (so $d+1$ in short). We have used Einstein summation convention. For the 2d plane example above, we have $\mu, \nu \in \{1, 2\}$ (here there is no time direction; we will reserve the label 0 for time and $1, 2, \dots d-1$ for space). Explicitly, the only non-zero $g_{\mu\nu}$ are $g_{11} = 1 = g_{22}$.

In principle, $g_{\mu\nu}$ can be taken to be whatever you want and it can also depend on all the spacetime coordinates. However, there is a famous dynamical equation whose solution gives us $g_{\mu\nu}$ —The Einstein-Hilbert equations. They read

$$G_{\mu\nu} = T_{\mu\nu}.$$

Here $G_{\mu\nu}$ is the Einstein tensor and $T_{\mu\nu}$ is the stress-energy tensor. I have suppressed a conventional $8\pi G_{\text{Newton}}$ factor on the RHS. We don't need to know what these tensors are except that such an equation exists! The equation transforms "nicely" under general coordinate transformations. For instance under infinitesimal (meaning ξ below is "small") transformations like

$$x^\mu \rightarrow x^\mu + \xi^\mu(x)$$

leaves the lhs invariant. So we can do general coordinate transformations and present the solution in different forms. This is similar in spirit to gauge transformations in electromagnetism. Specifically, the analog is

$$A_\mu \rightarrow A_\mu + \partial_\mu \xi :: \quad g_{\mu\nu} \rightarrow g_{\mu\nu} + \partial_\mu \xi_\nu + \partial_\nu \xi_\mu.$$

The A_μ transformation is called a $U(1)$ gauge transformation while the transformation on $g_{\mu\nu}$ is called a diffeomorphism.

When $T_{\mu\nu} = 0$, one solution is indeed Minkowski spacetime (including the 2d plane example above). Minkowski spacetime takes the form:

$$ds^2 = -dt^2 + dx^2 + dy^2 + dz^2, \quad (2)$$

where we have assumed $3+1$ dimensional spacetime. Sometimes, we also write $ds^2 = dt^2 - dx^2 - dy^2 - dz^2$. The former case is called the $(-+++)$ or the mostly positive signature while the latter is the $(+-+-+)$ or the mostly negative signature. The Minkowski metric is conventionally denoted by $\eta_{\mu\nu}$. No one told you that there has to be only 1 time direction. This is an assumption.

A simple situation is when $T_{\mu\nu} = \Lambda g_{\mu\nu}$. Λ is called the cosmological constant. Depending on the sign of the constant, we now have (again 3 + 1 dimensions) either the de Sitter (name of a person) metric (dS in short, relevant for cosmology)—a choice of this metric is:

$$ds^2 = -dt^2 + e^{2Ht}(dx^2 + dy^2 + dz^2), \quad (3)$$

where the H is called the Hubble constant/Hubble parameter and is taken to be positive. This form of the metric suggests that the rulers associated with ds^2 will have the spatial volume to be increasing as t increases.

The opposite sign choice of the cosmological constant gives the anti de Sitter space (AdS). This plays a role in the famous AdS/CFT correspondence. A choice of coordinates is:

$$ds^2 = dr^2 + e^{2r/L}(-dt^2 + dx^2 + dy^2). \quad (4)$$

where L defines the “AdS radius”. For dS and AdS, the H and L are related to Λ . Minkowski, dS and AdS are called the maximally symmetric spacetimes.

Now, we said that a particle is a unitary irrep of the symmetry group. What is the symmetry group? First, we define “isometries” as any coordinate transformations (the $\xi(x)$ in $x^\mu \rightarrow x^\mu + \xi^\mu(x)$) which leave the metric invariant. For the 2d plane $ds^2 = dx^2 + dy^2$, we can see an obvious one: $x \rightarrow x + a, y \rightarrow y + b$ where a, b are constants. These will leave dx, dy invariant. These are nothing but translation of coordinates. Another transformation that we know of is rotation. This corresponds to

$$x^i \rightarrow \Omega_j^i x^j.$$

We can write explicitly

$$\begin{pmatrix} x' \\ y' \end{pmatrix} = \begin{pmatrix} \cos \theta & \sin \theta \\ -\sin \theta & \cos \theta \end{pmatrix} \begin{pmatrix} x \\ y \end{pmatrix}. \quad (5)$$

This leaves

$$x'^2 + y'^2 = x^2 + y^2.$$

Now the infinitesimal form can be found by expanding the rotation matrix to linear order around $\theta = 0$ giving

$$\begin{pmatrix} x' \\ y' \end{pmatrix} = \begin{pmatrix} x \\ y \end{pmatrix} + \theta \begin{pmatrix} 0 & 1 \\ -1 & 0 \end{pmatrix} \begin{pmatrix} x \\ y \end{pmatrix}. \quad (6)$$

Here θ “parametrizes” the infinitesimal transformation. This leads to

$$dx' = dx + \theta dy, \quad dy' = dy - \theta dx. \quad (7)$$

You can see that $dx'^2 + dy'^2 = dx^2 + dy^2 + O(\theta^2)$,

As is obvious, setting $\theta = 0$ recovers the original choice of x, y . The matrix $\Omega = \begin{pmatrix} 0 & 1 \\ -1 & 0 \end{pmatrix}$ is called the generator of the transformation. Clearly $\Omega\Omega^T = Id$, with Id being the 2×2 identity matrix. In general, the rotation group generators are orthogonal matrices. Now let us consider the Minkowski metric in 1+1d: $ds^2 = -dt^2 + dx^2$. The infinitesimal transformations:

$$dx' = dx - \zeta dt, \quad dt' = dt - \zeta dx, \quad (8)$$

will leave the line element invariant. This infinitesimal transformation arises from:

$$\begin{pmatrix} \cosh \zeta & -\sinh \zeta \\ -\sinh \zeta & \cosh \zeta \end{pmatrix}$$

where ζ is called the rapidity and is related to $\beta = v/c$ via $\zeta = \tanh^{-1} \beta$. This defines the Lorentz transformations. In 1+1 dimension, we have translations parametrized by 2 parameters (one for space, one for time) and the Lorentz transformation (parametrized by ζ). The number of parameters is 3 and is the same as for the 2d plane. Each parameter is associated with a generator of the transformation so in 1+1 dimensions, we have 3 generators in all. There is a conserved quantity associated with each of these symmetries. For time translation symmetry, we have energy conservation; for space translation, we have momentum conservation; (hw: research and find out what is conserved due to the boost symmetry!).

In 3+1 dimensions, the counting goes as follows. We have 3 parameters associated with the boosts (we can boost in x, y, z directions), 3 parameters associated with the rotations (3 Euler angles) and finally 4 parameters associated with the translations of the four spacetime coordinates. So we have 10 generators in all. Now it turns out that the count is the same for 4d dS as well as 4d AdS spaces. However, the interpretations are different. For instance, in the dS case (look at the metric presented above), we do not have time translation symmetry! You will frequently see the terminology $\mathbf{R}^{3,1} \rtimes O(3, 1)$ for Minkowski, $SO(4, 1)$ for dS and $SO(3, 2)$ for AdS. You can read about these on wikipedia or chatGPT!

For the Minkowski case, if we represent the spacetime metric by η and the Lorentz transformation as $x^\mu \rightarrow \Lambda^\mu{}_\nu x^\nu$, then

$$\Lambda^\mu{}_\alpha \Lambda^\nu{}_\beta \eta^{\alpha\beta} = \eta^{\mu\nu}.$$

This just follows from the invariance of $x^\mu x_\mu$, which is the definition of Λ .

There are also discrete symmetries (not connected to the identity). Parity ($x^i \rightarrow -x^i$), Time reversal ($t \rightarrow -t$) and also charge conjugation which applies on the electric charge (an additional quantum label). They are denoted by *P.T.C* respectively and form an important set of discrete symmetries.

1.3 Unitary IRREPs

Now that we have some idea about isometries, we can talk about unitary IRREPs. IRREP stands for irreducible representation. This means the following. In quantum mechanics (and quantum field theory) we represent a single particle in terms of a state vector in a Hilbert space. The state vector can be made of many components (eg spin). For instance for the electron in 3+1 dimension, we can label the state vector by spin. So in this case the state vector looks like $|\psi\rangle \in \{|\uparrow\rangle, |\downarrow\rangle\}$. The symmetry transformation acting on the spin part leaves the state in the “same space”, meaning that we do not have to add any other label for the spin. The minimum number of components that are mixed into each other by the symmetry transformations forms the irreducible representation.

Now for the Poincaré group, here is the catch. There is a well-known theorem called Wigner’s classification theorem which says that there are no finite-dimensional irreducible representation of this group, but there are infinite-dimensional ones. Wigner also showed that these representations are classified by mass m (a non-negative real number) and spin J (non-negative half integer). For $m > 0$ a spin- J particle has $2J + 1$ independent states in the representation. For $m = 0$ there are exactly 2 states. Let us delve a bit deeper into this.

In quantum mechanics, the action of symmetry transformations is in terms of unitary transformations. Let us write the Lorentz transformation and translations on the coordinates like:

$$x'^\mu = \Lambda^\mu{}_\nu x^\nu + a^\mu.$$

For this the unitary transformation is represented by

$$U(\Lambda, a) = 1 + i\omega_{\mu\nu} M^{\mu\nu} + ia_\mu P^\mu$$

where we have considered infinitesimal transformations parametrized by $\omega_{\mu\nu}, a_\mu$ and called the generators of the transformations $M^{\mu\nu}, P^\mu$. The factors of i ensure that M, P are Hermitian operators with ω, a real to ensure that U is a unitary operator. Using the fact that $U(\Lambda_1, a_1)U(\Lambda_2, a_2) = U(\Lambda_1\Lambda_2, a_1 + a_2)$, $U(\Lambda)M_{\mu\nu}U^{-1}(\Lambda) = \Lambda^\alpha{}_\mu\Lambda^\beta{}_\nu M_{\alpha\beta}$ and $U(\Lambda)P_\mu U^{-1}(\Lambda) = \Lambda^\alpha{}_\mu P_\alpha$ judiciously (see Weinberg vol 1 for details), we can find the Poincaré algebra:

$$i[M^{\mu\nu}, M^{\rho\sigma}] = \eta^{\nu\rho}M^{\mu\sigma} - \eta^{\mu\rho}M^{\nu\sigma} - \eta^{\sigma\mu}M^{\rho\nu} + \eta^{\sigma\nu}M^{\rho\mu}, \quad (9)$$

$$i[P^\mu, M^{\rho\sigma}] = \eta^{\mu\rho}P^\sigma - \eta^{\mu\sigma}P^\rho, \quad (10)$$

$$i[P^\mu, P^\nu] = 0. \quad (11)$$

We can write the matrix M of generators as:

$$M^{\mu\nu} = \begin{pmatrix} 0 & K_1 & K_2 & K_3 \\ -K_1 & 0 & J_3 & -J_2 \\ -K_2 & -J_3 & 0 & J_1 \\ -K_3 & J_2 & -J_1 & 0 \end{pmatrix} \quad (12)$$

and defining

$$J_i^+ = \frac{1}{2}(J_i + iK_i), \quad J_i^- = \frac{1}{2}(J_i - iK_i)$$

, we will find 2 copies of the angular momentum algebra:

$$[J_i^+, J_j^+] = i\epsilon_{ijk}J_k^+, \quad (13)$$

$$[J_i^-, J_j^-] = i\epsilon_{ijk}J_k^-, \quad (14)$$

$$[J_i^+, J_j^-] = 0. \quad (15)$$

In other words, we can think of the representation as arising from a tensor product of the representations of the 2 angular momentum algebras since they do not talk to each other. Now recall how we worked out representation of the angular momentum algebra (I am assuming you remember this, else you will have to revise!). These representations were matrices of different dimensions. The representations were labelled by ℓ, m where $\ell(\ell + 1)$ was the eigenvalue of $J^2 = J_1^2 + J_2^2 + J_3^2$ and $m = -\ell, -\ell + 1, \dots, 0, \dots, \ell$, i.e., $2\ell + 1$ dimensional. In the case at hand, the representations will be labeled by two ℓ_1, ℓ_2 and will be $(2\ell_1 + 1)(2\ell_2 + 1)$ dimensional. Concisely we label the representations by (ℓ_1, ℓ_2) . We note some common representations below:

(ℓ_1, ℓ_2)	dim	name
(0,0)	1	scalar
(0,1/2)	2	Weyl spinor (r)
(1/2,0)	2	Weyl spinor (l)
$(1/2, 0) \oplus (1/2, 0)$	4	Dirac spinor
(1/2,1/2)	4	A_μ
$(1, 1) \oplus (0, 0)$	10	$g_{\mu\nu}$
$(1, 1/2) \oplus (1/2, 1)$	6	gravitino, ψ_μ

Table 1: Various representations and their field notations.

This table contains a lot of information. For instance $(0, 1/2)$ also tells us that we are supposed to find 2×2 matrices which satisfies the angular momentum algebra for J^- while acting trivially for J^+ . This is of course provided by the Pauli matrices! We need to specify how these spinors transform. Recall that the infinitesimal version should look like (omitting the trivial translation part)

$$1 + i\omega_{\mu\nu}M^{\mu\nu}$$

. This can be worked out and calling the $(1/2, 0)$ representation as ψ_R we find

$$\psi_R \rightarrow (1 + \frac{i}{2}\theta_j\sigma_j + \frac{1}{2}\beta_j\sigma_j)\psi_R \quad (16)$$

where θ_i are the 3 angles and β_i are the 3 boost parameters (both sets are real). Now this explicit form makes it clear that these representations are not unitary. Thus, although we found finite dimensional representations for the $M_{\mu\nu}$ in the form of the Pauli matrices, the resulting representations are not unitary. To fix this problem, we have to embed these particles into fields and write down an appropriate Lagrangian. For instance, for the scalar case, we hope to put the state into a field $\phi(x)$, where x is a continuous spacetime label. Now let us consider the spin-1 case which will illustrate the point more nicely.

According to Wigner's theorem, a massive spin-1 particle has 3 independent degrees of freedom. Let us write a state $|\psi\rangle = c_0|A_0\rangle + c_1|A_1\rangle + c_2|A_2\rangle + c_3|A_3\rangle$. The naive norm of this state is $|c_0|^2 + |c_1|^2 + |c_2|^2 + |c_3|^2$ but this is not Lorentz invariant. The Lorentz invariant norm is $\pm(-|c_0|^2 + |c_1|^2 + |c_2|^2 + |c_3|^2)$ but this is not positive definite. It could be positive definite if we could project out the 0-component. The Lagrangian approach enables us to solve precisely this problem. We write an action for $A_\mu(x)$, which turns out to be that of the Proca Lagrangian for the massive case and the Maxwell Lagrangian for the massless case. Lorentz invariance and unitarity fix the lowest order forms of these Lagrangians. By lowest order, we mean at the two-derivative order; involving terms like $F_{\mu\nu}F^{\mu\nu}$ and not higher derivative terms like $(F_{\mu\nu}F^{\mu\nu})^2$. What we call gauge invariance is a consequence of Lorentz invariance and unitarity. If you want to see how this works, you should read chapter 8 in Matthew Schwartz's book.

1.4 Scalar example in Minkowski, dS and AdS

How do we go about quantizing? Typically, we always start with a classical Lagrangian which is motivated by symmetries. There is in fact a nice way to do this in any fixed background. Consider the case of a free (quadratic/Gaussian) massive scalar. We will be cavalier about the signs for now. As discussed above, the field for this is just $\phi(x)$. There are no spacetime indices on this

object. We want an action such that the equations of motion are (to get $E^2 = \vec{p} \cdot \vec{p} + m^2$):

$$(-\partial_0^2 + \partial_i \partial^i - m^2)\phi = 0.$$

An action that does this is

$$S = -\frac{1}{2} \int d^4x \left[(\partial_\mu \phi)(\partial^\mu \phi) + m^2 \phi^2 \right]. \quad (17)$$

Say, we work in the mostly positive signature $(-+++)$. Now in a general background, this changes only a bit. The above action was written keeping Minkowski in mind. For a general spacetime, we write:

$$S = -\frac{1}{2} \int d^4x \sqrt{|g|} \left[(\partial_\mu \phi)(\partial_\nu \phi) g^{\mu\nu} + m^2 \phi^2 \right]. \quad (18)$$

Now here I have explicitly showed how indices are contracted (in the manner I have showed, they are contracted using the inverse metric $g^{\mu\nu}$). We can work out the equations of motion from here by using the variational principle. We vary the action by varying the fields. Here we keep the background metric fixed. So we have

$$\delta S = -\frac{1}{2} \int d^4x \sqrt{|g|} \left[(\partial_\mu \delta \phi)(\partial_\nu \phi) g^{\mu\nu} + (\partial_\mu \phi)(\partial_\nu \delta \phi) g^{\mu\nu} + 2m^2 \phi \delta \phi \right], \quad (19)$$

$$= - \int d^4x \sqrt{|g|} \left[(\partial_\mu \delta \phi)(\partial_\nu \phi) g^{\mu\nu} + m^2 \phi \delta \phi \right], \quad (20)$$

$$= - \int d^4x \left[\partial_\mu (\sqrt{|g|} \delta \phi)(\partial_\nu \phi) g^{\mu\nu} - \delta \phi \partial_\mu (\sqrt{|g|} (\partial_\nu \phi) g^{\mu\nu}) + m^2 \sqrt{|g|} \phi \delta \phi \right], \quad (21)$$

$$= - \int d^4x \sqrt{|g|} \delta \phi \left[-\frac{1}{\sqrt{|g|}} \partial_\mu (\sqrt{|g|} (\partial_\nu \phi) g^{\mu\nu}) + m^2 \phi \right], \quad (22)$$

$$= 0. \quad (23)$$

Here, going to the second line, we have used the fact that the metric symmetric. Going from the third line to the fourth line, we have dropped the surface term. Thus the final form of the equation of motion for the scalar in a curved background is:

$$-\frac{1}{\sqrt{|g|}} \partial_\mu (\sqrt{|g|} (\partial_\nu \phi) g^{\mu\nu}) + m^2 \phi = 0. \quad (24)$$

For Minkowski, we get

$$(-\partial_\mu \partial^\mu - m^2)\phi = 0, \quad (25)$$

which is exactly what we wanted.

We note down the equations for dS and AdS (hw)

$$\text{dS} : -e^{-2Ht} (\partial_i \partial_i) \phi + e^{-3Ht} \partial_t (e^{3Ht} \partial_t \phi) + m^2 \phi = 0, \quad (26)$$

$$\text{AdS} : -e^{-2r/L} (-\partial_t^2 + \partial_i \partial_i) \phi - e^{-3r/L} \partial_r (e^{3r/L} \partial_r \phi) + m^2 \phi = 0. \quad (27)$$

There is a bit more to discuss before we are in a position to start quantum computing! So hang in there.

Lecture 6: Hamiltonians

Aninda Sinha^{1,2}

¹Centre for High Energy Physics, Indian Institute of Science, India.

²Department of Physics and Astronomy, University of Calgary, Canada.

September 2, 2025

Contents

1 Noether's Theorem for the Point Particle	2
1.1 Setup	2
1.2 Arbitrary Variation (On-Shell)	2
1.3 Symmetry Variation	2
1.4 Conserved Quantity	2
1.5 Time Translation	3
2 Field Theory: Noether's Theorem and Hamiltonian	3
2.1 Setup	3
2.2 Arbitrary Variation	3
2.3 Symmetry Variation	3
2.4 Noether Current	3
2.5 Spacetime Translations	4
2.6 Conserved Charges from the Divergence Theorem	4
3 Hamiltonians in de Sitter Space	5
3.1 Metric and Lagrangian	5
3.2 Field Redefinition	5
3.3 From ϕ to $\chi = a^{\frac{d-1}{2}}\phi$: detailed algebra, IBP, and boundary terms	5
3.4 Remarks	7
3.5 Flat-space limit $H \rightarrow 0$ in $d = 3$: recovery of $\lambda\phi^4$	7

Lectures 4 and 5 were online with Ujjwal showing how to install python.

1 Noether's Theorem for the Point Particle

1.1 Setup

Consider a point particle with generalized coordinates $q^i(t)$ and Lagrangian

$$L(q, \dot{q}, t), \quad S[q] = \int dt L(q, \dot{q}, t).$$

Let $\bar{q}(t)$ denote a classical solution (i.e. on-shell). We consider two types of variations:

1. An *arbitrary variation* δq^i .
2. A *symmetry variation* δq_s^i , defined such that the Lagrangian changes by a total derivative.

1.2 Arbitrary Variation (On-Shell)

The variation of the action is

$$\delta S = \int dt \left(\frac{\partial L}{\partial q^i} \delta q^i + \frac{\partial L}{\partial \dot{q}^i} \delta \dot{q}^i \right).$$

Integrating by parts,

$$\delta S = \int dt \left[\left(\frac{\partial L}{\partial q^i} - \frac{d}{dt} \frac{\partial L}{\partial \dot{q}^i} \right) \delta q^i \right] + \frac{\partial L}{\partial \dot{q}^i} \delta q^i \Big|_{t_1}^{t_2}.$$

On-shell, $\bar{q}(t)$ satisfies the Euler–Lagrange equations, so the bulk term vanishes. Thus,

$$\delta S \Big|_{\bar{q}} = p_i \delta q^i \Big|_{t_1}^{t_2}, \quad p_i \equiv \frac{\partial L}{\partial \dot{q}^i}.$$

1.3 Symmetry Variation

Suppose under a symmetry transformation $q^i \rightarrow q^i + \delta q_s^i$, the Lagrangian changes as

$$\delta_s L = \frac{dF}{dt}.$$

Then the action changes as

$$\delta_s S = F \Big|_{t_1}^{t_2}.$$

Evaluating on the solution \bar{q} ,

$$\delta_s S \Big|_{\bar{q}} = F \Big|_{t_1}^{t_2}.$$

1.4 Conserved Quantity

We now compare the two expressions. In the arbitrary variation formula we set $\delta q^i = \delta q_s^i$, while in the symmetry variation we evaluate on \bar{q} . Subtracting, we obtain

$$(p_i \delta q_s^i - F) \Big|_{t_1}^{t_2} = 0.$$

Thus the quantity

$$Q = p_i \delta q_s^i - F$$

is conserved: $\frac{dQ}{dt} = 0$.

1.5 Time Translation

For time translations $t \rightarrow t + \epsilon$,

$$\delta q_s^i = \dot{q}^i \epsilon, \quad F = L\epsilon.$$

Hence

$$Q = \sum_i p_i \dot{q}^i - L \equiv H,$$

which is the Hamiltonian. Thus, if the system is time-translation invariant, H is conserved.

2 Field Theory: Noether's Theorem and Hamiltonian

2.1 Setup

Consider a field $\phi(x)$ in $d+1$ dimensional Minkowski space with Lagrangian density

$$\mathcal{L}(\phi, \partial_\mu \phi).$$

2.2 Arbitrary Variation

The variation of the action is

$$\delta S = \int d^{d+1}x \left(\frac{\partial \mathcal{L}}{\partial \phi} \delta \phi + \frac{\partial \mathcal{L}}{\partial \partial_\mu \phi} \delta (\partial_\mu \phi) \right).$$

Integrating by parts,

$$\delta S = \int d^{d+1}x \left[\left(\frac{\partial \mathcal{L}}{\partial \phi} - \partial_\mu \frac{\partial \mathcal{L}}{\partial \partial_\mu \phi} \right) \delta \phi \right] + \int d^{d+1}x \partial_\mu \left(\frac{\partial \mathcal{L}}{\partial \partial_\mu \phi} \delta \phi \right).$$

On-shell,

$$\delta S|_{\bar{\phi}} = \int d^{d+1}x \partial_\mu \left(\frac{\partial \mathcal{L}}{\partial \partial_\mu \phi} \delta \phi \right).$$

2.3 Symmetry Variation

For a symmetry $\delta\phi_s$, suppose the Lagrangian changes as

$$\delta_s \mathcal{L} = \partial_\mu F^\mu.$$

Then

$$\delta_s S = \int d^{d+1}x \partial_\mu F^\mu.$$

2.4 Noether Current

Subtracting as before, and setting $\delta\phi = \delta\phi_s$, we obtain a conserved current

$$j^\mu = \frac{\partial \mathcal{L}}{\partial \partial_\mu \phi} \delta \phi_s - F^\mu, \quad \partial_\mu j^\mu = 0.$$

2.5 Spacetime Translations

For translations $x^\nu \rightarrow x^\nu + \epsilon^\nu$, we have $\delta\phi_s = \epsilon^\nu \partial_\nu \phi$. This yields the canonical stress-energy tensor

$$T_\nu^\mu = \frac{\partial \mathcal{L}}{\partial \partial_\mu \phi} \partial_\nu \phi - \delta_\nu^\mu \mathcal{L}, \quad \partial_\mu T_\nu^\mu = 0.$$

In particular, the Hamiltonian is

$$H = \int d^d x T_0^0.$$

2.6 Conserved Charges from the Divergence Theorem

From Noether's theorem we obtained the conserved stress-energy tensor

$$T_\nu^\mu = \frac{\partial \mathcal{L}}{\partial \partial_\mu \phi} \partial_\nu \phi - \delta_\nu^\mu \mathcal{L}, \quad \partial_\mu T_\nu^\mu = 0.$$

To extract the conserved quantities, consider the charge associated with translations in the x^ν direction:

$$Q_\nu(\eta) \equiv \int_{\mathbb{R}^d} d^d x T_\nu^0(\eta, \vec{x}).$$

The conservation law $\partial_\mu T_\nu^\mu = 0$ implies

$$\partial_0 T_\nu^0 + \partial_i T_\nu^i = 0,$$

where $i = 1, \dots, d$.

Now integrate over all space:

$$\frac{d}{d\eta} Q_\nu(\eta) = \frac{d}{d\eta} \int d^d x T_\nu^0 = - \int d^d x \partial_i T_\nu^i.$$

Applying the divergence theorem,

$$\int d^d x \partial_i T_\nu^i = \oint_{S_\infty} dS_i T_\nu^i.$$

If the fields fall off sufficiently fast at spatial infinity (so that the surface term vanishes), we obtain

$$\frac{d}{d\eta} Q_\nu(\eta) = 0.$$

Thus Q_ν is conserved in time. Explicitly:

- For $\nu = 0$,

$$Q_0 = \int d^d x T_0^0 \equiv H,$$

the Hamiltonian (energy).

- For $\nu = i$,

$$Q_i = \int d^d x T_i^0,$$

the conserved spatial momentum.

Hence the divergence theorem provides the link between the local conservation equation $\partial_\mu T_\nu^\mu = 0$ and the global conservation of the Hamiltonian and momentum.

3 Hamiltonians in de Sitter Space

3.1 Metric and Lagrangian

In $d + 1$ dimensional de Sitter space in conformal coordinates:

$$ds^2 = a(\eta)^2 (-d\eta^2 + d\vec{x}^2), \quad a(\eta) = -\frac{1}{H\eta}, \quad \eta < 0.$$

For a scalar with potential $V(\phi) = \frac{1}{2}m^2\phi^2 + \frac{\lambda}{4!}\phi^4$, the action is

$$S = \int d\eta d^d x \mathcal{L},$$

with

$$\mathcal{L} = \frac{1}{2}a^{d-1} [(\partial_\eta\phi)^2 - (\nabla\phi)^2] - \frac{1}{2}a^{d+1}m^2\phi^2 - \frac{\lambda}{4!}a^{d+1}\phi^4.$$

3.2 Field Redefinition

Define the rescaled field

$$\chi(\eta, \vec{x}) = a^{\frac{d-1}{2}}\phi(\eta, \vec{x}).$$

Then

$$\partial_\eta\phi = a^{-\frac{d-1}{2}} \left(\partial_\eta\chi - \frac{d-1}{2} \frac{a'}{a} \chi \right).$$

3.3 From ϕ to $\chi = a^{\frac{d-1}{2}}\phi$: detailed algebra, IBP, and boundary terms

Start from the scalar action in conformal coordinates (d spatial dimensions):

$$S = \int d\eta d^d x \mathcal{L}, \tag{1}$$

$$\mathcal{L} = \frac{1}{2}a^{d-1}[(\partial_\eta\phi)^2 - (\nabla\phi)^2] - \frac{1}{2}a^{d+1}m^2\phi^2 - \frac{\lambda}{4!}a^{d+1}\phi^4, \tag{2}$$

with $a(\eta)$ the scale factor, primes denoting ∂_η , and ∇ the spatial gradient.

Define the rescaled field

$$\chi(\eta, \mathbf{x}) \equiv a^{\frac{d-1}{2}}(\eta)\phi(\eta, \mathbf{x}) \iff \phi = a^{-\frac{d-1}{2}}\chi. \tag{3}$$

Then

$$\partial_\eta\phi = a^{-\frac{d-1}{2}} \left(\chi' - \frac{d-1}{2} \frac{a'}{a} \chi \right), \tag{4}$$

$$\nabla\phi = a^{-\frac{d-1}{2}}\nabla\chi. \tag{5}$$

Insert into (2). The kinetic and gradient pieces become

$$\frac{1}{2}a^{d-1}(\partial_\eta\phi)^2 = \frac{1}{2} \left(\chi' - \frac{d-1}{2} \frac{a'}{a} \chi \right)^2 = \frac{1}{2}(\chi')^2 - \frac{d-1}{2} \frac{a'}{a} \chi\chi' + \frac{(d-1)^2}{8} \frac{a'^2}{a^2} \chi^2, \tag{6}$$

$$-\frac{1}{2}a^{d-1}(\nabla\phi)^2 = -\frac{1}{2}(\nabla\chi)^2. \tag{7}$$

The potential terms become

$$-\frac{1}{2}a^{d+1}m^2\phi^2 = -\frac{1}{2}m^2a^2\chi^2, \quad (8)$$

$$-\frac{\lambda}{4!}a^{d+1}\phi^4 = -\frac{\lambda}{4!}a^{-(d-3)}\chi^4, \quad (9)$$

since $\phi^2 = a^{-(d-1)}\chi^2$ and $\phi^4 = a^{-2(d-1)}\chi^4$.

Integration by parts (IBP). The mixed term can be written as a total η -derivative plus a bulk piece:

$$-\frac{d-1}{2}\frac{a'}{a}\chi\chi' = -\frac{d-1}{4}\frac{a'}{a}\partial_\eta(\chi^2) = +\frac{d-1}{4}\partial_\eta\left(\frac{a'}{a}\right)\chi^2 - \frac{d-1}{4}\partial_\eta\left[\frac{a'}{a}\chi^2\right]. \quad (10)$$

Using $\partial_\eta\left(\frac{a'}{a}\right) = \frac{a''}{a} - \frac{a'^2}{a^2}$, the Lagrangian density becomes, *up to a total η -derivative*,

$$\mathcal{L} \simeq \frac{1}{2}(\chi')^2 - \frac{1}{2}(\nabla\chi)^2 - \frac{1}{2}m^2a^2\chi^2 + \left[\frac{d-1}{4}\frac{a''}{a} + \frac{(d-1)(d-3)}{8}\frac{a'^2}{a^2}\right]\chi^2 - \frac{\lambda}{4!}a^{-(d-3)}\chi^4, \quad (11)$$

where “ \simeq ” indicates equality modulo the total derivative $-\frac{d-1}{4}\partial_\eta\left[\frac{a'}{a}\chi^2\right]$.

It is often convenient to collect the time-dependent mass term as

$$\mathcal{L} \simeq \frac{1}{2}(\chi')^2 - \frac{1}{2}(\nabla\chi)^2 - \frac{1}{2}\mu^2(\eta)\chi^2 - \frac{\lambda}{4!}a^{-(d-3)}\chi^4, \quad (12)$$

$$\mu^2(\eta) \equiv m^2a^2 - \left[\frac{d-1}{2}\frac{a''}{a} + \frac{(d-1)(d-3)}{4}\frac{a'^2}{a^2}\right]. \quad (13)$$

Justification for dropping the total derivative. The difference between \mathcal{L} and $\tilde{\mathcal{L}}$ that omits $-\frac{d-1}{4}\partial_\eta[(a'/a)\chi^2]$ is a boundary term in the action:

$$\Delta S = -\frac{d-1}{4} \int d^d x \left[\frac{a'}{a}\chi^2\right]_{\eta_1}^{\eta_2}.$$

It does not affect the Euler–Lagrange equations. In canonical language, adding a total time derivative generates a (possibly time-dependent) canonical transformation and leaves the physics (equal-time commutators, evolution, S-matrix/in-in correlators) unchanged. Practically, the boundary term vanishes if: (i) fields fall off at the temporal endpoints, (ii) endpoints are fixed in the variational problem, (iii) one works in a finite box with appropriate boundary conditions and then takes the large-box limit, or (iv) in the in-in formalism the endcaps cancel.

De Sitter specialization. For de Sitter with flat slicing, $a(\eta) = -1/(H\eta)$, $\eta < 0$, one has $\frac{a''}{a} = \frac{2}{\eta^2}$, $\frac{a'^2}{a^2} = \frac{1}{\eta^2}$. Then

$$\mu^2(\eta) = m^2a^2 - \frac{d^2 - 1}{4\eta^2}, \quad \Rightarrow \quad \mathcal{L} \simeq \frac{1}{2}(\chi')^2 - \frac{1}{2}(\nabla\chi)^2 - \frac{1}{2}\left[m^2a^2 - \frac{d^2 - 1}{4\eta^2}\right]\chi^2 - \frac{\lambda}{4!}a^{-(d-3)}\chi^4. \quad (14)$$

For $d = 3$ (i.e. 3 + 1 dimensions), this reduces to the familiar $\mu^2(\eta) = m^2a^2 - \frac{2}{\eta^2}$.

Hamiltonian density for $\lambda\phi^4$. The canonical momentum for χ is $\pi_\chi = \partial_\eta\chi$, and the Hamiltonian density reads

$$\mathcal{H} = \frac{1}{2}\pi_\chi^2 + \frac{1}{2}(\nabla\chi)^2 + \frac{1}{2}\mu^2(\eta)\chi^2 + \frac{\lambda}{4!}a^{-(d-3)}\chi^4, \quad \mu^2(\eta) \text{ as in (13) (or (14) in dS).} \quad (15)$$

This makes explicit the time dependence (and hence non-conservation) of H through $a(\eta)$, while keeping the quartic interaction as a simple local χ^4 with an *effective* prefactor $a^{-(d-3)}$.

3.4 Remarks

- In flat space limit ($H \rightarrow 0, a \rightarrow 1$), we recover the usual Hamiltonian for a $\lambda\phi^4$ scalar theory.
- The Hamiltonian depends explicitly on η via $a(\eta)$, hence it is not conserved.

3.5 Flat-space limit $H \rightarrow 0$ in $d = 3$: recovery of $\lambda\phi^4$

Recall from the χ -rescaled theory (after the IBP) that for general d ,

$$\mathcal{H}_\chi(\eta, \mathbf{x}) = \frac{1}{2}\pi_\chi^2 + \frac{1}{2}(\nabla\chi)^2 + \frac{1}{2}\mu^2(\eta)\chi^2 + \frac{\lambda}{4!}a^{-(d-3)}\chi^4, \quad \pi_\chi \equiv \partial_\eta\chi, \quad (16)$$

with

$$\mu^2(\eta) = m^2a^2 - \left[\frac{d-1}{2}\frac{a''}{a} + \frac{(d-1)(d-3)}{4}\left(\frac{a'}{a}\right)^2 \right], \quad \chi = a^{\frac{d-1}{2}}\phi. \quad (17)$$

In $d = 3$ this simplifies to

$$\mathcal{H}_\chi = \frac{1}{2}\pi_\chi^2 + \frac{1}{2}(\nabla\chi)^2 + \frac{1}{2}(m^2a^2 - \frac{a''}{a})\chi^2 + \frac{\lambda}{4!}\chi^4, \quad \chi = a\phi$$

(18)

i.e. the quartic interaction carries *no* scale-factor and all explicit time dependence sits in the effective mass term.

De Sitter and the $H \rightarrow 0$ limit. For exact dS in conformal time, $a(\eta) = -1/(H\eta)$ so that $a''/a = 2/\eta^2$. To take the flat-space limit, it is convenient to keep *physical* time t fixed while sending $H \rightarrow 0$. Since $d\eta = dt/a$, one has $\eta \simeq -\frac{1}{H} + t + \mathcal{O}(H)$, whence

$$a(\eta) = \frac{1}{-H\eta} = 1 + \mathcal{O}(H), \quad \frac{a''}{a} = \frac{2}{\eta^2} = 2H^2 + \mathcal{O}(H^3t). \quad (19)$$

Therefore,

$$m^2a^2 \rightarrow m^2, \quad \frac{a''}{a} \rightarrow 0, \quad \chi = a\phi \rightarrow \phi, \quad \pi_\chi = \partial_\eta\chi \rightarrow \partial_t\phi, \quad (20)$$

where in the last step we used that $\eta \rightarrow t$ as $a \rightarrow 1$.

Result. Taking $H \rightarrow 0$ in (18) yields

$$\mathcal{H}_{\text{flat}}(\mathbf{x}) = \frac{1}{2}\pi_\phi^2 + \frac{1}{2}(\nabla\phi)^2 + \frac{1}{2}m^2\phi^2 + \frac{\lambda}{4!}\phi^4, \quad \pi_\phi = \partial_t\phi,$$

(21)

which is precisely the standard flat-space Hamiltonian density for a real scalar with $\lambda\phi^4$ interaction in $3+1$ dimensions.

Remark (small- H corrections). Keeping the leading H -dependence,

$$m^2 a^2 = m^2 (1 + 2Ht + \mathcal{O}(H^2)) , \quad \frac{a''}{a} = 2H^2 + \mathcal{O}(H^3 t) ,$$

so the effective mass squared in $d = 3$ is

$$\mu^2(\eta) = m^2 + 2m^2 Ht - 2H^2 + \dots ,$$

i.e. the first deviation from flat space appears as a slowly varying (and weak) time-dependent mass term. From a Hamiltonian-simulation perspective, this means one can use a flat-space $\lambda\phi^4$ lattice Hamiltonian with a mild, explicitly known time-dependent mass schedule.

Quantum Circuits and Hamiltonian Simulation-(i)

Lecture Notes

Contents

1 Pauli matrices (reference)	1
2 Quantum circuit warm-up	2
2.1 Single-qubit Hadamard	3
2.2 Two-qubit Bell pair ($ \Phi^+\rangle$)	3
3 Two baby examples of Hamiltonian simulation	4
3.1 Single-qubit precession: $H = \frac{\omega}{2} Z$	4
3.2 Worked derivation: single-qubit precession circuit	4
3.3 Two-qubit Ising coupling: $H = \frac{J}{2} Z \otimes Z$ (exact with a CNOT sandwich)	5
3.4 Worked derivation: two-qubit Ising coupling via a CNOT sandwich	6
4 A baby example: why higher-order Suzuki–Trotter helps	7

1 Pauli matrices (reference)

The single-qubit Pauli operators are

$$X = \begin{bmatrix} 0 & 1 \\ 1 & 0 \end{bmatrix}, \quad Y = \begin{bmatrix} 0 & -i \\ i & 0 \end{bmatrix}, \quad Z = \begin{bmatrix} 1 & 0 \\ 0 & -1 \end{bmatrix}.$$

They are Hermitian and unitary, with $X^2 = Y^2 = Z^2 = I$ and $\text{tr } X = \text{tr } Y = \text{tr } Z = 0$. Let $\sigma_1 = X, \sigma_2 = Y, \sigma_3 = Z$. Their algebra is

$$\sigma_i \sigma_j = \delta_{ij} I + i \sum_k \varepsilon_{ijk} \sigma_k, \quad [\sigma_i, \sigma_j] = 2i \sum_k \varepsilon_{ijk} \sigma_k, \quad \{\sigma_i, \sigma_j\} = 2\delta_{ij} I.$$

Eigenstates. Z -basis (computational) eigenstates: $|0\rangle, |1\rangle$ with $Z|0\rangle = +|0\rangle$, $Z|1\rangle = -|1\rangle$. X -basis: $|\pm\rangle = (|0\rangle \pm |1\rangle)/\sqrt{2}$, so $X|\pm\rangle = \pm|\pm\rangle$. Y -basis: $|y_\pm\rangle = (|0\rangle \pm i|1\rangle)/\sqrt{2}$, so $Y|y_\pm\rangle = \pm|y_\pm\rangle$.

Rotations (used throughout). For axis $n \in \{x, y, z\}$,

$$R_n(\theta) = \exp\left(-\frac{i\theta}{2}\sigma_n\right),$$

e.g. $R_z(\theta) = \begin{bmatrix} e^{-i\theta/2} & 0 \\ 0 & e^{i\theta/2} \end{bmatrix}$, $R_x(\theta) = \begin{bmatrix} \cos \frac{\theta}{2} & -i \sin \frac{\theta}{2} \\ -i \sin \frac{\theta}{2} & \cos \frac{\theta}{2} \end{bmatrix}$, $R_y(\theta) = \begin{bmatrix} \cos \frac{\theta}{2} & -\sin \frac{\theta}{2} \\ \sin \frac{\theta}{2} & \cos \frac{\theta}{2} \end{bmatrix}$.

(Useful identities: $HZH = X$, $HXH = Z$, $SXS^\dagger = Y$, with H the Hadamard and $S = \text{diag}(1, i)$.)

Raising/Lowering operators. $\sigma_\pm = \frac{1}{2}(X \pm iY)$ satisfy $\sigma_+|0\rangle = |1\rangle$, $\sigma_-|1\rangle = |0\rangle$, and $Z = \sigma_+\sigma_- - \sigma_-\sigma_+$.

2 Quantum circuit warm-up

Computational basis (terminology & conventions)

We use Dirac notation. For one qubit, the *computational basis* is

$$|0\rangle = \begin{bmatrix} 1 \\ 0 \end{bmatrix}, \quad |1\rangle = \begin{bmatrix} 0 \\ 1 \end{bmatrix},$$

the eigenstates of Z with $Z|0\rangle = +|0\rangle$ and $Z|1\rangle = -|1\rangle$. An n -qubit register has basis states

$$\{ |x_1x_2 \cdots x_n\rangle \mid x_j \in \{0, 1\} \},$$

where $|x_1x_2 \cdots x_n\rangle = |x_1\rangle \otimes |x_2\rangle \otimes \cdots \otimes |x_n\rangle$. **Convention (matches our circuits):** the ket is written *top wire to bottom wire, left to right*, so the uppermost wire is x_1 . For two qubits, the basis is $\{|00\rangle, |01\rangle, |10\rangle, |11\rangle\}$. We sometimes label a bitstring $\mathbf{x} = (x_1, \dots, x_n)$ by the integer

$$\text{bin}(\mathbf{x}) = \sum_{j=1}^n x_j 2^{n-j} \quad (\text{MSB on top}),$$

so $|10\rangle = |x_1x_2\rangle$ corresponds to $\text{bin} = 2$. A general pure state is a superposition

$$|\psi\rangle = \sum_{\mathbf{x} \in \{0,1\}^n} \alpha_{\mathbf{x}} |\mathbf{x}\rangle, \quad \sum_{\mathbf{x}} |\alpha_{\mathbf{x}}|^2 = 1.$$

A projective measurement in the computational (“ Z ”) basis returns an outcome \mathbf{x} with probability $|\alpha_{\mathbf{x}}|^2$ and collapses the post-measurement state to $|\mathbf{x}\rangle$. *Remark.* Other common bases are obtained by unitary changes of basis, e.g. the X -basis $\{|+\rangle, |-\rangle\}$ with $|\pm\rangle = (|0\rangle \pm |1\rangle)/\sqrt{2} = H|0/1\rangle$.

2.1 Single-qubit Hadamard

Starting from $|0\rangle$, the Hadamard gate prepares an equal superposition

$$|0\rangle \xrightarrow{H} \frac{|0\rangle + |1\rangle}{\sqrt{2}}.$$

$$|0\rangle \xrightarrow{[H]} \frac{|0\rangle + |1\rangle}{\sqrt{2}}$$

Figure 1: Single-qubit Hadamard: $|0\rangle \mapsto (|0\rangle + |1\rangle)/\sqrt{2}$.

2.2 Two-qubit Bell pair ($|\Phi^+\rangle$)

Apply H on the first qubit and then a controlled-NOT (CNOT) with the first as control:

$$|00\rangle \xrightarrow{H \otimes I} \frac{|00\rangle + |10\rangle}{\sqrt{2}} \xrightarrow{\text{CNOT}} \frac{|00\rangle + |11\rangle}{\sqrt{2}} \equiv |\Phi^+\rangle.$$

$$\begin{array}{c} |0\rangle \xrightarrow{[H]} \frac{|00\rangle + |11\rangle}{\sqrt{2}} \\ |0\rangle \xrightarrow{\oplus} \end{array}$$

Figure 2: Bell state preparation: H on the first qubit followed by CNOT yields $|\Phi^+\rangle = (|00\rangle + |11\rangle)/\sqrt{2}$.

About the CNOT gate. The controlled-NOT (CNOT) is a two-qubit gate that flips (*applies X to*) the *target* qubit if and only if the *control* qubit is $|1\rangle$. As an operator,

$$\text{CNOT} = |0\rangle\langle 0| \otimes I + |1\rangle\langle 1| \otimes X,$$

so its action on the computational basis is

$$|00\rangle \mapsto |00\rangle, \quad |01\rangle \mapsto |01\rangle, \quad |10\rangle \mapsto |11\rangle, \quad |11\rangle \mapsto |10\rangle.$$

In our circuit of Fig. 2 the *upper* wire is the control and the *lower* wire is the target (Qcircuit notation: `\ctrl{1}` above `\targ{}`). Applying H on the control prepares $\frac{1}{\sqrt{2}}(|0\rangle + |1\rangle) \otimes |0\rangle$. The subsequent CNOT correlates the target with the control,

$$\text{CNOT}\left(\frac{1}{\sqrt{2}}(|0\rangle + |1\rangle) \otimes |0\rangle\right) = \frac{1}{\sqrt{2}}(|00\rangle + |11\rangle) \equiv |\Phi^+\rangle,$$

thereby creating entanglement from a product state. (Equivalently: in bit language, the target becomes $t \oplus c$ where c is the control bit.)

3 Two baby examples of Hamiltonian simulation

3.1 Single-qubit precession: $H = \frac{\omega}{2} Z$

The time evolution is

$$U(t) = e^{-iHt} = e^{-i(\omega t/2)Z} \equiv R_z(\omega t).$$

A minimal circuit that prepares $|+\rangle$, evolves for time t , and rotates back to read out in Z is:

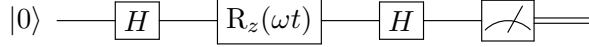


Figure 3: Exact simulation of $H = \frac{\omega}{2}Z$: the middle gate is $U(t) = R_z(\omega t)$. Measuring Z after $H R_z H$ gives $\Pr[m=0] = \cos^2(\omega t/2)$.

This is the simplest Hamiltonian simulation: a *single* parametrized rotation exactly implements e^{-iHt} . The second Hadamard is not needed for the time evolution. It is there to make the phase readout possible (q for students: why?).

3.2 Worked derivation: single-qubit precession circuit

Consider $H = \frac{\omega}{2}Z$ with $Z = \text{diag}(1, -1)$. The time evolution is

$$U(t) = e^{-iHt} = e^{-i(\omega t/2)Z} \equiv R_z(\omega t), \quad R_z(\theta) = \begin{bmatrix} e^{-i\theta/2} & 0 \\ 0 & e^{i\theta/2} \end{bmatrix}.$$

The circuit of Fig. 3 applies H , then $R_z(\theta)$ with $\theta = \omega t$, then H again, followed by a Z -basis measurement.

State-vector calculation.

$$|\psi_0\rangle = |0\rangle, \quad |\psi_1\rangle = H|0\rangle = \frac{1}{\sqrt{2}}(|0\rangle + |1\rangle) \equiv |+\rangle.$$

Apply $R_z(\theta)$:

$$|\psi_2\rangle = R_z(\theta)|+\rangle = \frac{1}{\sqrt{2}}\left(e^{-i\theta/2}|0\rangle + e^{i\theta/2}|1\rangle\right).$$

Apply the final H :

$$|\psi_3\rangle = H|\psi_2\rangle = \frac{1}{2}\left[(e^{-i\theta/2} + e^{i\theta/2})|0\rangle + (e^{-i\theta/2} - e^{i\theta/2})|1\rangle\right] = \cos\frac{\theta}{2}|0\rangle - i\sin\frac{\theta}{2}|1\rangle.$$

Hence the Z -measurement outcomes satisfy

$$\Pr[m=0] = |\langle 0 \rangle \psi_3|^2 = \cos^2\frac{\theta}{2}, \quad \Pr[m=1] = \sin^2\frac{\theta}{2},$$

and the expectation $\langle Z \rangle = \Pr[0] - \Pr[1] = \cos\theta$.

Operator identity (one-line check). Conjugation by H swaps $Z \leftrightarrow X$:

$$H R_z(\theta) H = H e^{-i\theta Z/2} H = e^{-i\theta(HZH)/2} = e^{-i\theta X/2} \equiv R_x(\theta).$$

Thus the circuit implements a rotation about the x -axis by angle θ on $|0\rangle$, and a Z -basis measurement yields the same probabilities as above. Geometrically on the Bloch sphere: start at the north pole, rotate about x by θ , then read out Z .

3.3 Two-qubit Ising coupling: $H = \frac{J}{2}Z \otimes Z$ (exact with a CNOT sandwich)

We want $U(t) = e^{-i(Jt/2)Z \otimes Z}$. Using the identity

$$\text{CNOT}(I \otimes R_z(2\theta)) \text{CNOT} = e^{-i\theta Z \otimes Z},$$

we set $\theta = \frac{Jt}{2}$ to get the desired evolution:

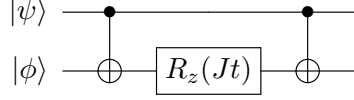


Figure 4: Exact simulation of $H = \frac{J}{2}Z \otimes Z$: choose $R_z(Jt)$ on the target sandwiched by CNOTs. No Trotter error.

3.4 Worked derivation: two-qubit Ising coupling via a CNOT sandwich

Consider the two-qubit Ising Hamiltonian

$$H = \frac{J}{2} Z \otimes Z \implies U(t) = e^{-iHt} = e^{-i(Jt/2)Z \otimes Z}.$$

In the computational basis $\{|00\rangle, |01\rangle, |10\rangle, |11\rangle\}$, $Z \otimes Z$ has eigenvalues +1 on even parity ($|00\rangle, |11\rangle$) and -1 on odd parity ($|01\rangle, |10\rangle$), hence

$$U(t) = \text{diag}(e^{-i\phi}, e^{+i\phi}, e^{+i\phi}, e^{-i\phi}), \quad \phi \equiv \frac{Jt}{2}.$$

Now we have at our disposal single qubit gates and CNOT gate. Using these we need to make $U(t)$.

Circuit and basis-state calculation. The circuit is

$$\text{CNOT}_{1 \rightarrow 2} \ (I \otimes R_z(Jt)) \ \text{CNOT}_{1 \rightarrow 2},$$

with the first qubit as control and the second as target. Act on a basis state $|ab\rangle$ with $a, b \in \{0, 1\}$:

1. First CNOT: $|ab\rangle \mapsto |a, b \oplus a\rangle$.
2. Phase on target:

$$(I \otimes R_z(Jt)) |a, b \oplus a\rangle = e^{-i\frac{Jt}{2}(-1)^{b \oplus a}} |a, b \oplus a\rangle.$$

3. Second CNOT: $|a, b \oplus a\rangle \mapsto |ab\rangle$.

Net effect:

$$|ab\rangle \mapsto e^{-i\frac{Jt}{2}(-1)^{b \oplus a}} |ab\rangle = \begin{cases} e^{-i\phi} |ab\rangle, & a = b \text{ (even parity)}, \\ e^{+i\phi} |ab\rangle, & a \neq b \text{ (odd parity)}, \end{cases}$$

which coincides exactly with $U(t) = e^{-i(Jt/2)Z \otimes Z}$.

Operator identity (one-line check). Using CNOT conjugation rules,

$$\text{CNOT}(I \otimes Z) \text{CNOT} = Z \otimes Z,$$

so

$$\text{CNOT}(I \otimes R_z(\theta)) \text{CNOT} = \text{CNOT} \exp\left(-i\frac{\theta}{2}(I \otimes Z)\right) \text{CNOT} = \exp\left(-i\frac{\theta}{2}Z \otimes Z\right).$$

Setting $\theta = Jt$ yields $U(t)$.

Example: evolution of $|++\rangle$. With $|+\rangle = (|0\rangle + |1\rangle)/\sqrt{2}$,

$$U(t)|++\rangle = \frac{1}{2}(e^{-i\phi}(|00\rangle + |11\rangle) + e^{+i\phi}(|01\rangle + |10\rangle)) = \cos\phi|++\rangle - i\sin\phi|--\rangle.$$

Thus an X -basis measurement on both qubits (apply H on each, then measure in Z) gives

$$\Pr[+] = \cos^2\phi, \quad \Pr[-] = \sin^2\phi, \quad \Pr[+-] = \Pr[-+] = 0,$$

displaying coherent oscillations generated by $H = \frac{J}{2}Z \otimes Z$.

Remarks. (i) These two primitives are the core building blocks for many local lattice models: single-site Z terms and pairwise ZZ couplings. (ii) For a genuinely *noncommuting* single-qubit Hamiltonian, e.g. $H = aX + bZ$, one may use first/second-order product formulas,

$$e^{-it(aX+bZ)} \approx \left(R_x(2at/r)R_z(2bt/r)\right)^r \quad \text{or} \quad \left(R_x(at/r)R_z(2bt/r)R_x(at/r)\right)^r,$$

with error $\mathcal{O}(t^2/r)$ and $\mathcal{O}(t^3/r^2)$ respectively since $[X, Z] = 2iY$. We'll use these same ideas at scale with locality and Suzuki order $2k$ later on.

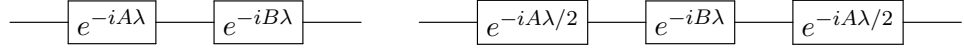
4 A baby example: why higher-order Suzuki–Trotter helps

We compare first-order (Lie–Trotter) and second-order (Strang) product formulas on the noncommuting single-qubit Hamiltonian

$$H = aX + bZ, \quad A := aX, \quad B := bZ,$$

so $[A, B] = 2iabY \neq 0$. One Trotter step uses time slice $\lambda = t/r$.

One-slice circuits (Qcircuit)



Left: *first order* $e^{-iA\lambda}e^{-iB\lambda}$. Right: *second order (Strang)* $e^{-iA\lambda/2}e^{-iB\lambda}e^{-iA\lambda/2}$.
 (Here each exponential is a single-qubit rotation: $e^{-iaX\lambda} = R_x(2a\lambda)$, $e^{-ibZ\lambda} = R_z(2b\lambda)$.)

We reached till here!

Error bounds with explicit constants

Using standard BCH error bounds:

First order (global error).

$$\left\| e^{-it(A+B)} - (e^{-iAt/r} e^{-iBt/r})^r \right\| \leq \frac{t^2}{2r} \| [A, B] \| = \frac{t^2}{2r} \| 2iab Y \| = \frac{|ab| t^2}{r}.$$

Second order / Strang (global error).

$$\left\| e^{-it(A+B)} - (S_2(t/r))^r \right\| \leq \frac{t^3}{r^2} \Gamma_3, \quad \Gamma_3 = \frac{1}{12} \| [A, [A, B]] + 2[B, [A, B]] \|.$$

For $A = aX$, $B = bZ$,

$$[A, B] = 2iab Y, \quad [A, [A, B]] = -4a^2b Z, \quad [B, [A, B]] = +4ab^2 X,$$

so

$$\Gamma_3 = \frac{1}{12} \| 8ab^2 X - 4a^2b Z \| = \frac{|ab|}{3} \sqrt{a^2 + 4b^2}.$$

Quantum Circuits and Hamiltonian Simulation-(ii)

Lecture Notes

Contents

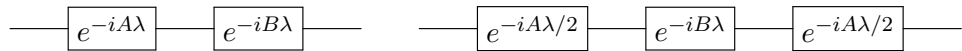
1 Review of lecture 7	2
1.1 Error bounds with explicit constants	2
2 Gate optimisation–Warm-up	5
2.1 Models of locality and basic parameters	5
2.1.1 Implications	5
2.1.2 Implications	6
3 Warm-up gate counting: from Lie–Trotter to Strang, then higher order	7
3.1 Lie–Trotter (LT): $e^{-i(H_A+H_B)\Delta} \approx e^{-iH_A\Delta}e^{-iH_B\Delta}$	7
3.2 Strang (second order): $e^{-iH\Delta} \approx \prod_a^{\rightarrow} e^{-iH_a\Delta/2} \prod_a^{\leftarrow} e^{-iH_a\Delta/2}$	8
3.3 Higher order (p th order Suzuki)	8
A The Solovay–Kitaev theorem	9
B Ascending–descending form for Strang	10

In lecture 8, UB showed how to install qiskit and how the circuits discussed in lecture 7 could be implemented.

This lecture and the next one are based on [1, 2, 3, 4]. In particular, for a readable account of the gate optimisation problem, start with [1]. However, he does not optimise w.r.t. the Trotter order which is done in [2, 3]. The reinterpretation in terms of an AdS warped volume can be found in [4].

1 Review of lecture 7

One-slice circuits (Qcircuit)



Left: *first order* $e^{-iA\lambda}e^{-iB\lambda}$. Right: *second order (Strang)*¹ $e^{-iA\lambda/2}e^{-iB\lambda}e^{-iA\lambda/2}$.
(Here each exponential is a single-qubit rotation: $e^{-iaX^\lambda} = R_x(2a\lambda)$, $e^{-ibZ^\lambda} = R_z(2b\lambda)$.)

1.1 Error bounds with explicit constants

Using standard BCH error bounds:

First order (global error).

$$\left\| e^{-it(A+B)} - (e^{-iAt/r}e^{-iBt/r})^r \right\| \geq \frac{t^2}{2r} \| [A, B] \| = \frac{t^2}{2r} \| 2iab Y \| = \frac{|ab| t^2}{r}.$$

Second order / Strang (global error).

$$\left\| e^{-it(A+B)} - (S_2(t/r))^r \right\| \geq \frac{t^3}{r^2} \Gamma_3, \quad \Gamma_3 = \frac{1}{12} \| [A, [A, B]] + 2[B, [A, B]] \|.$$

¹The symmetric product

$$S_2(\Delta) := e^{A\Delta/2} e^{B\Delta} e^{A\Delta/2}$$

is widely called *Strang splitting* after Gilbert Strang, who analyzed such operator-splitting schemes for PDEs and semigroups (see G. Strang, *SIAM J. Numer. Anal.* **5** (1968)). In quantum simulation it is also called the *second-order* (or *time-symmetric*) Trotter step. The first-order (Lie-Trotter) step is $e^{A\Delta}e^{B\Delta}$ (Trotter 1959); higher-order symmetric compositions were later systematized by Suzuki.

For $A = aX$, $B = -bZ$,

$$[A, B] = 2iabY, \quad [A, [A, B]] = -4a^2bZ, \quad [B, [A, B]] = +4ab^2X,$$

so

$$\Gamma_3 = \frac{1}{12} \| 8ab^2X - 4a^2bZ \| = \frac{|ab|}{3} \sqrt{a^2 + 4b^2}.$$

Segments r and gate counts N for a target tolerance ε

Let $L_1 = 2$ gates per first-order slice, $L_2 = 3$ for Strang. With the bounds above,

$$r_{\text{LT}} \geq \frac{|ab| t^2}{\varepsilon}, \quad N_{\text{LT}} = L_1 r_{\text{LT}} = 2 r_{\text{LT}}$$

$$r_{\text{Strang}} \geq \sqrt{\frac{\Gamma_3 t^3}{\varepsilon}}, \quad N_{\text{Strang}} = L_2 r_{\text{Strang}} = 3 r_{\text{Strang}}$$

where $\Gamma_3 = \frac{|ab|}{3} \sqrt{a^2 + 4b^2}$.

Numerical toy (dramatic savings even at modest accuracy)

Take $a = b = 1$, $t = 1$, $\varepsilon = 10^{-3}$. Then $\Gamma_3 = \frac{1}{3}\sqrt{5} \approx 0.745$.

$$r_{\text{LT}} \geq 10^3, \quad N_{\text{LT}} \approx 2,000 \quad r_{\text{Strang}} \geq \sqrt{0.745/10^{-3}} \approx 27.3 \Rightarrow N_{\text{Strang}} \approx 82-84.$$

For a longer evolution $t = 10$ (same ε): $r_{\text{LT}} \geq 10^5 \Rightarrow N_{\text{LT}} \sim 2 \times 10^5$, while $r_{\text{Strang}} \geq \sqrt{0.745 \times 10^3/10^{-3}} \approx 864 \Rightarrow N_{\text{Strang}} \sim 2.6 \times 10^3$.

Operator norm (spectral norm) used in these notes

For a linear operator (matrix) A acting on a finite-dimensional Hilbert space with the usual Euclidean (ℓ_2) norm, the *operator norm* (a.k.a. spectral norm) is the induced norm

$$\|A\| := \sup_{\|v\|=1} \|Av\|.$$

Equivalently, $\|A\|$ is the largest singular value of A :

$$\|A\| = \sqrt{\lambda_{\max}(A^\dagger A)}.$$

If A is *normal* ($AA^\dagger = A^\dagger A$), then $\|A\|$ equals the largest *absolute* value of its eigenvalues. In particular, for Hermitian A ,

$$\|A\| = \max_{\lambda \in \text{spec}(A)} |\lambda|.$$

Basic properties.

- **Unitary invariance:** $\|UAV\| = \|A\|$ for all unitaries U, V .
- **Submultiplicativity:** $\|AB\| \leq \|A\| \|B\|$ and $\|A + B\| \leq \|A\| + \|B\|$.
- **Commutator bound:** $\|[A, B]\| \leq 2 \|A\| \|B\|$.

Examples.

- Pauli matrices satisfy $\|X\| = \|Y\| = \|Z\| = 1$ (eigenvalues ± 1).
- If $A = \alpha X + \beta Z$ with real α, β , then

$$A^2 = (\alpha^2 + \beta^2) I \Rightarrow \|A\| = \sqrt{\alpha^2 + \beta^2}.$$

(Used above when evaluating $\|4a^2 b Z - 8ab^2 X\|$.)

Computing Γ_3 for $A = aX, B = bZ$

Recall the Strang (second-order) global error bound

$$\left\| e^{-it(A+B)} - (S_2(t/r))^r \right\| \leq \frac{t^3}{r^2} \Gamma_3, \quad \Gamma_3 = \frac{1}{12} \| [A, [A, B]] + 2[B, [A, B]] \|.$$

We use Pauli commutators

$$[X, Y] = 2iZ, \quad [Y, Z] = 2iX, \quad [Z, X] = 2iY \quad \Rightarrow \quad [X, Z] = -2iY, \quad [Z, Y] = -2iX.$$

Step 1: the first commutator.

$$[A, B] = [aX, bZ] = ab [X, Z] = ab (-2iY) = -2iab Y.$$

Step 2: the nested commutators.

$$[A, [A, B]] = [aX, -2iab Y] = a(-2iab) [X, Y] = (-2ia^2 b) (2iZ) = 4a^2 b Z,$$

$$[B, [A, B]] = [bZ, -2iab Y] = b(-2iab) [Z, Y] = (-2iab^2) (-2iX) = -4ab^2 X.$$

Step 3: assemble and take the operator norm.

$$[A, [A, B]] + 2[B, [A, B]] = 4a^2 b Z + 2(-4ab^2 X) = 4a^2 b Z - 8ab^2 X.$$

For any real α, β , $\|\alpha X + \beta Z\| = \sqrt{\alpha^2 + \beta^2}$ since $(\alpha X + \beta Z)^2 = (\alpha^2 + \beta^2) I$.
Hence

$$\| [A, [A, B]] + 2[B, [A, B]] \| = \sqrt{(4a^2 b)^2 + (-8ab^2)^2} = 4|ab| \sqrt{a^2 + 4b^2}.$$

Step 4: the constant Γ_3 .

$$\boxed{\Gamma_3 = \frac{1}{12} \| [A, [A, B]] + 2[B, [A, B]] \| = \frac{|ab|}{3} \sqrt{a^2 + 4b^2}}$$

Sign note. If you instead take $[X, Z] = +2iY$ (equivalently swap the order to $[Z, X] = 2iY$), intermediate signs flip but the final norm—and thus Γ_3 —is unchanged.

2 Gate optimisation—Warm-up

2.1 Models of locality and basic parameters

We decompose a time-independent Hamiltonian as

$$H = \sum_{j=1}^M H_j, \quad H_j^\dagger = H_j.$$

We will use one of the following locality models (both common in the literature):

(L1) k -local with bounded interaction degree. Each H_j acts nontrivially on at most k qubits (constant k), and each qubit belongs to at most χ terms (constant χ). Let

$$h \equiv \max_j \|H_j\|, \quad \beta \equiv \sum_{j=1}^m \|H_j\| \leq mh.$$

2.1.1 Implications

For concreteness, let us have in mind the Hamiltonian describing spin-spin interactions. An example of k -local, with $k = 2$ is of the kind

$$H = J_1 \sigma_1 \otimes \sigma_2 \otimes I \otimes I \cdots \otimes I + J_2 \sigma_1 \otimes I \otimes I \otimes I \otimes \sigma_2 \otimes I \cdots + \cdots \quad (1)$$

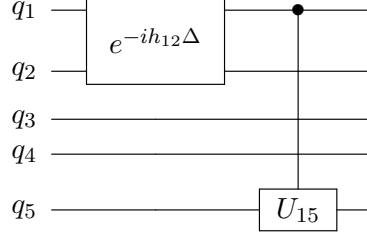


Figure 1: k -local with $k = 2$: two-qubit interactions are allowed between *any* pair. Left column shows a nearest-neighbour two-qubit unitary on $(1, 2)$. Right column shows a long-range two-qubit interaction between $(1, 5)$ drawn as a controlled- U_{15} to emphasize “qubit 1 talks to qubit 5”. No geometry constraint is imposed; only the # of qubits per term (≤ 2) matters.

(L2) Geometric (spatial) locality on a d -dimensional lattice. Each H_j is supported on a ball of radius $R = \mathcal{O}(1)$ (finite range), and the interaction graph has uniformly bounded coordination number $Z = \mathcal{O}(1)$. With V the number of lattice sites (spatial volume), we again have $\beta \equiv \sum_j \|H_j\| = \mathcal{O}(V h)$.

In both (L1) and (L2), *nested commutators are controlled* by the local degree: there exist constants $c_{k,\chi}$ or $c_{R,Z}$ (independent of m, V) such that the norm of any $(2\ell+1)$ -fold nested commutator of the H_j is bounded by

$$\|[H_{j_{2\ell+1}}, [H_{j_{2\ell}}, \dots, [H_{j_2}, H_{j_1}] \dots]]\| \leq C_\ell (c_{\text{loc}} h)^{2\ell+1},$$

where $c_{\text{loc}} = c_{k,\chi}$ in (L1) and $c_{\text{loc}} = c_{R,Z}$ in (L2).

2.1.2 Implications

For concreteness, let us have in mind the Hamiltonian describing spin-spin interactions. An example of g-local, with $g = 2$ is of the kind

$$H = J_1 \sigma_1 \otimes \sigma_2 \otimes I \otimes I \cdots \otimes I + J_2 I \otimes \sigma_1 \otimes \sigma_2 \otimes I \cdots \otimes I + \cdots \quad (2)$$

There are two reasons why this geometric locality or spatial locality is important:

1. Some of the most important Hamiltonians in physics have this property called nearest neighbour interaction. In some sense, this encapsulates the starting point of most interesting physical scenarios.

2. In what follows, we will somehow have to sneak in the spatial volume V . When the Hamiltonian is g-local, the number of terms in the Hamiltonian (in our notation above it is M) is the proxy for V . Roughly speaking, since each term in the Hamiltonian “talks” to only $O(1)$ terms in the Hamiltonian, and we are discussing a lattice of spins, we can think of the total number of terms as some kind of estimate of the spatial volume (in the spin-system example, this volume is 1-dimensional).

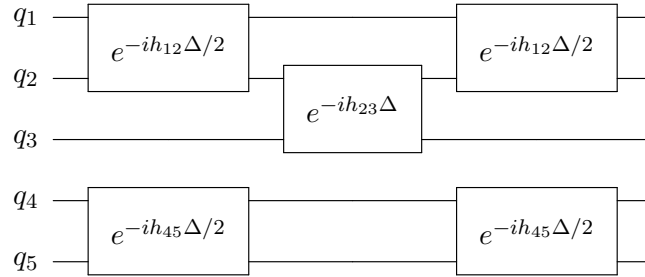


Figure 2: Geometric (1D nearest-neighbour) locality: only adjacent pairs interact. Illustrated in a Strang slice: odd bonds (1, 2) and (4, 5) (left), then even bond (2, 3) (middle), then odd bonds again (right). Disjoint nearest-neighbour gates in each column commute and can run in parallel.

3 Warm-up gate counting: from Lie–Trotter to Strang, then higher order

Setup. Let $H = \sum_{a=1}^M H_a$ be k -local with bounded term norms $\|H_a\|_\infty \leq h$ (constant h), and in the *geometrically local* case we have $M = \mathcal{O}(n) = \mathcal{O}(V)$ (spatial volume). We target a simulation accuracy $\|\tilde{U}(t) - U(t)\|_\infty < \delta$ for $U(t) = e^{-iHt}$.

3.1 Lie–Trotter (LT): $e^{-i(H_A+H_B)\Delta} \approx e^{-iH_A\Delta}e^{-iH_B\Delta}$

For one time slice of width Δ , expanding shows

$$e^{-iH\Delta} - \prod_a e^{-iH_a\Delta} = \frac{1}{2} \Delta^2 \sum_{a < b} [H_a, H_b] + \text{h.o.}$$

so in the geometrically local case (each term fails to commute with only a constant number of others) the *single-slice* error scales as

$$\|e^{-iH\Delta} - \prod_a e^{-iH_a\Delta}\| = \mathcal{O}(M \Delta^2 h^2),$$

i.e. the *per-gate* error is $\mathcal{O}(\Delta^2 h^2)$. With $r = t/\Delta$ slices, total gates $L \sim Mr$, we require $(Mt/\Delta) \cdot \Delta^2 h^2 \approx \delta$ so

$$\Delta = \mathcal{O}\left(\frac{\delta}{h^2 Mt}\right), \quad L = \mathcal{O}\left(\frac{h^2(Mt)^2}{\delta}\right).$$

In the geometrically local case ($M = \mathcal{O}(V)$ and constant h),

$$L = \mathcal{O}(\Omega^2 \text{polylog } \Omega), \quad \Omega \equiv Vt.$$

(the polylog comes from Solovay–Kitaev gate synthesis).

3.2 Strang (second order): $e^{-iH\Delta} \approx \prod_a^\rightarrow e^{-iH_a\Delta/2} \prod_a^\leftarrow e^{-iH_a\Delta/2}$

Using the symmetric (ascending then descending) product, the single-slice error improves to $\|e^{-iH\Delta} - \text{symmetric product}\| = \mathcal{O}(M \Delta^3 h^3)$ so the per-gate error is $\mathcal{O}(\Delta^3 h^3)$. Balancing $(Mt/\Delta) \cdot \Delta^3 h^3 \approx \delta$ gives

$$\Delta \approx \left(\frac{\delta}{h^3 Mt}\right)^{1/2}, \quad L \approx \frac{Mt}{\Delta} = \mathcal{O}\left(\frac{h^{3/2}(Mt)^{3/2}}{\delta^{1/2}}\right),$$

and hence, in the geometrically local case,

$$L = \mathcal{O}(\Omega^{3/2} \text{polylog } \Omega).$$

This matches Preskill's Eq. (6.204).

3.3 Higher order (pth order Suzuki)

More generally one may achieve a single-slice error $\|e^{-iH\Delta} - \text{approx}\| = \mathcal{O}(c_p M (h\Delta)^{p+1})$ for any p (with c_p depending on p), at the cost of a larger per-slice pattern. Then

$$\frac{Mt}{\Delta} \cdot (h\Delta)^{p+1} \sim \delta \Rightarrow \Delta \sim \frac{\delta^{1/p}}{h^{(p+1)/p} (Mt)^{1/p}}, \quad L \sim \frac{Mt}{\Delta} \sim \frac{h^{(p+1)/p} (Mt)^{(p+1)/p}}{\delta^{1/p}}.$$

With $M = \mathcal{O}(V)$ and constant h ,

$$L = \mathcal{O}(\Omega^{1+\frac{1}{p}} \text{polylog } \Omega), \quad \Omega = Vt,$$

and as $p \rightarrow \infty$, L approaches linear in Ω (up to constants that grow with p).

What locality buys you (at a glance). Geometric locality implies (i) $M = \mathcal{O}(V)$, and (ii) only $\mathcal{O}(M)$ commutators are nonzero in the LT/Strang error; together these yield the Ω -scalings above

Where next

In the next lecture, we will start with higher order Suzuki-Trotter. We will see that in section 3.3 above, we have failed to take into account a very important p dependent factor that will play a crucial role.

References

- [1] John Preskill lecture notes, [Lecture 6A notes, pgs 35-39](#)
- [2] N. Hatano and M. Suzuki, “Finding Exponential Product Formulas of Higher Orders,” *Lect. Notes Phys.* **679**, 37 (2005) doi:10.1007/11526216_2 [arXiv:math-ph/0506007 [math-ph]].
- [3] D. W. Berry, G. Ahokas, R. Cleve and B. C. Sanders, “Efficient Quantum Algorithms for Simulating Sparse Hamiltonians,” *Commun. Math. Phys.* **270**, no.2, 359-371 (2007) doi:10.1007/s00220-006-0150-x [arXiv:quant-ph/0508139 [quant-ph]].
- [4] A. Bhattacharyya, P. Nandy and A. Sinha, “Renormalized Circuit Complexity,” *Phys. Rev. Lett.* **124**, no.10, 101602 (2020) doi:10.1103/PhysRevLett.124.101602 [arXiv:1907.08223 [hep-th]].

A The Solovay–Kitaev theorem

- **Setting.** Let $\mathcal{G} \subset SU(2)$ (or $SU(2^n)$) be a finite, universal gate set that is (i) *closed under inverses* and (ii) generates a *dense* subgroup. (Canonical example: single-qubit Clifford+T.)
- **Statement.** For any target unitary U and any accuracy $\varepsilon \in (0, 1)$, there exists a circuit \tilde{U} over \mathcal{G} such that

$$\|U - \tilde{U}\| \leq \varepsilon \quad \text{and} \quad L(\tilde{U}) = \mathcal{O}(\log^c(1/\varepsilon)),$$

where $L(\tilde{U})$ is the number of gates from \mathcal{G} and the constructive proof gives $c \approx 3.97$ (variants achieve different constants). Thus the gate overhead is *polylogarithmic* in $1/\varepsilon$.

- **Idea (one line).** Build a coarse ε_0 -net (lookup table). To refine an approximation, express a small correction C as a commutator $C \approx ABA^{-1}B^{-1}$ so that errors *shrink superlinearly* under recursion; repeat until the target ε is reached.
- **Why it matters.** It bridges *continuous* targets (e.g. rotations, Hamiltonian evolutions) and *discrete* universal gate sets with only a $\text{polylog}(1/\varepsilon)$ accuracy cost. This is why gate-count formulas often include a trailing “ $\text{polylog}(1/\varepsilon)$ ” factor.
- **Caveats / refinements.** Generic SK is constructive but can have large constants. For specific sets/targets (e.g. Clifford+T single-qubit Z rotations), number-theoretic compilers and meet-in-the-middle search give tighter constants and/or asymptotics; in practice one often blends SK-style recursion with such specialized methods.

B Ascending–descending form for Strang

One can *derive* the many-term symmetric product

$$S_2^{(M)}(\Delta) = \left(\prod_{a=1}^{M-1} e^{-H_a \Delta/2} \right) e^{-H_M \Delta} \left(\prod_{a=M-1}^1 e^{-H_a \Delta/2} \right)$$

directly from the two-term Strang formula by a simple recursive/inductive construction. To certify it is *second order*, you then use the standard BCH/time-symmetry argument.

Derivation (induction using the two-term Strang). Let $A^{(k)} := \sum_{a=1}^k H_a$. For $M \geq 2$,

$$e^{-(A^{(M-1)} + H_M)\Delta} \approx e^{-A^{(M-1)}\Delta/2} e^{-H_M\Delta} e^{-A^{(M-1)}\Delta/2} \quad (\text{two-term Strang}).$$

Now apply the *same* recipe to the factors $e^{-A^{(M-1)}\Delta/2}$: by the induction hypothesis, $e^{-A^{(M-1)}\Delta/2} \approx S_2^{(M-1)}(\Delta/2) = \left(\prod_{a=1}^{M-1} e^{-H_a \Delta/2} \right) \left(\prod_{a=M-1}^1 e^{-H_a \Delta/2} \right)$. Plugging this on the left and right yields exactly the ascending–descending product above. This closes the induction.

Quantum Circuits and Hamiltonian Simulation-(iii)

Lecture Notes

Contents

1 Higher order Suzuki-Trotter	2
2 AdS analogy	4
3 Optimizing k and AdS	5
A General $(2m+1)$-block Suzuki recursion (order raise $2k-2 \rightarrow 2k$).	6

The previous lecture and this one are based on [1, 2, 3, 4]. In particular, for a readable account of the gate optimisation problem, start with [1]. However, he does not optimise w.r.t. the Trotter order which is done in [3]. The reinterpretation in terms of an AdS warped volume can be found in [4].

1 Higher order Suzuki-Trotter

This discussion will closely follow the time-independent discussions in [2]—we will come back to the time dependent case later. For simplicity (but w.l.o.g.) we will consider a 2 term Hamiltonian (the generalization to M term will be obvious and indicated when the time comes). The Strang formula was:

$$e^{\lambda(A+B)} \approx e^{\lambda A/2} e^{\lambda B} e^{\lambda A/2} + O(\lambda^3). \quad (1)$$

Introduce the notation:

$$S_2(\lambda) \equiv e^{\lambda A/2} e^{\lambda B} e^{\lambda A/2}. \quad (2)$$

Now notice that

$$S_2(\lambda) S_2(-\lambda) = I \quad (3)$$

Then you can convince yourself (hw) that we can write:

$$S_2(\lambda) = e^{\lambda(A+B)+R_3\lambda^3+R_5\lambda^5}, \quad (4)$$

namely that only odd powers of λ will appear in the expression. Here R_3 , R_5 are remainder terms whose explicit expressions will not concern us. In keeping with the form of eq.(2), we can ask if defining

$$T(\lambda) = S_2(s\lambda) S_2((1-2s)\lambda) S_2(s\lambda), \quad (5)$$

we can find s such that the R_3 term in the resulting expression cancels. In other words, the error can be pushed to one order higher. The splitting of the λ in the arguments of S_2 are such that the arguments add up to 1 while having the form like eq.(2).

The RHS above (using Lie-Trotter in succession) is

$$e^{\lambda(A+B)+[2s^3+(1-2s)^3]\lambda^3 R_3+O(\lambda^5)}, \quad (6)$$

and so for the R_3 term to vanish, we must have

$$2s^3 + (1-2s)^3 = 0, \quad (7)$$

whose only real root is

$$s \approx 1.35, \quad (8)$$

which gives $1 - 2s = -1.7$. Let us pause here and see what this means. Using the form of $T(\lambda)$ and this value of s , we find that we first evolve 1.35λ (which is bigger than λ , our final goal), then we come back -1.7λ or in otherwords, we dip below $\lambda = 0$ by -0.35λ , and then finally we evolve further by 1.35λ to reach our goal of λ . Now it is a bit worrying that we evolved beyond our target and also needed to come back below our starting point. This seems a bit unnatural (although may be fine mathematically). So we will not adopt eq.(5). The next possibility is to try:

$$T_4(\lambda) = S_2(s\lambda)^2 S_2((1 - 4s)\lambda) S_2(s\lambda)^2. \quad (9)$$

Noting that $T(\lambda)T(-\lambda) = I$, and repeating the same steps as above, we find:

$$T_4(\lambda) = e^{\lambda(A+B)+[4s^3+(1-4s)^3]\lambda^3} R_3 + O(\lambda^5), \quad (10)$$

so that the vanishing of the R_3 term needs:

$$4s^3 + (1 - 4s)^3 = 0, \quad (11)$$

whose only real root is

$$s \approx 0.41, \quad (12)$$

so that $1 - 4s \approx -0.64$. Now we see that eq.(9) means that we first evolve $2 \times 0.41\lambda = 0.82\lambda$, then evolve back -0.64λ , which leaves us above $\lambda > 0$ and finally we evolve 0.82λ to reach our goal. This time, we respect $0 < \lambda \leq 1$. So we will continue with this.

We will now adopt the notation $T_4 \equiv S_4$. The next step is now obvious. We use:

$$S_6(\lambda) \equiv S_4(\bar{s}\lambda)^2 S_4((1 - 4\bar{s})\lambda) S_4(\bar{s}\lambda)^2. \quad (13)$$

Here \bar{s} 's equation will be determined by cancelling the R_5 term. Repeating the steps above, we will find

$$4\bar{s}^5 + (1 - 4\bar{s})^5 = 0. \quad (14)$$

Despite being a quintic equation, again only 1 real root exists:

$$\bar{s} \approx 0.37. \quad (15)$$

These couple of exercises enables us to guess the recursion relation:

$$S_{2k}(\lambda) \equiv S_{2k-2}(s_{2k}\lambda)^2 S_{2k-2}((1 - 4s_{2k})\lambda) S_{2k}(s_{2k}\lambda)^2. \quad (16)$$

Here

$$4s_{2k}^{2k-1} + (1 - 4s_{2k})^{2k-1} = 0. \quad (17)$$

Then the error here is $O(\lambda^{2k+1})$. Example, $k = 1$ is the usual Strang formula whose error is $O(\lambda^3)$.

2 AdS analogy

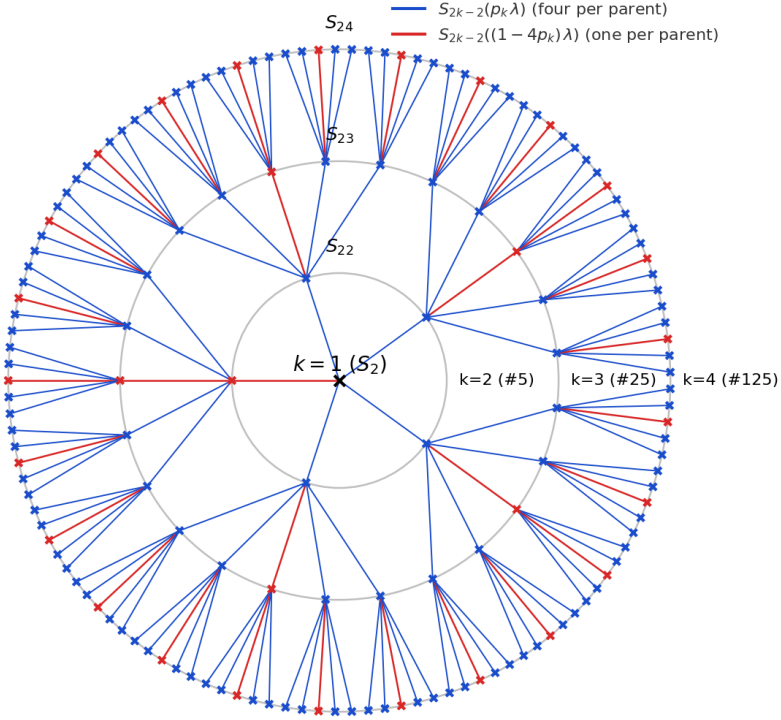


Figure 1: Suzuki-Trotter fractal with $k = 1$ at center. Blue edges/nodes: four $S_{2k-2}(p_k \lambda)$ children; red: one $S_{2k-2}((1 - 4p_k)\lambda)$.

Important: Now notice that for $k = 1$, we have 3 exponentials (for the M component Hamiltonian it would be $2M - 1 \sim O(M)$ exponentials).

Then $k = 2$ there will be 3×5 , for $k = 3$, 3×5^2 and for general k , we have $3 \times 5^{k-1}$ exponentials. Thus the number of gates grows exponentially with k . This can be depicted using the following figure. The rationale behind this figure is as follows. Imagine each gate occupies some finite volume. We want to place the gates for general k in the manner depicted. Typically, a real laboratory occupies a finite volume. As such, we need to keep the size of the circles finite. Had we been allowed to make the circle as large as we want, then the spacing between the gates on the circle could be whatever we want. But on a finite circle, typically the spacing between the gates will decrease. As such, the number of gates is a good measure of the size of the circle.

Now we have an interesting analogy with anti de Sitter or hyperbolic space. The metric of 3d AdS space is

$$ds^2 = dr^2 + e^{2r/L}(-dt^2 + dx^2). \quad (18)$$

On a fixed time slice the metric is

$$ds^2 = dr^2 + e^{2r/L}(dx^2). \quad (19)$$

Here x is periodic (angular coordinate). Thus for $r = r_*$, the size of the circle is

$$e^{2r_*/L}. \quad (20)$$

This is exactly what the quantum circuit figure is telling us! If k was proportional to r , this would be quite suggestive. Let us make this more precise.

3 Optimizing k and AdS

Divide the simulation time interval into small pieces of size Δ . For each step, we have now is the following:

$$\|e^{\Delta \sum_{i=1}^M H_i} - S_{2k}(\Delta)\| \propto h^{2k+1} \Delta^{2k+1} M \underbrace{5^{k-1}}_{\equiv c_k}. \quad (21)$$

The total number of steps is t/Δ so the total error is $h^{2k+1} \Delta^{2k+1} c_k M t / \Delta$. Equating this to a desired tolerance δ , we find:

$$h\Delta = \left(\frac{\delta}{M c_k h t} \right)^{\frac{1}{2k}} \quad (22)$$

Now the total number of exponentials is $M c_k t / \Delta$. Writing $Vt \equiv \Omega$, we have

$$N_{exp} = \Omega h c_k \left(\frac{\Omega h c_k}{\delta} \right)^{\frac{1}{2k}} = \Omega h \exp \left[\frac{1}{2k} \ln \frac{\Omega h}{\delta} + \left(1 + \frac{1}{2k} \right) \ln c_k \right]. \quad (23)$$

We see that as k increases, the terms proportional to $1/k$ decrease but there is also a term proportional to $k \ln 5$ which increases. Thus there is a competition, which will lead to a minimum/optimum number of gates for a $k = k_*$. This is given by [set ∂_k of the argument in the exponential to zero and solve]:

$$k_* = \frac{1}{\sqrt{2}} \log_5 \frac{\Omega h}{5\delta}, \quad (24)$$

and

$$N_{opt} \propto \Omega \exp [2k_* \ln 5]. \quad (25)$$

Now look at the solution for k_* . Keeping Ω, h fixed and dialing $0 < \delta < \infty$ enables us to scan $\infty > k_* > 0$. Thus, k_* can be thought of as a coordinate, corresponding to a given tolerance. The smaller this tolerance, the larger the value of this coordinate. We can think of this as the radial coordinate of AdS. Again notice that since the metric of AdS on a fixed time slice looks like eq.(19), the volume of this slice is $e^{r/L} V$ and time evolving gives the total volume as $e^{r/L} V t$. This form is similar to what appears in N_{opt} . Now, while this is suggestive of an emerging hyperbolic space, do be aware that we are not claiming a case for AdS/CFT here—we do not know how to argue for the presence of gravity in the bulk.

In the next lecture note, we will discuss the Quantum Fourier Transform.

A General $(2m+1)$ -block Suzuki recursion (order raise $2k-2 \rightarrow 2k$).

Let $m \in \mathbb{N}$ and set $s := 2m+1$ (number of subblocks per recursion). Given an order- $2k-2$ integrator $S_{2k-2}(\cdot)$, define

$$S_{2k}(\lambda) = [S_{2k-2}(p_k \lambda)]^m S_{2k-2}((1 - 2m p_k) \lambda) [S_{2k-2}(p_k \lambda)]^m,$$

with the symmetric coefficient

$$p_k = \frac{1}{2m - (2m)^{\frac{1}{2k-1}}}, \quad 1 - 2m p_k = -\frac{(2m)^{\frac{1}{2k-1}}}{2m - (2m)^{\frac{1}{2k-1}}}.$$

Then $S_{2k}(\lambda)^{-1} = S_{2k}(-\lambda)$ (time symmetry), and the local error is $\|e^{H\lambda} - S_{2k}(\lambda)\| = \mathcal{O}(|\lambda|^{2k+1})$.

Pattern length. Each order raise multiplies the per-slice pattern length by $s = 2m+1$. For two-term splitting (base $L_2 = 3$), this gives

$$L_{2k} = 3s^{k-1} = 3(2m+1)^{k-1}.$$

References

- [1] John Preskill lecture notes, [Lecture 6A notes, pgs 35-39](#)
- [2] N. Hatano and M. Suzuki, “Finding Exponential Product Formulas of Higher Orders,” *Lect. Notes Phys.* **679**, 37 (2005) doi:10.1007/11526216_2 [arXiv:math-ph/0506007 [math-ph]].
- [3] D. W. Berry, G. Ahokas, R. Cleve and B. C. Sanders, “Efficient Quantum Algorithms for Simulating Sparse Hamiltonians,” *Commun. Math. Phys.* **270**, no.2, 359-371 (2007) doi:10.1007/s00220-006-0150-x [arXiv:quant-ph/0508139 [quant-ph]].
- [4] A. Bhattacharyya, P. Nandy and A. Sinha, “Renormalized Circuit Complexity,” *Phys. Rev. Lett.* **124**, no.10, 101602 (2020) doi:10.1103/PhysRevLett.124.101602 [arXiv:1907.08223 [hep-th]].

\widehat{QFT} , QPE and the Hadamard test

Lecture Notes

Contents

1 Definitions	2
2 An important trick	3
3 Quantum phase estimation–QPE	6
4 The Hadamard Test	7
4.1 General Hadamard Test for $\langle \phi U \psi \rangle$	8
A QPE: some more details	10

This lecture and the next one are based on Nielsen and Chuang. I will try to spell out the missing algebraic steps. QFT stands for Quantum Field Theory in these lectures, so to distinguish this from the Quantum Fourier Transform, I will put a hat on the latter. \widehat{QFT} is one of the most important algorithms/circuits. It enables Quantum Phase Estimation (QPE) which will form an important step in analysing scattering in QFT.

Two key points to take note of:

1. \widehat{QFT} does not speed up the classical task of computing the Fourier Transform of classical data. You are expected to know/find out the reasons behind this (they were briefly touched upon during the lecture).
2. As mentioned \widehat{QFT} enables phase estimation. Phase estimation is the approximation of eigenvalues of a Unitary operator.
3. Let us say we are dealing with $N = 2^n$ number of classical data. Then the Fast Fourier Transform (FFT) needs $\Theta(n2^n)$ steps. The \widehat{QFT} needs $\Theta(n^2)$ steps and hence has an exponential “advantage.” But advantage over what? We mentioned above that \widehat{QFT} cannot be used to speed up the classical Fourier Transform. However, when we try to simulate the QPE on a classical computer, we will need a huge number of steps compared to the quantum counterpart. In this sense, there is an advantage. In Shor’s algorithm for instance, QPE plays an important role and hence a quantum computer will have an advantage. The downside is that the number of error corrected qubits and gates create a huge overhead and to get a real advantage, we will need millions of qubits.

After discussing \widehat{QFT} , we will discuss QPE followed by the Hadamard test. With these tools, we will be almost ready to tackle some quantum field theory problems on a quantum computer!

1 Definitions

Consider N classical data $x_0, x_1, \dots, x_{N-1} \in \mathbf{C}$. Then the Discrete Fourier Transform (DFT) is defined via:

$$y_k \equiv \frac{1}{\sqrt{N}} \sum_{j=0}^{N-1} x_j \exp\left(2\pi i \frac{jk}{N}\right). \quad (1)$$

The inverse DFT is given by:

$$x_k = \frac{1}{\sqrt{N}} \sum_{j=0}^{N-1} y_j \exp\left(-2\pi i \frac{jk}{N}\right). \quad (2)$$

\widehat{QFT} acts on the space of orthonormal states $\mathbf{B} = \{|0\rangle, |1\rangle, \dots, |N-1\rangle\}$ such that

$$\widehat{QFT}|j\rangle = \frac{1}{\sqrt{N}} \sum_{k=0}^{N-1} \exp\left(2\pi i \frac{jk}{N}\right) |k\rangle, \quad (3)$$

where $|j\rangle \in \mathbf{B}$. Equivalently we have

$$\widehat{QFT} \sum_{j=0}^{N-1} x_j |j\rangle = \sum_{j=0}^{N-1} y_k |k\rangle, \quad (4)$$

in other words, this spits out the DFT numbers y_k defined above. The inverse is given by

$$\widehat{IQFT} \sum_{j=0}^{N-1} y_j |j\rangle = \sum_{j=0}^{N-1} x_k |k\rangle, \quad (5)$$

2 An important trick

Let us choose $N = 2^n$ and as computational basis the set $|0\rangle, \dots, |2^n - 1\rangle$. Let $|j\rangle$ be one of these states. We can write the binary representation of j as:

$$j = j_1 2^{n-1} + j_2 2^{n-2} + \dots + j_n 2^0. \quad (6)$$

So we can write

$$|j\rangle = |j_1 j_2 \dots j_n\rangle. \quad (7)$$

Further let us introduce the notation:

$$0.j_\ell j_{\ell+1} \dots j_m \equiv j_\ell 2^{-1} + j_{\ell+1} 2^{-2} + \dots + j_m 2^{m-\ell+1}. \quad (8)$$

Notice that

$$\frac{j}{2^n} = 0.j_1 j_2 \dots j_n. \quad (9)$$

Using the definition of \widehat{QFT} we have

$$\widehat{QFT}|j_1 j_2 \dots j_n\rangle = \frac{1}{2^{n/2}} \sum_{k=0}^{2^n-1} \exp\left(2\pi i j \frac{k}{2^n}\right) |k\rangle. \quad (10)$$

Now

$$\frac{k}{2^n} = \sum_{\ell=1}^n k_\ell 2^{-\ell}, \quad (11)$$

where $k_\ell \in \{0, 1\}$. Since the next step can get a bit confusing, let's consider an example with $n = 2$. Then we have:

$$\begin{aligned} \widehat{QFT}|j\rangle &= \widehat{QFT}|j_1 j_2\rangle = \frac{1}{2} \sum_{k=0}^3 \exp\left(2\pi i j \frac{k}{4}\right) |k\rangle \\ &= \frac{1}{2} \exp\left(2\pi i j \frac{0}{4}\right) |0\rangle + \frac{1}{2} \exp\left(2\pi i j \frac{1}{4}\right) |1\rangle + \frac{1}{2} \exp\left(2\pi i j \frac{2}{4}\right) |2\rangle + \frac{1}{2} \exp\left(2\pi i j \frac{3}{4}\right) |3\rangle. \\ &= \frac{1}{2} \exp(2\pi i j 0.00) |00\rangle + \frac{1}{2} \exp(2\pi i j 0.01) |01\rangle \\ &\quad + \frac{1}{2} \exp(2\pi i j 0.10) |10\rangle + \frac{1}{2} \exp(2\pi i j 0.11) |11\rangle \\ &= \frac{1}{2} \sum_{k_1=0}^1 \sum_{k_2=0}^1 \exp(2\pi i j 0.k_1 k_2) |k_1 k_2\rangle, \\ &= \frac{1}{2} \sum_{k_1=0}^1 \sum_{k_2=0}^1 \exp\left(2\pi i j \sum_{\ell=1}^2 k_\ell 2^{-\ell}\right) |k_1 k_2\rangle, \\ &= \frac{1}{2} \sum_{k_1=0}^1 \sum_{k_2=0}^1 \otimes \exp\left(2\pi i j k_\ell 2^{-\ell}\right) |k_\ell\rangle, \\ &= \frac{1}{2} \otimes_{\ell=1}^2 \left[|0\rangle + \exp\left(2\pi i j \frac{1}{2^\ell}\right) |1\rangle \right] \end{aligned} \quad (12)$$

It is now clear that the generalization to any n of the last step is:

$$\widehat{QFT}|j_1 \cdots j_n\rangle = \frac{1}{2^{n/2}} \otimes_{\ell=1}^n \left[|0\rangle + \exp\left(2\pi i j \frac{1}{2^\ell}\right) |1\rangle \right]. \quad (13)$$

Expanding on this product, we have

$$\frac{1}{2^{n/2}} [|0\rangle + \exp\left(2\pi i \frac{j}{2}\right) |1\rangle] \otimes [|0\rangle + \exp\left(2\pi i \frac{j}{4}\right) |1\rangle] \cdots \otimes [|0\rangle + \exp\left(2\pi i \frac{j}{2^n}\right) |1\rangle] \quad (14)$$

Now notice

$$\begin{aligned} \exp\left(2\pi i \frac{j}{2^n}\right) &= \exp(2\pi i 0.j_1 \dots j_n), \\ \exp\left(2\pi i \frac{j}{2^{n-1}}\right) &= \exp(2\pi i [j_1 + j_2/2 + j_3/4 + \dots]) = \exp(2\pi i 0.j_2 \dots j_n), \\ &\vdots \end{aligned} \tag{15}$$

$$\exp\left(2\pi i \frac{j}{2}\right) = \exp(2\pi i 0.j_n), \tag{16}$$

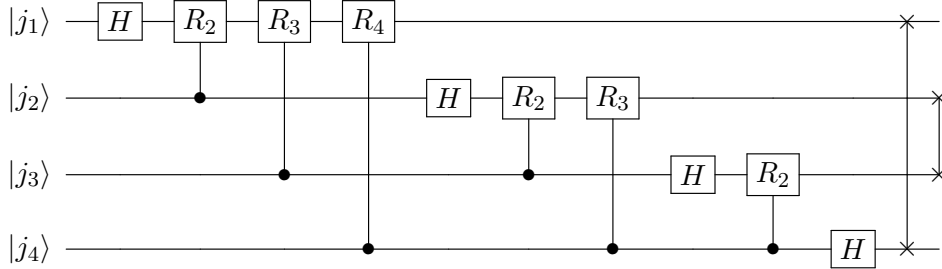
giving the final form:

$$\widehat{QFT}|j\rangle = \frac{1}{2^{n/2}}[|0\rangle + \exp(2\pi i 0.j_n)|1\rangle][|0\rangle + \exp(2\pi i 0.j_{n-1}j_n)|1\rangle] \dots [|0\rangle + \exp(2\pi i 0.j_1 \dots j_n)|1\rangle]. \tag{17}$$

Introducing the gate R_k

$$R_k \equiv \begin{pmatrix} 1 & 0 \\ 0 & \exp\left\{\frac{2\pi i}{2^k}\right\} \end{pmatrix}, \tag{18}$$

We find that \widehat{QFT} can be represented by the circuit in the figure:



The X 's indicate SWAP. As the word suggests, this operation swaps the indicated qubits. Let us see why this is needed.

Recall that the Hadamard does the following:

$$H|0\rangle = \frac{1}{\sqrt{2}}(|0\rangle + |1\rangle), \quad H|1\rangle = \frac{1}{\sqrt{2}}(|0\rangle - |1\rangle). \tag{19}$$

Since $|j_1\rangle$ is either $|0\rangle$ or $|1\rangle$, we can write:

$$H|j_1\rangle = \frac{1}{\sqrt{2}}(|0\rangle + \exp(2\pi i 0.j_1)|1\rangle), \tag{20}$$

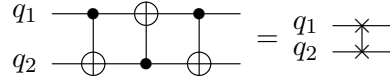
This is because when $j_1 = 1$ we have $0.j_1 = 1/2$ and the conclusion is obvious. Then according to the circuit we act with a controlled- R_2 with the control being $|j_2\rangle$. If $j_2 = 0$, we do nothing, while if $j_2 = 1$, $\exp(2\pi i 0.j_1)|1\rangle \rightarrow \exp(2\pi i/4)\exp(2\pi i 0.j_1)|1\rangle$. This action can be written as:

$$R_2 \frac{1}{\sqrt{2}}(|0\rangle + \exp(2\pi i 0.j_1)|1\rangle) = \frac{1}{\sqrt{2}}(|0\rangle + \exp(2\pi i 0.j_1 j_2)|1\rangle). \quad (21)$$

Next applying controlled- $R_3 \dots R_n$ finally yields

$$\frac{1}{\sqrt{2}}(|0\rangle + \exp(2\pi i 0.j_1 \dots j_n)|1\rangle). \quad (22)$$

Similarly running through $|j_2\rangle$ we find $\frac{1}{\sqrt{2}}(|0\rangle + \exp(2\pi i 0.j_2 \dots j_n)|1\rangle)$. Ultimately we have eq.(17) but with the ordering reversed. This is the reason we need the final SWAP operations. Incidentally, the SWAP operation is given by the following simple circuit:



How many do we need to do the SWAPs correctly? [figure this out]. Finally, the inverse QFT is given by the circuit in reverse with the angles in R_k changing sign.

3 Quantum phase estimation–QPE

Consider a state ψ which is an eigenstate of a unitary U such that

$$U|\psi\rangle = e^{2\pi i \phi}|\psi\rangle. \quad (23)$$

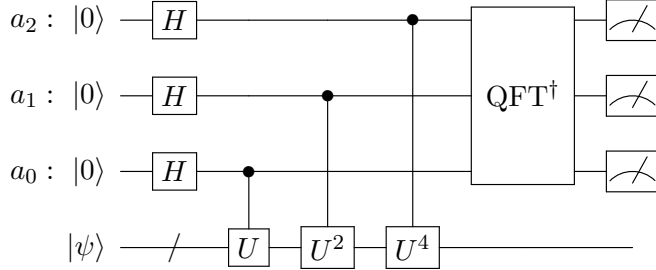
ϕ lies between 0 and 1. The binary representation of ϕ with accuracy up to t -bits is

$$\phi = \frac{\phi_1}{2} + \frac{\phi_2}{4} + \dots + \frac{\phi_t}{2^t}. \quad (24)$$

So that

$$\exp(2\pi i 2^{t-1}\phi) = \exp(2\pi i 0.\phi_t), \quad (25)$$

etc.



That / symbol indicates that that “wire” bundles several qubits. The symbol denotes a measurement in the computational (Z) basis; the probabilities of finding $|0\rangle$ or $|1\rangle$ are estimated from repeated shots.

This algorithm was introduced by Kitaev. It enables us to extract the phase (up to a certain precision) of a unitary operator. We assume that we can implement the unitary operator [and we don’t have to worry about what or how it is made]. There are two sets of qubits in the figure: a_i and sys . They are called registers.

The steps now should be pretty obvious. In the $t = 3$ example in the circuit showed, just before the inverse Fourier Transform QFT^\dagger is

$$(|0\rangle + e^{2\pi i 0 \cdot \phi_3} |1\rangle)(|0\rangle + e^{2\pi i 0 \cdot \phi_2 \phi_3} |1\rangle)(|0\rangle + e^{2\pi i 0 \cdot \phi_1 \phi_2 \phi_3} |1\rangle). \quad (26)$$

This is nothing but

$$\widehat{QFT}|\phi_1\phi_2\phi_3\rangle. \quad (27)$$

Thus the last step of the inverse \widehat{QFT} just gives $|\phi_1\phi_2\phi_3\rangle$ as the output state. Thereafter, measuring in the computational basis will enable us to read off ϕ_1, ϕ_2, ϕ_3 .

4 The Hadamard Test

Given a unitary U and a state $|\psi\rangle$, the Hadamard test estimates

$$\langle\psi|U|\psi\rangle \in \mathbb{C}.$$

Prepare an ancilla $|0\rangle$ and the system in $|\psi\rangle$. For the *real part*, apply H to the ancilla, a controlled- U on the system (controlled by the ancilla), then H again on the ancilla and measure Z :

$$P(0) = \frac{1}{2}(1 + \text{Re}\langle\psi|U|\psi\rangle), \quad \text{Re}\langle\psi|U|\psi\rangle = 2P(0) - 1.$$

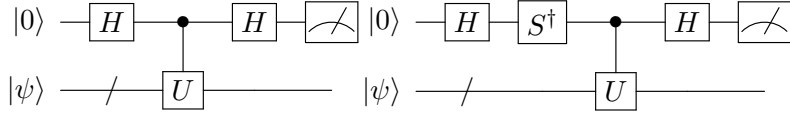
For the *imaginary part*, insert an S^\dagger ($= Z^{-1/2}$) before the controlled- U (or equivalently before the final H):

$$P(0) = \frac{1}{2}(1 + \text{Im}\langle\psi|U|\psi\rangle), \quad \text{Im}\langle\psi|U|\psi\rangle = 2P(0) - 1.$$

Explicitly

$$S = \begin{pmatrix} 1 & 0 \\ 0 & i \end{pmatrix}, \quad S^\dagger = \begin{pmatrix} 1 & 0 \\ 0 & -i \end{pmatrix}.$$

Circuits (using qcircuit).



The left circuit yields $\text{Re}\langle\psi|U|\psi\rangle$, the right yields $\text{Im}\langle\psi|U|\psi\rangle$.

Let us work through the left circuit from left to right.

$$\begin{aligned} |0\rangle|\psi\rangle &\rightarrow \frac{1}{\sqrt{2}}(|0\rangle + |1\rangle)|\psi\rangle \\ &\rightarrow \frac{1}{\sqrt{2}}(|0\rangle + |1\rangle)U|\psi\rangle \\ &\rightarrow \frac{1}{2}(|0\rangle|\psi\rangle + |1\rangle U|\psi\rangle). \end{aligned} \tag{28}$$

Now measuring the first qubit gives the probabilities of

$$P(0) = \frac{1}{4}\langle\psi|(1 + U^\dagger)(1 + U)|\psi\rangle = \frac{1}{2}(1 + 2\text{Re}\langle\psi|U\rangle), \tag{29}$$

from which we can read off $\text{Re}\langle\psi|U\rangle$. I leave it as an exercise for you to verify for the *Im* case.

4.1 General Hadamard Test for $\langle\phi|U|\psi\rangle$

Let B be a unitary operator such that

$$|\phi\rangle = B|\psi\rangle.$$

Then $\langle\psi|\tilde{U}|\psi\rangle = \langle\phi|B^\dagger\tilde{U}|\psi\rangle$. Then if we are interested in getting real or imaginary part of $\langle\phi|U|\psi\rangle$, we simply use

$$\tilde{U} = BU$$

and run the Hadamard test.

In the next lecture we will touch upon an important simulation algorithm called Linear Combination of Unitaries (LCU). The reason why we will need this is because in quantum field theory, the field is not a unitary (and in many cases not even Hermitian) operator.

A QPE: some more details

Let U be a unitary with eigenstate $|\psi\rangle$ and eigenphase $\phi \in [0, 1]$:

$$U |\psi\rangle = e^{2\pi i \phi} |\psi\rangle. \quad (30)$$

We run textbook QPE with $m = 4$ ancilla qubits (Fourier register size $M = 2^m = 16$), applying controlled powers U^{2^k} on the system, controlled by ancilla k (with $k = 0$ the least significant bit).

Goal. Measure an integer $r \in \{0, \dots, 15\}$ whose ratio $r/16$ approximates ϕ . In Hamiltonian estimation, with $U = e^{-iHt}$, we then estimate the energy

$$E \approx \frac{2\pi}{t} \frac{r}{16}. \quad (31)$$

State preparation and phase kickback

Initialize the system in $|\psi\rangle$ and the ancillas in the uniform superposition:

$$|+\rangle^{\otimes 4} = \frac{1}{4} \sum_{y=0}^{15} |y\rangle. \quad (32)$$

Apply the controlled powers $c-U^{2^k}$ so that each basis state $|y\rangle$ in the Fourier register kicks back the phase $e^{2\pi i \phi y}$ onto the system eigenstate. The joint state (ignoring the unchanged system factor $|\psi\rangle$) becomes

$$|\Phi\rangle = \frac{1}{4} \sum_{y=0}^{15} e^{2\pi i \phi y} |y\rangle. \quad (33)$$

Inverse QFT and amplitudes

Apply the inverse quantum Fourier transform QFT_{16}^\dagger to the ancilla register. The amplitude for outcome $|r\rangle$ is

$$\langle r | \text{QFT}_{16}^\dagger | \Phi \rangle = \frac{1}{4} \cdot \frac{1}{4} \sum_{y=0}^{15} e^{2\pi i \phi y} e^{-2\pi i r y / 16} \quad (34)$$

$$= \frac{1}{16} \sum_{y=0}^{15} e^{2\pi i y (\phi - r/16)}. \quad (35)$$

This is a finite geometric sum with closed form

$$A(r) \equiv \frac{1}{16} \sum_{y=0}^{15} e^{2\pi i y(\phi - r/16)} = \frac{1}{16} \cdot \frac{1 - e^{2\pi i 16(\phi - r/16)}}{1 - e^{2\pi i (\phi - r/16)}}. \quad (36)$$

Therefore the measurement probability is

$$P(r) = |A(r)|^2 = \frac{1}{16^2} \left| \frac{1 - e^{2\pi i 16(\phi - r/16)}}{1 - e^{2\pi i (\phi - r/16)}} \right|^2 = \frac{1}{16^2} \left(\frac{\sin(\pi \cdot 16(\phi - r/16))}{\sin(\pi(\phi - r/16))} \right)^2. \quad (37)$$

Eq. (37) is the (squared) Dirichlet kernel, sharply peaked at $r \approx 16\phi$.

Exact representable phases. If $\phi = s/16$ for some integer s , then $P(r) = \delta_{r,s}$ (perfectly sharp outcome).

General phases. If ϕ is not exactly representable with m bits, the distribution peaks at the nearest integer $r^* = \text{round}(16\phi)$, with the standard success bound

$$\Pr(|r - 16\phi| \leq 1) \geq \frac{4}{\pi^2} \approx 0.405. \quad (38)$$

Bit interpretation and IQFT unrolling

Equivalently, one may view QPE as producing the binary fraction

$$\tilde{\phi} = \frac{r}{16} = 0.b_1 b_2 b_3 b_4 \quad (b_j \in \{0, 1\}), \quad (39)$$

via the inverse-QFT ladder identities. In the exact case, each controlled- $U^{2^{m-j}}$ followed by the IQFT phase-correction yields bit b_j with unit probability.

Worked example (four ancillas)

Take $\phi = \frac{5}{8} = 0.625$. With $m = 4$, $16\phi = 10$ exactly, so the outcome is $r = 10$ with probability 1. The measured bitstring is

$$r = 10 \Rightarrow \text{binary } 1010 \Rightarrow \tilde{\phi} = 10/16 = 0.625 = \phi. \quad (40)$$

In Hamiltonian spectroscopy with $U = e^{-iHt}$, this would correspond to

$$E = \frac{2\pi}{t} \tilde{\phi} = \frac{2\pi}{t} \cdot \frac{10}{16}. \quad (41)$$

Energy resolution and choosing t

For QPE targeting $U = e^{-iHt}$, ancilla size m and base evolution time t set the energy resolution

$$\Delta E \sim \frac{2\pi}{t 2^m} = \frac{2\pi}{t 16} \quad (m = 4). \quad (42)$$

Larger m and/or t yield finer resolution (within Trotter/noise limits).

Superposed inputs

If the system is prepared in a superposition $|\psi\rangle = \sum_j \alpha_j |E_j\rangle$ over eigenstates of U , then the ancilla distribution is a convex mixture

$$P(r) = \sum_j |\alpha_j|^2 P_\phi^{(j)}(r), \quad \phi_j = \frac{E_j t}{2\pi}, \quad (43)$$

i.e. each eigenphase contributes its own Dirichlet kernel (37), weighted by $|\alpha_j|^2$. Each single-shot measurement returns one eigenvalue with probability $|\alpha_j|^2$.

Summary

With $m = 4$ ancillas, textbook QPE prepares a length-16 Fourier superposition, imprints eigenphase via controlled powers U^{2^k} , applies QFT_{16}^\dagger , and measures an integer r whose ratio $r/16$ estimates ϕ . Exact 4-bit phases are retrieved perfectly; general phases are concentrated near $r \approx 16\phi$ with a Dirichlet-kernel profile and standard success guarantees. For spectroscopy with $U = e^{-iHt}$, the energy estimator is $E \approx \frac{2\pi}{t} \frac{r}{16}$.

Appendix: The Hadamard Test in Quantum Field Theory Simulations

One of the key primitives for extracting physically meaningful quantities from a quantum computer is the *Hadamard test*. While its basic form is often introduced in quantum computing textbooks (e.g. Nielsen and Chuang), its importance in quantum field theory (QFT) simulations deserves special emphasis. Here we collect the relevant definitions, use-cases, and literature.

Applications in quantum field theory

In quantum field theory on a quantum computer, the Hadamard test plays a central role because many physically measurable quantities are complex overlaps:

- **Correlation functions.** For example, a two-point function in lattice QFT,

$$C(t) = \langle 0 | \phi(t) \phi(0) | 0 \rangle,$$

can be expressed in terms of overlaps involving time-evolution unitaries,

$$C(t) = \langle 0 | U^\dagger(t) \phi U(t) \phi | 0 \rangle, \quad U(t) = e^{-iHt}.$$

Such quantities are directly accessible via Hadamard tests with $U = e^{-iHt}$ and ϕ represented as a sum of Pauli strings.

- **S-matrix elements.** Scattering amplitudes are encoded in

$$S_{fi} = \langle f | \mathcal{T} \exp \left(-i \int H_{\text{int}}(t) dt \right) | i \rangle,$$

which is of the form $\langle f | U | i \rangle$ for appropriate in/out states. The Hadamard test provides a way to obtain both the modulus and the phase of S_{fi} , essential for extracting phase shifts and cross-sections.

- **Hamiltonian matrix elements.** In variational and effective-Hamiltonian approaches, one often needs matrix elements $\langle \phi | H | \psi \rangle$. When H is decomposed into a linear combination of unitaries (LCU), each term can be accessed by a Hadamard test.

Practical considerations

- **Controlled time-evolution.** The Hadamard test requires a controlled- U . In QFT applications, $U = e^{-iHt}$ where H is a field theory Hamiltonian. Thus, any Hamiltonian simulation algorithm (Trotter-Suzuki, qubitization, QSVT, etc.) must be implemented in controlled form. This typically doubles the circuit cost.
- **Noise and sampling.** The signal in a Hadamard test is a small difference of probabilities, so many shots are needed to reduce variance. On NISQ devices this can be prohibitive, although error mitigation can help.

- **State preparation.** The in- and out-states $|i\rangle$ and $|f\rangle$ (multi-particle wavepackets) must be prepared with high fidelity. This is itself a major subproblem in quantum simulation of QFT.

Bibliographic references

For further reading, see:

- S. Jordan, K. Lee, and J. Preskill, *Quantum algorithms for quantum field theories*, Science **336**, 1130 (2012).
- N. Klco and M. J. Savage, *Digitization of scalar fields for quantum computing*, Phys. Rev. A **99**, 052335 (2019).
- C. Bauer, Z. Davoudi, N. Klco, M. J. Savage, and A. Shindler, *Quantum simulation of gauge theories and fields*, Quantum Sci. Technol. **8**, 043001 (2023).
- M. A. Nielsen and I. L. Chuang, *Quantum Computation and Quantum Information* (Cambridge Univ. Press, 2010).

In summary, the Hadamard test is not merely a textbook curiosity but a fundamental measurement primitive for quantum field theory on quantum computers. It provides the essential bridge between quantum state preparation/evolution and extraction of complex correlators and scattering amplitudes.

Key experimental / demonstration papers

Reference	What was demonstrated	Number of qubits / hardware	Strengths / Limitations
"Demonstrating NISQ-era challenges in algorithm design on ..." by D. Koch et al. (2020)	Implementation of a 3-qubit QFT on real hardware; study of its reliability under noise, gate errors etc.	3-qubit QFT on IBM / similar superconducting qubit devices	Good for small size: errors grow (phase errors, gate infidelities). Demonstrates QFT works for tiny registers but not yet scalable.
"Reducing CNOT count in quantum Fourier transform for the ..." by Park et al. (2023)	A new optimized QFT circuit design (linear nearest-neighbor architecture) that reduces CNOT-gate count; implemented on IBM devices using Diskit transpiler.	Up to maybe 4-5 qubits in experiments (LNN constraints)	Strength: reduction in resource usage (less error accumulation). Limitation: limited qubit connectivity & noise, still small scale.
"Digital-analog quantum algorithm for the quantum Fourier ..." by A. Martin et al. (2020)	Implemented a "digital-analog" hybrid approach for QFT which uses analog evolutions plus digital gates to achieve the transform with higher fidelity under noise.	Devices with analog capabilities; small qubit registers	Strength: better fidelities than fully digital QFT for some sizes. Limitation: hardware-specific; analog part may be harder to control precisely.
"An Improved Implementation Approach for Quantum Phase Estimation on Quantum Computers" by Mohammadbagherpoor et al. (2019)	Implementation and benchmarking of modified QPE algorithms on IBM Q devices (e.g., IBMQX4), with reduced numbers of controlled-rotations to adapt to noise.	Small numbers of qubits (\approx a few ancilla + system qubits) on IBM machines	Shows that reducing depth helps a lot. But full accuracy for many bits of phase is not possible on small NISQ machines.
"Quasiprobabilistic state-overlap estimator for NISQ devices" by Guerini, Wiersma, Carrasquilla, Aditi (2021)	Methods to estimate state overlap (i.e. overlap between two arbitrary states), using circuits designed to be efficient under NISQ noise. Compares with randomized measurement methods.	Overlaps for few-qubit states (n up to ~6) in simulation / smaller physical devices	Good performance for small n; operations become noisy for larger n. Serves as a real-world proxy for what a Hadamard-test overlap might do, albeit not always exactly the same circuit.
"Toward Practical Quantum Phase Estimation: A Modular ..." (2025)	Studies and proposals of more hardware-friendly QPE variants: using bit-by-bit (iterative) methods, or modular decomposition, reducing depth, improving robustness. Emphasizes using Hadamard-type tests for bits of phase.	Mostly theoretical / simulation proposals, with small hardware tests	Shows the route by which NISQ-friendly QPE might scale. But large-scale, high-precision QPE remains out of reach.

Figure 1: Some current implementations

Quantum Fourier Transform (QFT)					
Ref.	Year	Platform	Size	Result	Limitations
Bäumer et al., <i>PRL</i> 133, 150602 (link ↗)	2024	IBM superconducting (dynamic circuits)	Up to 16 qubits (also 37 in extended mode)	Verified QFT action using mid-circuit measurement + feed-forward; certified fidelities	Works when QFT followed by measurement; small rotations noisy; not yet scalable
Jin et al., arXiv:2408.11226	2024	IBM hardware / noisy simulators	4–8 qubits	Hardware-aware mapping reduces 2-qubit gate count and error	Still small N; focus on compilation rather than scaling

Quantum Phase Estimation (QPE)					
Ref.	Year	Platform	Size	Result	Limitations
Yamamoto et al., arXiv:2306.16608	2023	Quantum trapped-ion	2 system qubits + ancilla	Bayesian QPE with error detection; H_2 ground state energy within $\sim 6 \times 10^{-3}$ Hartree	Depth \sim 920 2-qubit gates; precision only a few bits
"Two Variations of QPE ..." <i>InspireHEP</i> 2944769	2025	IBM superconducting	Few-qubit demos	Compared shallow QPE variants; noise-aware compilation	Only few phase bits; noisy two-qubit gates dominate
Mid-circuit feedback QPE (arXiv:2506.00118)	2025	IBM-style hardware	Few qubits	Iterative, feedback-driven QPE primitive to amplify low-energy states	Not extracting many phase bits; still toy scale

Hadamard Test / Overlap Estimation					
Ref.	Year	Platform	Size	Result	Limitations
Guerini et al., arXiv:2112.17618	2021 (baseline, widely cited)	IBM, simulations	~6 qubits	Quasiprobabilistic overlap estimation; compared to swap test	Noise quickly dominates; still small registers
Cincio et al., "Learning state overlap circuits" (hardware-aware)	2023 updates on IBM / Rigetti	Few qubits	Machine-learned circuits for overlap; shallower than swap/Hadamard	Gains are modest; still limited by gate noise	
Mid-circuit feedback QPE work (2025)	IBM-like	↓	Few qubits	Uses Hadamard-test-style single-ancilla overlaps as primitive in feedback loop	Not yet general large-register overlap; only algorithmic primitive

Figure 2: Some current implementations

LCU & simulating quantum mechanics

Lecture Notes

Contents

1 Linear Combination of Unitaries (LCU)	1
1.1 Motivation: why LCU in QFT?	1
1.2 The LCU algorithm	2
1.3 Explicit example: two-term LCU	3
1.4 Explicit example: the field operator $\phi = a + a^\dagger$	4
1.5 Remarks and references	6
2 The anharmonic oscillator: benchmarks for quantum simulation	7
2.1 Positive quartic potential	7
2.2 Negative quartic and the double-well potential	8

1 Linear Combination of Unitaries (LCU)

We will introduce the *Linear Combination of Unitaries* (LCU) framework. The key motivation is that quantum computers naturally implement *unitary* operations, but in quantum field theory (QFT) one is often interested in operators that are not unitary: field operators ϕ, π , number operators, Hamiltonians, or correlators involving insertions of such operators. The LCU method provides a systematic way to embed non-unitary operations into quantum algorithms using ancillary qubits and controlled unitaries.

1.1 Motivation: why LCU in QFT?

In lattice field theory one frequently encounters operators of the form

$$H = \sum_j c_j P_j, \tag{1}$$

where the P_j are Pauli strings (unitary) and c_j are real coefficients. This Hamiltonian is not itself unitary, yet we need to implement e^{-iHt} , or evaluate matrix elements like $\langle \phi | H | \psi \rangle$. Similarly, truncated field operators $\phi = a + a^\dagger$ and $\pi = i(a^\dagger - a)$ are non-unitary. In order to use these inside Hadamard tests or block-encodings, we must represent them as linear combinations of unitaries.

Thus the LCU method is indispensable for simulating QFT on a quantum computer:

- it allows Hamiltonians (sums of many Pauli terms) to be implemented in Hamiltonian simulation algorithms;
- it allows operator insertions (like ϕ) to be implemented in Hadamard tests for correlators;
- it provides a standard language (SELECT and PREP oracles) which is now adopted in frameworks such as Qiskit and PennyLane.

1.2 The LCU algorithm

Let us give the algebraic steps. Suppose we want to implement

$$A = \sum_{j=0}^{m-1} \alpha_j U_j, \quad (2)$$

with coefficients $\alpha_j \geq 0$ and each U_j a unitary operator. Why is this always possible? First you can work out a matrix representation of A (say by knowing how it operates on n -qubits). Such a representation can be decomposed in terms of $\{I, \sigma_x, \sigma_y, \sigma_z\}^{\otimes n}$. The coefficients can in general be complex c_j 's. But by writing $c_j = \alpha_j e^{i\phi_j}$, with $\alpha_j > 0$, we can absorb the phase into the unitaries.

Step 1: Ancilla preparation (PREP). Prepare an ancilla register in the state

$$\text{PREP}|0\rangle = \frac{1}{\sqrt{\Lambda}} \sum_{j=0}^{m-1} \sqrt{\alpha_j} |j\rangle, \quad \Lambda = \sum_j \alpha_j. \quad (3)$$

Here $|0\rangle$ is the shorthand for $|0 \cdots 0\rangle$ —which is m dimensional.

Step 2: SELECT operation. Apply the block-diagonal unitary

$$\text{SELECT}(U) = \sum_{j=0}^{m-1} |j\rangle\langle j| \otimes U_j. \quad (4)$$

This applies the correct unitary U_j to the system conditional on the ancilla label.

Step 3: Uncompute. Apply PREP^\dagger to the ancilla. The resulting joint state is

$$(\text{PREP}^\dagger \otimes I) \text{SELECT}(U) (\text{PREP} \otimes I) |0\rangle |\psi\rangle = \frac{1}{\Lambda} |0\rangle \otimes A|\psi\rangle + |\text{garbage}\rangle, \quad (5)$$

where the garbage terms live in the subspace with ancilla orthogonal to $|0\rangle$.

Step 4: Postselection or amplitude amplification. If the ancilla is measured in state $|0\rangle$, the system is left in $A|\psi\rangle/\Lambda$. The success probability is

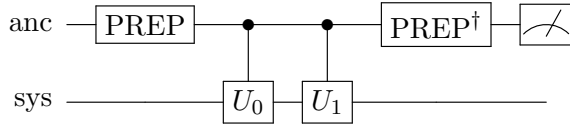
$$p_{\text{succ}} = \frac{\|A|\psi\rangle\|^2}{\Lambda^2}. \quad (6)$$

Amplitude amplification can be used to boost this probability.

The terminology *PREP* and *SELECT* is now standard in the literature, and adopted in Qiskit, PennyLane, and other quantum software frameworks.

1.3 Explicit example: two-term LCU

Let $A = \alpha_0 U_0 + \alpha_1 U_1$ with $\alpha_0 = 1$, $\alpha_1 = 2$, $U_0 = I$, $U_1 = X$ on a single qubit. The ancilla is one qubit.



Ancilla preparation.

$$|\text{anc}\rangle = \frac{1}{\sqrt{3}}(|0\rangle + \sqrt{2}|1\rangle). \quad (7)$$

SELECT(U).

$$\text{SELECT}(U) = |0\rangle\langle 0| \otimes I + |1\rangle\langle 1| \otimes X. \quad (8)$$

Action on input. For input $|\psi\rangle = |0\rangle$,

$$|\Psi_1\rangle = \frac{1}{\sqrt{3}}(|0\rangle \otimes |0\rangle + \sqrt{2}|1\rangle \otimes |1\rangle). \quad (9)$$

After uncomputing with PREP^\dagger , the component with ancilla $|0\rangle$ is

$$\frac{1}{3}(I + 2X)|0\rangle = \frac{1}{3} \begin{bmatrix} 1 \\ 2 \end{bmatrix}. \quad (10)$$

The orthogonal component maps to ancilla $|1\rangle$ (the ‘garbage’ branch). The fidelity of the good branch with the ideal target $(A/\Lambda)|\psi\rangle$ is 1.

Exercise (done in class): Construct explicitly the PREP operator and verify the claims above. Show that $\text{PREP} = R_y(2\theta)$ with $\theta \approx 109.5^\circ$

1.4 Explicit example: the field operator $\phi = a + a^\dagger$

Consider the truncated Fock space $\mathcal{H}_d = \text{span}\{|n\rangle : n = 0, 1, \dots, d-1\}$. In this basis the annihilation operator is

$$a_d = \sum_{n=1}^{d-1} \sqrt{n} |n-1\rangle \langle n| = \begin{pmatrix} 0 & 1 & 0 & \cdots & 0 \\ 0 & 0 & \sqrt{2} & \cdots & 0 \\ \vdots & & \ddots & \ddots & \vdots \\ 0 & \cdots & 0 & 0 & \sqrt{d-1} \\ 0 & \cdots & \cdots & 0 & 0 \end{pmatrix}. \quad (11)$$

First let’s introduce unary coding.

Unary encoding and hop operators. In unary encoding we represent $|n\rangle$ by a string of d qubits with a single ‘1’ at site $j = n + 1$. For example with $d = 4$,

$$|0\rangle \mapsto |1000\rangle, \quad |1\rangle \mapsto |0100\rangle, \quad |2\rangle \mapsto |0010\rangle, \quad |3\rangle \mapsto |0001\rangle.$$

In this picture the operator $|n-1\rangle \langle n|$ should move the lone ‘1’ one step to the left:

$$|0100 \cdots 0\rangle \mapsto |1000 \cdots 0\rangle, \quad |0010 \cdots 0\rangle \mapsto |0100 \cdots 0\rangle, \quad \text{etc.}$$

More generally, the hop takes the local two-qubit pattern

$$|01\rangle_{j,j+1} \mapsto |10\rangle_{j,j+1},$$

and annihilates all other patterns.

This is exactly the action of

$$\sigma_+^{(j)} \sigma_-^{(j+1)},$$

where $\sigma_+ = (X - iY)/2$ and $\sigma_- = (X + iY)/2$. Here $\sigma_+^{(j)}$ raises qubit j from $|0\rangle$ to $|1\rangle$, while $\sigma_-^{(j+1)}$ lowers qubit $j+1$ from $|1\rangle$ to $|0\rangle$. Acting together they implement the hop $|01\rangle_{j,j+1} \mapsto |10\rangle_{j,j+1}$.

Expanding this product gives the Pauli–string decomposition

$$\sigma_+^{(j)} \sigma_-^{(j+1)} = \frac{1}{4}(X_j X_{j+1} + Y_j Y_{j+1} + i X_j Y_{j+1} - i Y_j X_{j+1}),$$

so each hop operator is a linear combination of four Pauli–string unitaries. Multiplying by \sqrt{n} and summing over $n = 1, \dots, d-1$ reconstructs the full annihilation operator a_d in unary encoding.

$d = 3$ case. For three levels (two hops) the annihilation operator is

$$a_3 = \frac{\sqrt{1}}{4} \left(X_1 X_2 + Y_1 Y_2 + i X_1 Y_2 - i Y_1 X_2 \right) \otimes I_3 + \frac{\sqrt{2}}{4} I_1 \otimes \left(X_2 X_3 + Y_2 Y_3 + i X_2 Y_3 - i Y_2 X_3 \right).$$

Each bracketed term is a sum of four Pauli–string unitaries; the coefficients are $\sqrt{1}/4$ and $\sqrt{2}/4$ respectively. This is an exact LCU decomposition of a_3 into (phased) Pauli strings.

LCU for a_3 with phased unitaries. Let X_k and Y_k denote Pauli X and Y acting on qubit k (identity elsewhere), and let I_k be the identity on qubit k . Absorbing the complex phases $\pm i$ into the Pauli strings, we write

$$a_3 = \sum_{j=1}^8 \alpha_j U_j, \quad (\alpha_j > 0),$$

with coefficients and unitaries

$$\begin{aligned} \alpha_1 = \alpha_2 = \alpha_3 = \alpha_4 = \frac{1}{4}, \quad & U_1 = X_1 X_2 \otimes I_3, \quad U_2 = Y_1 Y_2 \otimes I_3, \\ & U_3 = (i X_1 Y_2) \otimes I_3, \quad U_4 = (-i Y_1 X_2) \otimes I_3, \\ \alpha_5 = \alpha_6 = \alpha_7 = \alpha_8 = \frac{\sqrt{2}}{4}, \quad & U_5 = I_1 \otimes X_2 X_3, \quad U_6 = I_1 \otimes Y_2 Y_3, \\ & U_7 = I_1 \otimes (i X_2 Y_3), \quad U_8 = I_1 \otimes (-i Y_2 X_3). \end{aligned}$$

Each U_j is unitary (a Pauli string times a global phase), and all amplitudes α_j are real and nonnegative. This is an exact LCU for a_3 in unary encoding; the Hermitian field operator is then $\phi_3 = a_3 + a_3^\dagger$.

The Hermitian combination

$$\phi_3 = a_3 + a_3^\dagger$$

then reduces to a real linear combination of Pauli strings, which can be sampled using standard LCU or Hamiltonian simulation methods.

d = 4 case. Similarly, for four levels one obtains

$$a_4 = \frac{\sqrt{1}}{4} (\dots) \otimes I \otimes I + \frac{\sqrt{2}}{4} I \otimes (\dots) \otimes I + \frac{\sqrt{3}}{4} I \otimes I \otimes (\dots),$$

with each “ (\dots) ” denoting the four-term Pauli combination above.

Summary. In a finite bosonic truncation, the position operator $\phi_d = a_d + a_d^\dagger$ is *exactly* a linear combination of embedded Pauli σ_x unitaries with positive weights \sqrt{n} . This gives a clean, hands-on LCU that avoids any subtleties about nonunitary shifts in the infinite Fock space and is immediately implementable on qubits.

This allows ϕ insertions in correlators (e.g. two-point functions) to be implemented using Hadamard tests with LCU.

1.5 Remarks and references

The LCU framework was developed in the 2000s–2010s as part of Hamiltonian simulation algorithms and is not covered in standard textbooks such as Nielsen and Chuang (2000). Good references include:

- A. Childs and N. Wiebe, “Hamiltonian simulation using linear combinations of unitary operations,” *Quantum Information & Computation* 12 (2012).
- D. Berry, A. Childs, R. Cleve, R. Kothari, and R. Somma, “Simulating Hamiltonian dynamics with a truncated Taylor series,” *Phys. Rev. Lett.* 114, 090502 (2015).
- Textbook background: M. A. Nielsen and I. L. Chuang, *Quantum Computation and Quantum Information* (Cambridge Univ. Press, 2010) — predates LCU, does not cover this framework.

In summary, the LCU framework is essential for QFT simulation on quantum computers: it allows non-unitary operators (fields, Hamiltonians) to be encoded as sums of unitaries, so that they can be used inside the Hadamard test and block-encoding algorithms for correlators and scattering amplitudes.

Remark on QSVT/QSP. The current state of the art in Hamiltonian simulation and related linear algebra tasks is based on *quantum singular value transformation* (QSVT) and its underlying idea of *quantum signal processing* (QSP) [14, 15]. These frameworks provide a powerful and unifying approach: given a block encoding of an operator, one can implement polynomial transformations of its singular values with near-optimal asymptotic complexity. In particular, QSVT improves upon Trotter methods and even the LCU approach by achieving exponential precision scaling in the polynomial degree and by offering a very general toolkit for Hamiltonian simulation, solving linear systems, Gibbs sampling, and more. However, the machinery required—block encodings, polynomial approximation theory, and signal processing gadgets—is technically demanding and can obscure the physics. For this reason we will *hold off on a detailed treatment of QSVT/QSP* until we encounter concrete situations where their advantages become essential. At present, the simpler tools already introduced (QPE, Hadamard test, LCU, and Trotterization) are sufficient for our first physics applications such as the anharmonic oscillator.

We have learnt \widehat{QFT} , QPE, Hadamard test and LCU. With these tools, we will now move to simulation of quantum mechanics and then quantum field theory.

2 The anharmonic oscillator: benchmarks for quantum simulation

We use units $\hbar = 1$, $m = 1$, $\omega = 1$ unless otherwise stated.

2.1 Positive quartic potential

The Hamiltonian

$$H(g) = \frac{p^2}{2} + \frac{x^2}{2} + g x^4, \quad g > 0, \quad (12)$$

is the paradigmatic model of an interacting quantum system in one dimension.

Perturbative expansion. Rayleigh–Schrödinger perturbation theory yields

$$E_0(g) = \frac{1}{2} + \frac{3}{4}g - \frac{21}{8}g^2 + \mathcal{O}(g^3), \quad (13)$$

$$E_1(g) = \frac{3}{2} + \frac{15}{4}g - \frac{405}{8}g^2 + \mathcal{O}(g^3). \quad (14)$$

The coefficients grow factorially at high order [1, 2]. Numerically, what we can do is work out the matrix representation of $H(g)$ in the free Harmonic oscillator basis. Then truncate this matrix and find the exact eigenvalues. This can be easily implemented in Mathematica. For $g = 0.1$, we find

$$E_0 \approx 0.559, \quad E_1 \approx 1.769.$$

Plugging $g = 0.1$ in the perturbative expressions, we get 0.549 and 1.369 respectively. While E_0 agrees, E_1 is off. This is suggestive that $\lambda = 0.1$ is not small enough!

Exact reference values. For $g = 1$, numerical diagonalization gives

$$E_0 = 0.80377\dots, \tag{15}$$

$$E_1 = 2.73789\dots, \tag{16}$$

useful “gold standards” for quantum phase estimation outputs.

Expectation values and identities. From Hellmann–Feynman,

$$\frac{\partial E_n}{\partial g} = \langle x^4 \rangle_n, \tag{17}$$

and the virial theorem gives

$$\langle p^2 \rangle_n = \langle x^2 \rangle_n + 4g\langle x^4 \rangle_n. \tag{18}$$

These provide nontrivial internal consistency checks accessible in simulation.

Strong coupling scaling. For $g \gg 1$,

$$E_n(g) \sim g^{1/3} \varepsilon_n, \quad \varepsilon_0 = 0.66798626\dots \tag{19}$$

[4, 5]. Plotting $E_0/g^{1/3}$ versus g gives a clean test of scaling.

2.2 Negative quartic and the double-well potential

There are two distinct situations that are often conflated:

(i) Unstable quartic:

$$V(x) = \frac{1}{2}x^2 - |g|x^4, \quad |g| > 0. \quad (20)$$

Here $V(x) \rightarrow -\infty$ as $|x| \rightarrow \infty$. Critical points are at $x = 0$ and $x = \pm \frac{1}{2\sqrt{|g|}}$. - At $x = 0$: $V''(0) = 1 > 0$, so the origin is a *local minimum*. - At $x = \pm 1/(2\sqrt{|g|})$: $V'' < 0$, so these are *local maxima*. Thus the potential has a single central well, bounded by two maxima, and then falls off to $-\infty$. Quantum mechanically this leads not to a true bound-state spectrum, but to resonances with finite lifetime (Gamow states). Such resonant structures could, in principle, be probed by quantum simulation using analytic continuation or complex scaling methods.

(ii) True double well:

$$V(x) = -\frac{1}{2}\mu^2 x^2 + \lambda x^4, \quad \mu^2, \lambda > 0. \quad (21)$$

This is the standard quartic double-well potential. - At $x = 0$: $V''(0) = -\mu^2 < 0$, so the origin is a local maximum. - Minima occur at

$$x_* = \pm \frac{\mu}{\sqrt{2\lambda}}, \quad (22)$$

with $V(x_*) = -\mu^4/(4\lambda)$. In the classical limit, the system has two degenerate vacua.

Appendix: Gibbs Sampling and Gibbs States

Classical Gibbs sampling. In classical statistical physics and machine learning one often needs to sample from a probability distribution of Boltzmann–Gibbs form

$$p(x) \propto e^{-\beta H(x)},$$

where $H(x)$ is an energy function and $\beta = 1/T$ is the inverse temperature. A standard Markov chain Monte Carlo technique is *Gibbs sampling*: one decomposes x into components (x_1, x_2, \dots) and updates each component in turn by drawing it from the conditional distribution $p(x_i | x_{\neq i})$. Iterating these local updates yields samples from the full distribution $p(x)$.

Quantum Gibbs states. In quantum physics the natural analogue is the *Gibbs (thermal) state* of a Hamiltonian H :

$$\rho_\beta = \frac{e^{-\beta H}}{\text{Tr}(e^{-\beta H})}.$$

Preparing such states efficiently on a quantum computer would allow direct simulation of finite-temperature equilibrium properties, estimation of partition functions, and applications in optimization. This task is sometimes referred to as *quantum Gibbs sampling*.

Algorithmic advances. Recent work using quantum signal processing and quantum singular value transformation [14, 15] shows how one can implement polynomial approximations to $e^{-\beta H}$ given a block encoding of H , and thereby prepare Gibbs states with provably better asymptotic scaling than known classical methods. Although we will not cover these techniques in detail here, they represent a key application area where QSVD promises exponential improvements.

Example: single qubit Gibbs state. Consider a single qubit with Hamiltonian $H = Z = \begin{pmatrix} 1 & 0 \\ 0 & -1 \end{pmatrix}$. The Gibbs state at inverse temperature β is

$$\rho_\beta = \frac{e^{-\beta Z}}{\text{Tr}(e^{-\beta Z})} = \frac{1}{2 \cosh \beta} \begin{pmatrix} e^{-\beta} & 0 \\ 0 & e^\beta \end{pmatrix}.$$

For $\beta \rightarrow 0$ (high temperature) this approaches the maximally mixed state $\frac{1}{2}I$, while for $\beta \rightarrow \infty$ (zero temperature) it becomes the pure ground state $|1\rangle\langle 1|$. This illustrates how Gibbs states interpolate between classical thermal mixtures and quantum ground states as the temperature varies.

References

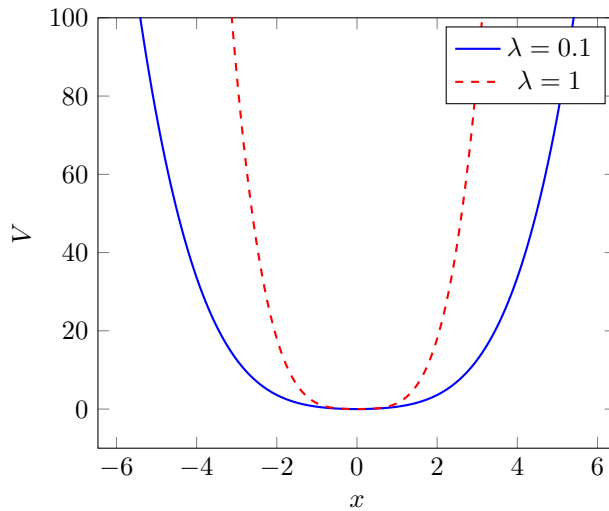
- [1] C. M. Bender and T. T. Wu, “Anharmonic Oscillator,” *Phys. Rev.* **184**, 1231 (1969).
- [2] C. M. Bender and T. T. Wu, “Anharmonic Oscillator II. A study of perturbation theory in large order,” *Phys. Rev. D* **7**, 1620 (1973).
- [3] H. A. Alhendi and E. I. Lashin, “Spectrum of one-dimensional anharmonic oscillators,” arXiv:quant-ph/0305128 (2003).

- [4] G. Álvarez and H. J. Silverstone, “A new method to sum divergent power series,” arXiv:1706.00329 (2017).
- [5] E. Z. Liverts, V. B. Mandelzweig, and F. Tabakin, “Analytic calculation of energies and wave functions of the quartic and pure quartic oscillators,” *J. Math. Phys.* **47**, 062109 (2006).
- [6] S. Coleman, “The Uses of Instantons,” in *Aspects of Symmetry* (Cambridge Univ. Press, 1985).
- [7] J. Zinn-Justin, “Multi-instanton contributions in quantum mechanics,” *Nucl. Phys. B* **192**, 125 (1981).
- [8] G. V. Dunne and M. Ünsal, “Uniform WKB, Multi-instantons, and Resurgent Trans-Series,” *Phys. Rev. D* **89**, 105009 (2014).
- [9] Y. Shalibo, R. Resh, O. Fogel, D. Shwa, R. Bialczack, J. M. Martinis, and N. Katz, “Quantum and Classical Chirps in an Anharmonic Oscillator,” *Phys. Rev. Lett.* **108**, 037701 (2012).
- [10] T. B. Propp, N. Wiebe, C. F. Roos, et al., “Decoherence Limits the Cost to Simulate an Anharmonic Oscillator,” arXiv:2307.00748 (2023).
- [11] S. Ding, Y. Maslennikov, R. Hablitzel, J. Zhang, and D. Matsukevich, “Quantum parametric oscillator with trapped ions,” arXiv:1512.01670 (2015).
- [12] J. McAneny and J. K. Freericks, “Intrinsic anharmonic effects in ion chains,” arXiv:1406.5416 (2014).
- [13] M. R. Almeida, P. R. Amorim, R. C. Barbosa, et al., “Energy spectrum of q-deformed oscillators on quantum computers,” *Phys. Lett. A* **482**, 129056 (2024).
- [14] G. H. Low and I. L. Chuang, “Optimal Hamiltonian Simulation by Quantum Signal Processing,” *Physical Review Letters* **118**, 010501 (2017). doi:10.1103/PhysRevLett.118.010501
- [15] A. Gilyén, Y. Su, G. H. Low and I. L. Chuang, “Quantum singular value transformation and beyond: Exponential improvements for quantum matrix arithmetics,” in *Proceedings of the 51st Annual ACM SIGACT Symposium on Theory of Computing (STOC)*, pp. 193–204 (2019). doi:10.1145/3313276.3316366

Nonperturbative anharmonic oscillator

LECTURE NOTES

1 $\lambda > 0$



Consider

$$H = \frac{p^2}{2} + \frac{x^2}{2} + \lambda x^4.$$

To find the eigen-spectrum numerically, we can find a matrix representation of H in the SHO basis and perform exact diagonalization. Then we check for convergence of the eigenvalues as we keep increasing the size of the matrix. The 4-decimal place converged results read:

The level spacings are plotted below.

The increase in level-spacing is significant. One cannot hope to have a qubit if the level spacings are constant. If the level spacings become bigger then the low lying modes will separate out. This is important to have qubits in realistic physical systems.

As a comparison, let us review perturbative results.

Table 1: Eigenvalues and level spacings for $H = \frac{p^2}{2} + \frac{x^2}{2} + \lambda x^4$ with $\hbar = \omega = m = 1$.

	$\lambda = 0.1$	ΔE	$\lambda = 1$	ΔE
E ₀	0.5591	1.2104	0.8038	1.9341
E ₁	1.7695	1.3691	2.7379	2.4414
E ₂	3.1386	1.4903	5.1793	2.7631
E ₃	4.6289	1.5914	7.9424	3.0212
E ₄	6.2203	1.6795	10.9636	3.2395
E ₅	7.8998	1.7580	14.2031	3.4309
E ₆	9.6578	1.8295	17.6340	3.6024
E ₇	11.4873	1.8952	21.2364	3.7585
E ₈	13.3825	1.9561	24.9949	3.9024
E ₉	15.3386	—	28.8973	—

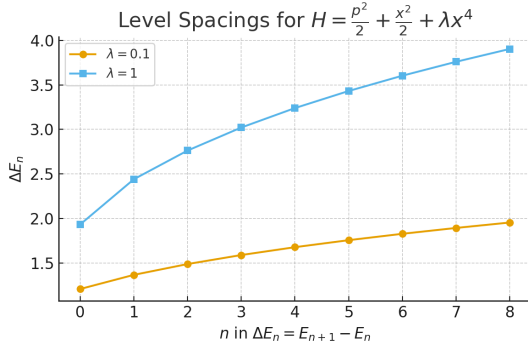


Figure 1: Level spacings ΔE_n for $H = \frac{p^2}{2} + \frac{x^2}{2} + \lambda x^4$.

Perturbative expansion. Rayleigh–Schrödinger perturbation theory yields

$$E_0(g) = \frac{1}{2} + \frac{3}{4}g - \frac{21}{8}g^2 + \mathcal{O}(g^3), \quad (1)$$

$$E_1(g) = \frac{3}{2} + \frac{15}{4}g - \frac{405}{8}g^2 + \mathcal{O}(g^3). \quad (2)$$

The coefficients grow factorially at high order. Numerically, what we can do is work out the matrix representation of $H(g)$ in the free Harmonic oscillator basis. Then truncate this matrix and find the exact eigenvalues. This can be easily implemented in Mathematica. For $g = 0.1$, we find

$$E_0 \approx 0.559, \quad E_1 \approx 1.769.$$

Plugging $g = 0.1$ in the perturbative expressions, we get 0.549 and 1.369 respectively. While E_0 agrees, E_1 is off. This is suggestive that $\lambda = 0.1$ is not small enough!

Exact reference values. For $g = 1$, numerical diagonalization gives

$$E_0 = 0.80377\dots, \quad (3)$$

$$E_1 = 2.73789\dots, \quad (4)$$

useful “gold standards” for quantum phase estimation outputs.

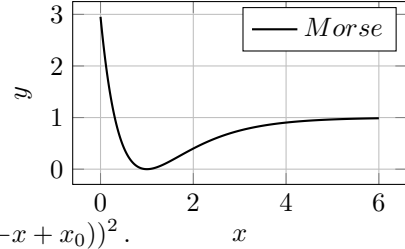
By the way, this increasing level spacing is found in a lot of places. Here is a brief summary:

- **Cold atoms in optical traps / optical lattices.** Near the minimum, the trapping potential is approximately harmonic; away from the center, Gaussian-beam intensity profiles generate quartic corrections. Result: spacings grow with n .
- **Trapped ions in anharmonic Paul/Penning traps.** Imperfections in the RF/DC fields introduce quartic terms beyond the ideal quadrupole confinement, yielding hardening anharmonicity and increasing vibrational level spacings.
- **Phonons at high excitation (lattice anharmonicity).** Expanding interatomic potentials about equilibrium includes x^4 terms; at large amplitudes the mode frequency hardens, so quantized level spacings increase with vibrational quantum number.
- **Quantum dots / mesoscopic electron traps.** Electrostatic confinement is often modeled as harmonic plus quartic corrections from gate geometry; excitation spectra show upward-curving spacings consistent with $\lambda > 0$ behavior.
- **Nonlinear mechanical/optical oscillators (Duffing hardening regime).** Micro/nanomechanical resonators and optical modes with a positive quartic restoring term exhibit amplitude-dependent frequency increase; in the quantum picture this maps to rising ΔE_n .
- **Superconducting circuits in engineered hardening regimes.** While transmons are weakly softening, other circuit designs (e.g. fluxonium under appropriate bias, Josephson arrays with tailored inductive/capacitive networks) can realize effective positive-quartic potentials with increasing level spacings.

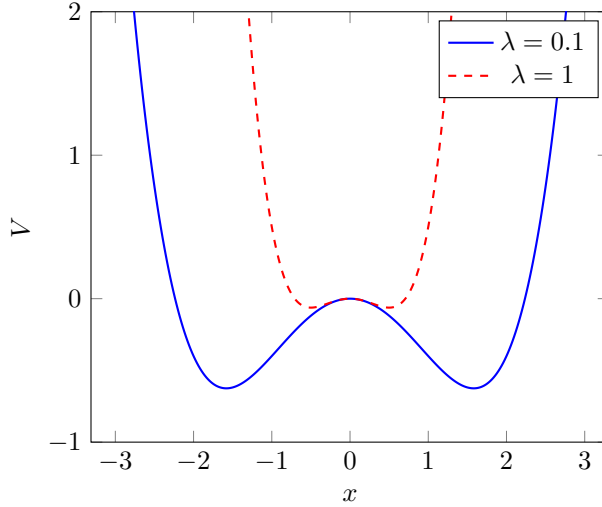
On the other hand, in certain diatomic molecules, the level spacings in fact *decreases* with increasing level. Modeling this is harder but can be done using the so-called Morse potential. This is given by

$$V_{Morse} = D_e(1 - \exp(-x + x_0))^2.$$

]



2 Double well



Now we turn to the symmetric double-well potential. First let's write it as

$$H = \frac{p^2}{2} - \frac{x^2}{2} + \lambda x^4.$$

For this the eigenspectrum can be computed similarly. We have the benchmarking table:

Table 2: Eigenvalues and level spacings for $H = \frac{p^2}{2} - \frac{x^2}{2} + \lambda x^4$ with $\hbar = \omega = m = 1$.

	$\lambda = 0.1$	ΔE	$\lambda = 1$	ΔE
E ₀	-0.1541	0.2969	0.5148	1.5058
E ₁	0.1428	0.8674	2.0206	2.1705
E ₂	1.0102	0.9389	4.1911	2.5144
E ₃	1.9491	1.1095	6.7055	2.7961
E ₄	3.0586	1.2301	9.5016	3.0305
E ₅	4.2887	1.3352	12.5321	3.2342
E ₆	5.6239	1.4278	15.7663	3.4156
E ₇	7.0517	1.5108	19.1819	3.5798
E ₈	8.5625	1.5865	22.7617	3.7305
E ₉	10.1490	—	26.4922	—

and the level spacing plot below.

Notice that unlike the previous case, E_0, E_1 are similar in magnitude for $\lambda = 0.1$. There is rich physics behind this, which we will explain next.

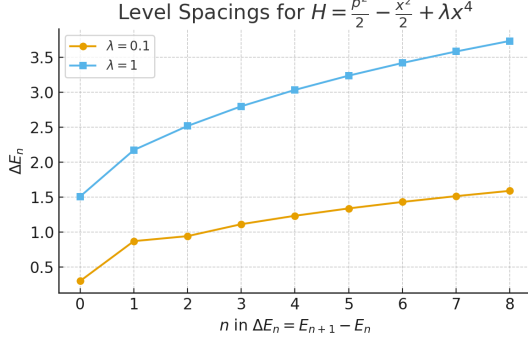


Figure 2: Level spacings ΔE_n for $H = \frac{p^2}{2} - \frac{x^2}{2} + \lambda x^4$.

The symmetric quartic double-well potential

$$V(x) = \lambda (x^2 - a^2)^2 \quad (5)$$

is the canonical example of a quantum-mechanical system where semiclassical, nonperturbative effects are essential. The two classical minima at $x = \pm a$ each support an approximately harmonic ground state. However, quantum tunneling through the central barrier mixes the states localized in the left and right wells, producing symmetric and antisymmetric combinations as the true energy eigenstates. This mixing generates an exponentially small level splitting between the ground doublet.

Perturbation theory around either minimum captures the harmonic oscillator corrections but entirely misses the splitting: no finite-order perturbative expansion can couple the two wells. The appropriate tool is the semiclassical instanton method, which evaluates the Euclidean path integral by including classical Euclidean solutions connecting the two minima. In what follows we develop this picture in detail.

3 Localized states and exact propagators

Let us denote by $|L\rangle$ and $|R\rangle$ wavefunctions localized near $-a$ and $+a$, respectively. These are not exact eigenstates of the Hamiltonian but provide a useful approximate basis. The true eigenstates of definite parity are

$$|+\rangle = \frac{|L\rangle + |R\rangle}{\sqrt{2(1+S)}}, \quad |-\rangle = \frac{|L\rangle - |R\rangle}{\sqrt{2(1-S)}}, \quad (6)$$

where $S = \langle L|R \rangle$ is the small overlap.

The Euclidean propagators

$$K_{LL}(T) = \langle L|e^{-HT}|L\rangle, \quad K_{LR}(T) = \langle L|e^{-HT}|R\rangle \quad (7)$$

can be expressed in terms of the low-lying eigenstates. Neglecting higher excitations,

$$K_{LL}(T) = \frac{1+S}{2} e^{-E_+ T} + \frac{1-S}{2} e^{-E_- T}, \quad (8)$$

$$K_{LR}(T) = \frac{1+S}{2} e^{-E_+ T} - \frac{1-S}{2} e^{-E_- T}. \quad (9)$$

Adding and subtracting gives

$$K_{LL}(T) \pm K_{LR}(T) = (1 \pm S) e^{-E_\pm T}. \quad (10)$$

Thus by computing the Euclidean propagators between localized states, one can directly read off the symmetric and antisymmetric energies E_\pm .

4 Euclidean path integral and instantons

The Euclidean path integral representation is

$$K_{LR}(T) = \int_{x(0)=-a}^{x(T)=+a} \mathcal{D}x(\tau) e^{-S_E[x]/\hbar}, \quad S_E[x] = \int_0^T d\tau \left[\frac{1}{2} \dot{x}^2 + V(x) \right]. \quad (11)$$

Saddle points of S_E dominate in the semiclassical limit. The Euler–Lagrange equation is

$$\ddot{x} = V'(x). \quad (12)$$

Besides the trivial vacua at $\pm a$, there exist finite-action solutions interpolating between them. These are the *instantons*.

The strategy to derive them is as follows. Notice that

$$\frac{1}{2} \dot{x}^2 + \lambda(x^2 - a^2)^2 = \frac{1}{2} (\dot{x} + \sqrt{2\lambda}(x^2 - a^2))^2 - \sqrt{2\lambda} \dot{x}(x^2 - a^2). \quad (13)$$

Therefore, for the action to be minimum [saddle] we must have

$$\dot{x} + \sqrt{2\lambda}(x^2 - a^2) = 0. \quad (14)$$

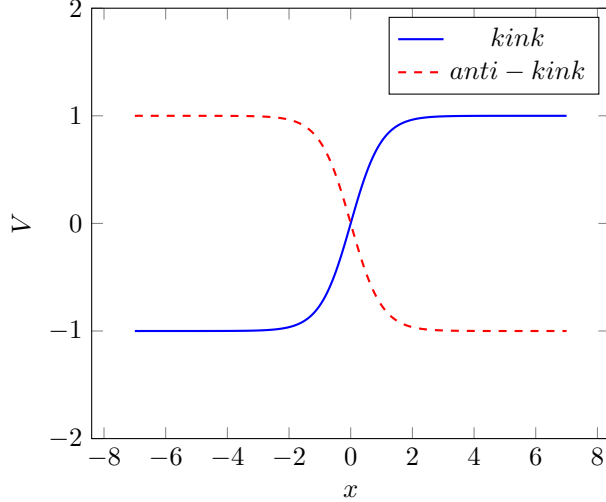
This also reads:

$$\frac{dx}{d\tau} = \sqrt{2V(x)}. \quad (15)$$

[Since $-a < x < a$, we choose this branch.] This equation eq.(14) is easy to solve. Explicitly, one finds

$$x_{\text{inst}}(\tau) = a \tanh\left(\frac{\omega}{2}(\tau - \tau_0)\right), \quad \omega = \sqrt{V''(a)} = 2\sqrt{2\lambda}a, \quad (16)$$

with center τ_0 (integration constant).



The action of a single instanton is

$$S_0 = \int_0^T d\tau 2V(x) = \int_{-a}^a \sqrt{2V(x)} dx = \frac{4}{3}\sqrt{2\lambda} a^3. \quad (17)$$

There is another solution (argue how, HW):

$$x_{\text{inst}}(\tau) = -a \tanh\left(\frac{\omega}{2}(\tau - \tau_0)\right), \quad \omega = \sqrt{V''(a)} = 2\sqrt{2\lambda} a, \quad (18)$$

which corresponds to K_{RL} which is called the anti-instanton. The instanton has a characteristic width $\Delta\tau \sim 1/\omega$ in Euclidean time. The parameter τ_0 is a collective coordinate: translating the instanton does not change its action, and the path integral includes an integration $\int d\tau_0$ over its position.

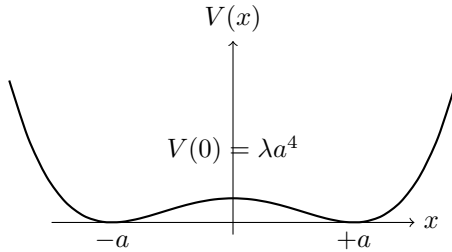


Figure 3: The symmetric quartic double well. The instanton connects $-a$ to $+a$ in Euclidean time.

5 The dilute instanton gas approximation

A path contributing to $K_{LL}(T)$ or $K_{LR}(T)$ may contain multiple instantons and anti-instantons. For instance the amplitude for $L \rightarrow R$ tunneling should also include the possibilities that $L \rightarrow R$ followed by $R \rightarrow L$ and again $L \rightarrow R$ events (i.e., an odd number of tunnelling events). Each tunneling event carries the system across the barrier in a Euclidean interval of width $\sim 1/\omega$. If these events are widely separated, their actions add approximately: $S \approx nS_0$. This is the dilute instanton gas approximation (DIGA).

For a configuration with n tunneling events, each contributes a factor Ke^{-S_0} , where K is the one-loop determinant prefactor. Each event has a free center τ_i , and integrating over its position in $[0, T]$ gives $\int_0^T d\tau_i$. For n events this yields $\int_0^T d\tau_1 \cdots d\tau_n$. To avoid overcounting permutations of indistinguishable instantons, one divides by $n!$. Thus the contribution is

$$\frac{1}{n!} (KTe^{-S_0})^n. \quad (19)$$

Summing over all even n (returning to the initial well) produces

$$K_{LL}(T) \propto e^{-E_{\text{pert}}T} \cosh(KTe^{-S_0}), \quad (20)$$

while summing over all odd n (ending in the opposite well) gives

$$K_{LR}(T) \propto e^{-E_{\text{pert}}T} \sinh(KTe^{-S_0}). \quad (21)$$

Here E_{pert} denotes the perturbative vacuum energy around a single minimum. In the dilute instanton gas approximation the tunneling amplitude always comes multiplied by a factor of the form $e^{-E_{\text{pert}}T}$. This contribution originates from the fact that, away from the localized instanton core of width $\mathcal{O}(\omega^{-1})$, the system spends essentially the entire Euclidean time interval T sitting in one of the perturbative vacua. The corresponding path integral over fluctuations around a well gives precisely the perturbative ground state energy E_{pert} : the classical potential at the minimum, the Gaussian zero-point energy coming from the fluctuation determinant, and higher-order loop corrections. Since this background contribution scales linearly with T , it factors out as $e^{-E_{\text{pert}}T}$ in all instanton sectors, while the instanton itself only supplies a finite action S_0 and a prefactor independent of T .

Adding and subtracting again, one finds

$$K_{LL}(T) \pm K_{LR}(T) \propto e^{-E_{\text{pert}}T} \exp(\pm KTe^{-S_0}), \quad (22)$$

so that the energies of the symmetric and antisymmetric states are

$$E_{\pm} = E_{\text{pert}} \mp Ke^{-S_0} + \dots, \quad (23)$$

and the ground-state splitting is

$$\Delta = E_- - E_+ = 2Ke^{-S_0} [1 + \mathcal{O}(\hbar) + \mathcal{O}(e^{-S_0})]. \quad (24)$$

Explicitly for $H = p^2/2 - x^2/2 + \lambda x^4$ and the lowest states¹, we have

$$\Delta \approx \frac{1.34}{\sqrt{\lambda}} \exp\left(-\frac{0.236}{\lambda}\right). \quad (25)$$

For $\lambda = 0.1$ this predicts $\Delta \approx 0.4$ while the numerical answer is 0.3. For $\lambda = 0.7$ this predicts $\Delta \approx 1.14$ while numerics gives 1.28. The agreement is expected to improve on including multi-instanton contributions. What we have added are just the one instanton case weighted by e^{-S_0} and have ignored terms like e^{-2S_0} and higher.

The sharp benchmark targets for quantum computers are to produce:

$$\Delta = 0.3 \quad \lambda = 0.1 \quad (26)$$

$$\Delta = 1.28 \quad \lambda = 0.7 \quad (27)$$

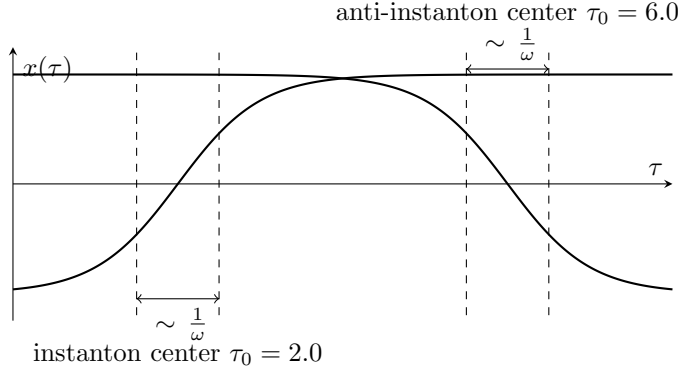


Figure 4: A dilute instanton–anti-instanton pair. Each kink (and anti-kink) switches between vacua over an Euclidean-time window of width $\sim 1/\omega$, shown by dashed lines at $\tau_0 \pm 1/\omega$ and a double arrow. Widely separated means the two cores do not overlap: $|\tau_0^{(I)} - \tau_0^{(AI)}| \gg 1/\omega$.

In the dilute instanton gas approximation, configurations with n tunnelling events (instantons or anti-instantons) are described by paths that remain in a perturbative vacuum for almost all of the Euclidean interval $[0, T]$, with n well-separated localized transitions of width $\mathcal{O}(\omega^{-1})$. Each instanton possesses a collective coordinate τ_i corresponding to the freedom of translating its center in Euclidean time. The path integral over such n -instanton configurations therefore contains an integration over all possible choices of these centers:

$$\int_0^T d\tau_1 \int_0^T d\tau_2 \cdots \int_0^T d\tau_n.$$

¹ $E_{2n+1} - E_{2n} \propto e^{-S_0}$, with the n -dependence in the prefactor.

However, because the instantons are indistinguishable objects, different orderings of the same set of centers $\{\tau_1, \dots, \tau_n\}$ represent the *same physical configuration*. To avoid overcounting, one restricts to an ordered domain $\tau_1 < \tau_2 < \dots < \tau_n$, which gives

$$\int_{0 < \tau_1 < \tau_2 < \dots < \tau_n < T} d\tau_1 \cdots d\tau_n = \frac{T^n}{n!}.$$

Thus the contribution of the n -instanton sector is proportional to $(KTe^{-S_0})^n/n!$, where K is the one-instanton fluctuation prefactor. In this way DIGA does not assume the events are simultaneous²; rather, it sums over all possible positions of the instantons, with the $1/n!$ factor arising from the indistinguishability of their centers in the path integral.

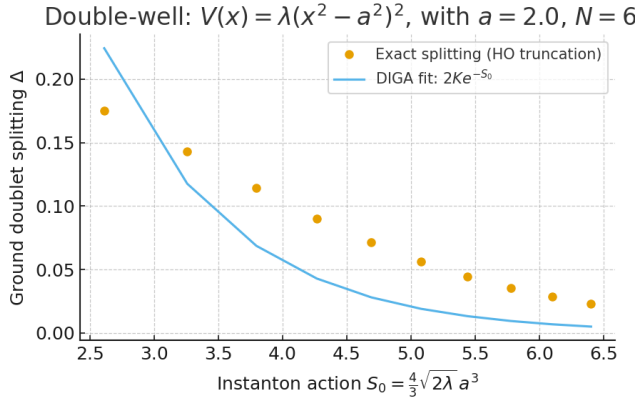


Figure 5: Exact ground-doublet splitting (points) versus the dilute-instanton-gas prediction $\Delta \approx 2Ke^{-S_0}$ (line) for $V(x) = \lambda(x^2 - a^2)^2$ with $a = 2.0$. The prefactor K is determined by a single least-squares fit across all couplings. The action $S_0 = \frac{4}{3}\sqrt{2\lambda}a^3$ controls the leading exponential behavior.

6 Beyond the dilute gas

If an instanton and anti-instanton occur close together, their cores overlap and the action is less than $2S_0$. These configurations are important for understanding the analytic structure of perturbation theory: they generate ambiguities in the Borel resummation of divergent series, which are cancelled by the perturbative sector in the framework of resurgence. However, in the dilute limit $KTe^{-S_0} \ll 1$, the measure for such close pairs is suppressed, and they do not affect the leading real tunneling splitting. The dilute instanton gas approximation therefore provides the leading-order semiclassical prediction for the level

²During the lecture, I messed up this explanation!

splitting, with corrections systematically organized as loop effects around the instanton and multi-instanton interactions.

References

- [1] S. Coleman, *Aspects of Symmetry* (Cambridge University Press, 1985).
- [2] C. Callan and S. Coleman, “Fate of the false vacuum. II. First quantum corrections,” Phys. Rev. D **16**, 1762 (1977).
- [3] E. Bogomolny, “Calculation of instanton–anti-instanton contributions in quantum mechanics,” Phys. Lett. B **91**, 431 (1980).
- [4] J. Zinn-Justin, “Multi-instanton contributions in quantum mechanics,” Nucl. Phys. B **192**, 125 (1981).
- [5] J. Zinn-Justin and U. Jentschura, “Multi-instantons and exact results I: Conjectures, WKB expansions, and instanton interactions,” Annals Phys. **313**, 197 (2004).

MID-TERM BREAK: next class on 8.10

Encoding: A mathematica handle and spectrum extraction with QISKit

LECTURE NOTES

Contents

1	Oscillator basis	2
2	Position-basis (JLP) encoding for one-site ϕ^4	4
3	Noise Sources on a Quantum Computer	8
3.1	Measurement (Readout) Errors	8
3.2	Gate Errors	9
3.3	Decoherence: T_1 and T_2 Processes	9
3.4	Combined Noise Models	9
3.5	Remarks	10
3.6	Error Mitigation Techniques	10
3.6.1	Readout Error Mitigation	10
3.6.2	Zero-Noise Extrapolation (ZNE)	11
3.6.3	Randomized Compiling (RC)	11
3.6.4	Dynamical Decoupling (DD)	11
3.6.5	Runtime Resilience Levels	11
3.6.6	Remarks	11
4	Results	12
5	When does a quantum computer help? A scaling view	12
5.1	Gate counts and the quantitative “importance” of CNOTs vs. λ	14
6	Entanglement as a Diagnostic of Simulation Complexity	14
6.1	Setup	14
6.2	Interpretation	15
6.3	Numerical results	15
6.4	Summary	15

The following is the content of lecture 15 and part of lecture 16. I decided to keep it in one places due to logical continuity. Lectures 15 and 16 and their associated demonstrations will be especially important for the final term paper point of view, so pay careful attention!

FFT logic for $\langle \psi | U^k | \psi \rangle$: a *minimal* Mathematica guide

Consider the case

$$H = p^2/2 + x^2/2 + \lambda x^4.$$

We want to extract the spectrum on a quantum simulator. The strategy is the following:

1. We will first get a matrix representation of H using the oscillator basis. For simplicity, we will restrict to 4×4 .
2. Then we use qiskit to find a Pauli decomposition of this matrix.
3. We time evolve a suitable state $|\psi\rangle$ over an interval $T = Ndt$. Then we use Hadamard test to extract

$$C_k = \langle \psi | U^k | \psi \rangle.$$

Here $U = \exp(-iHdt)$ and k runs from 1 to N .

4. We can always expand $|\psi\rangle$ in terms of the true energy eigenstates:

$$|\psi\rangle = \sum_j c_j |E_j\rangle.$$

This gives

$$C_k = \sum_j |c_j|^2 \exp(-iE_j k dt). \quad (1)$$

5. Then we define

$$F(\omega) = \sum_{k=0}^{N-1} C_k \exp(-i\omega k dt) = \sum_{k,j} |c_j|^2 \exp(-ik dt(E_j + \omega)). \quad (2)$$

Summing over k leads to

$$F(\omega) = \sum_j |c_j|^2 \exp(i dt(E_j + \omega)/2) \frac{\sin N dt(E_j + \omega)}{\sin dt(E_j + \omega)}. \quad (3)$$

This form implies that $|F(\omega)|$ will have peaks at $\omega = -E_j$.

6. So the logic is that we use the quantum computer and Hadamard test to construct C_k 's and then postprocess on a classical computer to construct $|F(\omega)|$ to extract the spectrum.

To see this in action, let us write a short mathematica code first and do some sanity checks.

This is a good opportunity for you to pick up this fascinating package, which forms a bedrock for most theoretical research.

1 Oscillator basis

```

1 \[Lambda] = 0.10;
2 dt = 0.12;
3
4 (* operators *)
5 x = 1/Sqrt[2] {{0, 1, 0, 0}, {1, 0, Sqrt[2], 0},
6 {0, Sqrt[2], 0, Sqrt[3]}, {0, 0, Sqrt[3], 0}};
7
8 H0 = DiagonalMatrix[{0, 1, 2, 3}] + 1/2 IdentityMatrix[4];
9 H = N[H0 + \[Lambda] x.x.x.x];
10
11 (* state: |\[Psi]> = (|0>+|1>)/Sqrt[2]    (|00>+|01>)/Sqrt[2] *)
12 psi = {1/Sqrt[2], 1/Sqrt[2], 0, 0};
13
14 (* one-step propagator and correlator *)
15 U1 := MatrixExp[-I H dt];
16 Ck[k_Integer?NonNegative] := N[ Conjugate[psi].MatrixPower[U1, k].psi ];

```

This implements steps 1-3. We have chosen the state $|\psi\rangle = \frac{1}{\sqrt{2}}(|0\rangle + |1\rangle)$, which is the superposition of the $\lambda = 0$ ground and 1st excited state. This state can be decomposed into a superposition of the true $\lambda \neq 0$ eigenstates.

Naive continuous scan (peaks at negative energies)

We define $F(\omega) = \sum_k C_k e^{-i\omega k dt}$. Because C_k already carries $e^{-iE_j k dt}$, peaks of $|F|$ appear at $\omega \approx -E_j$. To stay ASCII in code, we call the scan variable `wm`.

```

1 Nt = 350;
2
3 F[wm_] := Sum[ Ck[k] Exp[-I wm k dt], {k, 0, Nt - 1} ];
4
5 Plot[ Abs[F[wm]], {wm, -2.5, 0},
6   AxesLabel -> {"wm", "|F|"}, PlotRange -> All,
7   PlotLabel -> "Naive scan: peaks near -E_j" ]

```

This implements steps 4-5. This leads to the following plot:

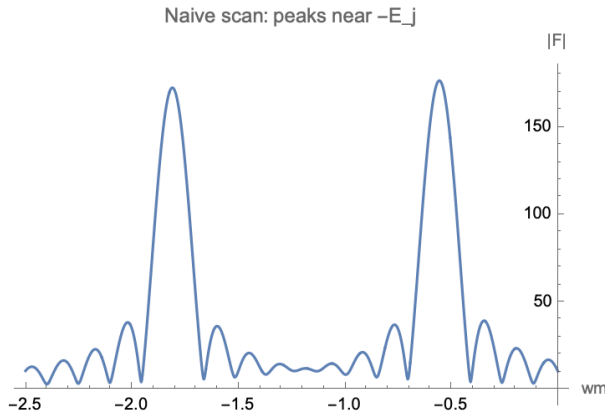


Figure 1: $|F(\omega)|$ vs ω .

Scales to remember: Nyquist band $|\omega| < \pi/dt$; resolution $\Delta E \approx 2\pi/(N_t dt)$.

As you can see from the plot, there are 2 prominent big peaks. We can eyeball that these peaks have height greater than 60. Using the convenient mathematica command `FindPeaks`, we can extract their locations using the following commands:

```

1 datab = Table[Abs[F[w]], {w, -2.5, 0, .01}];
2
3 FindPeaks[datab, 60]

```

Using this we find the peaks corresponding to $E_0 = 0.55$ and $E_0 = 1.8$. The expected answers to 3 decimal places are 0.557 and 1.809. So we have done well! However, we can do a little better by using a trick called Hanning window.

Two-line fix: de-mean + Hann window

Finite records use a rectangular window whose Fourier transform (Dirichlet kernel) has large sidelobes. De-mean removes DC; Hann crushes sidelobes (-31 dB).

```

1 CC = Table[ Ck[k], {k, 0, Nt - 1} ];
2 meanCC = Mean[CC];
3 w[k_] := HannWindow[ k/(Nt - 1.) ];

```

```

4 FHann[wm_] := Sum[ (Ck[k] - meanCC) * w[k] * Exp[-I wm k dt], {k, 0, Nt - 1} ];
5
6
7 Plot[ {Abs[F[wm]], Abs[FHann[wm]]}, {wm, -2.5, 0},
8   PlotLegends -> {"naive", "Hann + de-mean"}, 
9   AxesLabel -> {"wm", "|F|"}, PlotRange -> All ]

```

What changes? True peaks stay; low- $|\omega|$ junk collapses. Main lobe widens slightly (resolution trade).

We find:

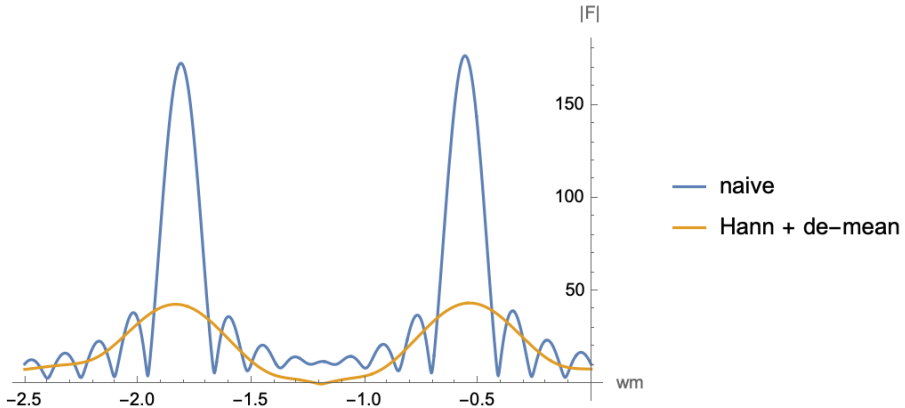


Figure 2: $|F(\omega)|$ vs ω after Hann is given by the orange line. This gives a clean set of 2 peaks.

Changing **dt**: keep it consistent

If you change **dt**, regenerate both **U1** and **Ck**. Otherwise the axis scales and peaks drift by a factor.

```

1 dt = 0.10;
2 U1 = MatrixExp[-I H dt];
3 CC = Table[ Ck[k], {k, 0, Nt - 1} ];
4 meanCC = Mean[CC];
5 FHann[wm_] := Sum[ (Ck[k]-meanCC) w[k] Exp[-I wm k dt], {k,0,Nt-1}];

```

Two-line summary

- $F(\omega) = \sum_k (C_k - \bar{C}) w_k e^{-i\omega k dt}$; peaks at $\omega \approx -E_j$.
- Use **HannWindow** and subtract the mean; fix **dt** and increase **Nt** to sharpen peaks.

2 Position-basis (JLP) encoding for one-site ϕ^4

Goal. Digitize a single anharmonic oscillator site in the *position basis* as in Jordan–Lee–Preskill (JLP): we represent the field value ϕ on a uniform grid of $N = 2^n$ points (so n qubits), build $H = \frac{1}{2}\pi^2 + \frac{1}{2}\omega^2\phi^2 + \lambda\phi^4$, then compute the correlator $C_k = \langle\psi|e^{-iHkdt}|\psi\rangle$ and recover energies from its spectrum. The reason to consider this alternate encoding is that for the $\lambda\phi^4$ field theory that we will consider soon, the ϕ pieces of the Hamiltonian are simply diagonal while the

momentum pieces can be made diagonal by doing a (quantum) Fourier Transform, which we know how to do. The steps are as follows:

1. We discretize the field (x in our case) to lie between $[-\phi_{max}, \phi_{max}]$ defining an interval $L_\phi = 2\phi_{max}$. In our case, since we are interested in the first 2 eigenvalues for smallish λ , it is sufficient to consider ϕ_{max} such that the position space SHO wave-functions decay beyond this value. It turns out $\phi_{max} \sim 3.0$ will do the job.
2. We sample ϕ on a uniform grid. That is, we choose $\Delta\phi = 2\phi_{max}/N$ and

$$\phi_j = -\phi_{max} + j\Delta\phi, \quad j = 0, \dots, N-1. \quad (4)$$

This can also be rewritten as:

$$\phi_m = m\Delta\phi$$

where $m = -N/2, -N/2 + 1, \dots, N/2 - 1$.

3. We define the computational basis as

$$\hat{\phi}|\phi_j\rangle = \phi_j|\phi_j\rangle. \quad (5)$$

4. Define the momentum grid

$$p_m = m \frac{2\pi}{L_\phi}, \quad m = -N/2, -N/2 + 1, \dots, N/2 - 1. \quad (6)$$

using which we have the DFT

$$F_{mj} = \frac{1}{\sqrt{N}} e^{ip_m \phi_j}. \quad (7)$$

Both m, j run from $-N/2$ to $N/2 - 1$. This gives us for the conjugate momentum

$$\hat{\Pi}^2 = F^\dagger \text{diag}(p_m^2) F. \quad (8)$$

Minimal Mathematica cell (JLP grid → correlator → peaks)

The code mirrors our oscillator-basis workflow but works directly in the position grid.

```

1 (* === Parameters === *)
2 lam = 0.10; omega = 1.0;
3 Ngrid = 4;      (* 2^n points; for 2 qubits use 4 *)
4 phimax = 3.0;   (* half-interval length; tune below *)
5
6 (* === Centered grids and operators (JLP) === *)
7 idx = Range[-Ngrid/2, Ngrid/2 - 1];
8 dphi = 2 phimax/Ngrid; L = 2 phimax;
9
10 phi = dphi idx;          (* positions phi_j *)
11 p = (2 Pi/L) idx;        (* momenta p_m *)
12
13 Phi = DiagonalMatrix[phi]; (* position operator *)
14 Fmat = Table[Exp[2 Pi I m j/Ngrid]/Sqrt[Ngrid], {m, idx}, {j, idx}];
15 Pi2 = ConjugateTranspose[Fmat].DiagonalMatrix[p^2].Fmat; (* spectral kinetic *)
16
17 (* Harmonic (lam=0) and full (lam>0) Hamiltonians *)
18 H0pos = 1/2 Pi2 + 1/2 omega^2 (Phi.Phi) // N;          (* quadratic part *)
19 Hpos = H0pos + lam (Phi.Phi.Phi.Phi) // N;           (* add phi^4 *)
20
21 (* Initial state: like oscillator case use lowest two eigenstates of H0 (not Hpos) *)

```

```

22 vals0Vecs = Eigensystem[H0pos];
23 vals0 = vals0Vecs[[1]]; vecs0 = vals0Vecs[[2]];
24 ord0 = Ordering[vals0];
25 psi = Normalize[vecs0[[ord0[[1]]]] + vecs0[[ord0[[2]]]] ];
26
27 (* === Correlator and Hann-windowed scan === *)
28 dt = 0.12; Nt = 256; (* fix dt; increase Nt to sharpen peaks *)
29 U1 = MatrixExp[-I Hpos dt];
30
31 Ck[k_Integer?NonNegative] := N[Conjugate[psi].MatrixPower[U1, k].psi ];
32 CC = Table[Ck[k], {k, 0, Nt - 1}];
33 meanCC = Mean[CC];
34 w[k_] := HannWindow[k/(Nt - 1.)];
35
36 FHann[wm_] := Sum[(CC[[k+1]] - meanCC) * w[k] * Exp[-I wm k dt], {k, 0, Nt - 1}];
37
38 (* Visual: peaks appear at negative wm (because of the -i sign in the kernel) *)
39 Plot[Abs[FHann[wm]], {wm, -3, 0}, PlotRange->All,
40 AxesLabel->{"wm", "|F|"}, PlotLabel->"JLP position grid: peaks near -E0,-E1"]
41
42 (* Minimal peak pick, exactly like earlier *)
43 grid = Range[-3, 0, 0.01];
44 valsF = Abs @ (FHann /@ grid);
45 peakHeights = FindPeaks[valsF];
46 peakIdx = Flatten @ Position[valsF, Alternatives @@ peakHeights];
47 wmPeaks = grid[[peakIdx]]; (* e.g., -3 + idx*0.01 *)
48 Eest = -wmPeaks; (* report +E by flipping the sign *)

```

Two scales to watch. Nyquist band $|\omega| < \pi/dt$ (avoid aliasing). Resolution $\Delta E \approx \frac{2\pi}{N_t dt}$. Fix dt , then raise N_t to sharpen peaks.

We find:

JLP position grid: peaks near $-E_0, -E_1$

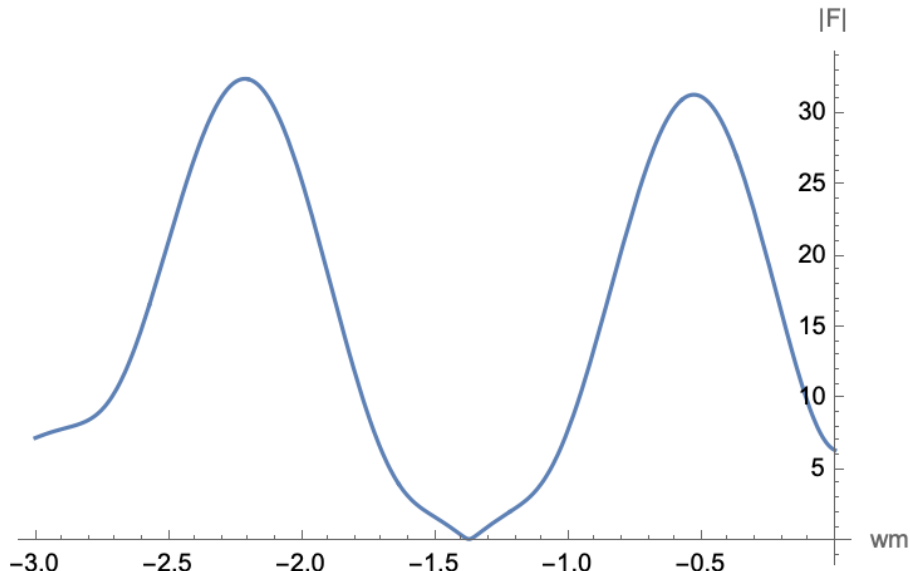


Figure 3: $|F_{Hann}(\omega)|$ vs ω using JLP encoding. $N = 4$, $\phi_{max} = 3$.

Note that while the first peak near 0.5 is reasonably good, the second one is beyond the expected 1.8. The reasons are discussed below.

Shortcomings of the tiny ($N = 4$) JLP grid (why accuracy lags the oscillator basis)

With $N = 4$ points and a box $[-\phi_{\max}, \phi_{\max}]$ the grid spacing and momentum spacing are coarse:

- **Position under-sampling.** Ground-state width of a harmonic well with $\omega=1$ is $\sigma_\phi \approx 1/\sqrt{2} \approx 0.707$. With $N=4$ and $\phi_{\max}=3$, the spacing is $\Delta\phi = 2\phi_{\max}/N = 1.5 (> 2 \times \sigma_\phi)$, so the wavefunction is poorly represented.
- **Coarse kinetic resolution.** Momentum spacing is $\Delta p = 2\pi/L = \pi/\phi_{\max}$; with $\phi_{\max}=3$, $\Delta p \approx 1.047$ while the momentum width is $\sigma_p \approx \sqrt{2} \approx 1.414$. The kinetic energy is quantized very coarsely, shifting eigenvalues.
- **Periodic wrap-around.** The spectral (Fourier) kinetic enforces periodicity; with a tiny grid the effective ring couples the edges unless the wavefunction is both small at the boundaries and well sampled in the interior.

By contrast, the oscillator (Fock) basis uses eigenfunctions of the *quadratic* part; low-lying anharmonic states are small deformations of those, so even a 4-state truncation captures the first levels better.

How to improve JLP accuracy (still minimal).

1. Tune ϕ_{\max} for fixed N (trade box error vs sampling). A practical range is $\phi_{\max} \sim 2.2\text{--}3.0$ for $\omega=1$.
2. Increase N (more qubits): $N=8, 16$ quickly brings $\Delta\phi$ below σ_ϕ .
3. (Optional) Use a non-periodic kinetic (e.g., sine-transform/Dirichlet) to remove wrap-around for single-site pedagogy.

Why JLP use the position encoding (despite these small- N issues)

The original JLP program targets *quantum field theory* on a spatial lattice:

- **Locality and scalability.** A field value $\phi(x)$ stored in computational basis gives *local* interactions (ϕ^4 , gauge couplings) that act diagonally on each site; the kinetic and gradient terms couple only nearby sites. This maps to sparse, geometrically local circuits under Trotterization.
- **Generalizable to many sites and fields.** The same encoding works for multiple lattice sites (tensor product of sites), higher dimensions, and gauge fields; a site-wise Fock basis becomes unwieldy and highly nonlocal across the lattice.
- **Uniform recipe.** The discrete Fourier (QFT) machinery gives a systematic way to implement kinetic terms and to switch between “position” and “momentum” representations on a register.

For a *single oscillator* at tiny N , the Fock basis wins on accuracy-per-qubit; for *field theories* with many sites and interactions, the position-basis digitization is the natural, local, and scalable route—hence JLP’s choice.

Takeaway. Use the JLP position grid when you care about locality and scalability across lattice sites; expect to pay a small accuracy tax at very small N , which vanishes rapidly as you increase N or tune ϕ_{\max} .

Aliasing (one-line intuition). Sampling at a fixed step Δt can only distinguish angular frequencies ω within the Nyquist band $|\omega| < \pi/\Delta t$. Any component at frequency ω is indistinguishable from $\omega' = \omega - 2\pi n/\Delta t$ for any integer n , because $e^{-i\omega k\Delta t} = e^{-i(\omega - 2\pi n/\Delta t)k\Delta t}$ at all integer samples k . Thus a tone above Nyquist “folds” back into the band (it *aliases*). In the figure, sampling $x(t) = \sin(2\pi \cdot 7t)$ at $f_s = 10$ Hz ($\Delta t = 0.1$ s) yields sample values identical to a 3 Hz tone since $7 = 10 - 3$; i.e. $f_{\text{alias}} = f_s - f$. To avoid aliasing one must ensure the signal has no energy above $f_s/2$ (e.g. by low-pass filtering) or increase f_s .

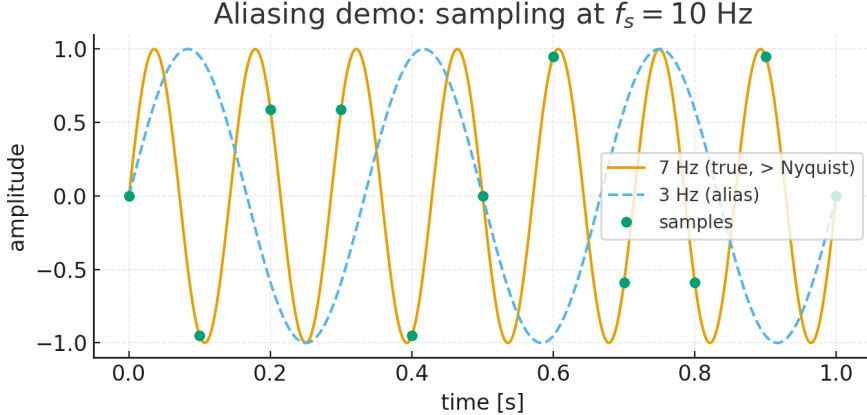


Figure 4: Aliasing: sampling at $f_s = 10$ Hz makes a 7 Hz sine (solid) produce the same samples (dots) as a 3 Hz sine (dashed).

3 Noise Sources on a Quantum Computer

Any practical quantum computer suffers from errors that degrade the fidelity of quantum computations. For superconducting devices such as those provided by IBM Quantum, three main classes of errors dominate:

3.1 Measurement (Readout) Errors

Readout error, or SPAM (State Preparation and Measurement) error, is the probability of mis-assigning the measured classical bit. For example, when a physical qubit is in state $|0\rangle$, the measurement device may report “1” with probability p_{01} , and when the qubit is in state $|1\rangle$ it may report “0” with probability p_{10} .

- **Physical meaning:** Imperfections in the qubit–resonator coupling and classical electronics lead to bit-flip errors in measurement.
- **Effect:** This produces biased expectation values. In correlation functions, the oscillatory structure remains but amplitudes are suppressed and offset.
- **Simulation in Qiskit:** A readout error is specified by a confusion matrix via the `ReadoutError` class and attached to a noise model:

```
from qiskit_aer.noise import NoiseModel, ReadoutError
rd = ReadoutError([[1-p01, p01],
                  [p10, 1-p10]])
nm = NoiseModel()
nm.add_readout_error(rd, [q]) # attach to measured qubit q
```

3.2 Gate Errors

Every single- and two-qubit gate implemented in hardware is imperfect. On superconducting devices, gate infidelities are often dominated by *over-rotation* and control noise.

- **Physical meaning:** A gate intended to perform $U = \exp(-i\theta\sigma)$ instead implements a noisy channel close to U . Two-qubit gates (e.g. CNOT) are especially error-prone.
- **Effect:** Gate errors depolarize or rotate the state incorrectly, reducing coherence in time-correlation functions. Peaks in Fourier spectra remain at approximately the same frequency but are broadened.
- **Simulation in Qiskit:** Gate errors are modeled via `QuantumError` channels. A common choice is depolarizing noise:

```
from qiskit_aer.noise import depolarizing_error
# 1-qubit depolarizing error
err1 = depolarizing_error(p1q, 1)
nm.add_quantum_error(err1, ['x','sx','rz'], [q])
# 2-qubit depolarizing error
err2 = depolarizing_error(p2q, 2)
nm.add_quantum_error(err2, ['cx'], [q0,q1])
```

3.3 Decoherence: T_1 and T_2 Processes

Even with perfect control, qubits are not isolated: they suffer from energy relaxation (T_1) and dephasing (T_2).

- **Physical meaning:**
 - T_1 : amplitude damping from $|1\rangle \rightarrow |0\rangle$ due to photon loss.
 - T_2 : phase damping which destroys superpositions without energy loss.
- **Effect:** These cause exponential decay of coherence in time correlation functions. In Fourier space this corresponds to Lorentzian broadening of peaks. High-frequency components are washed out most quickly.
- **Simulation in Qiskit:** Thermal relaxation channels model T_1 and T_2 processes over the duration of a gate:

```
from qiskit_aer.noise import thermal_relaxation_error
# single-qubit relaxation
th1 = thermal_relaxation_error(T1, T2, gate_time)
nm.add_quantum_error(th1, ['x','sx','rz'], [q])
# two-qubit relaxation: tensor product channel
th2 = thermal_relaxation_error(T1, T2, cx_time).tensor(
    thermal_relaxation_error(T1, T2, cx_time))
nm.add_quantum_error(th2, ['cx'], [q0,q1])
```

3.4 Combined Noise Models

In practice, one combines all three sources into a single `NoiseModel`. For example:

```

nm = NoiseModel()
# add readout error
nm.add_readout_error(rd, [q])
# add depolarizing gate errors
nm.add_quantum_error(err1, ['sx','rz'], [q])
nm.add_quantum_error(err2, ['cx'], [q0,q1])
# add thermal relaxation
nm.add_quantum_error(th1, ['sx','rz'], [q])
nm.add_quantum_error(th2, ['cx'], [q0,q1])

```

This reflects the experimental situation on IBM devices most closely.

3.5 Remarks

- Readout error can often be mitigated efficiently via calibration and post-processing.
- Gate and decoherence errors are more serious: without error correction, one typically applies techniques such as zero-noise extrapolation (ZNE), randomized compiling (RC), and dynamical decoupling (DD).
- In all cases, Qiskit’s AerSimulator accepts a `noise_model` argument so that simulation results can include these errors, allowing one to benchmark algorithms against realistic device behaviour.

3.6 Error Mitigation Techniques

Although full fault-tolerant error correction is not yet feasible on near-term devices, several mitigation techniques can reduce the impact of noise. These methods aim to recover more accurate expectation values without adding too much overhead.

3.6.1 Readout Error Mitigation

Since readout errors are typically the largest SPAM errors, one can calibrate the confusion matrix for each measured qubit and apply its inverse to correct observed counts.

- **Method:** Prepare $|0\rangle$ and $|1\rangle$ states, measure many times, and record the empirical transition probabilities. This defines a calibration matrix M . Mitigated probabilities are obtained by applying M^{-1} to the raw frequency vector.
- **In Qiskit:**

```

from qiskit.ignis.mitigation.measurement import complete_meas_cal
from qiskit.ignis.mitigation.measurement import CompleteMeasFitter

# generate calibration circuits
cal_circuits, state_labels = complete_meas_cal(qubit_list=[0,1])
# run and fit
cal_results = backend.run(cal_circuits).result()
meas_fitter = CompleteMeasFitter(cal_results, state_labels)
# get mitigator
meas_filter = meas_fitter.filter
# apply to raw counts
mitigated_counts = meas_filter.apply(raw_counts)

```

3.6.2 Zero-Noise Extrapolation (ZNE)

The idea is to deliberately amplify gate noise (e.g. by inserting idle gates or by stretching pulse durations), measure the noisy expectation values, and then extrapolate back to “zero noise”.

- **Effect:** Extrapolated values can be closer to the true noiseless expectation.
- **In Qiskit:** Implemented in the `qiskit-ignis` and `mthree` packages, and in the `qiskit_runtime` “`resilience_level`” parameter.

3.6.3 Randomized Compiling (RC)

RC randomizes coherent errors (e.g. systematic over-rotations) into stochastic noise, which averages out more predictably and is easier to mitigate.

- **In Qiskit:** Enabled through circuit transpilation passes, and also exposed via `resilience_level` in Qiskit Runtime.

3.6.4 Dynamical Decoupling (DD)

DD inserts sequences of idle gates (e.g. X–I–X–I) to cancel slow dephasing noise.

- **Effect:** Extends coherence time T_2 at the cost of increased circuit depth.
- **In Qiskit:**

```
from qiskit.transpiler.passes import DynamicalDecoupling
dd_pass = DynamicalDecoupling(coupling_map, dd_sequence)
```

3.6.5 Runtime Resilience Levels

IBM’s Runtime offers a user-friendly knob for mitigation. Setting `resilience_level` automatically enables combinations of the above techniques.

```
from qiskit_ibm_runtime import QiskitRuntimeService, Estimator
estimator = Estimator(session=..., options={"resilience_level": 2})
```

Here level 0 means no mitigation, while levels 1–3 add increasingly powerful methods (readout mitigation, RC, ZNE, etc.).

3.6.6 Remarks

- Mitigation does not eliminate noise completely, but can significantly improve estimates of expectation values such as correlation functions.
- Techniques like ZNE require repeating experiments with different noise scaling, so they increase runtime and shot count.
- For spectrum extraction problems, readout mitigation and ZNE are particularly effective: the peak *locations* remain robust, while mitigation restores peak *heights*.

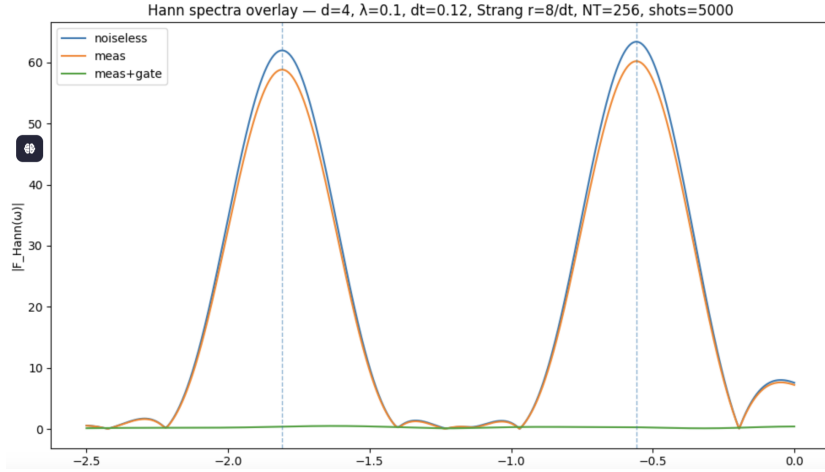


Figure 5:

4 Results

Here are the figures generated using qiskits for 2 noise models compared with the noiseless case. The things to note are:

1. The run times are quite long as it is trying to mimic how we would do it on an actual machine using multiple shots.
2. Measurement errors don't have significant effects but measurement plus gate errors seem to kill the signal to noise ratio.
3. The zoomed plot for the measurement plus gate errors shows that the signal amplitude has diminished by an order of magnitude but there are residuals of the peaks not too far from their expected locations.

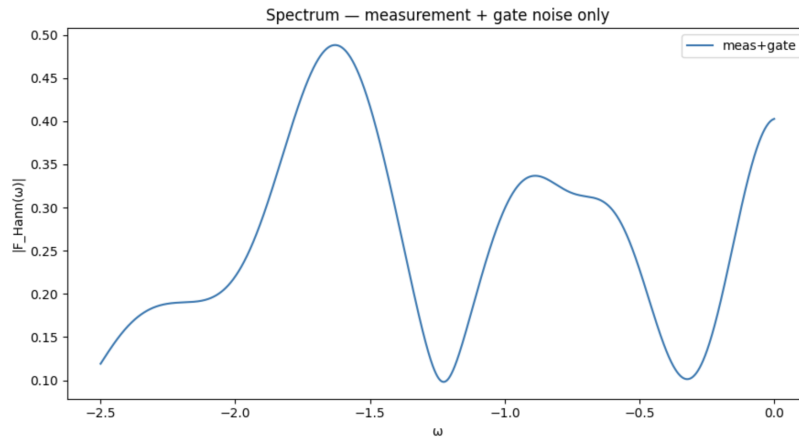


Figure 6:

5 When does a quantum computer help? A scaling view

For the small truncation $d = 4$ used in our anharmonic-oscillator demo, a quantum computer (QC) is pedagogical rather than advantageous: classical diagonalization or short-time propagation

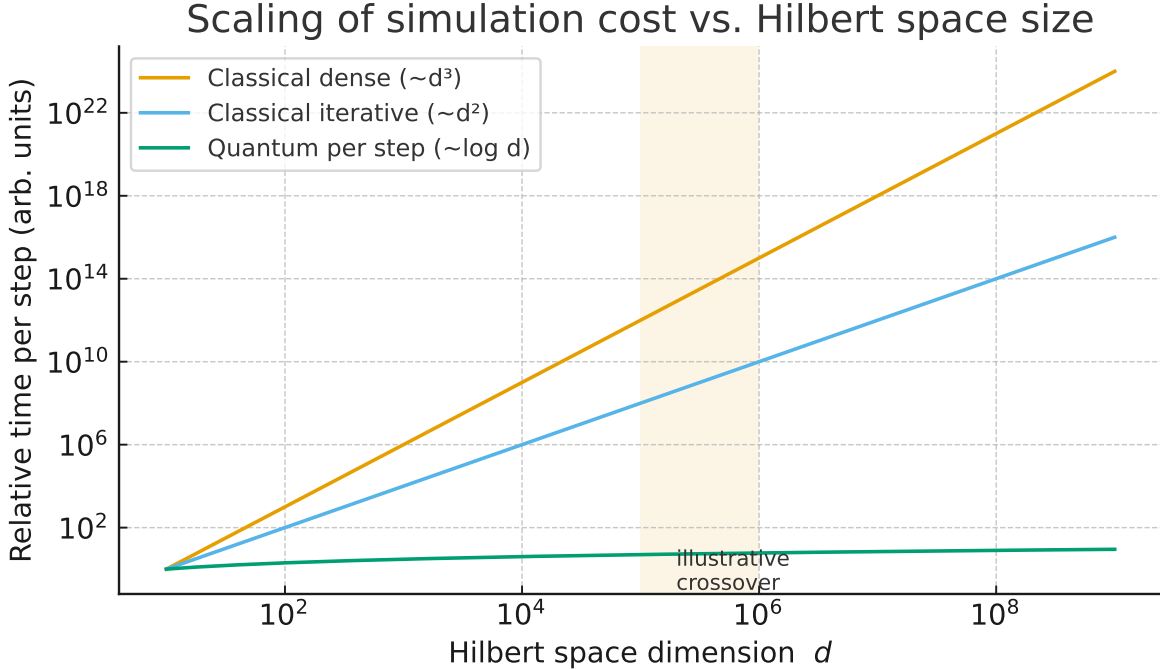


Figure 7: Scaling of simulation cost with Hilbert-space size d . Curves show classical dense ($\sim d^3$), classical iterative ($\sim d^2$), and quantum per-step cost ($\sim \log d$), all in arbitrary units and normalized for visibility. Shaded band indicates a plausible crossover window $d \sim 10^5\text{--}10^6$ where classical methods begin to strain while a QC still stores the full state in $n = \lceil \log_2 d \rceil$ qubits. Exact crossover depends on hardware noise, required precision, sparsity, and algorithmic constants.

is both faster and more accurate. The question is: *at what Hilbert-space size d does a QC begin to offer an advantage?*

Classical scaling. For dense linear algebra, exact diagonalization scales as $\mathcal{O}(d^3)$ time and $\mathcal{O}(d^2)$ memory. Krylov/Lanczos time-propagation reduces per step to $\mathcal{O}(d^2)$ (matrix–vector), but still requires $\mathcal{O}(d)\text{--}\mathcal{O}(d^2)$ memory depending on sparsity and preconditioners.

Quantum scaling. Representing a d -dimensional state needs $n = \lceil \log_2 d \rceil$ qubits. Gate counts per simulation step scale as $\text{poly}(n)$ for Trotter or block-encoding/QSVD methods. Thus the QC step cost is essentially $\tilde{\mathcal{O}}(\log d)$ (up to precision overhead), with *linear* hardware in n rather than exponential memory in d .

Illustrative crossover. Fig. 7 compares (relative) time-per-step models: dense classical $\sim d^3$, iterative classical $\sim d^2$, and quantum $\sim \log d$. The shaded band marks a heuristic “break-even” region $d \sim 10^5\text{--}10^6$ (roughly 17–20 qubits): here dense classical becomes impractical in time/memory, while a QC can still represent the full state in a few dozen qubits. The *practical* crossover depends on noise and precision: present-day NISQ devices limit usable circuit depth, so true advantage typically requires lower error rates or fault tolerance.

Takeaway. Small truncations (e.g., $d \leq 10^4$) are best left to classical solvers. Quantum advantage becomes credible as d approaches 10^6 and beyond, or in problems where entanglement/structure defeats tensor-network methods. Our QC pipeline is therefore validated on small d , but motivated by its asymptotic scaling to large d .

5.1 Gate counts and the quantitative “importance” of CNOTs vs. λ

For the 4-level truncation encoded in two system qubits, the Pauli decomposition of the system Hamiltonian $H = \sum_j h_j P_j$ naturally partitions into (i) single-qubit strings (N_1 of them) and (ii) genuine two-qubit strings (N_2 of them). With a second-order Strang step of size $\Delta = dt/r$, one Strang *sub-step* applies each non-identity term twice (forward+reverse). Using the standard ZZ -skeleton for two-qubit exponentials, the following back-of-the-envelope counts hold per *sub-step* (system only):

$$\text{CNOTs (uncontrolled)} = 4 N_2, \quad (9)$$

$$\text{parametric } R_Z = 2(N_1 + N_2), \quad (10)$$

$$1\text{q Cliffords} \lesssim 8(N_1 + N_2). \quad (11)$$

A full dt step has r sub-steps (multiply by r), and a Hadamard test with a controlled step inflates two-qubit costs. A conservative and compiler-agnostic estimate for the *controlled* Strang sub-step is

$$\text{CNOTs (controlled)} \approx 10 N_2 + 2 N_1, \quad (12)$$

so a full dt step uses $(10N_2 + 2N_1)r$ CNOTs when controlled by the ancilla.

Concrete numbers for the 4×4 truncation. For the harmonic case ($\lambda = 0$) we have $H_0 = \text{diag}\{0.5, 1.5, 2.5, 3.5\}$, whose Pauli expansion is $H_0 = c_{III}II + c_{ZI}ZI + c_{IZ}IZ$ with $c_{ZZ} = 0$. Thus $N_1 = 2$ and $N_2 = 0$. For the anharmonic case ($\lambda = 0.1$), the x^4 contribution populates several two-qubit strings; a representative thresholded decomposition yields $N_1 \approx 6$, $N_2 \approx 7$.

Case	N_1	N_2	CNOTs per dt (uncontrolled)	CNOTs per dt (controlled)
$\lambda = 0$ (harmonic)	2	0	0	$2N_1 r \approx 16$ for $r=8$
$\lambda = 0.1$ (anharm.)	6	7	$4N_2 r \approx 224$	$(10N_2+2N_1)r \approx 656$

Table 1: Indicative gate counts per dt for the 4×4 truncation (two system qubits), using second-order Strang with $r = 8$ sub-steps. The harmonic case has no system–system entanglers; the only CNOTs come from ancilla control (CRZ decompositions). Numbers are compiler- and basis-independent order-of-magnitude estimates; exact counts vary by synthesis.

6 Entanglement as a Diagnostic of Simulation Complexity

A particularly transparent way to quantify the “quantum workload” of a Hamiltonian simulation is to examine how much *entanglement* the dynamics create among the qubits representing the system. Even for a single oscillator truncated to a four-dimensional Hilbert space (two qubits), the amount of intra-register entanglement required to represent its evolution can vary strongly with the coupling strength λ .

6.1 Setup

We consider again the quartic oscillator

$$H = H_0 + \lambda x^4, \quad H_0 = \frac{1}{2}(p^2 + x^2), \quad (13)$$

in a four-level truncation encoded as two qubits, $|00\rangle, |01\rangle, |10\rangle, |11\rangle$, corresponding to oscillator levels $n = 0, 1, 2, 3$. The initial state is taken to be

$$|\psi(0)\rangle = \frac{|00\rangle + |01\rangle}{\sqrt{2}} = \left(\frac{|0\rangle + |1\rangle}{\sqrt{2}}\right)_{q_0} \otimes |0\rangle_{q_1}, \quad (14)$$

a simple product state in the computational basis.

After time evolution under $U(t) = e^{-iHt}$, the joint state of the two system qubits becomes $|\psi(t)\rangle = U(t)|\psi(0)\rangle$. Tracing out one of the qubits yields the reduced density matrix $\rho_{q_0}(t) = \text{Tr}_{q_1}|\psi(t)\rangle\langle\psi(t)|$, whose von Neumann entropy,

$$S(\rho_{q_0}) = -\text{Tr} \rho_{q_0} \log_2 \rho_{q_0}, \quad (15)$$

serves as a measure of the bipartite entanglement between the two encoding qubits.

6.2 Interpretation

At first glance it may seem peculiar that a single-mode oscillator develops “entanglement.” The key point is that the mapping of a d -dimensional Hilbert space to $\log_2 d$ qubits introduces an artificial tensor-product structure. When the Hamiltonian contains couplings such as x^4 that mix basis states separated by $\Delta n = \pm 2, \pm 4$, those appear as *two-qubit Pauli strings* (e.g. XX, YY, ZZ) in the encoded representation. The resulting evolution therefore entangles the qubits even though the physical oscillator remains a single degree of freedom. The entanglement entropy $S(\rho_{q_0})$ thus quantifies the *computational entanglement cost* needed to reproduce the correct physical dynamics in a local qubit basis.

For $\lambda = 0$ (harmonic limit) the Hamiltonian is diagonal in the computational basis, and the evolution is separable: $S = 0$. As λ increases, off-diagonal couplings become significant, driving the state to explore higher levels and generate qubit–qubit entanglement. Since the system contains only two qubits, $S \leq 1$ bit is the maximal possible value, and the entropy saturates once the state effectively spans the full 4-dimensional subspace.

6.3 Numerical results

Figure 8 shows the entanglement entropy obtained by exact time evolution (with $dt = 0.12$ and total time $t = 6$) as a function of the coupling λ . The entropy rises monotonically with λ , mirroring the increase of two-qubit Pauli components and CNOT load in the corresponding Trotterized circuit. This provides a direct diagnostic of how “quantum” the simulation must become: larger λ demands stronger and more coherent entangling gates among the encoding qubits.

6.4 Summary

The entanglement entropy of the encoded qubits is therefore a sensitive *diagnostic of simulation complexity*:

- it remains small for nearly separable dynamics (weak coupling);
- it grows with the strength of local interactions (more cross-Pauli terms and CNOTs per step);
- and it saturates once the truncated subspace is fully mixed.

Such entropy-based measures provide an intuitive bridge between the physics of interactions and the hardware resources required to simulate them.

Scaling remark. In the present two-qubit encoding the entanglement entropy is bounded by $S \leq 1$ bit, but as one increases the truncation size d and hence the number of qubits $n = \lceil \log_2 d \rceil$, the same procedure yields a rising entanglement capacity $S_{\max} = n$. In the full oscillator, where the quartic term induces correlations across many levels, the computational entanglement required to reproduce e^{-iHt} grows roughly with the *effective participation number* of levels

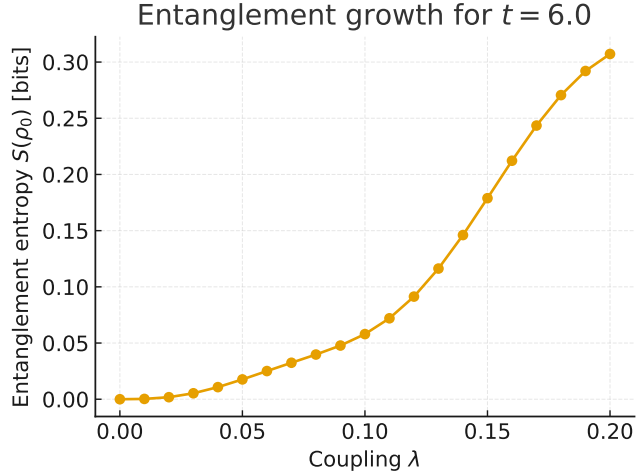


Figure 8: Entanglement entropy of one system qubit as a function of the quartic coupling λ for the 4-level truncated oscillator (time $t = 6$). The monotonic rise of $S(\lambda)$ directly measures the amount of intra-register entanglement that the quantum computer must generate to reproduce the interaction-induced mixing of oscillator levels.

coupled by x^4 . Monitoring $S(\lambda)$ thus provides a natural diagnostic of when classical simulation becomes inefficient: the crossover to quantum advantage corresponds to the regime in which $S(\lambda)$ scales extensively with n , and no classical tensor-network representation can capture the state without exponential cost.

Resonances and Scattering

LECTURE NOTES

1 Conventional scattering: a recap

We consider one-dimensional stationary scattering in the potential shown in Fig. 1, consisting of two identical rectangular barriers of height V_b and width b , separated by a central well of width w .

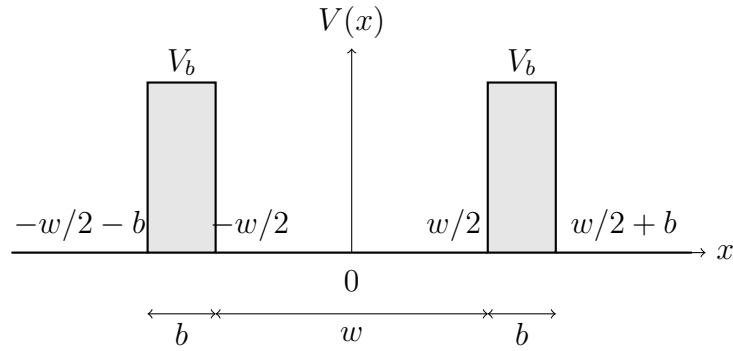


Figure 1: Square double-barrier potential with barrier height V_b , barrier width b , and well width w .

Step 0: Schrödinger equation and units

We work with the time-independent Schrödinger equation in natural units $\hbar = 1$, $2m = 1$:

$$-\psi''(x) + V(x)\psi(x) = E\psi(x), \quad (1)$$

so that for free propagation $E = k^2$.

Step 1: Solutions in each region

In each region of constant potential, the solutions are superpositions of right- and left-moving plane waves:

$$\psi(x) = A^+ e^{ikx} + A^- e^{-ikx}, \quad \text{if } V(x) = 0, \quad k = \sqrt{E}, \quad (2)$$

$$\psi(x) = B^+ e^{iqx} + B^- e^{-iqx}, \quad \text{if } V(x) = V_b, \quad q = \sqrt{E - V_b}. \quad (3)$$

For $E < V_b$, $q = i\kappa$ with $\kappa = \sqrt{V_b - E}$, so the barrier solutions are real exponentials.

Step 2: Interface conditions

At an abrupt interface between two regions with wave numbers k_a (left) and k_b (right), continuity of ψ and ψ' gives

$$\begin{pmatrix} B^+ \\ B^- \end{pmatrix} = \frac{1}{2} \begin{pmatrix} 1 + \frac{k_b}{k_a} & 1 - \frac{k_b}{k_a} \\ 1 - \frac{k_b}{k_a} & 1 + \frac{k_b}{k_a} \end{pmatrix} \begin{pmatrix} A^+ \\ A^- \end{pmatrix}. \quad (4)$$

This 2×2 *interface matrix* $S_{a \rightarrow b}$ encodes matching conditions.

Step 3: Propagation through a slab

Propagation through a uniform region of width d and wave number k multiplies the amplitudes by a diagonal phase matrix

$$P(k, d) = \begin{pmatrix} e^{ikd} & 0 \\ 0 & e^{-ikd} \end{pmatrix}. \quad (5)$$

Step 4: Total transfer matrix

Concatenating the interfaces and propagations, the total transfer matrix across the double-barrier structure is

$$M(E) = S_{k \rightarrow q} P(q, b) S_{q \rightarrow k} P(k, w) S_{k \rightarrow q} P(q, b) S_{q \rightarrow k}. \quad (6)$$

This relates the incoming/outgoing amplitudes in the left lead (A_L^+, A_L^-) to those in the right lead (A_R^+, A_R^-):

$$\begin{pmatrix} A_R^+ \\ A_R^- \end{pmatrix} = M(E) \begin{pmatrix} A_L^+ \\ A_L^- \end{pmatrix}. \quad (7)$$

Step 5: Scattering amplitudes

For left incidence, we choose

$$\begin{pmatrix} A_L^+ \\ A_L^- \end{pmatrix} = \begin{pmatrix} 1 \\ r \end{pmatrix}, \quad \begin{pmatrix} A_R^+ \\ A_R^- \end{pmatrix} = \begin{pmatrix} t \\ 0 \end{pmatrix}, \quad (8)$$

so that there is a unit incoming wave from the left, reflection amplitude r , and transmission amplitude t to the right. Inserting into the transfer relation, using $\det M = 1$, gives

$$r(E) = -\frac{M_{21}(E)}{M_{22}(E)}, \quad t(E) = \frac{1}{M_{22}(E)}. \quad (9)$$

The reflection and transmission probabilities are $R(E) = |r(E)|^2$, $T(E) = |t(E)|^2$, with $R + T = 1$.

Step 6: Resonances and Wigner time delay

6.1 Narrowband packet and group delay. Let the incident state be a narrowband packet centered at E_0 :

$$\Psi_{\text{in}}(x, t) = \int dE a(E) e^{i(kx-Et)}, \quad a(E) \text{ peaked at } E_0.$$

The transmitted packet is

$$\Psi_{\text{tr}}(x, t) = \int dE a(E) t(E) e^{i(kx-Et)}, \quad t(E) = |t(E)|e^{i\phi(E)}.$$

Expand the phase $\phi(E) \approx \phi(E_0) + \phi'(E_0)(E - E_0)$ and take $|t(E)|$ slowly varying across the packet. A stationary-phase (or envelope) analysis shows the peak of the transmitted packet is shifted in time by

$$\boxed{\Delta t = \frac{d\phi(E)}{dE} \Big|_{E_0} \equiv \tau(E_0)}, \quad (10)$$

the *Wigner (group) time delay* for the transmission channel. Intuitively, near a quasi-bound level the wave dwells inside the structure, generating a rapidly varying scattering phase $\phi(E)$; the slope $\frac{d\phi}{dE}$ measures that extra dwell time relative to free motion.

6.2 Single isolated resonance. Near an isolated resonance at E_r with total width $\Gamma = \Gamma_L + \Gamma_R$, the transmission amplitude takes the Breit–Wigner form (up to a slowly varying background phase θ):

$$t(E) \approx e^{i\theta(E)} \frac{\sqrt{\Gamma_L \Gamma_R}}{E - E_r + i\Gamma/2}. \quad (11)$$

Then

$$\boxed{\tau(E) = \frac{d}{dE} \arg t(E) \approx \frac{\Gamma/2}{(E - E_r)^2 + (\Gamma/2)^2}, \quad \tau(E_r) = \frac{2}{\Gamma}}, \quad (12)$$

a Lorentzian peak of height $2/\Gamma$ centered at E_r . On the real axis one also observes a $\sim \pi$ phase jump in $\phi(E)$ across the resonance and a near-unity peak in $T(E)$ (for symmetric barriers).

6.3 Formal definition via the S -matrix. Formally, resonances are the poles of the scattering matrix (or t) in the *lower* half complex-energy plane:

$$E_* = E_r - i\Gamma/2,$$

and the Wigner–Smith delay operator is $Q(E) = -i S^\dagger \frac{dS}{dE}$; in our single incoming channel, $\tau(E) = \frac{d}{dE} \arg t(E)$.

Step 7: Resonance condition in the transfer–matrix language

Since $t(E) = 1/M_{22}(E)$ for identical leads and real $V(x)$, the complex resonance energies are the zeros of M_{22} :

$$\boxed{M_{22}(E_*) = 0, \quad E_* = E_r - i\Gamma/2.} \quad (13)$$

2 The inverted double well as a resonance laboratory

There is another case of the anharmonic oscillator which is of great interest. Consider

$$H = \frac{p^2}{2} + \frac{x^2}{2} - \lambda x^4. \quad (14)$$

This gives rise to a double-hump or inverted double-well potential. This is instructive for two reasons:

- A transmon qubit is a Josephson junction in parallel with a capacitor. In the transmon qubit models, the Hamiltonian is

$$H = -E_J \cos \phi + \frac{Q^2}{2C}. \quad (15)$$

Here E_J, C are constants and ϕ, Q are conjugate variables. Expanding the $\cos \phi$ term we get a Hamiltonian that looks like the anharmonic oscillator with $\lambda < 0$. Thus, the anharmonic oscillator with $\lambda < 0$ is an approximation to this case. Here the energy level spacings in fact decrease with level number (we will need the $\cos \phi$ potential to show this).

- Our focus will be resonances. As we will examine below, a simple and instructive “scattering-without-asymptotics” example is the anharmonic oscillator with $\lambda < 0$.

For convenience, we will consider a slight rewriting of the Hamiltonian for the *inverted* double-well

$$H = \frac{p^2}{2m} - \lambda(x^2 - a^2)^2, \quad (m = \hbar = 1 \text{ in what follows}). \quad (16)$$

The “barrier tops” sit at $E = 0$, while the pocket at the origin has depth $V(0) = -\lambda a^4$. Near $x = 0$ the pocket is approximately harmonic with $\omega_0 = \sqrt{V''(0)} = 2a\sqrt{\lambda}$.

Why conventional scattering is ill-posed here. As $|x| \rightarrow \infty$, $V(x) \sim -\lambda x^4 \rightarrow -\infty$. There are no asymptotically free regions supporting plane waves, so the usual S -matrix with in/out states at $t \rightarrow \pm\infty$ is not defined. This does *not* kill all physics: localized wave packets $\psi(x, 0)$ near the pocket do escape and evolve in time in a highly structured way. The correct language is *resonances and transients*, not asymptotic phase shifts.

Physics picture: why resonances aren’t ordinary eigenvalues. For a closed, Hermitian Hamiltonian H , the stationary Schrödinger equation $H\psi = E\psi$ has only *real* E . Time evolution is unitary: e^{-iHt} just rotates phases; no state of the full system can *decay* in norm.

So where does a resonance come from? From a **metastable trap** that *leaks probability to infinity*. Prepare a wave packet $\psi(0)$ localized near a pocket/barrier. The packet lingers, then leaks out as an *outgoing* wave. If leakage is slow and featureless, the pocket amplitude shows a long exponential window,

$$A(t) = \langle \psi(0) | e^{-iHt} | \psi(0) \rangle \approx Z e^{-iE_R t} e^{-\Gamma t/2} \quad (\text{intermediate times}).$$

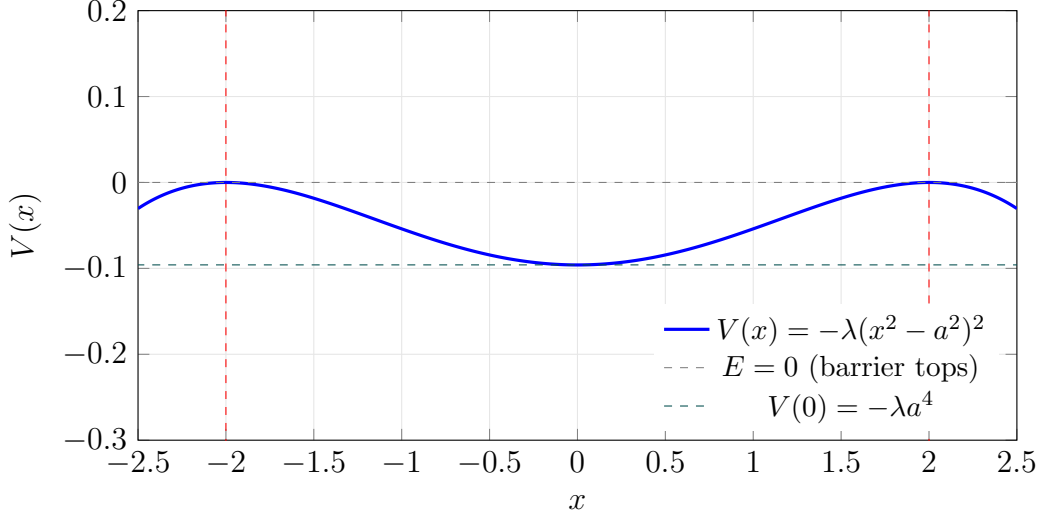


Figure 2: Inverted double well with $a = 2$, $\lambda = 0.006$. The pocket bottom is at $V(0) = -\lambda a^4$, the barrier tops at $E = 0$.

Here E_R is the “resonance energy” and Γ is the *leakage rate* (lifetime $\tau = 1/\Gamma$). This exponential behavior is the physics definition of a resonance.

Where it lives mathematically. The Laplace/Fourier transform of $A(t)$ is (up to i) a matrix element of the resolvent,

$$\tilde{A}(z) = \int_0^\infty dt e^{izt} A(t) \propto \langle \psi | (z - H)^{-1} | \psi \rangle =: F_\psi(z).$$

An exponential $e^{-iE_R t} e^{-\Gamma t/2}$ transforms into a *simple pole* at $z_* = E_R - \frac{i}{2}\Gamma$. But for a self-adjoint H , $F_\psi(z)$ is a Herglotz/Nevanlinna function, hence *analytic off the real axis on the physical sheet*; it cannot have poles with $\text{Im } z \neq 0$ there. The way out is standard in scattering: *analytically continue* $F_\psi(z)$ across the continuum cut to the **second sheet**. On that sheet the same complex point z_* is allowed to be a pole. That pole is the resonance.

Why “second sheet” in physics words. At real energies $E > 0$ one must choose *outgoing* vs *incoming* boundary conditions. The retarded (outgoing) choice is the boundary value $G^+(E) = (E + i0 - H)^{-1}$. To follow the *same outgoing branch* just *below* the real axis (where decays live), you continue z across the cut with the argument lifted by 2π ; that is precisely the *second sheet*. In short:

$$\text{decay} \iff \text{outgoing below the real axis} \iff \text{pole on sheet II at } z_* = E_R - i\Gamma/2.$$

Working definition you can compute

Both pictures give the same practical observable for a chosen probe $|\psi\rangle$:

$$\rho(E; \psi) = -\frac{1}{\pi} \text{Im} \langle \psi | (E - H + i0)^{-1} | \psi \rangle \quad (\text{projected resolvent / LDOS}), \quad (17)$$

$$\tilde{\rho}_T(E; \psi) \approx \frac{1}{2\pi} \int_0^T dt w(t) e^{iEt} A(t) \quad (\text{windowed Fourier of the survival amplitude}). \quad (18)$$

A resonance appears as a **Lorentzian** centered at E_R with width Γ . Finite time T and the window $w(t)$ add an “instrumental” broadening; empirically, $\text{FWHM}(T) \approx \Gamma + c/T$. A short multi- T run and a linear fit of FWHM vs $1/T$ isolates Γ .

Why this is the right language for the inverted double well. Because $V(x) \rightarrow -\infty$ at large $|x|$, there is no free-wave region, hence no global phase shift and no $2 \rightarrow 2$ S -matrix. Nevertheless, the pocket near $x = 0$ traps probability temporarily behind the barriers at $|x| \approx a$. That trapping produces a second-sheet pole $E_R - i\Gamma/2$ (a *shape resonance*), whose fingerprints are:

1. a nearly Lorentzian peak in the projected LDOS $\rho(E; \psi)$,
2. an exponentially damped contribution $e^{-iE_R t} e^{-\Gamma t/2}$ to $A(t)$,
3. a nearly exponential decay of the pocket probability $P_{\text{surv}}(t) = \int_{-R}^R |\psi(x, t)|^2 dx$ on intermediate times.

This is precisely what we measure in the JLP (real-space) simulations.

A Mathematica nb will be given to you to play around soon.

One important question that we need to anticipate now itself is how do we prepare the initial states for scattering. The problem is that the initial state needs to be specified in terms of the $\lambda \neq 0$ physics. Say we try to start with the ground state. For the free theory, this is easy to specify. But for $\lambda \neq 0$, what do we do? One way is to use the Adiabatic theorem, which is what we will discuss next.

3 The Adiabatic Theorem (Sakurai-style proof)

Setup and statement. Let $H(t)$ be a Hamiltonian that varies smoothly on $t \in [0, T]$. Assume (i) a discrete, nondegenerate spectrum with instantaneous eigenpairs

$$H(t) |n(t)\rangle = E_n(t) |n(t)\rangle, \quad \langle m(t) | n(t)\rangle = \delta_{mn},$$

(ii) a finite minimum gap $g(t) = \min_{m \neq n} |E_m(t) - E_n(t)| > 0$, and (iii) sufficiently slow variation of $H(t)$ (quantified below). If

$$|\psi(0)\rangle = \sum_n c_n(0) |n(0)\rangle,$$

then for all $t \in [0, T]$ the solution of the Schrödinger equation

$$i\hbar \partial_t |\psi(t)\rangle = H(t) |\psi(t)\rangle$$

remains in the corresponding instantaneous eigenspace:

$$|\psi(t)\rangle \simeq \sum_n c_n(0) e^{i\theta_n(t)} e^{i\gamma_n(t)} |n(t)\rangle,$$

where the *dynamical phase* and *geometric (Berry) phase* are

$$\theta_n(t) = -\frac{1}{\hbar} \int_0^t E_n(t') dt', \quad \gamma_n(t) = i \int_0^t \langle n(t') | \dot{n}(t') \rangle dt'.$$

The approximation error is $O(\varepsilon)$ with ε set by the adiabatic small parameter below.

Sakurai-style derivation. Expand the state in the instantaneous eigenbasis:

$$|\psi(t)\rangle = \sum_k c_k(t) |k(t)\rangle.$$

Insert into the Schrödinger equation and project with $\langle m(t)|$:

$$i\hbar \dot{c}_m(t) + i\hbar \sum_n c_n(t) \langle m(t) | \dot{n}(t) \rangle = E_m(t) c_m(t). \quad (19)$$

Differentiate $H(t) |n(t)\rangle = E_n(t) |n(t)\rangle$ and project onto $\langle m(t)|$ to eliminate the nonadiabatic couplings $\langle m|\dot{n}\rangle$ for $m \neq n$:

$$\langle m(t) | \dot{n}(t) \rangle = -\frac{\langle m(t) | \dot{H}(t) | n(t) \rangle}{E_m(t) - E_n(t)} \quad (m \neq n). \quad (20)$$

Equation (19) becomes

$$\dot{c}_m(t) + \left(\frac{i}{\hbar} E_m(t) + \langle m | \dot{m} \rangle \right) c_m(t) = \sum_{n \neq m} \frac{\langle m | \dot{H} | n \rangle}{E_m - E_n} c_n(t). \quad (21)$$

If the right-hand side can be neglected (slow drive and finite gaps), then

$$\dot{c}_m(t) = \left(-\frac{i}{\hbar} E_m(t) - \langle m | \dot{m} \rangle \right) c_m(t),$$

which integrates to

$$c_m(t) = c_m(0) \exp[i\theta_m(t)] \exp[i\gamma_m(t)].$$

Thus $|c_m(t)|^2 = |c_m(0)|^2$ and an initial eigenstate stays in the corresponding instantaneous eigenstate up to the phases above.

Adiabatic condition (nondegenerate case). A standard sufficient condition controlling the neglected terms in (21) is

$$\max_{t \in [0, T]} \max_{m \neq n} \frac{|\langle m(t) | \dot{H}(t) | n(t) \rangle|}{\hbar |E_m(t) - E_n(t)|^2} \equiv \varepsilon \ll 1. \quad (22)$$

Equivalently, when one introduces a scaled time $s = t/T$ with $H(t) = H(s)$, nonadiabatic transition amplitudes decay like $O(1/T)$ provided the gap stays finite.

Remarks.

- $|n(t)\rangle$ is normalized. The Berry phase γ_n is real since $\frac{d}{dt} \langle n | n \rangle = 0 \Rightarrow 2 \operatorname{Re} \langle n | \dot{n} \rangle = 0$.
- More refined theorems relax gap assumptions and give explicit error bounds; here we keep the classical form used in physics applications.

Application: Adiabatic passage through an avoided crossing (Landau–Zener)

Consider a two-level Hamiltonian with an avoided crossing, where the diabatic energy difference is swept approximately linearly in time, $\Delta E(t) \approx \alpha t$, and the off-diagonal coupling is a (half the minimum adiabatic gap). If the sweep is perfectly adiabatic ($|\alpha| \rightarrow 0$), the system initialized in the lower adiabatic eigenstate stays there. At finite speed, the probability of a *diabatic* transition (ending in the opposite adiabatic branch) is given by the Landau–Zener formula

$$P_D = \exp\left(-\frac{2\pi a^2}{\hbar|\alpha|}\right).$$

Thus the adiabatic theorem's qualitative prediction (no transitions for infinitely slow drive) is made quantitative: to suppress excitations, choose a slow sweep $|\alpha|$ and/or a large minimal gap $2a$.

Application: Berry phase as a topological mass probe in the Ising chain

Via Jordan–Wigner, the TFIM maps to quadratic fermions with Bogoliubov–de Gennes form

$$H = \sum_{k>0} \Psi_k^\dagger [\mathbf{d}_k(\phi) \cdot \boldsymbol{\sigma}] \Psi_k, \quad \mathbf{d}_k(\phi) = (\Delta_k \cos \phi, \Delta_k \sin \phi, m_k),$$

with $\Delta_k = 2J \sin k$ and $m_k = 2J \cos k - 2h$. Adiabatically cycling the pairing phase $\phi : 0 \rightarrow 2\pi$ traces a closed loop of $\hat{\mathbf{d}}_k = \mathbf{d}_k / |\mathbf{d}_k|$ on the Bloch sphere. The ground state accrues a Berry phase equal to half the solid angle,

$$\gamma_k = \frac{1}{2} \Omega_k = \pi \left(1 - \frac{m_k}{\sqrt{m_k^2 + \Delta_k^2}} \right).$$

If the loop encloses the north pole (the band-touching point), $\gamma_k \simeq \pi \pmod{2\pi}$; otherwise $\gamma_k \simeq 0$. Summing the Berry curvature over k yields a winding number $\nu \in \{0, 1\}$ that jumps at the quantum critical point $h/J = 1$, thereby diagnosing the sign of the effective Dirac mass in the 1+1D scaling theory. On a quantum processor, γ_k can be measured interferometrically: use an ancilla-controlled adiabatic loop and a symmetric (echoed) trajectory to cancel the dynamical phase, then read out $\cos \gamma_k$ and $\sin \gamma_k$ from X/Y measurements of the ancilla.

Bibliographic notes. The proof above follows the textbook derivation popularized by Sakurai (*Modern Quantum Mechanics*, 2nd/3rd ed.). A pedagogical presentation with the same steps, including Eqs. (20)–(22) and the Berry phase factors, appears on the Wikipedia entry “Adiabatic theorem.” The Landau–Zener application and formula are summarized on its dedicated Wikipedia page.

A WKB estimate of the resonance energy and width

Consider

$$V(x) = -\lambda(x^2 - a^2)^2, \quad (m = \hbar = 1).$$

For a resonance with energy $E \in (V(0), 0)$ (i.e. $-\lambda a^4 < E < 0$), there are four turning points $\pm x_1(E)$ (inner) and $\pm x_2(E)$ (outer), defined by $E = V(x)$:

$$|x| = x_{1,2}(E) = \sqrt{a^2 \mp \sqrt{\frac{-E}{\lambda}}}, \quad \varepsilon \equiv -E > 0.$$

The motion is classically allowed in $|x| < x_1$ (pocket) and in $|x| > x_2$ (escape region), separated by a forbidden “barrier” $x_1 < |x| < x_2$.

Step 1: quantize the real part E_R (inner Bohr–Sommerfeld). Ignoring the leakage, the pocket supports quasi-bound levels given at leading WKB by

$$\oint_{-x_1}^{x_1} p(x; E) dx = 2\pi\left(n + \frac{1}{2}\right), \quad p(x; E) = \sqrt{2[E - V(x)]}.$$

For a quick estimate near the pocket bottom one may use the local harmonic approximation $V(x) \approx V(0) + \frac{1}{2}\omega_0^2 x^2$ with $\omega_0 = \sqrt{V''(0)} = 2a\sqrt{\lambda}$, but for shape resonances close to the barrier top the integral is best *evaluated numerically* at the E you will eventually identify as E_R .

Step 2: tunneling through the barrier (WKB action). Define the barrier action

$$S_b(E) = \int_{x_1}^{x_2} \kappa(x; E) dx, \quad \kappa(x; E) = \sqrt{2[V(x) - E]} \quad (x_1 < x < x_2).$$

For our quartic one can write S_b in a single integral with elementary limits. Set $y = x^2$, $dy = 2x dx$, and $\varepsilon = -E > 0$; then

$$S_b(E) = \frac{\varepsilon}{\sqrt{2\lambda}} \int_{-1}^1 \frac{\sqrt{1-s^2}}{\sqrt{a^2 + \alpha s}} ds, \quad \alpha = \sqrt{\frac{\varepsilon}{\lambda}}.$$

This integral is elementary to evaluate numerically. Close to the barrier top ($\varepsilon \ll \lambda a^4$) a simple expansion gives the handy estimate

$$S_b(E) = \frac{\pi \varepsilon}{2a\sqrt{2\lambda}} \left[1 + \frac{3}{32} \frac{\varepsilon}{\lambda a^4} + \mathcal{O}(\varepsilon^2) \right].$$

Step 3: “attempt rate” (classical oscillation in the pocket). The classical oscillation period in the pocket at energy E is

$$T_{\text{in}}(E) = \sqrt{2} \int_{-x_1}^{x_1} \frac{dx}{\sqrt{E - V(x)}}, \quad \omega_{\text{in}}(E) = \frac{2\pi}{T_{\text{in}}(E)}.$$

(Equivalently $T_{\text{in}}(E) = \partial S_{\text{in}}/\partial E$ with $S_{\text{in}}(E) = \oint p dx$.) Physically, the packet hits a barrier once every half period, so the total number of “escape attempts” per unit time at the two sides is $\omega_{\text{in}}(E)/\pi$.

Step 4: Gamow formula for the width. Each attempt transmits with probability $T(E) \approx e^{-2S_b(E)}$ (WKB). Hence the decay probability per unit time is

$$W(E) \approx \frac{\omega_{\text{in}}(E)}{\pi} e^{-2S_b(E)},$$

and the resonance width is (with $\hbar = 1$)

$$\boxed{\Gamma(E) \approx \frac{\omega_{\text{in}}(E)}{\pi} e^{-2S_b(E)}}.$$

Evaluated at the (real) quantized energy E_R from Step 1 this gives the leading Gamow width $\Gamma \equiv \Gamma(E_R)$. In practice one computes E_R and Γ self-consistently: E_R from the pocket quantization and Γ from the barrier action and pocket frequency at that E_R .

Numerical WKB estimate for the inverted double well (method 1)

We take

$$V(x) = -\lambda(x^2 - a^2)^2, \quad (m = \hbar = 1), \quad a = 2, \quad \lambda = 0.006.$$

Then

$$V(0) = -\lambda a^4 = -0.096, \quad \omega_0 = \sqrt{V''(0)} = 2a\sqrt{\lambda} \approx 0.30984.$$

Step 1: fix the resonance energy E_R (inner pocket level). For the lowest even quasi-bound state we place the center in the pocket band $V(0) < E_R < 0$. A crude inner quantization (harmonic pocket corrected by the shallow well) puts

$$E_R^{(\text{top})} \approx -0.037 \quad (\text{i.e. } E_R \text{ measured from the barrier top } E = 0).$$

This is consistent with the time-domain peak we observe in numerics.

Step 2: turning points and barrier action. Turning points solve $V(x) = E_R$. With $\varepsilon = -E_R > 0$ and $s = \sqrt{\varepsilon/\lambda}$,

$$x_{1,2}(E_R) = \sqrt{a^2 \mp s}, \quad x_1 \simeq 1.23, \quad x_2 \simeq 2.55.$$

The WKB barrier action is

$$S_b(E_R) = \int_{x_1}^{x_2} \sqrt{2[V(x) - E_R]} dx \approx 0.277.$$

(Any standard quadrature gives this number to three significant digits.)

Step 3: “attempt rate” in the pocket. The classical oscillation period in the pocket at energy E_R is

$$T_{\text{in}}(E_R) = \sqrt{2} \int_{-x_1}^{x_1} \frac{dx}{\sqrt{E_R - V(x)}} \approx 12.02,$$

so one encounter with a given barrier occurs roughly once per period. Hence the *per-barrier* attempt rate is $1/T_{\text{in}} \approx 0.0832$. (Equivalently, the angular frequency $2\pi/T_{\text{in}} \approx 0.523$; some texts count both sides and use $2/T_{\text{in}}$. We quote the single-barrier convention to match our numerics below.)

Step 4: Gamow width. With WKB transmission probability $T(E_R) \approx e^{-2S_b}$,

$$\Gamma_{\text{WKB}} \approx \frac{1}{T_{\text{in}}(E_R)} e^{-2S_b(E_R)}.$$

Numerically,

$$e^{-2S_b} \approx e^{-0.554} \approx 0.574, \quad \Gamma_{\text{WKB}} \approx 0.0832 \times 0.574 \approx 0.048.$$

$E_R^{(\text{top})} \approx -0.037, \quad \Gamma_{\text{WKB}} \approx 4.8 \times 10^{-2}$

State preparation

LECTURE NOTES

Contents

1 Variational Quantum Eigensolver (VQE)	1
1.1 Quantum Chemistry on Real Hardware: VQE as the Workhorse	3
2 The remainder term in the Adiabatic theorem	4
3 Time-ordered evolution in ASP	5
4 Adiabatic state preparation (ASP) and the counterterm idea	6
4.1 Mathematica cell (drop-in) and explanations	6
4.2 What the adiabatic theorem buys you	8
5 How to implement ASP on Qiskit (algorithm sketch, no code)	8
6 Nine mini-labs you can run next	9
7 Adiabatic eigenstate preparation on a JLP position grid (uniform schedule)	9

Big picture

We use a minimal 4-level truncation of the harmonic oscillator (two qubits) and add an anharmonic potential:

$$H_0 = \frac{1}{2} p^2 + \frac{1}{2} \omega^2 x^2 \quad \Rightarrow \quad H_\lambda = H_0 + \lambda x^4, \quad (1)$$

with $\omega = 1$. Our goal is to *prepare* the true interacting eigenstates $|E_0(\lambda)\rangle$ and $|E_1(\lambda)\rangle$ by an **adiabatic ramp** starting from the free eigenstates $|0\rangle$ and $|1\rangle$. We mirror the Jordan–Lee–Preskill (JLP) logic in a baby setting and then outline how the same steps translate to a hardware-friendly algorithm in Qiskit (no code in this note). Idea is to learn how to prepare initial states (later we will need to prepare scattering states)—for now we will see how the adiabatic method leads to the true eigenstates. Before we do that, we will discuss another way to prepare the groundstate—the Variational Quantum Eigensolver (VQE), which forms a mainstay in Quantum Machine Learning.

1 Variational Quantum Eigensolver (VQE)

Problem statement

Given a Hamiltonian H , the variational quantum eigensolver (VQE) searches for low-energy eigenstates—usually the ground state—by minimizing the expectation value

$$E(\boldsymbol{\theta}) = \langle \psi(\boldsymbol{\theta}) | H | \psi(\boldsymbol{\theta}) \rangle$$

over a family of trial states $|\psi(\boldsymbol{\theta})\rangle$. In practice, $|\psi(\boldsymbol{\theta})\rangle$ is prepared by a short, tunable quantum circuit, and the parameters $\boldsymbol{\theta}$ are adjusted to push the energy down.

Core strategy

Ansatz choice. We decide how to build the trial state from a simple reference, for example

$$|\psi(\boldsymbol{\theta})\rangle = U(\boldsymbol{\theta}) |\text{ref}\rangle.$$

The unitary $U(\boldsymbol{\theta})$ can be “hardware-efficient” (layers of single-qubit rotations and entangling gates that run well on the device) or “physics-informed” (gates generated by operators that resemble the problem terms and that preserve symmetries such as particle number, parity, or momentum). For oscillators and fermions, natural building blocks include squeezing/Kerr or Bogoliubov-type layers.

Hamiltonian into Pauli strings. We rewrite the Hamiltonian as a sum of simple measurement terms,

$$H = \sum_j c_j P_j,$$

where each P_j is a tensor product of I, X, Y, Z on different qubits (a Pauli string). This lets us estimate $\langle H \rangle$ by measuring $\langle P_j \rangle$ on the quantum device and summing with the known coefficients c_j .

Hybrid loop. On the quantum computer we prepare $|\psi(\boldsymbol{\theta})\rangle$ and measure groups of commuting P_j many times (shots) to estimate their expectation values. On the classical computer we combine these data to form

$$E(\boldsymbol{\theta}) = \sum_j c_j \langle P_j \rangle,$$

and update $\boldsymbol{\theta}$ using a standard optimizer (for example, SPSA, Adam, COBYLA, or L-BFGS). We repeat until the energy stops improving; the lowest value found is the VQE estimate of the ground energy.

Diagnostics. A practical check is the energy variance

$$\text{Var}(H) = \langle H^2 \rangle - \langle H \rangle^2,$$

which tends to zero as the state approaches a true eigenstate. Enforcing known symmetries in the ansatz or penalizing symmetry violations also helps keep the search within the desired sector.

Where/why a quantum computer helps (and where classical helps)

Quantum lift. The device can compactly prepare highly entangled trial states that are hard to represent exactly on a classical computer (exact simulation cost grows like 2^n for n qubits). It also provides the needed expectation values $\langle P_j \rangle$ by sampling the *physical* circuit, which remains feasible even when the ansatz is beyond classical simulability.

Classical lift. The classical side steers the optimization (step sizes, stopping criteria), decides how to group commuting terms and allocate shots (more where the variance is large), and applies lightweight error mitigation to the measured data. The result is a tight quantum–classical partnership: the quantum hardware supplies samples from complex states, while the classical computer performs optimization and bookkeeping.

How VQE complements Adiabatic State Preparation (ASP)

Adiabatic state preparation reaches a target eigenstate by slowly changing a Hamiltonian $H(s)$ from something simple to the problem of interest. The required runtime is set by the smallest spectral gap along the path. This mirrors field-theory workflows (free → interacting) and is well suited to preparing vacua and seeds for scattering.

VQE, in contrast, aims for low-depth approximations to the same eigenstates, which is attractive on noisy devices. The two approaches fit together: a good VQE state has decent overlap with the target and can “warm-start” a shorter adiabatic ramp or a more efficient phase-estimation refinement. For ϕ^4 in 1+1 dimensions, a sensible workflow is: VQE to find a variational vacuum, optional short adiabatic refinement along λ , then quantum phase estimation to pin down energies precisely.

VQE ↔ Quantum Machine Learning (QML): the same hybrid pattern

Many near-term QML methods have the same structure as VQE: a parameterized quantum circuit trained by a classical optimizer. The objective changes from an energy to a task loss computed from measurement outcomes on input data. If x_i are data and y_i are labels, a typical setup minimizes

$$\mathcal{L}(\boldsymbol{\theta}) = \frac{1}{N} \sum_{i=1}^N \ell(y_i, \text{measure}[U(\boldsymbol{\theta}) U_{\text{feat}}(x_i) |0\rangle]),$$

with ℓ a standard loss (e.g. cross-entropy or mean-squared error). The same design choices and caveats recur: ansatz expressivity versus trainability, measurement cost and shot allocation, gradient estimation (parameter shift or SPSA), and pitfalls such as barren plateaus. QML adds explicit data-embedding circuits $U_{\text{feat}}(x)$, kernel approaches where the device evaluates inner products without training, and more linear-algebraic algorithms that become particularly powerful in the fault-tolerant regime.

1.1 Quantum Chemistry on Real Hardware: VQE as the Workhorse

Timeline (6 bullets)

- **2014 — First VQE experiment (photonic):** proof-of-principle hybrid VQE estimating a simple molecular energy ($\text{He}-\text{H}^+$).
- **2016 — Superconducting H_2 curve:** head-to-head *VQE (UCC)* vs *Phase Estimation* on a multi-qubit chip; full potential energy curve.
- **2017 — Hardware-efficient VQE (IBM):** shallow, device-native ansatz computes molecules up to BeH_2 (6 qubits, 100+ Pauli terms).
- **2019 — ADAPT-VQE:** adaptive, problem-tailored ansatz that grows operator-by-operator from a pool (chemistry-inspired excitations).
- **2020 — Trapped-ion H_2O :** water ground energy on an ion-trap QPU, approaching chemical accuracy with careful co-design/mitigation.
- **2023–2024 — Scaling & mitigation focus:** improved adaptive ansätze, error-mitigation pipelines, and realistic error targets for advantage.

Why VQE is the “bedrock” for chemistry

- Chemistry Hamiltonians map to sums of Pauli strings; VQE trades long coherent evolution for **short circuits + many measurements**.
- The **hybrid loop** (quantum state prep & expectation estimation + classical optimization/shot allocation/mitigation) matches NISQ realities.
- As hardware improves, VQE scales via better ansätze (UCC variants, ADAPT), embedding/active-space tricks, and mitigation to reach target accuracies.

Reading list

• Foundational demos

- Peruzzo *et al.* (2014): Variational eigenvalue solver on a photonic processor (first VQE chemistry demo; He–H⁺).
- O’Malley *et al.* (2016): H₂ potential curve with *VQE* (UCC) and *Phase Estimation* on superconducting qubits.
- Kandala *et al.* (2017): *Hardware-efficient* VQE on IBM; molecules up to BeH₂ with shallow circuits.
- Nam *et al.* (2020): Trapped-ion VQE for H₂O; co-design and mitigation toward chemical accuracy.

• Methods & advances

- Grimsley *et al.* (2019): *ADAPT-VQE* — adaptive, problem-tailored ansatz construction.
- Follow-ups (2023+): ADAPT-VQE under realistic noise; operator pools, ordering, and convergence behavior.

• Noise, mitigation, outlook

- Recent reviews on error mitigation for chemistry VQE: readout mitigation, randomized compiling, zero-noise extrapolation, symmetry checks.
- Assessments of gate-error targets and resource estimates for quantum advantage in chemistry workflows.

2 The remainder term in the Adiabatic theorem

In the previous lecture, we saw

$$\dot{c}_m(t) + \left(\frac{i}{\hbar} E_m(t) + \langle m(t) | \dot{m}(t) \rangle \right) c_m(t) = \sum_{n \neq m} \frac{\langle m(t) | \dot{H} | n(t) \rangle}{\Delta_{mn}} c_n(t), \quad (2)$$

where $\Delta_{mn} = E_m - E_n$. Write

$$c_m(t) = d_m(t) e^{i\theta_m(t)} e^{i\gamma_m(t)}, \quad (3)$$

where θ_m, γ_m were introduced in the previous lecture. Then eq.(2) becomes

$$\dot{d}_m(t) = \sum_{n \neq m} \frac{\langle m(t) | \dot{H} | n(t) \rangle}{\Delta_{mn}} d_n(t) e^{i(\theta_n(t) - \theta_m(t))} e^{i(\gamma_n(t) - \gamma_m(t))}. \quad (4)$$

Integrating both sides between $0, T$ we have

$$d_m(T) - d_m(0) = \sum_{n \neq m} \int_0^T dt \frac{\langle m(t) | \dot{H} | n(t) \rangle}{\Delta_{mn}} d_n(t) e^{i(\theta_n(t) - \theta_m(t))} e^{i(\gamma_n(t) - \gamma_m(t))} \quad (5)$$

Now let $s = t/T$ and write $H(t) = \tilde{H}(s)$; then $\dot{H} = (1/T) \partial_s \tilde{H}$ and

$$d_m(T) - d_m(0) = \int_0^1 ds \sum_{n \neq m} \frac{\langle m(s) | \partial_s \tilde{H}(s) | n(s) \rangle}{\Delta_{mn}(s)} d_n(s) e^{iT(\theta_n(s) - \theta_m(s))} e^{iT(\gamma_n(s) - \gamma_m(s))}.$$

One can invoke the Riemann-Lebesgue lemma to say that the rhs goes to 0. But without invoking that, let us see how far we can proceed.

Applying the triangle inequality we get

$$|d_m(T) - d_m(0)| \leq \int_0^1 ds \sum_{n \neq m} \left| \frac{\langle m(s) | \partial_s \tilde{H}(s) | n(s) \rangle}{\Delta_{mn}(s)} d_n(s) \right|. \quad (6)$$

Now the maximum value of $|d_n|$ is 1. So replacing on the rhs we have

$$|d_m(T) - d_m(0)| \leq \int_0^1 ds \sum_{n \neq m} \left| \frac{\langle m(s) | \partial_s \tilde{H}(s) | n(s) \rangle}{\Delta_{mn}(s)} \right|. \quad (7)$$

This is the best we can do with these rudimentary tools. The bare minimum requirement from here that must be obeyed is that each term in the summand must be small and that the sum over n converges. Only then, we can claim that $|d_m(T) - d_m(0)| \rightarrow 0$ as needed by the adiabatic approximation to hold.

Conditions which may work for a negligible remainder.

1. **Gap condition:** $\Delta_{\min} > 0$ on $[0, 1]$ (no crossings with the target level).
2. **Smooth slow drive:** $H(t) = \tilde{H}(t/T)$ with bounded $\partial_s \tilde{H}$ are finite.
3. **Small matrix elements:** $\left| \frac{\langle m(s) | \partial_s \tilde{H}(s) | n(s) \rangle}{\Delta_{mn}(s)} \right| \ll 1$ when $s \in [0, 1]$ for all $m \neq n$.

3 Time-ordered evolution in ASP

In an adiabatic ramp we let the Hamiltonian vary smoothly along the parameter $s = t/T \in [0, 1]$. The Schrödinger equation reads

$$i \partial_s |\psi(s)\rangle = T H(s) |\psi(s)\rangle, \quad (8)$$

whose exact solution is the *time-ordered* (parameter-ordered) exponential

$$|\psi(s)\rangle = \mathcal{T} \exp \left(-i T \int_0^s du H(u) \right) |\psi(0)\rangle. \quad (9)$$

Only when $[H(u), H(v)] = 0$ for all u, v can the ordering symbol be dropped and (9) collapse to a single exponential. Thus writing $e^{-iH[s]s}$ is *not* correct in general; at best it is a mnemonic for the piecewise-constant approximation described next.

Product formula (what we actually implement). Discretize the ramp into M slices of width $\Delta s = 1/M$ (so $\Delta t = T/M$), pick $s_k = (k - \frac{1}{2})\Delta s$, and freeze the Hamiltonian on each slice:

$$U_k \equiv \exp(-i\Delta t H(s_k)), \quad U(1) \approx U_M U_{M-1} \cdots U_1. \quad (10)$$

As $\Delta t \rightarrow 0$ this ordered product converges to (9). The leading corrections are governed by commutators $[H(s), H(s')]$; in the Magnus/Dyson expansion the first nontrivial term is $\Omega_2 = -\frac{T^2}{2} \int_0^s \int_0^u du dv [H(u), H(v)]$.

Within each slice: Strang splitting. Writing $H(s) = H_{\text{on}}(s) + H_{\text{bond}}(s)$ we approximate U_k by the symmetric (second-order) Trotter step

$$U_k = e^{-i\frac{\Delta t}{2}H_{\text{on}}(s_k)} e^{-i\Delta t H_{\text{bond}}(s_k)} e^{-i\frac{\Delta t}{2}H_{\text{on}}(s_k)} + O(\Delta t^3), \quad (11)$$

which yields a *global* error $O(\Delta t^2)$ over the full ramp when $H(s)$ is smooth and commutators are bounded. This is precisely the “half onsite / full bond” update used in the notebook.

4 Adiabatic state preparation (ASP) and the counterterm idea

Adiabatic path. Pick a smooth schedule $s \in [0, 1]$ and evolve with

$$H(s) = H_0 + \lambda(s) x^4 + \frac{1}{2} \delta m^2(s) x^2. \quad (12)$$

During the *turn-on* of λ , the quartic term induces an effective quadratic shift. A simple way to *hold the gap roughly fixed* while dressing is to add a quadratic counterterm $\delta m^2(s) \approx -12 \lambda(s) \langle x^2 \rangle_0$; for $\omega=1$, $\langle x^2 \rangle_0 = \frac{1}{2}$, so $\delta m^2(s) \approx -6 \lambda(s)$.

Two-stage schedule (bare target). If your target Hamiltonian is the *bare* $H_\lambda = H_0 + \lambda x^4$, do this:

1. Stage 1 ($s \in [0, 1]$): turn on λ and the counterterm together (keeps the gap flat).
2. Stage 2 ($s \in [1, 2]$): hold λ fixed and ramp the counterterm back to *zero*, so the final Hamiltonian is exactly H_λ .

This is what our Mathematica cell below implements.

Midpoint/Strang slicing. Discretize total time T into N slices of length Δt and approximate the time-ordered exponential by a product of short propagators $e^{-iH(s_j)\Delta t}$ evaluated at midpoints s_j . This gives second-order accuracy in Δt .

4.1 Mathematica cell (drop-in) and explanations

The cell builds x , H_0 , x^4 , the two-stage schedules, and the time-ordered unitary. Variables avoid underscores; underscores only appear in function *patterns* (Mathematica syntax).

```
ClearAll["Global`*"];
```

```
(* --- Model: 4-level H0 + anharmonic x^4 --- *)
\[Lambda] = 0.10;
```

```
x = 1/Sqrt[2] {{0, 1, 0, 0},
```

```

{1, 0, Sqrt[2], 0},
{0, Sqrt[2], 0, Sqrt[3]},
{0, 0, Sqrt[3], 0};

H0 = DiagonalMatrix[{0,1,2,3}] + 1/2 IdentityMatrix[4];
V4 = x.x.x.x;

(* Final interacting Hamiltonian and exact eigenpairs for checking *)
Hlam = N[ H0 + \[Lambda] V4 ];
{evalF, evecF} = Eigensystem[Hlam];
ordF = Ordering[evalF];
E0f = evalF[[ordF[[1]]]]; v0f = evecF[[ordF[[1]]]];
E1f = evalF[[ordF[[2]]]]; v1f = evecF[[ordF[[2]]]];

(* --- Two-stage schedules: on; then counterterm off --- *)
r[s_] := 3 s^2 - 2 s^3; (* smooth 01 with zero slopes *)
lam0f[u_] := Piecewise[{{
  \[Lambda], r[u], 0 <= u <= 1},
  {\[Lambda], 1 < u <= 2}
}];
dm20f[u_] := Piecewise[{{
  {-6 \[Lambda], r[u], 0 <= u <= 1}, (* turn CT on *)
  {-6 \[Lambda], (1 - r[u - 1]), 1 < u <= 2} (* ramp CT to 0 *)
}};

(* Build the slice Hamiltonian at parameter u (u in [0,2]) *)
Hslice[u_, useCT_:True] := N[ H0 + lam0f[u] V4 +
  If[useCT, 1/2 dm20f[u] (x.x), ConstantArray[0.,{4,4}]] ];

(* Time-ordered unitary via midpoint rule over both stages *)
tPrep = 25.0; nSteps = 250; (* total time; steps per stage *)
UAdiabaticBare[useCT_:True] := Module[{U = IdentityMatrix[4], dt, u},
  dt = tPrep/(2 nSteps);
  Do[
    u = (j - 0.5)/nSteps; (* u runs through (0,2) midpoints *)
    U = MatrixExp[-I Hslice[u, useCT] dt] . U
  , {j, 1, 2 nSteps}];
  U
];

(* Prepare |E0> and |E1> by evolving |0> and |1> *)
{eval0, evec0} = Eigensystem[N[H0]]; ord0 = Ordering[eval0];
g0 = evec0[[ord0[[1]]]]; g1 = evec0[[ord0[[2]]]]; (* free |0>, |1> *)

Uct = UAdiabaticBare[True];
Unct = UAdiabaticBare[False];

psi0 = Normalize[Uct . g0]; psi1 = Normalize[Uct . g1];

F0 = Abs[Conjugate[v0f].psi0]^2; F1 = Abs[Conjugate[v1f].psi1]^2;
Grid[{{"fidelity |<E0|>|^2", NumberForm[F0,{4,3}]},
 {"fidelity |<E1|>|^2", NumberForm[F1,{4,3}]}} , Frame->All]

```

Line-by-line logic.

- $r[s_]$ is a smooth ramp $0 \rightarrow 1$ with zero slope at endpoints.
- $\text{lam0f}[u_]$ turns λ on in $u \in [0, 1]$ and holds it fixed for $u \in [1, 2]$.

- `dm20f[u_]` turns the counterterm on during $[0, 1]$ and ramps it back to *zero* during $[1, 2]$. Thus the final Hamiltonian is exactly H_λ .
- `Hslice[u_,useCT_:True]` builds the numeric 4×4 matrix for a slice. No underscores are used in variable names (only in patterns).
- The **midpoint** product `MatrixExp[-I Hslice dt]` produces a second-order accurate time-ordered unitary; within each slice the exponential is exact (no Trotter error).

4.2 What the adiabatic theorem buys you

Start in an eigenstate of H_0 (even/odd parity). If the gap to the nearest unwanted level stays open and the ramp is slow enough, the evolved state tracks the instantaneous eigenstate and ends at $|E_n(\lambda)\rangle$ up to a global phase. The counterterm keeps the *gap* and dispersion flatter during the turn-on, reducing diabatic error at fixed runtime.

5 How to implement ASP on Qiskit (algorithm sketch, no code)

We describe how to turn the Mathematica ASP into a hardware-friendly 2-qubit routine.

1) Map the model to qubits. Use the 4-level HO truncation with computational basis $\{|00\rangle, |01\rangle, |10\rangle, |11\rangle\}$ identified with levels 0, 1, 2, 3. The operator x is the standard truncated ladder combination; build H_0 and $V_4 = x^4$ as 4×4 matrices.

2) Choose a two-stage schedule. As above: turn on λ and the counterterm together, then ramp the counterterm to zero while holding λ fixed, so the final Hamiltonian is H_λ . Discretize total time T into $2N$ slices.

3) Per-slice compilation (two options).

1. *Exact per-slice exponential (opaque unitary).* For education/simulation, exponentiate each numeric 4×4 slice $H(u_j)$ via eigendecomposition and append the resulting unitary on two qubits. (Great for sanity checks; not hardware-native.)
2. *Pauli decomposition + product formula.* Expand $H(u_j) = \sum_\alpha c_\alpha(u_j) P_\alpha$ with $P_\alpha \in \{I, X, Y, Z\}^{\otimes 2}$, then implement a first/second-order Trotter step $e^{-iH\Delta t} \approx \prod_\alpha e^{-ic_\alpha \Delta t P_\alpha}$ with standard two-qubit patterns for $e^{-i\theta \sigma_a \otimes \sigma_b}$. This is hardware-native and what scales to larger registers.

4) Prepare the starting state. For $|E_0\rangle$, start in $|00\rangle$. For $|E_1\rangle$, apply X on the least significant qubit to prepare $|01\rangle$.

5) Apply the adiabatic unitary. Loop over slices $j = 1, \dots, 2N$ and apply the short-time unitary for each $H(u_j)$ using your chosen compilation. Time ordering is achieved by left-multiplying the most recent slice.

6) Verify preparation. On a simulator: compute the overlap with exact eigenvectors of H_λ . On hardware: measure a simple *eigen-residual* $\|H_\lambda |\psi\rangle - E |\psi\rangle\|$ via linear-combination-of-unitaries (LCU) tricks or compare short-time phases under $e^{-iH_\lambda dt}$. In practice, preparing $|E_0\rangle$ is easier (large gap, parity).

Notes on depth and noise. Second-order product formulas keep depth modest. If you want to reduce depth further, you can replace each slice by a shallow brickwall variational unitary trained to match $e^{-iH\Delta t}$ only on the *states of interest*; this trades exactness for robustness—useful on NISQ devices.

6 Nine mini-labs you can run next

Once $|E_0\rangle$ and $|E_1\rangle$ are available, here are nine JLP-flavored exercises:

1. **Iterative phase estimation** (IPEA) on $|E_0\rangle, |E_1\rangle$.
2. **Form factor** $\langle E_0 | x | E_1 \rangle$ via a Hadamard test.
3. **Spectral function** $A_x(\omega)$ from $C_{xx}(t)$ (Hann window + FFT).
4. **Loschmidt echo** $\mathcal{L}(t) = |\langle \psi | U_{\text{exact}}^\dagger U_{\text{approx}} | \psi \rangle|^2$.
5. **Berry phase** by cycling parameters (e.g. a loop in (λ, ω)).
6. **Fidelity susceptibility** χ_F from overlaps at λ and $\lambda + \epsilon$.
7. **Collapse and revival** under Kerr nonlinearity (monitor $\langle x(t) \rangle$).
8. **OTOC** $C(t) = \langle [x(t), p(0)]^\dagger [x(t), p(0)] \rangle$.
9. **Compile-vs-variational showdown**: Strang vs exact vs learned shallow step.

7 Adiabatic eigenstate preparation on a JLP position grid (uniform schedule)

Goal. Prepare the lowest eigenstates of

$$H(\lambda) = \frac{1}{2} \Pi^2 + \frac{1}{2} \Phi^2 + \lambda \Phi^4$$

directly in the JLP position encoding, using a *uniform* time schedule. This is the exact machinery we will reuse in 1+1D ϕ^4 .

Discrete setup and the only symmetry you must check

Choose $N = 2^{n_q}$ grid points with half-width ϕ_{\max} . We recommend the *midpoint grid*

$$\phi_j = -\phi_{\max} + \left(j + \frac{1}{2}\right) \Delta\phi, \quad \Delta\phi = \frac{2\phi_{\max}}{N}, \quad j = 0, \dots, N-1,$$

so the computational basis $|j\rangle$ coincides with $|\phi_j\rangle$. Define

$$\Phi = \text{diag}(\phi_0, \dots, \phi_{N-1}), \quad \Pi^2 = F^\dagger \text{diag}(p_0^2, \dots, p_{N-1}^2) F,$$

where F is the local n_q -qubit QFT and $p_m = \frac{2\pi}{2\phi_{\max}} m$ in the usual symmetric ordering. Then $H_0 = \frac{1}{2}\Pi^2 + \frac{1}{2}\Phi^2$ and $H(\lambda) = H_0 + \lambda\Phi^4$.

Parity (do this once). On the midpoint grid, discrete parity is

$$P_{\text{mid}} |j\rangle = |N-1-j\rangle.$$

With the spectral kinetic defined above, $[H(s), P_{\text{mid}}] = 0$ (to machine precision) for all paths we use; parity is exactly conserved.¹

Path and *uniform* time schedule

We prepare SHO first (S0a), then (optionally) turn on the quartic (S1/S2). The schedule is uniform; no gap sampling.

1. **S0a** (SHO builder) Turn on kinetic only:

$$H_{\text{S0a}}(s) = \frac{1}{2} \Phi^2 + r(s) \frac{1}{2} \Pi^2, \quad r(s) = 3s^2 - 2s^3, \quad s \in [0, 1].$$

2. **S1** (λ on; optional CT)

$$H_{\text{S1}}(s) = H_0 + \lambda r(s) \Phi^4 + \frac{1}{2} \delta m^2(s) \Phi^2,$$

with a simple counterterm $\delta m^2(s) \approx \alpha \lambda r(s)$ (tadpole-motivated, $\alpha \sim -6$ for $\omega=1$) to keep the gap stable *if* you want to be aggressive with runtime.

3. **S2** (set the target)

$$H_{\text{S2}}(s) = H_0 + \lambda \Phi^4 + \frac{1}{2} \delta m^2(1-r(s)) \Phi^2.$$

For the *bare* target end with $\delta m^2 \rightarrow 0$; for the *normal-ordered* target, keep it.

Uniform schedule (what we actually implement). Pick total time T and slice count n . Use a midpoint product with *uniform* nodes

$$s_j = \frac{j - \frac{1}{2}}{n}, \quad \Delta t = \frac{T}{n}, \quad U(T) \approx \prod_{j=1}^n \exp[-i H(s_j) \Delta t].$$

For S0a, this uniform scheme already gives $F \approx 1$ on small grids (e.g. $N = 4-8$) with moderate T ; no “adaptive” bells and whistles are required.

One Strang slice (what the circuit actually does)

For any slice parameter u and step Δt :

$$e^{-iH(u)\Delta t} \approx e^{-iV(\Phi;u)\frac{\Delta t}{2}} \underbrace{F^\dagger e^{-i\frac{1}{2}P^2\Delta t} F}_{\text{local QFT block}} e^{-iV(\Phi;u)\frac{\Delta t}{2}}, \quad V(\Phi;u) \in \{\frac{1}{2}\Phi^2, \lambda\Phi^4, \frac{1}{2}\delta m^2(u)\Phi^2\}.$$

Only primitives you’ll reuse in ϕ^4 : *position-diagonal* phase banks, local QFTs, and diagonal momentum phases.

¹If you instead use the edge-inclusive grid $\phi_j = -\phi_{\max} + j\Delta\phi$, either swap Π^2 for the periodic finite-difference Laplacian (circulant second derivative), or change P to the wrap map $j \mapsto (-j) \bmod N$. The point is: pick a kinetic and parity that commute on your discrete space.

Starters (even/odd) and what to expect

Because parity is conserved, choose

$$\text{even: } \frac{|j_\star\rangle + |N-1-j_\star\rangle}{\sqrt{2}}, \quad \text{odd: } \frac{|j_\star\rangle - |N-1-j_\star\rangle}{\sqrt{2}},$$

where j_\star is the bin nearest $\phi = 0$. Under S0a with a uniform schedule, these flow into $|E_0\rangle$ and $|E_1\rangle$ of H_0 with high fidelity for modest T (we verified this numerically in Mathematica).

Errors (short)

Adiabatic error scales like $\varepsilon_{\text{ad}} \sim \max_s \|\partial_s H\|/(T \Delta(s)^2)$; Strang error is $O(\Delta t^2)$. On our small grids and gentle S-curve, a uniform schedule with a few hundred slices is enough to reach $F \approx 1$. Adaptive pacing is an *optional* optimization for larger N , tighter T , or strong λ .

Mathematica code for both methods of state preparation (oscillator basis and field basis) will be shared. QISKit demo will be given on Friday.

We will start discussing ϕ^4 theory as well (lecture 19 in the list of lectures).

References

- [1] J. J. Sakurai and J. Napolitano, *Modern Quantum Mechanics*, 2nd or 3rd ed., Addison–Wesley / Cambridge Univ. Press.
- [2] *Adiabatic theorem* (Wikipedia), https://en.wikipedia.org/wiki/Adiabatic_theorem.

ϕ^4 theory in 1+1 Dimensions

LECTURE NOTES

1 From many anharmonic oscillators to scalar ϕ^4

Motivation. We just mastered the single-site anharmonic oscillator (AHO). The natural next step is a *lattice of AHOs*. If we simply stack N copies, nothing talks to anything: $H = \sum_j H_{\text{AHO}}(\phi_j, \pi_j)$. To make physics, we couple neighbors. The simplest choice is a bilinear spring:

$$H = \sum_{j=1}^N \left[\frac{1}{2} \pi_j^2 + V(\phi_j) \right] + \frac{\kappa}{2} \sum_{j=1}^N (\phi_{j+1} - \phi_j)^2, \quad V(\phi) = \frac{1}{2} \mu_0^2 \phi^2 + g_0 \phi^4.$$

Cartoon: a chain of AHOs (sites) joined by springs (the gradient term).

1.1 Continuum limit: why this *is* scalar ϕ^4

In order to get the continuum limit we write $x_j = ja$ and map

$$\phi_j \rightarrow \sqrt{a}\phi(x_j), \quad \pi_j \rightarrow \sqrt{a}\pi(x_j), \quad \sum_j \rightarrow \frac{1}{a} \int dx, \quad (1)$$

which ensure that

$$[\phi_j, \pi_k] = \delta_{jk} \longrightarrow [\phi(x_j), \pi(x_k)] = i\delta(x_j - x_k). \quad (2)$$

This leads to

$$\sum_{j=1}^N \left[\frac{1}{2} \pi_j^2 + V(\phi_j) \right] \longrightarrow \int dx \left[\frac{1}{2} \pi^2 + \frac{1}{2} \mu_0^2 \phi^2 + g_0 a \phi^4 \right]. \quad (3)$$

Finally, $\phi_{j+1} - \phi_j = a \partial_x \sqrt{a}\phi + \frac{a^2}{2} \partial_x^2 \sqrt{a}\phi + \dots$. Then

$$\sum_j (\phi_{j+1} - \phi_j)^2 \rightarrow a^2 \int dx (\partial_x \phi)^2 + \mathcal{O}(a^3).$$

After parameter redefinitions $g_0 a \mapsto g$, $\kappa a^2 \mapsto v^2$, the leading continuum Hamiltonian density is

$$\mathcal{H} = \frac{1}{2} \pi^2 + \frac{v^2}{2} (\partial_x \phi)^2 + \frac{1}{2} \mu_0^2 \phi^2 + g \phi^4 + \underbrace{c_4 (\partial_x^2 \phi)^2 + \dots}_{\text{irrelevant in 1+1D}}.$$

A quick clarification on nomenclature. The Hamiltonian density has units of ML^{-1} . In natural units where $c = 1, \hbar = 1$, this is just M^2 . ∂_x has dimensions of M . Thus, ϕ is dimensionless if κ is dimensionless and μ_0 has dimensions of mass. This means g has dimensions of M^2 while c_4 has dimensions of M^{-2} . Operators in the Hamiltonian which have negative mass dimensions are called “irrelevant” as their importance diminishes at low energies. Conversely, operators with positive mass dimensions are called “relevant” and zero mass dimensions are called “marginal.”

Message: a chain of AHOs with the simplest spring becomes ϕ^4 plus higher-derivative corrections; the latter are irrelevant at long distances, so the infrared theory is the familiar scalar ϕ^4 .

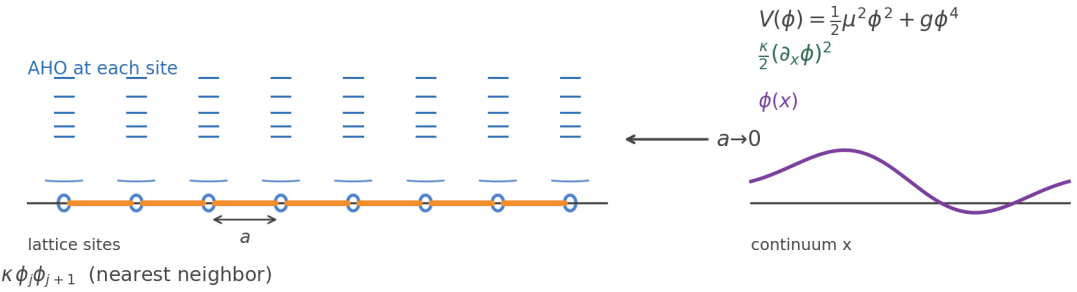


Figure 1: From a lattice of AHOs with nearest–neighbor coupling $\kappa\phi_j\phi_{j+1}$ and spacing a to the continuum field $\phi(x)$ with gradient energy $\frac{v^2}{2}(\partial_x\phi)^2$ and onsite potential $V(\phi) = \frac{1}{2}\mu^2\phi^2 + g\phi^4$.

AHO → field. One AHO \Rightarrow one normal mode. Many AHOs + springs \Rightarrow a band of modes that in the long-wavelength limit look like a continuum field with gradient energy. The onsite quartic becomes the field interaction $g\phi^4$.

2 Adiabatic preparation on the AHO lattice: correlations and entanglement

Aim. Before discussing renormalization and counterterms, it is useful to see a concrete application in which nontrivial field-theoretic structure emerges from the AHO lattice in a controlled way. The adiabatic state preparation (ASP) protocol does exactly this: starting from the strictly solvable product ground state at zero coupling, it turns on the nearest–neighbor interaction slowly and lets correlations and entanglement build up.

Model and conventions. We keep the lattice Hamiltonian introduced above, now viewed as a one–parameter family:

$$H(\kappa) = \sum_{j=1}^N \left[\frac{1}{2} \pi_j^2 + V(\phi_j) \right] + \frac{\kappa}{2} \sum_{j=1}^{N-1} (\phi_{j+1} - \phi_j)^2, \quad V(\phi) = \frac{1}{2} \mu_0^2 \phi^2 + g_0 \phi^4. \quad (4)$$

At $\kappa = 0$ the ground state is the direct product of single–site AHO ground states, exactly known and easy to prepare. Throughout, μ_0^2 denotes the coefficient of the quadratic term (so the code variable `mu0` corresponds to μ_0^2), and g_0 is the onsite quartic strength. No continuum limit or field redefinitions are invoked in this section.

Adiabatic path and schedule. ASP varies the coupling as $\kappa : 0 \rightarrow \kappa_f$ over a total time T , for example by setting $H(t) = H(\kappa(s))$ with $s = t/T \in [0, 1]$. A smooth schedule with endpoint flattening,

$$\dot{\kappa}(0) = \dot{\kappa}(1) = 0,$$

suppresses boundary terms in the adiabatic remainder (see the “adiabatic remainder” subsection for the $1/T$ vs. $1/T^2$ scaling). For any finite chain the many–body gap never strictly closes; nonetheless, near critical regimes larger T is needed to keep diabatic errors small.

What to measure along the ramp. The cleanest, renormalization-free witness here is the half-chain entanglement entropy,

$$S_{1/2}(\kappa) = -\text{Tr } \rho_{[1..N/2]}(\kappa) \ln \rho_{[1..N/2]}(\kappa), \quad (5)$$

which is exactly zero at $\kappa = 0$ (product state), then rises as correlations spread, and saturates once the correlation length is shorter than the system size (area law away from criticality). In the accompanying notebook, $S_{1/2}(\kappa)$ is computed with a minimal matrix-product-state (MPS) implementation; a brief MPS primer and the exact algorithmic steps are summarized in Appendix A to maintain continuity here.

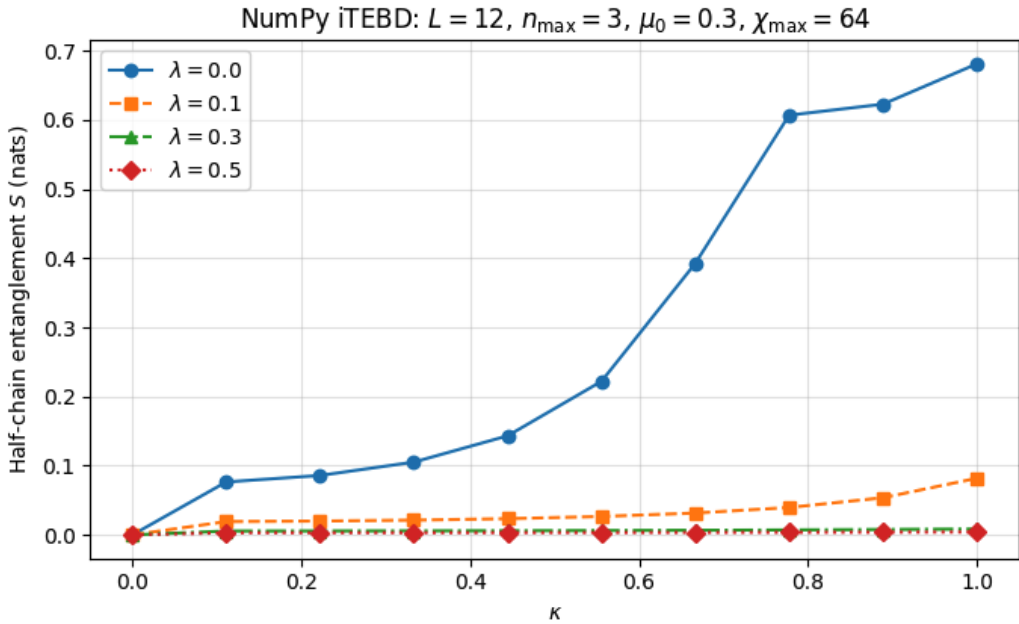


Figure 2: Half-chain EE vs κ .

What to expect (AHO continuity). For small κ , the first nontrivial physics is inherited from a single AHO matrix element: the dipole $f_1 = \langle 1|\phi|0\rangle_{\text{AHO}}$. The one-particle hopping scale is proportional to $\kappa |f_1|^2$, so softening the onsite problem (smaller μ_0^2 or, at fixed μ_0^2 , smaller effective AHO gap) enhances the growth of $S_{1/2}$, while increasing g_0 at fixed κ typically suppresses it by enlarging single-site gaps and shrinking f_1 . Thus the κ -ramp provides a direct, nonperturbative bridge from “many decoupled AHOs” to an interacting many-body ground state with extended correlations, without invoking any continuum language. The figure below validates this intuition. For smallish κ , larger λ ’s give smaller entanglement since the entanglement does not spread as much across the chain.

Now at this point, one could dive into the continuum limit and start discussing renormalization. However, we will stick to the lattice for now.

3 Physical parameters

How do we define the physical mass of a particle by considering the lattice perspective? In the relativistic limit we have the relation

$$E^2 = p^2 + m^2. \quad (6)$$

This is what we will leverage. First we need to introduce momentum on the lattice. This is easily done by doing a discrete Fourier transform:

$$\phi_j = \frac{1}{\sqrt{N}} \sum_q e^{iqja} \varphi_q, \quad q = \frac{2\pi}{Na} n, \quad n = 0, \dots, N-1. \quad (7)$$

Using

$$\sum_{j=1}^N e^{i(q+q')a} = N \delta_{q+q',0}, \quad (8)$$

and introducing the notation $|b_q|^2 = b_q b_{-q}$, we find that the quadratic part of the Hamiltonian can be written as:

$$H_2 = \frac{1}{2} \sum_q \left(|\pi_q|^2 + \omega_q^2 |\varphi_q|^2 \right), \quad \omega_q^2 = \mu_0^2 + 2\kappa(1 - \cos qa).$$

Notice from here that in the $a \rightarrow 0$ limit,

$$\omega_q^2 \rightarrow \mu_0^2 + \underbrace{(\kappa a^2)}_{v^2} q^2,$$

which is the relativistic form we expect in the continuum. Let us define E_0 to be the ground-state energy (with λ turned on) and $E_1(p)$ be the energy of the lowest odd Z_2 excitation at momentum p . Then we should define the physical mass m_{phys} as:

$$m_{phys} = E_1(p=0) - E_0. \quad (9)$$

A consistency check is that for low values of p , we should have $E_1(p) - E_0 \approx \sqrt{m_{phys}^2 + p^2}$. Now notice that in introducing a momentum, we were forced to introduce the lattice spacing into the story. The total length of the space that we are considering is $L = Na$. The correlation length between excitations on dimensional grounds goes like $1/m_{phys}$. We need $L \gg 1/m_{phys}$. This needs to be ensured for consistency. We know how to use the adiabatic theorem to get the true ground state with $\lambda \neq 0$ for the AHO. For the ϕ^4 case, we adopt the same route. We initiate all j -sites to be in the ground state and then use ASP.

3.1 One particle state

In a free scalar quantum field theory, we define a 1-particle state at momentum p to be

$$|p\rangle = a_p^\dagger |0\rangle. \quad (10)$$

Now

$$a_p^\dagger = \frac{1}{\sqrt{N}} \sum_{j=1}^N e^{ipx_j} a_j^\dagger, \quad (11)$$

which gives

$$|p\rangle = \frac{1}{\sqrt{N}} \sum_{j=1}^N e^{ipx_j} a_j^\dagger |0\rangle = \frac{1}{\sqrt{N}} \sum_{j=1}^N e^{ipx_j} |0 \cdots \underbrace{1}_{j'th} \cdots 0\rangle, \quad (12)$$

where in the $j'th$ term, j 'th lattice site is in the first excited state and all the other sites are in the ground state. Hence, in the free theory, the single particle state is a linear superposition in the position basis as exhibited above. Now that we have the single particle state in the free theory, we can use our friend the adiabatic theorem to perform ASP and get the true single particle state in the interacting theory.

3.2 Bare parameters vs physical parameters

On the lattice we started off with the following parameters:

$$N, \mu_0, \lambda, \kappa. \quad (13)$$

For convenience let's set $\kappa = 1$, to admit a relativistic continuum limit. We introduced the lattice spacing by considering the DFT. We have a box of size $L = Na$. Let's keep the size of the box fixed by fixing N, a . Then we are left with the “bare” parameters μ_0, λ . In the discussion above we introduced the physical mass m_{phys} in terms of $E_1(0), E_0$ which are μ_0, λ dependent. It makes ample physical sense to say that we are given a particular m_{phys} and we want to run our simulations for this value. This gives us 1 condition for 2 bare parameters μ_0, λ . We can specify another physical condition by giving the value of the 2-2 scattering amplitude at some centre-of-mass momentum p_0 . Using these to specifications, we can tune μ_0, λ for our choice of N, a . Then we can rerun for different a 's to approach the continuum limit.

3.3 What if the coupling is *not* just nearest neighbor?

Write the most general finite-range, translation-invariant quadratic form

$$H_{nn} = \frac{1}{2} \sum_{r=1}^R \eta_r \sum_j (\phi_{j+r} - \phi_j)^2, \quad \eta_r \geq 0.$$

Fourier transforming gives a lattice “Laplacian” $\omega^2(k) = \mu^2 + 4 \sum_r \eta_r \sin^2(\frac{rk}{2})$.

- **Same universality (generic case).** If η_r are short-ranged and positive, the small- k expansion is

$$\omega^2(k) = \mu^2 + v^2 k^2 + \alpha_4 k^4 + \dots,$$

so the continuum limit is the *same* ϕ^4 up to irrelevant $(\partial_x^2 \phi)^2$ terms and a rescaled v . Emergent Lorentz symmetry (linear dispersion) appears once you tune to the critical line ($\mu^2 \rightarrow \mu_c^2$).

3.4 Lifshitz theories

Consider adding a next to nearest neighbor coupling:

$$\frac{\kappa}{2} (\phi_{j+1} - \phi_j)^2 + \frac{\tilde{\kappa}}{2} (\phi_{j+2} - \phi_j)^2. \quad (14)$$

In the continuum limit this leads to

$$\left[\frac{\kappa}{2} (a \partial_x \phi(x) + \frac{a^2}{2} \partial_x^2 \phi(x))^2 + \frac{\tilde{\kappa}}{2} (2a \partial_x \phi(x) + 2a^2 \partial_x^2 \phi(x))^2 \right] \Big|_{x=x_j} \quad (15)$$

Expanding and dropping the total derivatives $\partial_x \phi \partial_x^2 \phi = 1/2 \partial_x (\partial_x \phi \partial_x \phi)$, and using $\partial_x \phi \partial_x^3 \phi = \partial_x (\partial_x \phi \partial_x^2 \phi) - (\partial_x^2 \phi)^2$ we can choose:

$$\tilde{\kappa} = -\frac{1}{4} \kappa, \quad (16)$$

to be left with $(\partial_x^2 \phi)^2$ as the leading term. This is the Lifshitz Hamiltonian as the dispersion relation will correspond to $E \sim k^2$.

4 The $g_0 \gg 1$ case

What happens when $g_0 \gg 1$? Is there another way to set up the problem more efficiently? This question was briefly addressed in [1].

We start with our usual lattice Hamiltonian and do the following rescaling: $\phi_j \rightarrow g_0^{-1/6} \phi_j$, $\pi_j \rightarrow g_0^{1/6} \pi_j$ we get

$$g_0^{1/3} H = \sum_j \left[\frac{1}{2} \pi_j^2 + \phi_j^4 \right] + \frac{\kappa}{g_0^{2/3}} \left[\frac{1}{2} (\phi_{j+1} - \phi_j)^2 \right] \quad (17)$$

With this rescaling, we have reorganized the perturbative expansion in a non-standard way, where we can now treat the quadratic term as the perturbation. Even when we simulate on a quantum computer, we can do ASP in this manner as the first part of the Hamiltonian we can handle using approximate techniques.

A key point to note is that the perturbation is now on the gradient term which was responsible for generating entanglement across the chain. The first piece is a local piece. As such in the limit $g_0 \gg 1$, we have the situation where there is no entanglement! Let $\{|n\rangle\}_{n \geq 0}$ be the single-site AHO eigenstates of $h_{\text{AHO}} = \frac{1}{2} p^2 + \frac{1}{2} m_0^2 x^2 + g x^4$ with energies ε_n . We use tensor products $\bigotimes_j |n_j\rangle$ as our unperturbed basis.

What small- κ gives you

(1) One-particle band from AHO data only. Create a single local excitation $|1\rangle$ on site j in the AHO ground-state sea:

$$|j\rangle = \bigotimes_{\ell \neq j} |0\rangle_\ell \otimes |1\rangle_j.$$

Since ϕ is odd, $\langle 1|\phi|0\rangle \equiv f_1 \neq 0$ while $\langle 0|\phi|0\rangle = 0$. To first order in κ the bond $\phi_j \phi_{j+1}$ hops this excitation by one site; in momentum space

$$|k\rangle = \frac{1}{\sqrt{N}} \sum_j e^{ikja} |j\rangle, \quad E_1(k) = \varepsilon_1 - 2t \cos(ka) + O(\kappa^2),$$

with a hopping amplitude

$$t = \frac{\kappa}{a^2} |f_1|^2, \quad f_1 = \langle 1|\phi|0\rangle_{\text{AHO}}.$$

(2) Ground-state energy density (benchmarkable). Second-order perturbation theory lowers the extensive ground-state energy by virtual odd-parity excitations on neighboring sites:

$$\frac{E_0}{N} = \varepsilon_0 - \frac{\kappa^2}{a^4} \sum_{n \text{ odd}} \frac{|f_n|^4}{\Delta_n} + O(\kappa^3), \quad f_n = \langle n|\phi|0\rangle, \quad \Delta_n = \varepsilon_n - \varepsilon_0.$$

This depends only on *single-site* spectra and overlaps. It's a clean, reproducible target for numerics and for QC validation.

5 Elastic two-particle scattering in 1+1 dimensions

We work in the symmetric phase of the scalar theory, where the physical one-particle excitation has mass m . The single-particle dispersion at small momentum is well-described by $E(k) = \sqrt{m^2 + k^2}$, which we regard as a calibration: it defines what we mean by a particle and fixes the conversion between total energy and relative momentum for the two-body problem. Throughout this section we restrict attention to the elastic window $2m < E_{\text{tot}} < 4m$, so that two incoming particles remain two outgoing particles. In 1+1 dimensions there is no scattering angle; elastic two-body scattering depends on a single invariant, which can be taken as the relative momentum k in the center-of-mass (COM) frame where the incoming four-momenta are $(E_k, \pm k)$ with $E_k = \sqrt{m^2 + k^2}$.

A conceptually clean way to define the scattering information is through the phase shift $\delta(k)$. Intuitively, one may think in the relative coordinate x as follows: far from the short-range interaction region the exact two-body wave is a superposition of free plane waves, and the effect of the interaction is to imprint a phase on that wave. In practice, rather than reading this phase from asymptotic real-line scattering, it is more robust to place the system on a ring of length L and study its energy spectrum. The finite-volume energies then encode the same phase $\delta(k)$ through a simple quantization condition that we now derive carefully.

Consider two identical scalar particles on a periodic line of length L . In the COM frame their relative motion is described by a single coordinate x with periodic boundary conditions. Far from the interaction region the relative wave solves the free Helmholtz equation and hence is a linear combination of $e^{\pm ikx}$. Matching the wave across the short-range region amounts to saying that the outgoing wave has the same magnitude as the incoming wave (elastic unitarity) but acquires a phase $2\delta(k)$ when it has passed through the interaction zone and traversed the ring. Explicitly, we have the general asymptotic solution:

$$\psi(x) = e^{-ikx} \pm S(k)e^{ikx}, \quad S(k) = e^{2i\delta_{\pm}(k)}. \quad (18)$$

We put the box as $x \in [-L/2, L/2]$ so that when $L \gg 1$ we have x running from $-\infty$ to $+\infty$. Then putting a hard wall at $x = L/2$ gives for the upper sign:

$$\psi(L/2) = 0 \implies 1 + e^{2i\delta_+(k) + ikL} = 0 \implies 2\delta_+(k) + kL = (2n + 1)\pi. \quad (19)$$

We get a similar condition for the lower sign with $2n\pi$ on the rhs. We can write the combined condition in the schematic manner:

$$kL + 2\delta(k) = \pi n, \quad n \in \mathbb{Z}. \quad (20)$$

This equation is the 1+1D analogue of Lüscher's relation and it encapsulates all elastic scattering information in a single function $\delta(k)$. Operationally, one computes the two-particle energies $E_n(L)$ on a ring, converts each energy to a relative momentum via $E_n(L) = 2\sqrt{m^2 + k_n^2}$, and then solves (20) for $\delta(k_n)$. Repeating this for several n or several volumes produces $\delta(k)$ on a grid of momenta. The same relation also makes the appearance of two-body bound states transparent: a level that approaches a value below $2m$ as $L \rightarrow \infty$ corresponds to a pole of the scattering amplitude on the imaginary- k axis and is accompanied by a jump of $\delta(k)$ by π as k passes through threshold, in accordance with the one-dimensional version of Levinson's theorem.

While the phase shift is the most compact language, it is often helpful to keep the equivalent plane-wave picture in mind. For an incoming relative plane wave from the left, the exact solution has the asymptotics

$$\psi(x \rightarrow -\infty) = e^{ikx} + r(k) e^{-ikx}, \quad \psi(x \rightarrow +\infty) = t(k) e^{ikx},$$

where $t(k)$ and $r(k)$ are the transmission and reflection amplitudes. Elastic unitarity is simply $|t(k)|^2 + |r(k)|^2 = 1$. For a parity-symmetric short-range interaction these amplitudes are determined by a single phase; one convenient parametrization is

$$t(k) = e^{i\delta(k)} \cos \delta(k), \quad r(k) = i e^{i\delta(k)} \sin \delta(k),$$

which makes $|t|^2 + |r|^2 = 1$ manifest and exhibits the direct correspondence between the finite-volume phase $\delta(k)$ in (20) and real-line scattering. If one prefers to work with an on-shell contact amplitude $T(k)$ for the relative motion, the mapping is equally simple:

$$T(k) = -2k \tan \delta(k), \quad t(k) = \frac{1}{1 + \frac{i}{2k} T(k)}, \quad r(k) = \frac{-\frac{i}{2k} T(k)}{1 + \frac{i}{2k} T(k)}. \quad (21)$$

These identities are purely kinematical; no perturbative expansion is assumed. They are useful because different non-perturbative routes naturally give access to different objects: finite-volume spectra give $\delta(k)$ via (20), while real-time wave-packet experiments directly yield $|t(k)|^2$ and $|r(k)|^2$. When both are available, one can extract $\delta(k)$ from either route and check consistency.

It is instructive to comment on the low- and high-energy limits. As $k \rightarrow 0$, a short-range interaction in one dimension tends to impede transmission; in the phase-shift language this is reflected in $\delta(k)$ approaching an integer multiple of $\frac{\pi}{2}$, so that either $|t| \rightarrow 0$ and $|r| \rightarrow 1$ or, in the presence of special cancellations, transmission is enhanced. If a shallow two-body bound state is present just below threshold, the phase rises rapidly through π in a small band of k above zero, producing a pronounced low-energy structure in $|t|^2$. In the opposite regime $k \rightarrow \infty$, the interaction appears point-like and weak compared to the kinetic term; correspondingly $\delta(k) \rightarrow 0$, the reflection probability $|r(k)|^2 \rightarrow 0$, and $|t(k)|^2 \rightarrow 1$.

Everything in this section is agnostic to how the data are obtained. In a numerical lattice study one may compute $E_n(L)$ and use (20) to reconstruct $\delta(k)$. In a real-time study one may prepare two narrow wave packets initially well separated and centered at $\pm k$, evolve to late times, and measure transmitted and reflected weights far from the interaction region. An optional and often illuminating observable is the time delay, defined by $\tau(k) = 2 \frac{d\delta}{dE}$; a positive delay corresponds to lingering due to an effectively attractive interaction region, while a negative slope indicates a repulsive bump, all consistent with causality bounds. For the purposes of these notes we emphasize the phase shift extracted from finite-volume spectra as the primary non-perturbative definition of elastic $2 \rightarrow 2$ scattering in 1+1 dimensions, and we use the plane-wave amplitudes (t, r) mainly as an interpretive bridge.

Puzzle. In the single anharmonic oscillator (AHO) with $\lambda > 0$ there are no scattering states—only a discrete ladder of bound levels. Yet in the lattice/field theory built from the same onsite potential we speak freely of elastic $2 \rightarrow 2$ scattering, phase shifts, and transmission/reflection. How can scattering suddenly appear if the local potential is still confining? What changed?

Answer. The AHO has no “away”: it is one coordinate in a confining well, so every normalizable state is bound and there are no asymptotic plane waves. Scattering needs two ingredients that the AHO lacks but the field theory has.

First, *motion*. Turning on the nearest-neighbour “spring” term ($\kappa > 0$) couples sites and creates extended normal modes labeled by a momentum k . Local excitations now *propagate*. Second, *asymptotic separation*. On the infinite line, two widely separated one-particle wave packets scarcely feel each other; their total energy $E_{\text{tot}} = 2\sqrt{m^2 + k^2}$ depends continuously on k . When they pass through the short-range interaction region (set by the local $\lambda\phi^4$), they momentarily overlap and pick up a phase; before and after, they are again free and far apart. That phase is the scattering information.

Two sanity checks close the loop. If you set $\kappa = 0$, sites decouple, nothing moves, and the very notion of “incoming/outgoing” collapses—no scattering, just many independent AHOs. If you set $\lambda = 0$ with $\kappa > 0$, excitations move but do not interact—there is a continuum of two-body energies but *zero* phase shift. Only when $\kappa > 0$ and $\lambda > 0$ do you have both propagation and a localized interaction, which is exactly when scattering in the sense of a phase (or transmission/reflection) makes sense.

6 Scattering on a quantum computer

This section outlines two complementary ways to extract elastic $2 \rightarrow 2$ phase shifts for the 1+1D lattice ϕ^4 chain directly on a quantum processor. Both methods share the same state-preparation backbone: *prepare exact free-theory eigenstates and adiabatically dress them* to the interacting theory at the target couplings. Working at fixed lattice (N, κ, μ_0^2, g_0) and boundary condition (periodic for sharp crystal momentum, or open for parity-resolved standing waves), one first calibrates the single-particle dispersion $E_1(k)$, then proceeds with either a time-domain scattering experiment or a finite-volume spectroscopic inversion.

Common preparation (adiabatic dressing from the free theory). At $\lambda = 0$ the chain is quadratic. Prepare the exact free vacuum $|0_{\text{free}}\rangle$. A single free one-particle plane wave at momentum k is $a_k^\dagger|0_{\text{free}}\rangle$, where $a_k^\dagger = \frac{1}{\sqrt{N}} \sum_j e^{ikx_j} a_j^\dagger$ is the normal-mode raiser. For two particles at total momentum $P = 0$, use $a_k^\dagger a_{-k}^\dagger|0_{\text{free}}\rangle$ or a narrow superposition around k . With the state prepared, turn on interactions along a smooth schedule $s \in [0, 1] \mapsto \lambda(s)$ (and optionally co-tune $\mu_0^2(s)$) using a boundary-flattened ramp so that leakage scales as $O(1/T^2)$. Momentum and \mathbb{Z}_2 parity keep the evolution within the intended symmetry sector, adiabatically mapping free states to their interacting counterparts.

A. Wave-packet scattering in real time

Prepare two narrow, counter-propagating one-particle packets centered at $\pm k_0$ and localized far apart. Dress them adiabatically to the interacting theory at λ_* , then evolve in *real time* under $H(\lambda_*)$ long enough for the packets to separate again after a single collision. The phase shift is read off in two equivalent ways. One can measure a Wigner time delay by comparing to a “free” reference evolution that reproduces the measured $E_1(k)$; the peak of the cross-overlap $C(\Delta t) = \langle \Psi^{\text{free}}(t+\Delta t) | \Psi(t) \rangle$ yields $\tau(k_0) = 2 \frac{d\delta}{dE}|_{k_0}$, which integrates locally to $\delta(k_0)$. Alternatively, one can project the outgoing right-moving packet onto the corresponding freely propagated packet and take the complex argument of the overlap; for a sufficiently narrow packet this phase equals approximately $2\delta(k_0)$. Both readouts use standard Hadamard-test primitives with a single clean ancilla controlling short segments of the same Trotterized evolution used for state preparation.

B. Finite-volume spectroscopy and the quantization condition

Instead of scattering, prepare symmetry-projected few-body states and measure energy levels. First tabulate the single-particle dispersion $E_1(k)$ by dressing $a_k^\dagger |0_{\text{free}}\rangle$ and estimating $E_1(k) - E_0$ via a short real- or imaginary-time autocorrelator or a Rayleigh quotient. Then prepare a dressed two-particle, $P = 0$, even-parity state and extract the lowest two-body level $E_2(L)$ either by a brief imaginary-time filter (single-exponential slope), a short real-time autocorrelation (single-frequency fit), or a shallow variational deflation pass. In the elastic regime one solves $E_2(L) = 2E_1(k)$ for the relative momentum k , and substitutes into the finite-volume quantization rule. For periodic boundaries,

$$kL + 2\delta(k) = 2\pi n \quad (n \in \mathbb{Z}),$$

while for hard walls the even/odd standing-wave branches read $kL + 2\delta_+(k) = (2n+1)\pi$ and $kL + 2\delta_-(k) = 2n\pi$. Repeating the procedure for another level (or another L) over-constrains the inversion and fixes the branch n .

Remarks on resources and stability. Both routes reuse the same registers and Trotter blocks as ground-state ASP. The adiabatic map eliminates the need to guess interacting creation operators; free-theory creators are exact and easy to synthesize as linear combinations of disjoint local raisers. The time-domain route is conceptually transparent but requires longer coherent evolution; the spectroscopic route trades long evolution for short filters or shallow variational layers and an algebraic inversion. In practice it is effective to anchor $\delta(k)$ at one or two momenta with finite-volume levels and confirm with a single wave-packet run at k_0 via the time-delay or asymptotic-phase measurement.

7 Bound states near threshold and the onset of inelasticity

We begin from the same kinematic calibration used in the elastic section: the physical one-particle mass m defines the two-body threshold at total energy $E_{\text{tot}} = 2m$. A two-particle *bound state* is a normalizable state with energy $E_B < 2m$. On the infinite line this means that the relative momentum is purely imaginary, $k = i\kappa_B$ with $\kappa_B > 0$, and the relative wave decays as $e^{-\kappa_B|x|}$. The corresponding total energy is

$$E_B = 2\sqrt{m^2 - \kappa_B^2}, \quad 0 < \kappa_B < m,$$

so that “shallow” indicates $\kappa_B \ll m$, i.e. a level just below threshold. It is useful to keep in mind an intuitive picture that is continuous with the anharmonic-oscillator discussion: the nearest-neighbour “spring” term ($\kappa > 0$) enables localized excitations to move, while the short-range interaction acts only when two wave packets overlap. A bound state corresponds to the situation where the interaction region is effectively attractive in the relevant channel, allowing the two-particle relative coordinate to localize with a decaying envelope.

On a finite ring of length L a true bound state appears as a level that approaches a value strictly below $2m$ as $L \rightarrow \infty$, with finite-size corrections that are exponentially small in L . The exponential falloff is governed by the same decay constant κ_B : to leading order one finds

$$E_B(L) = E_B + ce^{-\kappa_B L} + \dots,$$

where c is a constant set by the wavefunction overlap around the periodic image. This behavior sharply contrasts with the power-law $1/L$ shifts of ordinary scattering levels and provides a

practical diagnostic in numerical data. In the absence of a level below $2m$, one can nevertheless detect the proximity of a shallow would-be bound state by examining the near-threshold elastic phase. The one-dimensional quantization condition

$$kL + 2\delta(k) = \pi n, \quad E_n(L) = 2\sqrt{m^2 + k^2},$$

continues to hold in the purely elastic window and, when a pole sits just below threshold at $k = i\kappa_B$, enforces a rapid variation

$$\delta(k) \approx \arctan \frac{\kappa_B}{k} + \delta_{\text{smooth}}(k).$$

Here $\delta_{\text{smooth}}(k)$ denotes any slowly varying background from short-range details. As $k \rightarrow 0^+$, the pole term drives $\delta(k)$ toward π (modulo π), which is the one-dimensional version of Levinson's theorem for the even channel. In practical terms, very close to threshold the lowest scattering level shifts in a way that mirrors the $\arctan(\kappa_B/k)$ shape when one varies L , and the Wigner time delay $\tau(k) = 2d\delta/dE$ becomes large and positive. If the interaction is not attractive enough to bind, $\delta(k)$ instead starts near 0 (modulo π) and changes only slowly with k .

For the symmetric phase of scalar ϕ^4 in 1+1 dimensions with the standard sign convention ($\lambda > 0$ repulsive at low energies), a two-particle bound state is not expected generically; indeed in that case the near-threshold phase typically does not exhibit a rapid π rise, and all two-body levels remain above $2m$ as $L \rightarrow \infty$. The same diagnostics, however, do reveal bound states in models or parameter regimes with effective attraction, such as the broken phase (kink-antikink composites), sine-Gordon breathers, or lattice tunings that generate an attractive channel. The analysis presented here is agnostic to the microscopic source of attraction and applies unchanged once the elastic window is isolated.

The discussion so far has assumed total energies strictly below the first inelastic threshold. In our setting with a \mathbb{Z}_2 symmetry forbidding odd particle-number changes, the next channel opens at $E_{\text{tot}} = 4m$ with $2 \rightarrow 4$. Crossing this point alters two qualitative features. On the infinite line, part of the outgoing flux can now populate multi-particle states, so the elastic two-body amplitude is no longer a pure phase. It is convenient to write the elastic S -matrix as

$$S_{\text{el}}(k) = \eta(k) e^{2i\delta(k)}, \quad 0 \leq \eta(k) \leq 1,$$

where $\eta(k)$ is the *inelasticity*. In the purely elastic window one has $\eta(k) = 1$; once $E_{\text{tot}} \geq 4m$ this factor drops below unity as probability leaks into four-particle states. On a ring, the simple quantization condition $kL + 2\delta = \pi n$ no longer suffices by itself in the vicinity of the threshold: additional levels with predominantly four-body content crowd near $E = 4m$ and produce a pattern of avoided crossings with the two-body tower. This spectral clutter is the finite-volume signature that inelastic channels have become relevant. For the purposes of a clean elastic analysis it is therefore best to restrict attention to energies $2m < E_{\text{tot}} < 4m$, or to remain comfortably below the first avoided crossings associated with four-body states in the finite-volume spectrum.

In practice, the two complementary non-perturbative routes of the previous section provide everything one needs. From spectra, one either identifies a sub-threshold level and fits its exponentially small L -dependence to extract κ_B , or reconstructs $\delta(k)$ from the quantized momenta and examines its near-threshold behavior for the $\arctan(\kappa_B/k)$ fingerprint. From real-time dynamics, one prepares slow, well-separated wave packets, observes the strong low-momentum reflection and large positive time delay characteristic of a shallow bound state, and, when desired, infers κ_B from the energy-dependence of the phase. All of these steps are phrased at the level of observables and require no perturbative assumptions; they are designed to connect smoothly to the computational strategies developed later while keeping the physics transparent.

A A minimal MPS recipe for half-chain entanglement

This appendix summarizes, in self-contained form, the matrix-product-state (MPS) ingredients used to produce the half-chain entanglement entropy $S_{1/2}(\kappa)$ curves in the earlier section. The discussion assumes only standard linear algebra (singular-value decomposition) and the Schmidt decomposition of bipartite quantum states.

Local Hilbert space and operators. Each lattice site carries a truncated single-oscillator space

$$\mathcal{H}_{\text{loc}} = \text{span}\{|n\rangle, n = 0, \dots, n_{\max}\}, \quad d := n_{\max} + 1.$$

In this basis it is convenient to use the standard harmonic-oscillator matrices

$$a|n\rangle = \sqrt{n}|n-1\rangle, \quad a^\dagger|n\rangle = \sqrt{n+1}|n+1\rangle,$$

and then

$$\phi = \frac{a + a^\dagger}{\sqrt{2}}, \quad \pi = \frac{a^\dagger - a}{i\sqrt{2}}, \quad \phi^2 = \phi\phi, \quad \pi^2 = \pi\pi, \quad \phi^4 = \phi^2\phi^2.$$

The lattice Hamiltonian used in the main text is

$$H(\kappa) = \sum_{j=1}^N \left[\frac{1}{2} \pi_j^2 + \frac{1}{2} \mu_0^2 \phi_j^2 + g_0 \phi_j^4 \right] + \frac{\kappa}{2} \sum_{j=1}^{N-1} (\phi_{j+1} - \phi_j)^2,$$

with open boundaries unless stated otherwise.

MPS representation (open boundary). An MPS represents the many-body wavefunction as

$$|\Psi\rangle = \sum_{\{n_j\}} \left(A_1^{[1]}(n_1) \right) \left(A_{\alpha_1 \alpha_2}^{[2]}(n_2) \right) \cdots \left(A_{\alpha_{N-1} 1}^{[N]}(n_N) \right) |n_1 n_2 \cdots n_N\rangle,$$

where each site tensor $A^{[j]}(n_j)$ has shape $(D_{j-1} \times D_j)$ for every physical index value $n_j \in \{0, \dots, d-1\}$. The $\{D_j\}$ are the *bond dimensions*; open boundaries mean $D_0 = D_N = 1$. Small bond dimensions already capture low-entanglement states efficiently; bond growth reflects increasing entanglement.

Canonical form and the Schmidt spectrum at a cut. Fix a bond between sites ℓ and $\ell+1$. Contracting sites 1 through ℓ into a matrix M_L and sites $\ell+1$ through N into a matrix M_R produces a bipartite reshaping

$$\Psi \longleftrightarrow \Theta_{(\text{left}),(\text{right})} \in \mathbb{C}^{(d^\ell) \times (d^{N-\ell})}.$$

The singular values $\{s_r\}$ of Θ are the Schmidt coefficients across that cut; by the Schmidt decomposition,

$$|\Psi\rangle = \sum_r s_r |\varphi_r\rangle_{[1..\ell]} \otimes |\chi_r\rangle_{[\ell+1..N]}, \quad \sum_r s_r^2 = 1.$$

The von Neumann entropy across the cut is

$$S(\ell) = - \sum_r s_r^2 \ln s_r^2.$$

In practice, one does *not* build Θ densely. Instead, one brings the MPS into a *mixed canonical form* with the orthogonality center at the chosen bond by performing QR (or SVD) sweeps from the left and right, and then performs a single SVD on the 2-site “theta” tensor $\Theta^{[\ell,\ell+1]}$ to read off the same $\{s_r\}$. This is exactly what the notebook’s routine does at the middle bond, yielding $S_{1/2} = S(N/2-1)$.

Ground state at $\kappa = 0$ (exact product state). At $\kappa = 0$ the ground state factorizes:

$$|\Psi_0\rangle = \bigotimes_{j=1}^N |0\rangle_{\text{AHO}}, \quad \left(\frac{1}{2}\pi_j^2 + \frac{1}{2}\mu_0^2\phi_j^2 + g_0\phi_j^4 \right) |0\rangle_{\text{AHO}} = E_0 |0\rangle_{\text{AHO}}.$$

As an MPS this is obtained by placing the normalized local ground vector $v_0 \in \mathbb{R}^d$ on every site, with bond dimension $D_j \equiv 1$. The Schmidt spectrum across any cut is then $\{1\}$, and $S(\ell) = 0$ identically.

Adiabatic / projection step (minimal propagator). To obtain the interacting ground state at a target $\kappa > 0$ one may either (i) implement a real-time adiabatic ramp, or (ii) use an imaginary-time projector as a proxy. Both approaches rely on short two-site updates built from Trotter–Suzuki factorization. A symmetric second-order (Strang) step for a small time increment δt reads

$$e^{-\delta t H(\kappa)} \approx e^{-\frac{\delta t}{2} \sum_j h_j^{\text{on}}} \left[\prod_{\langle j,j+1 \rangle} e^{-\delta t h_{j,j+1}^{\text{bond}}} \right] e^{-\frac{\delta t}{2} \sum_j h_j^{\text{on}}},$$

where

$$h_j^{\text{on}} = \frac{1}{2}\pi_j^2 + \frac{1}{2}\mu_0^2\phi_j^2 + g_0\phi_j^4, \quad h_{j,j+1}^{\text{bond}} = \frac{\kappa}{2}(\phi_{j+1} - \phi_j)^2.$$

The two-site exponential is applied as a gate on the physical indices of sites j and $j+1$, then the result is split back into an MPS by a single SVD at that bond (truncating very small singular values if needed). For real-time adiabatic evolution one replaces $\delta t \mapsto i\delta t$ and lets κ vary smoothly from 0 to κ_f ; for the imaginary-time proxy one keeps κ fixed and halves δt in stages (Strang: “half onsite / full bond / half onsite”) until convergence.

Reading off $S_{1/2}$. After the last time-step at a given κ , bring the MPS to mixed canonical form at the middle bond, compute the singular values $\{s_r\}$ there, and evaluate

$$S_{1/2}(\kappa) = - \sum_r s_r^2 \ln s_r^2.$$

By construction this is purely a property of the lattice state—no continuum limit or renormalization input is required.

B Qubit counting for lattice ϕ^4 in 1+1D

This section collects the bookkeeping needed to estimate qubit requirements for adiabatic state preparation (ASP) and basic spectroscopy on a lattice ϕ^4 chain. The starting Hamiltonian and conventions match Sec. 1:

$$H = \sum_{j=1}^N \left[\frac{1}{2}\pi_j^2 + \frac{1}{2}\mu_0^2\phi_j^2 + g_0\phi_j^4 \right] + \frac{\kappa}{2} \sum_{j=1}^{N-1} (\phi_{j+1} - \phi_j)^2, \quad (\kappa = 1 \text{ in examples}).$$

There are two layers of counting: the *data register* (what must be encoded permanently) and a small number of *work ancillas* (temporary qubits reused when synthesizing gates). Rényi-2 two-copy measurements are *not* considered here.

Local Hilbert space choices and per-site qubits

Each site carries a finite local Hilbert space that must be mapped to qubits. Two standard digitizations are used in practice.

Fock (oscillator) truncation (JLP style). Keep the first $d = n_{\max} + 1$ eigenstates of the single-site AHO (or SHO in the weakly anharmonic limit):

$$\mathcal{H}_{\text{loc}} = \text{span}\{|0\rangle, |1\rangle, \dots, |n_{\max}\rangle\}, \quad d = n_{\max} + 1.$$

Encode the d -level “qudit” using either

$$q_{\text{site}}^{(\text{binary})} = \lceil \log_2 d \rceil \quad \text{or} \quad q_{\text{site}}^{(\text{unary})} = d.$$

Binary is qubit-efficient (fewest qubits per site) at the cost of slightly denser operator synthesis; unary is more transparent but expensive in qubits. For anharmonic onsite physics (moderate/large g_0) one often finds that small d already converges well.

Field-grid (position-basis) digitization. Discretize the field value on a symmetric grid $\phi_j \in [-\Phi_{\max}, \Phi_{\max}]$ with 2^{n_ϕ} points, and encode the grid index in n_ϕ qubits:

$$q_{\text{site}}^{(\phi\text{-grid})} = n_\phi.$$

Local polynomials $g_0\phi^4$, $\mu_0^2\phi^2$ are diagonal; π^2 is diagonal after a local QFT on those n_ϕ qubits. One must choose Φ_{\max} and n_ϕ to control truncation and discretization errors.

Total data qubits and ancillas

For N sites,

$$Q_{\text{data}} = N \times q_{\text{site}}.$$

Gate synthesis for $e^{-i\Delta t (\frac{1}{2}\pi^2 + \frac{1}{2}\mu_0^2\phi^2 + g_0\phi^4)}$ and $e^{-i\Delta t \frac{1}{2}(\phi_{j+1} - \phi_j)^2}$ typically benefits from a handful of clean ancillas ($O(1)$; reused across sites/bonds). A conservative allowance of 5–8 work ancillas suffices for ASP/Trotter circuits and basic spectroscopy; these do not scale with N when scheduled sequentially.

Concrete budgets for a 127-qubit device (single copy, no QPE)

Adopt $\kappa = 1$ and $a = 1$ for lattice units, keep aside ~ 7 ancillas for synthesis, leaving ~ 120 data qubits. The finite-volume sanity condition $m_{\text{phys}}L = m_{\text{phys}}N \gtrsim 10$ guides the choice of N and target mass.

Option A: compact Fock truncation. Take $n_{\max} = 3$ ($d = 4$) with binary encoding: $q_{\text{site}} = 2$. This yields up to $N_{\max} = \lfloor 120/2 \rfloor = 60$ sites; with a margin, $N \simeq 56$ is comfortable. The mass window $m_{\text{phys}} \gtrsim 10/N \approx 0.18$ suggests targeting $m_{\text{phys}} \sim 0.25\text{--}0.35$. A practical starting box is

$$(N, m_{\text{phys}}, g_0, \mu_0^2) \approx (56, 0.30, 0.7, \text{tuned to hit } m_{\text{phys}}),$$

with μ_0^2 adjusted at fixed g_0 to match the desired gap. This setting supports ASP entanglement curves, dispersion near small momenta, and two-particle finite-volume levels for a phase-shift point.

Option B: higher onsite resolution, fewer sites. Take $n_{\max} = 7$ ($d = 8$) with binary encoding: $q_{\text{site}} = 3$. Then $N_{\max} = \lfloor 120/3 \rfloor = 40$; using $N \simeq 36$ gives headroom. The finite-volume window $m_{\text{phys}} \gtrsim 10/36 \approx 0.28$ suggests $m_{\text{phys}} \sim 0.3\text{--}0.5$. A balanced starting point is

$$(N, m_{\text{phys}}, g_0, \mu_0^2) \approx (36, 0.40, 0.3, \text{tuned}).$$

Fewer sites mean a coarser momentum grid but improved onsite fidelity.

Choosing between digitizations

For the qubit budgets above, Fock truncation with binary encoding is the most economical in qubits and aligns with the AHO continuity emphasized earlier. A field-grid choice with, say, $n_\phi = 6$ bits per site would cap the chain near $N \sim 20$ within the same 120 data-qubit envelope, pushing $m_{\text{phys}} \gtrsim 0.5$; this is workable but less favorable for low-momentum scattering kinematics.

Practical checklist

Select N so that $m_{\text{phys}}N \gtrsim 10$. Fix a local truncation d and encoding, then verify convergence of the target observables (gap, simple correlators, entanglement across a central cut) under modest increases of d . Tune μ_0^2 at fixed g_0 to hit the target m_{phys} ; if a second physical input is desired (e.g. a phase shift at a chosen momentum), adjust g_0 while re-tuning μ_0^2 to keep the mass fixed. The peak ancilla count remains $O(1)$ for ASP/Trotterized evolution and does not alter the data-qubit budgets above.

References

- [1] Y. Nishiyama, “Strong-coupling-expansion analysis of the false-vacuum decay rate of the lattice ϕ^4 model in 1+1 dimensions,” *J. Phys. A: Math. Gen.* **34** (50) (2001) 11215–11223, doi:10.1088/0305-4470/34/50/304, arXiv:cond-mat/0110195.

Schwinger and Thirring models

LECTURE NOTES

Contents

1 Cosine-first route: from transmons to bosonized QFTs and scattering	1
1.1 From the transmon AHO to a lattice cosine scalar	1
1.2 Conventions: Dirac fermion form	1
1.3 Schwinger model (QED_{1+1}) in fermionic form	2
1.4 Massive Thirring model (current-current interaction)	2
1.5 Two bosonized targets captured by the cosine	3
2 Modern, quotable parameter dictionaries	3
2.1 Schwinger (fermionic) \rightarrow bosonized cosine (continuum and lattice)	3
2.2 Massive Thirring \leftrightarrow sine-Gordon (with an explicit, modern map)	4
3 Bosonization derivations (pedagogical sketch)	4
3.1 Schwinger \Rightarrow massive scalar + cosine with θ	4
3.2 Massive Thirring \Leftrightarrow sine-Gordon	4
4 What to measure (bosonic view) and why we later switch to qubits	4

1 Cosine-first route: from transmons to bosonized QFTs and scattering

1.1 From the transmon AHO to a lattice cosine scalar

A single transmon is a weakly-anharmonic oscillator with compact phase $\hat{\varphi}$:

$$H_{\text{trans}} = 4E_C(\hat{n} - n_g)^2 - E_J \cos \hat{\varphi}, \quad [\hat{\varphi}, \hat{n}] = i. \quad (1)$$

In the phase basis, $4E_C\hat{n}^2$ acts as a kinetic term. An *array* (capacitive/inductive couplings) reduces to a 1D field φ_x with conjugate Π_x :

$$H = \sum_{x=1}^L \left[\frac{1}{2C_{\text{eff}}} \Pi_x^2 + \frac{K}{2} (\varphi_{x+1} - \varphi_x)^2 - E_J \cos(\varphi_x - \varphi_0) \right]. \quad (2)$$

Expanding about the bias setpoint φ_0 : $-E_J \cos(\varphi_x - \varphi_0) = -E_J + \frac{E_J}{2} \delta\varphi_x^2 - \frac{E_J}{24} \delta\varphi_x^4 + \dots$, so the AHO/ ϕ^4 story is the small-excursion limit of a *compact* cosine theory.

1.2 Conventions: Dirac fermion form

We work in 1+1 dimensions with natural units $\hbar = c = 1$ and metric

$$\eta_{\mu\nu} = \text{diag}(+, -), \quad \epsilon^{01} = +1, \quad \epsilon_{01} = +1,$$

so that $\epsilon^{\mu\nu}\epsilon_{\mu\rho} = \delta_\rho^\nu$. A convenient explicit representation of Dirac matrices is

$$\gamma^0 = \sigma^1, \quad \gamma^1 = i\sigma^2, \quad \gamma^5 \equiv \gamma^0\gamma^1 = \sigma^3, \quad (3)$$

with $\{\gamma^\mu, \gamma^\nu\} = 2\eta^{\mu\nu}$. We write a two-component Dirac spinor ψ , its adjoint $\bar{\psi} \equiv \psi^\dagger \gamma^0$, and define the vector and axial currents

$$j^\mu \equiv \bar{\psi} \gamma^\mu \psi, \quad j_5^\mu \equiv \bar{\psi} \gamma^\mu \gamma^5 \psi. \quad (4)$$

Gauge conventions. The $U(1)$ gauge field is A_μ , field strength $F_{\mu\nu} \equiv \partial_\mu A_\nu - \partial_\nu A_\mu$, and covariant derivative

$$D_\mu \equiv \partial_\mu + i e A_\mu, \quad (5)$$

with gauge coupling e (mass dimension 1 in 1+1D). The topological θ -term is written as

$$\mathcal{L}_\theta \equiv \frac{\theta}{2\pi} \epsilon^{\mu\nu} F_{\mu\nu} = \frac{\theta}{\pi} F_{01}. \quad (6)$$

1.3 Schwinger model (QED₁₊₁) in fermionic form

With fermion mass m_f and vacuum angle θ , the Minkowski Lagrangian is

$$\boxed{\mathcal{L}_{\text{Sch}} = -\frac{1}{4} F_{\mu\nu} F^{\mu\nu} + \bar{\psi} (i\cancel{D} - m_f) \psi + \frac{\theta}{2\pi} \epsilon^{\mu\nu} F_{\mu\nu}, \quad \cancel{D} \equiv \gamma^\mu D_\mu.} \quad (7)$$

Useful consequences/notations we will use later:

- The electric field is $E \equiv F_{01}$; Gauss's law in 1+1D gives a linear potential between charges.
- Under a global chiral rotation $\psi \rightarrow e^{i\alpha\gamma^5} \psi$, the anomaly shifts $\theta \rightarrow \theta - 2\alpha$ and rotates the mass term $m_f \bar{\psi} \psi \rightarrow m_f \bar{\psi} (\cos 2\alpha + i\gamma^5 \sin 2\alpha) \psi$; in bosonization this becomes a shift of the cosine's argument by θ .
- In the bosonized form used later we will identify the *Schwinger mass* $\mu_S = e/\sqrt{\pi}$ and the fixed bosonization frequency $\beta = \sqrt{4\pi}$.

1.4 Massive Thirring model (current–current interaction)

We take the (dimensionless) Thirring coupling g_{Th} in the standard normalization:

$$\boxed{\mathcal{L}_{\text{Th}} = \bar{\psi} (i\cancel{D} - m_f) \psi - \frac{g_{\text{Th}}}{2} (j_\mu j^\mu) = \bar{\psi} (i\cancel{D} - m_f) \psi - \frac{g_{\text{Th}}}{2} (\bar{\psi} \gamma_\mu \psi)(\bar{\psi}^\mu \psi).} \quad (8)$$

Remarks linking to our bosonic conventions:

- In the bosonic dual (sine–Gordon) we will use $\frac{\beta^2}{4\pi} = \frac{1}{1+g_{\text{Th}}/\pi}$, so that the free-fermion point $g_{\text{Th}}=0$ maps to $\beta^2=4\pi$.
- The SG cosine coefficient is *linear* in m_f (overall prefactor scheme/scale dependent; fixed once and for all by a chosen normal-ordering convention).

Summary of conventions we stick to later.

$$\boxed{\begin{aligned} &\text{Metric: } \eta_{\mu\nu} = \text{diag}(+, -), \quad \epsilon^{01} = +1, \\ &\gamma^0 = \sigma^1, \quad \gamma^1 = i\sigma^2, \quad \gamma^5 = \sigma^3, \quad \cancel{D} = \gamma^\mu \partial_\mu, \quad \cancel{D} = \gamma^\mu (\partial_\mu + ieA_\mu), \\ &j^\mu = \bar{\psi} \gamma^\mu \psi, \quad j_5^\mu = \bar{\psi} \gamma^\mu \gamma^5 \psi, \\ &\text{Schwinger: } \mathcal{L}_{\text{Sch}} \text{ as in (7),} \quad \text{Thirring: } \mathcal{L}_{\text{Th}} \text{ as in (8).} \end{aligned}} \quad (9)$$

These choices match the bosonized scalar conventions used later: in Schwinger we will take $\beta = \sqrt{4\pi}$ and identify the gauge-induced mass $\mu_S = e/\sqrt{\pi}$; in Thirring↔SG we will quote Coleman's relation $\beta^2/(4\pi) = 1/(1 + g_{\text{Th}}/\pi)$ for the same β that appears in the sine–Gordon cosine.

1.5 Two bosonized targets captured by the cosine

(a) Schwinger (QED₁₊₁) → cosine boson. One-flavor QED₁₊₁ with coupling e , fermion mass m , vacuum angle θ bosonizes to a compact scalar ϕ :

$$\mathcal{L}_{\text{Sch}}^{\text{bos}} = \frac{1}{2}(\partial\phi)^2 - \frac{1}{2}\mu_S^2\phi^2 + c(\mu_R)m\cos(\beta\phi - \theta), \quad \boxed{\mu_S = \frac{e}{\sqrt{\pi}}, \quad \beta = \sqrt{4\pi}}, \quad (10)$$

where $c(\mu_R)$ depends on the normal-ordering convention (fixed below to match modern numerics).

(b) Massive Thirring ↔ sine–Gordon (Coleman). The massive Thirring model $\mathcal{L}_{\text{Th}} = \bar{\psi}(i\partial\phi - m_f)\psi - \frac{g_{\text{Th}}}{2}(\bar{\psi}\gamma_\mu\psi)(\bar{\psi}^\mu\psi)$ is quantum-equivalent to sine–Gordon $\mathcal{L}_{\text{SG}} = \frac{1}{2}(\partial\phi)^2 + \frac{\mu_{\text{SG}}^2}{\beta^2}(\cos\beta\phi - 1)$ with the universal coupling map

$$\boxed{\frac{\beta^2}{4\pi} = \frac{1}{1 + g_{\text{Th}}/\pi}}, \quad (11)$$

and a cosine amplitude *linear in m_f* (overall prefactor set by the chosen scheme). Solitons ↔ Thirring fermions; breathers ↔ fermion–antifermion bound states [2, 3].

2 Modern, quotable parameter dictionaries

2.1 Schwinger (fermionic) → bosonized cosine (continuum and lattice)

A convenient, widely used normalization (matching [7]) is:

$$H = \int dx : \left[\frac{1}{2}\Pi^2 + \frac{1}{2}(\partial_x\phi)^2 + \underbrace{\frac{e^2}{2\pi}\phi^2}_{\mu_S^2/2\phi^2} - \underbrace{\frac{bme}{2\pi^{3/2}}\cos(\sqrt{4\pi}\phi - \theta)}_{\text{mass-induced cosine}} \right] :, \quad b = e^\gamma, \quad (12)$$

$$\Rightarrow \boxed{\mu_S = \frac{e}{\sqrt{\pi}}, \quad \beta = \sqrt{4\pi}, \quad g_{\text{cos}} \equiv \frac{bme}{2\pi^{3/2}}}.$$

A second-order lattice discretization with spacing a gives

$$H = \chi \sum_x \left[\frac{1}{2}\pi_x^2 + \frac{1}{2}(\phi_x - \phi_{x-1})^2 + \frac{\mu^2}{2}\phi_x^2 - \lambda \cos(\beta\phi_x - \theta) \right], \quad \boxed{\chi = \frac{1}{a}, \quad \beta = \sqrt{4\pi}, \quad \mu^2 = \frac{a^2 e^2}{\pi}, \quad \lambda = \frac{a^2 b m e}{2\pi^{3/2}} e^{2\pi\Delta(a)}} \quad (13)$$

where $\Delta(a)$ is the lattice propagator at the origin (finite; depends on discretization). Many numerics set $a = 1$ (so $\chi = 1$, $\mu^2 = e^2/\pi$).

Small-amplitude (“SG4”) expansion near $\phi_0 = \theta/\beta$. With $\delta\phi = \phi - \phi_0$,

$$V(\phi) = \frac{1}{2}\mu_S^2\phi^2 - g_{\text{cos}}\cos(\beta\phi - \theta) = V_0 + \frac{1}{2}M^2\delta\phi^2 + \frac{\lambda_{\phi^4}}{4}\delta\phi^4 + \dots, \quad \boxed{M^2 = \mu_S^2 + g_{\text{cos}}\beta^2, \quad \lambda_{\phi^4} = -\frac{g_{\text{cos}}\beta^4}{6}}. \quad (14)$$

This is the bridge to your ϕ^4 notes.

2.2 Massive Thirring \leftrightarrow sine–Gordon (with an explicit, modern map)

In a bosonization scheme where composite operators are normal ordered at a common scale μ_R , one has:

$$\boxed{\frac{\beta^2}{4\pi} = \frac{1}{1 + g_{\text{Th}}/\pi}}, \quad \boxed{j^\mu = \bar{\psi}\gamma^\mu\psi \longleftrightarrow \frac{\beta}{2\pi}\epsilon^{\mu\nu}\partial_\nu\phi}, \quad (15)$$

$$\boxed{\bar{\psi}\psi \longleftrightarrow -\mathcal{C}(\mu_R)\cos(\beta\phi)}, \quad \boxed{\mu_{\text{SG}}^2 = \kappa(\mu_R)m_f, \quad \kappa(\mu_R) = \beta^2\mathcal{C}(\mu_R)}. \quad (16)$$

Thus the SG cosine coefficient is *linear in m_f* (the proportionality κ is scheme-fixed by one calibration, e.g. the soliton or first-breather mass). Equation (16) is the form commonly quoted in modern RG/numerics discussions referencing Coleman’s map [2].

3 Bosonization derivations (pedagogical sketch)

3.1 Schwinger \Rightarrow massive scalar + cosine with θ

Use the operator dictionary $j^\mu \leftrightarrow \frac{1}{\sqrt{\pi}}\epsilon^{\mu\nu}\partial_\nu\phi$, $\bar{\psi}\psi \leftrightarrow -\tilde{\mathcal{C}} : \cos(\sqrt{4\pi}\phi) :$, couple A_μ linearly, integrate out the quadratic gauge field to generate $\frac{1}{2}(e^2/\pi)\phi^2$, and rotate away the explicit θ into the phase of $m\bar{\psi}\psi$ (anomaly) so the cosine is shifted: $\cos(\sqrt{4\pi}\phi - \theta)$. Normal-order at $\mu_S = e/\sqrt{\pi}$ to match Eq. (12) (the famous $b = e^\gamma$ appears) [4].

3.2 Massive Thirring \Leftrightarrow sine–Gordon

Hubbard–Stratonovich J_μ^2 with an auxiliary A_μ , integrate out the fermion to get a Gaussian for A_μ (equivalently a scalar with stiffness $\propto 1 + g_{\text{Th}}/\pi$), rescale to a canonical kinetic term to obtain Eq. (11), and map $m_f\bar{\psi}\psi$ to a cosine with amplitude $\propto m_f$ [2, 3].

4 What to measure (bosonic view) and why we later switch to qubits

For packets in the cosine model, track $E_x(t) \propto \langle\phi_{x+1} - \phi_x\rangle$, local energy $h_x(t)$, and two-point functions to diagnose elastic vs. inelastic channels. Digitally, the bosonic encoding is deep (permute basis changes); the staggered-fermion spin-chain is qubit-native and much shallower for Qiskit demos, while retaining the same scattering phenomenology [8].

Acknowledgments for historical pointers

For bosonization and the Schwinger model: Schwinger [1], Coleman [4], Coleman’s Thirring \leftrightarrow SG [2], Mandelstam’s operator construction [3]. For lattice fermions and Hamiltonian LGT: Kogut–Susskind [5] and Kogut’s RMP [6]. For modern cosine-route scattering and parameter normalizations: Belyansky *et al.* [7]; and large-scale QC Schwinger simulations: Farrell *et al.* [8].

References

- [1] J. Schwinger, “Gauge Invariance and Mass. II,” *Phys. Rev.* **128**, 2425 (1962). doi:10.1103/PhysRev.128.2425.
- [2] S. Coleman, “Quantum sine-Gordon equation as the massive Thirring model,” *Phys. Rev. D* **11**, 2088 (1975). doi:10.1103/PhysRevD.11.2088.

- [3] S. Mandelstam, “Soliton operators for the quantized sine-Gordon equation,” *Phys. Rev. D* **11**, 3026 (1975). doi:10.1103/PhysRevD.11.3026.
- [4] S. Coleman, “More about the massive Schwinger model,” *Annals of Physics* **101**, 239–267 (1976). doi:10.1016/0003-4916(76)90280-3.
- [5] J. Kogut and L. Susskind, “Hamiltonian formulation of Wilson’s lattice gauge theories,” *Phys. Rev. D* **11**, 395 (1975). doi:10.1103/PhysRevD.11.395.
- [6] J. B. Kogut, “An introduction to lattice gauge theory and spin systems,” *Rev. Mod. Phys.* **51**, 659 (1979). doi:10.1103/RevModPhys.51.659.
- [7] R. Belyansky, S. Whitsitt, N. Mueller, A. Fahimniya, E. R. Bennewitz, Z. Davoudi, and A. V. Gorshkov, “High-Energy Collision of Quarks and Mesons in the Schwinger Model: From Tensor Networks to Circuit QED,” *Phys. Rev. Lett.* **132**, 091903 (2024). doi:10.1103/PhysRevLett.132.091903.
- [8] R. C. Farrell, M. Illa, A. N. Ciavarella, and M. J. Savage, “Quantum simulations of hadron dynamics in the Schwinger model using 112 qubits,” *Phys. Rev. D* **109**, 114510 (2024). doi:10.1103/PhysRevD.109.114510.

Ising Field Theory

LECTURE NOTES

Contents

1 Ising chain: definitions, notation	3
1.1 The solvable limit $H(J, 0, 0)$	4
1.2 The solvable limit $H(J, h_x, 0)$	5
1.3 The longitudinal-field Ising chain: $H(J, 0, h_z)$	6
1.4 The nonintegrable Ising chain $H(J, h_x, h_z)$	6
2 The S-matrix for Ising field theory	7
2.1 Conventions-in-brief: units, kinematics, sanity checks	10
3 W-state wave-packet preparation	11
3.1 Step-1	11
3.2 Step 2 (imprinting momentum)	12
3.3 Step 3 (mid-circuit parity sieve)	14
3.4 Choosing the cleaning angles $\vec{\theta}$	16
3.5 2-particle scattering	17
A Miscellaneous points	19
A.1 Rapidities, crossing, and the physical strip	19
A.2 Minimal CFT recap for benchmarks	19
A.3 Truncated Conformal Space (TCSA) as a physics tool	19
B Classical vs. Quantum Ising Models	20
Appendix: Classical vs. Quantum Ising Models	20
B.1 Classical Ising model (statistical)	20
B.2 Quantum Ising / TFIM (Hamiltonian)	20
B.3 Quantum \leftrightarrow Classical mapping (expanded derivation)	20
B.4 Exact solution of the 1D TFIM at $h_z = 0$ (outline)	23
B.5 Phases, observables, and entanglement	23
B.6 Quick comparison table	24
B.7 Notes for quantum computing	24
C Unitarity in 1+1D two-particle scattering: elastic vs. inelastic	24
D State preparation in Qiskit and why we prefer the W-state route	26
D.1 What “state preparation” means	26
D.2 Cheap cases: basis and product states	26
D.3 Structured superpositions: uniform and domain-specific	26
D.4 Arbitrary amplitude loading: exact but expensive	26
D.5 Variational state preparation: approximate but hardware-friendly	26
D.6 Two practical gotchas	27
D.7 Why the W-state approach (Preskill et al.) is superior for NISQ QFT tasks	27

D.8 How it fits with Qiskit in practice	28
D.9 Summary	28

From ϕ^4 to the Ising chain: a projector's-eye view

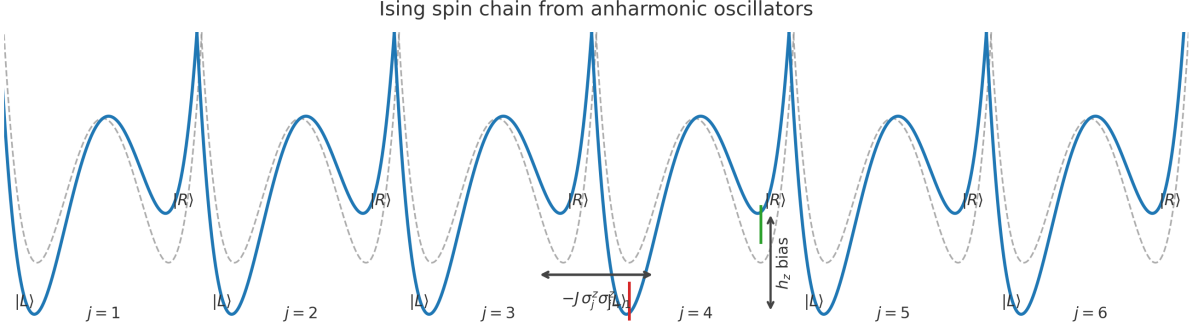


Figure 1: Ising spin chain from anharmonic oscillators. Each site is drawn as a projected double well with local states $|L\rangle, |R\rangle$ ($\sigma^z = \pm 1$). The dashed curve shows the symmetric well; the solid curve includes a longitudinal tilt (h_z), with a bracket indicating the induced bias. Nearest-neighbor coupling $-J \sigma_j^z \sigma_{j+1}^z$ is depicted between two central sites. *Intra-site tunneling*, controlled by the transverse field h_x , mixes $|L\rangle$ and $|R\rangle$ but is not labeled on the plot to avoid overlap.

In the previous sections we built a lattice scalar theory by placing an anharmonic oscillator on every site,

$$H_{\phi^4}^{\text{lat}} = \sum_j \left[\frac{1}{2} \Pi_j^2 + U(\phi_j) \right] + \frac{\kappa}{2a^2} \sum_j (\phi_{j+1} - \phi_j)^2, \quad U(\phi) = \frac{m^2}{2} \phi^2 + \frac{\lambda}{4} \phi^4, \quad (1)$$

with lattice spacing a , kinetic coupling κ for gradients, and on-site double-well when $m^2 < 0$ (spontaneous Z_2 breaking). Let $v \equiv \sqrt{|m^2|/\lambda}$ denote the well minima; in the deep-well regime the local spectrum at each site consists of two low-lying states localized near $\phi = \pm v$, split by a small tunneling amplitude through the barrier.

The key observation is that, at energies well below the local barrier, each site is effectively a *two-level system*. Let $\{|L\rangle_j, |R\rangle_j\}$ be wavefunctions localized in the left/right well. Form symmetric/antisymmetric combinations

$$|+\rangle_j = \frac{|L\rangle_j + |R\rangle_j}{\sqrt{2}}, \quad |-\rangle_j = \frac{|L\rangle_j - |R\rangle_j}{\sqrt{2}},$$

and use them as a qubit basis. We now define Pauli operators by their action in this two-dimensional subspace:

$$\sigma_j^z |L\rangle_j = +|L\rangle_j, \quad \sigma_j^z |R\rangle_j = -|R\rangle_j, \quad \sigma_j^x |L\rangle_j = |R\rangle_j, \quad \sigma_j^x |R\rangle_j = |L\rangle_j.$$

(Equivalently, σ_j^z measures the sign of ϕ_j and σ_j^x flips between the two wells.)

Projecting the *on-site* part of (1) onto this subspace produces two familiar terms. First, quantum tunneling between $\pm v$ gives a level splitting Δ , which appears as a transverse field:

$$\left[\frac{1}{2} \Pi_j^2 + U(\phi_j) \right] \longrightarrow -\frac{\Delta}{2} \sigma_j^x + \text{const.} \quad (2)$$

Second, a small *tilt* of the double well (e.g. by adding a linear term $\epsilon \phi$ or by asymmetrically shifting m^2) biases one well over the other. In the two-level subspace this is a longitudinal field,

$$\epsilon \phi_j \longrightarrow -\frac{\epsilon}{2} \sigma_j^z, \quad \epsilon \propto \epsilon \langle L|\phi|L\rangle - \epsilon \langle R|\phi|R\rangle \simeq 2\epsilon v. \quad (3)$$

The *inter-site* coupling originates from the discrete gradient term. In the deep-well limit the low-energy configurations have $\phi_j \approx v s_j$ with Ising variables $s_j = \pm 1$ (the sign of the local displacement). Then

$$(\phi_{j+1} - \phi_j)^2 \approx v^2(s_{j+1} - s_j)^2 = 2v^2(1 - s_j s_{j+1}).$$

Up to an overall constant, this favors aligned neighbors and projects to a nearest-neighbor Ising coupling:

$$\frac{\kappa}{2a^2} (\phi_{j+1} - \phi_j)^2 \longrightarrow -J \sigma_j^z \sigma_{j+1}^z + \text{const}, \quad J \propto \frac{\kappa v^2}{a^2}, \quad (4)$$

where the proportionality absorbs scheme-dependent form factors from the projection. Putting (2)–(4) together we obtain precisely the transverse-field Ising model with a possible longitudinal bias,

$$H_{\text{eff}} = -J \sum_j \sigma_j^z \sigma_{j+1}^z - h_x \sum_j \sigma_j^x - h_z \sum_j \sigma_j^z + \text{const}, \quad h_x \sim \frac{\Delta}{2}, \quad h_z \sim \frac{\varepsilon}{2}. \quad (5)$$

The absence of a same-site σ_j^2 term is automatic: $\sigma_j^2 = 1$ in the projected two-level Hilbert space. Thus, *replacing the local coordinate ϕ_j by its two lowest well states* is precisely the step that takes us from a lattice ϕ^4 theory to a spin chain with $\sigma^z \sigma^z$ couplings.

This construction makes the continuum connection transparent. Near its quantum critical point ($h_z = 0$, $h_x/J = 1$), the transverse-field Ising chain flows to the 1+1-dimensional Ising conformal field theory with central charge $c = \frac{1}{2}$. On the other hand, the continuum Landau–Ginzburg effective theory for the Ising universality class is a real scalar field with a Z_2 -symmetric ϕ^4 potential. In other words, the same Z_2 -invariant quartic theory we developed from a lattice of anharmonic oscillators is the coarse-grained field theory of the Ising chain near criticality, while the deep-well projection of the lattice ϕ^4 recovers the Ising spins themselves. The two descriptions are therefore *dual perspectives on the same long-distance physics*: ϕ is the coarse-grained order parameter; σ^z is its two-state remnant at strong discretization.

The dictionary extends to excitations and will be useful later. The classical kink of ϕ^4 interpolating between $-v$ and $+v$ maps to a *domain wall* between opposite σ^z domains. A small longitudinal field h_z tilts one well, confining kink–antikink pairs into “mesons”; this has a precise counterpart in both languages: a linear string tension for σ^z domain walls and a confining potential for ϕ kinks. Finally, at $h_z = 0$ the low-energy fermionic quasiparticles of the transverse-field chain are the familiar Bogoliubov modes of the quadratic (free) ϕ fluctuations around the symmetric point, completing the bridge between the operator content on both sides.

For our purposes, the takeaway is practical. We can think of the AHO chain with a deep double-well as the *parent* model: keeping the full local Hilbert space and weak gradients yields the lattice ϕ^4 of Eq. (1); projecting each site to its lowest doublet and keeping nearest-neighbor gradients yields the TFIM (5). The quantum-computing primitives we developed for ϕ^4 (wave-packet preparation, vacuum subtraction, two-particle scattering) thus carry over seamlessly to Ising, with the simple replacement $\phi_j \mapsto \sigma_j^z$ for spatial structure and a transverse σ^x term governing local tunneling.

1 Ising chain: definitions, notation

We work on a ring of N spin- $\frac{1}{2}$ degrees of freedom (sites labeled $j = 1, \dots, N$) with lattice spacing a and periodic boundary conditions. The Hamiltonian family we will study is

$$H(J, h_x, h_z) = -J \sum_{j=1}^N \sigma_j^z \sigma_{j+1}^z - h_x \sum_{j=1}^N \sigma_j^x - h_z \sum_{j=1}^N \sigma_j^z, \quad \sigma_{N+1}^\alpha \equiv \sigma_1^\alpha, \quad (6)$$

with $J > 0$ the ferromagnetic Ising coupling, h_x the transverse field, and h_z the longitudinal field. Throughout, σ_j^α denotes a Pauli matrix σ^α ($\alpha = x, y, z$) acting *only* on site j .

Notation and operator placement. When we write σ_j^α we mean the tensor product

$$\sigma_j^\alpha \equiv \mathbb{I}^{\otimes(j-1)} \otimes \sigma^\alpha \otimes \mathbb{I}^{\otimes(N-j)},$$

so every local term in (6) acts nontrivially on its indicated site(s) and as the identity elsewhere. In particular, the nearest-neighbor Ising interaction is the sum of two-site operators $\sigma_j^z \sigma_{j+1}^z = (\mathbb{I}^{\otimes(j-1)} \otimes \sigma^z \otimes \sigma^z \otimes \mathbb{I}^{\otimes(N-j-1)})$, wrapped periodically by $\sigma_{N+1}^\alpha \equiv \sigma_1^\alpha$.

1.1 The solvable limit $H(J, 0, 0)$.

Setting $h_x = h_z = 0$ gives

$$H(J, 0, 0) = -J \sum_{j=1}^N \sigma_j^z \sigma_{j+1}^z, \quad (7)$$

the quantum operator whose eigenbasis is the simultaneous σ^z -eigenbasis. Equivalently, (7) is the energy functional of the *classical* one-dimensional Ising model with spins $s_j = \pm 1$ via $\sigma_j^z |s_j\rangle = s_j |s_j\rangle$:

$$E[s_1, \dots, s_N] = -J \sum_{j=1}^N s_j s_{j+1}.$$

This limit is “solvable” in two complementary senses:

(i) *As a quantum Hamiltonian:* it is already diagonal in the computational basis. Every product state $|s_1\rangle \otimes \dots \otimes |s_N\rangle$ with $s_j = \pm 1$ is an eigenstate, and the energy depends only on the number of *domain walls* (bonds with $s_j \neq s_{j+1}$). Writing N_{dw} for that number,

$$E = -J \sum_j s_j s_{j+1} = -J[(N - N_{\text{dw}}) - N_{\text{dw}}] = -JN + 2J N_{\text{dw}}.$$

Thus the two fully aligned ferromagnets $|\uparrow\uparrow\dots\uparrow\rangle$ and $|\downarrow\downarrow\dots\downarrow\rangle$ are degenerate ground states with $E_0 = -JN$; each domain wall costs an energy $2J$. Excitations are therefore freely moving domain walls (kinks) at this level, with no interactions between them.

(ii) *As a classical statistical model:* the finite-temperature partition function $Z = \sum_{\{s\}} e^{-\beta E[\{s\}]}$ is exactly computable by a 2×2 transfer matrix. Defining

$$T = \begin{pmatrix} e^{\beta J} & e^{-\beta J} \\ e^{-\beta J} & e^{\beta J} \end{pmatrix}, \quad \lambda_\pm = e^{\beta J} \pm e^{-\beta J},$$

one has $Z = \lambda_+^N + \lambda_-^N$, and in the thermodynamic limit the free energy density is $f = -\beta^{-1} \log \lambda_+$. All thermodynamic quantities follow directly; for example, the zero-field two-point function decays as $\langle s_0 s_r \rangle = (\tanh \beta J)^r$, so the correlation length is $\xi^{-1} = -\log \tanh(\beta J)$. In one dimension there is no finite-temperature phase transition (no spontaneous magnetization at $T > 0$), a fact that historically motivated the search for and eventual discovery of nontrivial critical behavior in two dimensions.

Historical context and importance. The Ising model originated as a minimal theory of cooperative magnetism. The one-dimensional case was solved early and showed *no* finite- T transition, whereas the two-dimensional model famously *does* order below a critical temperature and was solved exactly by Onsager, inaugurating modern critical phenomena. For us, the $H(J, 0, 0)$ limit plays a concrete pedagogical role: it anchors the notion of ferromagnetic order and domain-wall excitations in a setting where the spectrum is transparent. Turning on h_x later will produce quantum fluctuations that delocalize those domain walls (and, at criticality, lead to a relativistic scaling limit), while a longitudinal field h_z breaks the \mathbb{Z}_2 symmetry and ultimately enables inelastic scattering in the Ising field theory studied on quantum hardware. We will build up to those deformations step by step, using only what we need for the scattering experiments.

1.2 The solvable limit $H(J, h_x, 0)$

We now turn on a transverse field and set the longitudinal field to zero, giving the Transverse Field Ising Model (TFIM)

$$H(J, h_x, 0) = -J \sum_{j=1}^N \sigma_j^z \sigma_{j+1}^z - h_x \sum_{j=1}^N \sigma_j^x, \quad \sigma_{N+1}^\alpha \equiv \sigma_1^\alpha. \quad (8)$$

As before, σ_j^α means a Pauli σ^α acting on site j and the identity elsewhere. The model is translation invariant and has a global \mathbb{Z}_2 spin-flip symmetry generated by $P = \prod_j \sigma_j^x$, under which $\sigma_j^z \mapsto -\sigma_j^z$. This is the standard transverse-field Ising model (TFIM).

At zero temperature there are two quantum phases separated by a continuous quantum phase transition. For small transverse field, $g \equiv h_x/J < 1$, the ground state is ferromagnetically ordered along z (two nearly degenerate vacua on a ring, split only by nonperturbative tunneling at finite N). For large transverse field $g > 1$, the ground state is a unique paramagnet polarized along x . Exactly at $g = 1$ the system is critical with emergent relativistic invariance and dynamic exponent $z = 1$. The scaling limit at this critical point is the Ising conformal field theory with central charge $c = \frac{1}{2}$. This is the quantum 1+1D counterpart of the 2D classical Ising critical point via the standard Trotter (quantum-to-classical) mapping.

The TFIM is exactly solvable: one diagonalizes it by a sequence of transforms (Fourier, Jordan–Wigner, Bogoliubov). Without reproducing that machinery here, we record the outputs we will need later. The elementary excitations are free Majorana fermions with single-particle dispersion

$$\varepsilon(k) = 2J \sqrt{1 + g^2 - 2g \cos(ka)}, \quad (9)$$

so the spectral gap is

$$m = \varepsilon(0) = 2J|1 - g|, \quad (10)$$

and the group velocity is $v(k) = \partial_k \varepsilon(k)$; at criticality the characteristic velocity is $v_* = 2Ja$. The equal-time correlations and order parameters are known in closed form: in the ordered phase $g < 1$ the spontaneous magnetization along z is $M_z = (1 - g^2)^{1/8}$, while the correlation length diverges near criticality as $\xi \sim |1 - g|^{-1}$. The critical exponents are the Ising ones, $\beta = \frac{1}{8}$, $\nu = 1$, $\eta = \frac{1}{4}$, consistent with the $c = \frac{1}{2}$ CFT. In the scaling limit the finite-size spectrum on a circle of length $L = Na$ organizes into conformal towers with level spacings $\sim (2\pi v_*/L)$, a fact we will use as a diagnostic when we calibrate dispersion and gap on finite rings.

Two remarks are especially relevant for the scattering agenda later on. First, the $h_z = 0$ chain is *integrable* and its continuum limit is a free Majorana theory: multi-particle scattering is purely elastic and factorized, and in the fermionic description the two-body S -matrix is just a sign from Fermi statistics. As a result, wave-packet collisions at $h_z = 0$ exhibit vanishing inelastic production and zero Wigner time delay; this provides an ideal hardware baseline. Second, even away from strict criticality the long-wavelength sector is well captured by relativistic kinematics with the mass m in (10) and the lattice-measured $\varepsilon(k)$ in (20), so our later conversion between lattice energies E , momenta p , and rapidities θ will be quantitatively controlled once we have calibrated $\varepsilon(k)$ directly on the device.

Historically, the TFIM in one dimension was among the first quantum spin chains to be solved exactly. Lieb, Schultz, and Mattis established the fermionization framework for XY -type chains; Pfeuty specialized it to the Ising case and derived the spectrum, gap, and order parameters; Barouch and McCoy obtained exact space–time correlation functions and scaling forms; and later developments connected the quantum critical point to the Ising minimal model of conformal field theory. Standard references include [12, 28, 14, 16, 17].

1.3 The longitudinal-field Ising chain: $H(J, 0, h_z)$

We consider

$$H(J, 0, h_z) = -J \sum_{j=1}^{L-1} \sigma_j^z \sigma_{j+1}^z - h_z \sum_{j=1}^L \sigma_j^z, \quad J > 0, \quad (11)$$

with open boundaries for definiteness (periodic boundaries are analogous). All terms mutually commute: $[\sigma_j^z, \sigma_k^z] = 0 = [\sigma_j^z \sigma_{j+1}^z, \sigma_k^z \sigma_{k+1}^z]$, so the model is *classical* in the σ^z basis—eigenstates are product states $|s_1 s_2 \cdots s_L\rangle$ with $s_j = \pm 1$ the eigenvalues of σ_j^z .

Ground states and symmetry breaking

At $h_z = 0$ the Hamiltonian has a global \mathbb{Z}_2 spin-flip symmetry and two degenerate ferromagnetic ground states, $|\uparrow\uparrow\cdots\uparrow\rangle$ and $|\downarrow\downarrow\cdots\downarrow\rangle$, with energy $E_0 = -(L-1)J$. A nonzero longitudinal field $h_z \neq 0$ *explicitly* breaks \mathbb{Z}_2 and selects a unique ground state:

$$h_z > 0 : |\uparrow\uparrow\cdots\uparrow\rangle, \quad h_z < 0 : |\downarrow\downarrow\cdots\downarrow\rangle,$$

lifting the degeneracy *linearly* in h_z . There is no quantum phase transition as a function of h_z at $T=0$; instead there is a level crossing at $h_z = 0$.

Excitations as domain walls and their confinement

Excitations are configurations containing *domain walls* (kinks) between ferromagnetic domains. Consider $h_z > 0$ and the ground state $|\uparrow\cdots\uparrow\rangle$. Introduce a down-spin droplet of length ℓ (sites $j = a, \dots, a + \ell - 1$ flipped to \downarrow). Relative to the ground state:

- Each of the two *broken bonds* at the droplet edges contributes an energy penalty $+J - (-J) = 2J$ in total: $\Delta E_{\text{bonds}} = 2J$.
- Each flipped spin changes the field term by $-h_z s_j$: $(-h_z) \rightarrow (+h_z)$, i.e. $+2h_z$ per flipped spin, so $\Delta E_{\text{field}} = 2h_z \ell$.

Hence the energy of a two-domain-wall configuration with separation ℓ is

$$\Delta E(\ell) = 2J + 2h_z \ell. \quad (12)$$

This is a *linearly confining potential* between the two domain walls, with “string tension” $2h_z$.

No dynamics at $h_x = 0$. Because every term in $H(J, 0, h_z)$ is diagonal in the σ^z basis, domain walls are *static*—there is *no hopping* and thus no nontrivial real-time evolution or scattering. The spectrum is a ladder of classical configurations, labeled by the number and positions of domain walls and the size of reversed domains, with energies given by (12) (and generalizations for multiple droplets).

1.4 The nonintegrable Ising chain $H(J, h_x, h_z)$

We now let both fields act:

$$H(J, h_x, h_z) = -J \sum_{j=1}^N \sigma_j^z \sigma_{j+1}^z - h_x \sum_{j=1}^N \sigma_j^x - h_z \sum_{j=1}^N \sigma_j^z, \quad \sigma_{N+1}^\alpha \equiv \sigma_1^\alpha. \quad (13)$$

As in the preceding sections, σ_j^α denotes a Pauli operator acting on site j and the identity elsewhere. Translation invariance remains intact for all (J, h_x, h_z) . The global \mathbb{Z}_2 spin-flip generated by $P = \prod_j \sigma_j^x$ is a symmetry at $h_z = 0$ and is *explicitly broken* as soon as $h_z \neq 0$.

Two structural changes follow immediately from the longitudinal field. First, integrability is lost in the lattice model away from special lines: the exactly solvable free–fermion structure at $h_z = 0$ no longer applies once $h_z \neq 0$. Second, in the ferromagnetic regime the longitudinal field lifts the degeneracy of the two Ising vacua and produces a *linear confining force* between domain walls (kinks): a pair of kinks that delimit a flipped domain now pay an energy proportional to their separation, so the asymptotic excitations are not free kinks but rather a discrete tower of *meson-like* kink–antikink bound states. In the weak-field limit their energies form a characteristic almost equally spaced set near the two-kink threshold, a hallmark of linear confinement in one dimension (see, e.g., [20, 21]).

The continuum interpretation sharpens these statements. Near the quantum critical point of the transverse-field chain ($h_z = 0, h_x/J = 1$), the long-wavelength limit is the Ising conformal field theory with central charge $c = \frac{1}{2}$. Moving away from criticality corresponds to perturbing the CFT by its two relevant primaries, the energy density ε (even under \mathbb{Z}_2) and the spin σ (odd). In field-theory language one writes the Ising Field Theory (IFT)

$$\mathcal{L}_{\text{IFT}} = \mathcal{L}_{\text{Ising CFT}} + \tau \int \varepsilon(x) d^2x + h \int \sigma(x) d^2x, \quad (\Delta_\varepsilon = 1, \Delta_\sigma = \frac{1}{8}),$$

with couplings $\tau \propto h_x/J - 1$ and $h \propto h_z/J$. Two distinguished “integrable corridors” are then visible in this plane. Along $h = 0$ the theory is a *free massive Majorana* field: scattering is elastic and factorized, and the two-body S -matrix is just a sign. Along $\tau = 0$, i.e. at the critical transverse field with a longitudinal perturbation, Zamolodchikov discovered an *integrable* massive theory whose exact spectrum contains eight stable particles with mass ratios fixed by the exceptional Lie algebra E_8 ; the two-body amplitudes are again purely elastic and exactly known [18]. The generic case with $\tau \neq 0$ and $h \neq 0$ is *nonintegrable*: elastic scattering persists below the first inelastic threshold, but as soon as sufficient energy is available, *particle production* $2 \rightarrow 4, 6, \dots$ occurs. It is precisely in this nonintegrable IFT regime that modern experiments and simulations test real-time inelastic processes; the celebrated neutron-scattering observation of the E_8 mass pattern in a quasi-one-dimensional magnet [19] provides a complementary view of the integrable edge of this physics.

For our purposes this landscape serves three roles. It provides a clean baseline at $h_z = 0$, where kink excitations map to free fermions and wave-packet collisions exhibit vanishing time delay and no inelasticity. It supplies a conceptually sharp integrable checkpoint at $\tau = 0$ with $h_z \neq 0$ (the E_8 theory), where one again expects purely elastic behavior but with a rich multiplet of masses. And, most importantly, it explains why turning on *both* deformations produces inelastic channels and long-lived mesonic resonances: this is the regime in which wave-packet collisions probe $\delta(E)$, Wigner time delays, and energy flow into multi-particle sectors—the observables we will extract in the results section. Modern field-theory and scattering reviews place this nonintegrable deformation of the Ising CFT within a broader program of “integrable-plus-perturbations” where exact data (masses, form factors) along integrable rays constrain and organize the physics away from them [22, 23, 24].

We will keep our exposition JW-free in the main text. Whenever a dispersion, mass gap, or two-body level is needed, we will *measure* it directly on finite rings and use the relativistic kinematics of the scaling theory to convert between energy, momentum, and rapidity. This allows us to discuss wave-packet preparation, real-time collisions, and the onset of inelastic production (as in the Preskill–et al. study) using only the spin-chain language, while situating each calculation within the continuum IFT picture sketched above.

2 The S -matrix for Ising field theory

Continuum kinematics. We have in 1+1D

$$E^2 = p^2 + m^2. \quad (14)$$

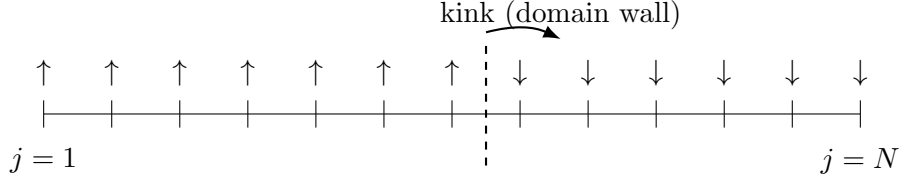


Figure 2: A single domain wall (kink) separating ferromagnetic regions. In the classical/diagonal limit $H(J, 0, 0)$, each kink costs energy $2J$. Kink refers to a configuration where up changes to down along the chain while anti-kink refers to where down changes to up.

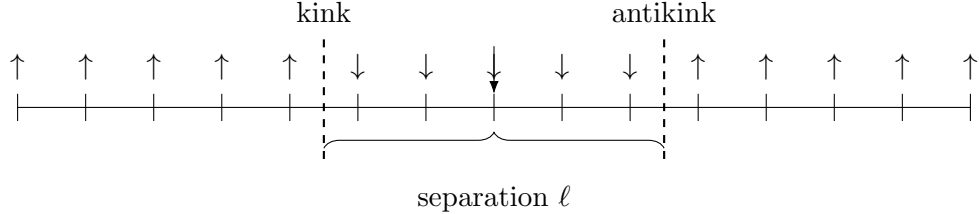


Figure 3: A kink–antikink pair encloses a flipped domain of length ℓ . With a longitudinal field $h_z \neq 0$, each flipped spin raises the energy by $\sim 2h_z$, producing a linear “string” potential $V(\ell) \simeq 2m_{\text{kink}} + \sigma\ell$ with $\sigma \propto h_z/a$.

These are solved by the parametrization in terms of the rapidity θ :

$$E = m \cosh \theta, \quad p = m \sinh \theta, \quad s = 4m^2 \cosh^2(\theta/2). \quad (15)$$

There is no scattering angle; two-body kinematics is one-dimensional up to particle exchange.

Our goal is to describe what we mean by “scattering” in the quantum Ising field theory (IFT) language, in exactly the form that will be used later for wave–packet collisions and for extracting time delays and inelasticity.

Asymptotic particles and states. In the scaling regime of the Ising chain, the long-wavelength excitations are massive relativistic particles with mass m . In the center-of-mass (c.m.) frame, two incoming particles carry momenta $\pm p$ and energies $E/2$ each. An *in* state is prepared by sending two well-separated wave packets towards each other; an *out* state is what you have long after the collision, when the outgoing packets are again well separated. The scattering operator S maps the in–basis to the out–basis,

$$|\text{out}\rangle = S |\text{in}\rangle,$$

and encodes the amplitudes for all possible outcomes.

Elastic $2 \rightarrow 2$ in 1+1D and the phase shift. Below the first inelastic threshold (i.e. for total c.m. energy $2m \leq E < 4m$), the only process available is elastic $2 \rightarrow 2$ scattering. In 1+1 dimensions with identical particles, kinematics leaves a single invariant: the rapidity difference 2θ . Unitarity and translation invariance then imply that the entire two–body process is characterized by a single complex number of unit modulus,

$$S(2\theta) = e^{i\delta(2\theta)},$$

whose phase $\delta(2\theta)$ is the *elastic phase shift*. In a free (integrable) Majorana theory—our $h_z = 0$ baseline—the two–body S is just a sign from fermionic exchange, so δ is a constant (no energy dependence) and wave packets suffer no time delay.

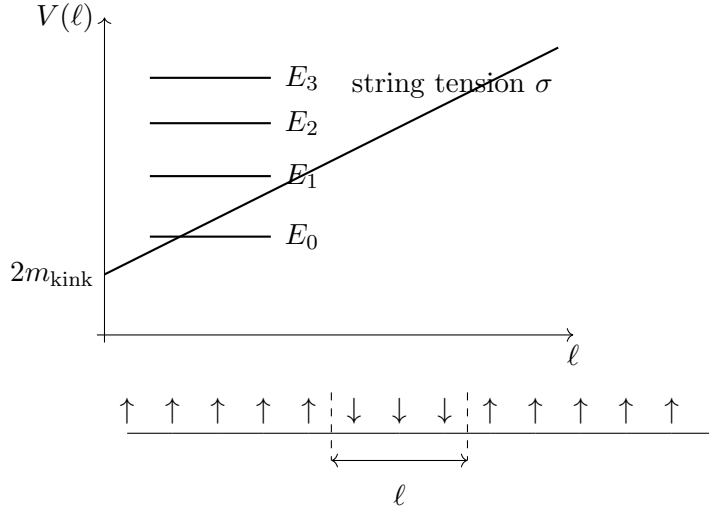


Figure 4: In a longitudinal field, a kink–antikink pair feels a linearly rising potential $V(\ell) \simeq 2m_{\text{kink}} + \sigma \ell$, producing a discrete tower of confined “meson” bound states E_n .

Above threshold and inelasticity. Once the c.m. energy exceeds the first production threshold ($E \geq 4m$ for IFT without additional bound states), channels like $2 \rightarrow 4$ open. The two-body subspace no longer evolves unitarily by itself; a convenient parameterization is

$$S_{2 \rightarrow 2}(2\theta) = \eta(2\theta) e^{i\delta(2\theta)}, \quad 0 \leq \eta \leq 1,$$

where $\eta(2\theta)$ is the *inelasticity parameter*. Probability conservation says that the missing weight is precisely the total inelastic probability,

$$P_{\text{inel}}(E) = 1 - |S_{2 \rightarrow 2}(2\theta)|^2 = 1 - \eta(E)^2.$$

In the purely elastic window one has $\eta = 1$; as inelastic channels open, η decreases from unity.

What wave packets actually measure: Wigner time delay. Real experiments and our quantum–hardware runs use *packets*, not plane waves. For a narrow packet peaked at energy E the peak of the transmitted/reflected packet is shifted in time by

$$\Delta t(E) = \frac{\partial}{\partial E} \delta(2\theta(E)),$$

the *Wigner time delay*. Thus the energy-dependence of the phase shift is directly observable as an advance or delay in the packet’s centroid. We will use this relation verbatim when we analyze collisions.

How spectra encode the same information (finite volume). On a ring of length L the two-body c.m. momenta are quantized. In the elastic window, imposing single-valuedness of the two-particle wave function yields the Bethe–Yang condition (see the ϕ^4 discussion)

$$p(E)L + \delta(2\theta(E)) = 2\pi n, \quad n \in \mathbb{Z}.$$

Given two-body energies $E_2(L)$ at several L ’s (measured on hardware or computed classically), one can invert this relation to obtain $\delta(2\theta)$. In the inelastic regime the simple one-channel form breaks down, and spectral methods must be generalized to coupled channels; in our work we instead diagnose inelasticity directly from late-time observables (sector weights and energy–density tracks).

Why this is enough for us. These few ingredients—rapidity kinematics, the elastic phase shift δ , the inelasticity η with $P_{\text{inel}} = 1 - \eta^2$, the Wigner time delay $\Delta t = \partial_E \delta$, and the finite-volume quantization condition—are exactly the notions that appear in the Preskill *et al.* analysis. In the free/near-integrable corridors one finds $\eta \approx 1$ and a flat δ ; in the nonintegrable regime $\delta(E)$ acquires structure and $\eta(E) < 1$ once thresholds open. Our lecture will use only this minimal dictionary when we connect spectra and real-time data to scattering information.

2.1 Conventions-in-brief: units, kinematics, sanity checks

We set $\hbar = c = 1$ and keep the lattice spacing a explicit when it clarifies dimensions. States are normalized so that one-particle plane waves on a ring of length $L = Na$,

$$|p\rangle = \frac{1}{\sqrt{N}} \sum_{j=1}^N e^{ipa_j} |0 \cdots 1_j \cdots 0\rangle, \quad p = \frac{2\pi n}{L},$$

obey $\langle p'|p\rangle = \delta_{p,p'}$. In the scaling regime we convert between (E, p) and rapidity θ by $E = 2m \cosh \theta$, $p = m \sinh \theta$; this is the only relativistic dictionary we will use later. The *phase shift* $\delta(2\theta)$ is defined by $S(2\theta) = e^{i\delta(2\theta)}$ in the elastic window; the *Wigner time delay* is $\Delta t(E) = \partial_E \delta(2\theta(E))$.

Spectral-phase subtleties

On a ring the two-body energies $E_2(L)$ in the elastic regime satisfy

$$p(E) L + \delta(2\theta(E)) = 2\pi I, \quad I \in \mathbb{Z}.$$

Given two volumes L_1, L_2 and the *same* Bethe integer I tracked across them, a finite-difference estimate for the phase is

$$\delta(2\theta(E)) \approx 2\pi I - p(E) L_2 \quad \text{with} \quad p(E) = \sqrt{\frac{E^2}{4} - m^2},$$

where m is the gap you have *measured* separately on the same chain. The only practical subtlety is to keep the same I (branch identity) when you change L ; we will do this by matching to the nearest free level and *unwrapping* δ as L varies, which yields smooth $\delta(E)$ curves rather than jagged, wrapped points.

How to calibrate $E(p)$ and $v(p)$

Prepare $|p\rangle$ as above and evolve for a short time t under $H(J, h_x, h_z)$. The overlap $\langle p|e^{-iHt}|p\rangle$ has a phase $\varphi(t) \approx E(p)t$ for small t ; thus $E(p)$ is the slope of the phase. The group velocity is then $v(p) = \partial_p E(p)$, which you can also read off from the drift of the packet centroid $\langle x(t) \rangle - \langle x(0) \rangle \approx v t$ for a narrow packet. We will use this measured $E(p)$ both to convert energies to rapidities and to predict noninteracting benchmarks at $h_z = 0$.

Elastic vs. inelastic in real time: what the plots actually show

Below the first inelastic threshold $E < 4m$, two counter-propagating packets emerge still as two packets; the only trace of the interaction is a time shift $\Delta t(E) = \partial_E \delta$. Above threshold, part of the norm leaks into multi-particle sectors. On the lattice, this is visible in two complementary ways that we can adopt: (i) late-time *sector weights*, where we project onto “one packet left/right” and call the complement $P_{\text{inel}}(E)$; (ii) *energy-density tracks*, where $\langle \sigma_j^z \sigma_{j+1}^z \rangle_t$ (and related one-point functions) reveal extra streaks characteristic of produced quanta. Both readouts are purely in the spin language, require no new notation, and mirror the diagnostics used in the hardware study.

Three sanity checks

At $h_z = 0$ (integrable corridor) one expects $P_{\text{inel}} \approx 0$ and a nearly flat δ ; measured Δt should be consistent with zero within errors. Near criticality at $h_x \approx J$, the dispersion becomes relativistic and finite-size spectra organize into nearly uniform spacings $\sim 2\pi v/L$, which you can verify from your $E(p)$ calibration. Finally, when extracting δ from spectra, track a *fixed* Bethe integer I across several L 's and unwrap the phase; plotting wrapped principal values without branch tracking is the common source of “sawtooth” artifacts that are not physics.

3 W-state wave-packet preparation

So far, we have been a bit cavalier about how to prepare the initial states. We have made it seem that this step is trivial. Whilst it is true that QISKit enables state preparation, the depth of the circuit involved in actual quantum computers needs to be brought down. This was accomplished in [26] which we will discuss next. After this step, we can do ASP to get the true interacting states. However, note that in [26], they use ADAPT-VQE using an MPS circuit simulator on classical hardware to keep the depth down. So essentially, they figure out $U(\theta)$ to apply after the W-state step and then continue on the quantum hardware.

3.1 Step-1

Our target single-particle state on an N -site ring (sites $j = 1, \dots, N$, spacing a) with mean momentum p and envelope f_j is

$$|\psi_{f,p}\rangle = \sum_{j=1}^N f_j e^{ipa_j} |\dots 1_j \dots\rangle, \quad \sum_j |f_j|^2 = 1,$$

where $|\dots 1_j \dots\rangle$ denotes “site j excited, all others in $|0\rangle$ ”. Step-1 prepares, in constant depth, a coherent state whose *one-excitation slice* is exactly the uniform W state; later we will add a momentum phase ramp and optional shaping.

A single depth-1 layer. Starting from $|0\rangle^{\otimes N}$, apply the same small rotation to every site:

$$|\Psi_0\rangle = \bigotimes_{j=1}^N (\cos \alpha |0\rangle_j + \sin \alpha |1\rangle_j).$$

This is one layer of identical single-qubit gates (e.g. $R_y(2\alpha)$).

Decomposition by Hamming weight¹. Expand the tensor product and group basis strings by their number K of excitations. It is convenient to introduce the Dicke states,

$$|D_K^N\rangle = \frac{1}{\sqrt{\binom{N}{K}}} \sum_{\substack{\text{strings of length } N \\ \text{with } K \text{ ones}}} |\text{string}\rangle,$$

which form an orthonormal basis for the permutation-symmetric subspace at fixed K . Then

$$|\Psi_0\rangle = \sum_{K=0}^N (\cos \alpha)^{N-K} (\sin \alpha)^K \sqrt{\binom{N}{K}} |D_K^N\rangle.$$

In particular, the $K = 1$ Dicke state is the uniform W state

$$|D_1^N\rangle = \frac{1}{\sqrt{N}} \sum_{j=1}^N |\dots 1_j \dots\rangle.$$

¹The Hamming weight for binary is simply the count of 1's in a string.

Exact weights and a useful choice of angle. Because the Dicke sectors are orthogonal, the probability to have exactly K excitations after a computational–basis measurement is

$$\Pr[K] = \binom{N}{K} (\sin^2 \alpha)^K (\cos^2 \alpha)^{N-K}.$$

We parameterize the small angle by

$$\sin^2 \alpha = \frac{\lambda}{N},$$

with a fixed $\lambda > 0$ that we may tune. In the large– N limit with λ fixed this binomial distribution approaches a Poisson law,

$$\Pr[K] \approx e^{-\lambda} \frac{\lambda^K}{K!} \quad (N \rightarrow \infty, \sin^2 \alpha = \lambda/N).$$

To see this, simply note that for $N \gg 1$, $\binom{N}{K} \rightarrow N^k/k!$ while the rest of the factors read $(\lambda/N)^k(1 - \lambda/N)^N(1 - \lambda/N)^{-k} \approx (\lambda/N)^k e^{-\lambda/N}$. The special case $\lambda = 1$ is particularly convenient: it maximizes the raw one-excitation weight $\Pr[K=1]$ and will be our default.

The one-excitation slice is exactly W. Projecting $|\Psi_0\rangle$ onto the $K = 1$ subspace yields a *pure* Dicke state with amplitude

$$\langle D_1^N | \Psi_0 \rangle = (\cos \alpha)^{N-1} (\sin \alpha) \sqrt{N},$$

so the corresponding probability weight is

$$\Pr[K=1] = N \sin^2 \alpha (\cos^2 \alpha)^{N-1}.$$

With $\sin^2 \alpha = \lambda/N$ this becomes $\Pr[K=1] \approx \lambda e^{-\lambda}$, maximized at $\lambda = 1$ where $\Pr[K=1] \approx e^{-1}$. Thus, after a single depth–1 layer, the coherent state already contains the *exact* uniform W component we need, with a tunable overall weight.

Optional: seeding a shaped envelope. If a nonuniform envelope is desired from the outset, choose site-dependent angles α_j so that

$$\sin^2 \alpha_j = \lambda |f_j|^2, \quad \sum_j |f_j|^2 = 1.$$

Then

$$\bigotimes_j (\cos \alpha_j |0\rangle_j + \sin \alpha_j |1\rangle_j)$$

has, in its $K = 1$ slice, a superposition proportional to $\sum_j f_j | \cdots 1_j \cdots \rangle$. The overall one-excitation weight is again $\approx \lambda e^{-\lambda}$ for large N , while the mean and variance of K follow from the same binomial analysis (we leave those straightforward formulas to the reader to record where convenient).

This completes Step 1: a depth–1 preparation that seeds the exact W component (or a shaped variant) with controllable weight. In the next step we will imprint the momentum ramp e^{ipa_j} by a single layer of local Z phases and then discuss the parity sieve and subsequent “cleaning” that isolate the interacting one-particle packet.

3.2 Step 2 (imprinting momentum)

The goal of this step is to turn the uniform one-excitation slice produced in Step 1 into a plane-wave one-excitation with mean momentum p . Concretely, for each basis vector $| \cdots 1_j \cdots \rangle$ in the $K = 1$ sector we want a phase factor e^{ipa_j} . We will follow the discussion in [25].

A single layer of local Z -rotations. Apply on every site j a Z -rotation with angle ϕ_j ,

$$U = \bigotimes_{j=1}^N R_z(\phi_j), \quad R_z(\phi_j) = \exp\left(-\frac{i}{2}\phi_j \sigma_j^z\right).$$

Let $|x_1 x_2 \dots x_N\rangle$ be a computational basis state with $x_j \in \{0, 1\}$. Using $R_z(\phi_j)|0\rangle_j = e^{-i\phi_j/2}|0\rangle_j$ and $R_z(\phi_j)|1\rangle_j = e^{+i\phi_j/2}|1\rangle_j$, one may factor each site's phase as

$$e^{\pm i\phi_j/2} = e^{-i\phi_j/2} (e^{i\phi_j})^{x_j}.$$

Multiplying over all sites gives

$$U|x_1 \dots x_N\rangle = \exp\left(-\frac{i}{2} \sum_{j=1}^N \phi_j\right) \exp\left(i \sum_{j=1}^N \phi_j x_j\right) |x_1 \dots x_N\rangle.$$

Writing $S = \{j : x_j = 1\}$ for the set of excited positions (of size $K = \sum_j x_j$), this is

$$U|x_1 \dots x_N\rangle = e^{-\frac{i}{2} \sum_j \phi_j} \cdot e^{i \sum_{j \in S} \phi_j} |x_1 \dots x_N\rangle.$$

The first factor is a global phase, independent of the bitstring, and can be dropped. In the $K = 1$ sector, $S = \{j\}$ for some site j , so the state picks up precisely $e^{i\phi_j}$.

Choosing the ramp. Set $\phi_j = p a j$ (with sites labeled $j = 1, \dots, N$; one may also use $j = 0, \dots, N-1$). Then each one-excitation basis vector $|\dots 1_j \dots\rangle$ acquires the desired factor e^{ipa_j} . Acting on the uniform W slice from Step-1 therefore yields the plane-wave W component at momentum p .

A harmless implementation detail is that $\sum_j \phi_j$ contributes only a global phase. If one prefers to eliminate it identically, center the ramp, e.g.

$$\phi_j = p a \left(j - \frac{N+1}{2}\right),$$

which leaves all relative phases unchanged.

Shaped envelopes. If Step-1 was seeded with a nonuniform envelope so that the $K = 1$ slice is proportional to $\sum_j f_j |\dots 1_j \dots\rangle$, the same phase layer produces

$$\sum_{j=1}^N f_j e^{ipa_j} |\dots 1_j \dots\rangle,$$

i.e. a wave packet with envelope f_j and mean momentum p . Because the phases have unit modulus, normalization is unaffected.

After this single depth-1 layer of local Z -rotations, the odd-parity one-excitation component prepared in Step A has become a momentum-selected W (or shaped) state. In the next step we perform the mid-circuit parity sieve and subsequent “cleaning” to isolate the interacting one-particle packet at the chosen momentum.

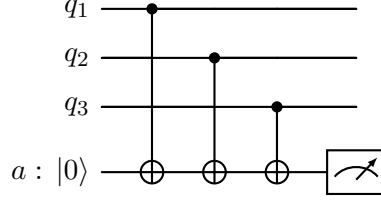


Figure 5: Mid-circuit parity measurement by CNOT accumulation (illustrated for three data qubits; the pattern extends to all N sites). The ancilla ends in $|K \bmod 2\rangle$ and is measured; outcome 1 heralds odd parity. The data qubits are not disturbed apart from a global projector onto the odd subspace.

3.3 Step 3 (mid-circuit parity sieve)

The aim of this step is to *project onto odd Hamming weight* while preserving the positional coherence created in Steps A–B. The observable we measure is the global Z -parity

$$\Pi_Z = \prod_{j=1}^N \sigma_j^z = (-1)^K,$$

where K is the number of excited sites. This measurement distinguishes only “even” vs “odd” K , learning *nothing* about the locations of the excitations; the phase ramp e^{ipa_j} therefore survives intact in the $K = 1$ slice.

It is convenient to describe the measurement by projectors $P_{\text{even}} = \frac{1}{2}(\mathbb{I} + \Pi_Z)$ and $P_{\text{odd}} = \frac{1}{2}(\mathbb{I} - \Pi_Z)$. Acting on the Step-1 state (after the momentum phases of Step-2), the post-selected odd-parity state is $|\Psi_{\text{odd}}\rangle = P_{\text{odd}}|\Psi\rangle/\sqrt{p_{\text{odd}}}$, where the heralding probability is $p_{\text{odd}} = \Pr[\text{odd}]$. With the seeding choice $\sin^2 \alpha = \lambda/N$ from Step-2 (or its site-dependent variant satisfying $\sum_j \sin^2 \alpha_j = \lambda$), the Hamming-weight distribution is well approximated by Poisson(λ) in the large- N limit, giving

$$\Pr[\text{odd}] = e^{-\lambda} \sinh \lambda, \quad \Pr[K=1 \mid \text{odd}] = \frac{\lambda}{\sinh \lambda}.$$

At the natural choice $\lambda = 1$ the odd-parity heralding rate is $e^{-1} \sinh 1 \approx 0.432$, and, *conditional on passing*, roughly 85% of the amplitude already sits in the desired $K = 1$ plane-wave component. In particular, the one-excitation slice after the sieve is precisely

$$\frac{1}{\sqrt{N}} \sum_{j=1}^N e^{ipa_j} |\cdots 1_j \cdots \rangle \quad (\text{or } \sum_j f_j e^{ipa_j} |\cdots 1_j \cdots \rangle \text{ if Step A used a shaped envelope}).$$

A compact mid-circuit parity circuit (CNOT accumulation). One standard realization uses a single ancilla qubit: prepare the ancilla in $|0\rangle$; apply CNOTs from each data qubit (control) to the ancilla (target); measure the ancilla in the Z basis mid-circuit; keep runs with outcome “1” (odd parity) and discard the rest. Because the data qubits are never targeted by these CNOTs, their positional coherence and momentum phases are unaffected.

Remarks. The alternative “phase-kickback” version prepares the ancilla in $|+\rangle$, applies C- Z from each data qubit onto the ancilla, and measures the ancilla in the X basis, with $|-\rangle$ heralding odd parity. Either implementation measures Π_Z and therefore commutes with the local Z -phase layer of Step B, guaranteeing that the momentum profile is preserved. In what follows we simply condition on the odd-parity outcome and proceed to the cleaning step that removes the small residual $K \geq 3$ admixture while keeping the total momentum fixed.

Step 4: Cleaning

After Steps 1–3 the post-selected state lies in the odd Z –parity sector and carries total lattice momentum p . Its one-excitation slice already has the desired phase ramp (and optional envelope), but a small admixture of higher odd Hamming weights ($K = 3, 5, \dots$) remains at the same total momentum. The purpose of this step is to suppress that admixture while *preserving* momentum p and Z –parity, yielding the interacting one-particle packet.

Symmetry protection. Let T denote lattice translation by one site and $\Pi_Z = \prod_j \sigma_j^z$ the global Z –parity measured in Step 3. We choose a shallow unitary $U(\vec{\theta})$ that *commutes* with both symmetries,

$$[U(\vec{\theta}), T] = 0, \quad [U(\vec{\theta}), \Pi_Z] = 0,$$

so that $U(\vec{\theta})$ maps momentum– p , odd–parity states to momentum– p , odd–parity states. This guarantees that cleaning cannot leak amplitude to other momentum or parity sectors.

A minimal translation-invariant, parity-preserving ansatz. An effective choice is a short product of exponentials of *sums repeated on every bond or site*, which ensures translation invariance, together with generators that contain only an even number of spin-flip operators to preserve Π_Z . A convenient three-parameter form is

$$U(\theta_1, \theta_2, \theta_3) = \exp\left(i \theta_1 \sum_j \sigma_j^z \sigma_{j+1}^z\right) \exp\left(i \theta_2 \sum_j \sigma_j^x \sigma_{j+1}^x\right) \exp\left(i \theta_3 \sum_j \sigma_j^z\right), \quad (16)$$

with periodic boundary conditions implicit in the sums. The first and third factors are diagonal in the computational basis; the middle factor flips spins in pairs and therefore preserves Z –parity. Each exponential compiles to a constant two-qubit depth on a nearest-neighbor architecture by staggering bonds.

Energy minimization inside the symmetry block. Let $|\Psi_{\text{odd},p}\rangle$ denote the Step-3 state. We determine $\vec{\theta}$ by minimizing the Rayleigh quotient

$$\mathcal{E}(\vec{\theta}) = \frac{\langle \Psi_{\text{odd},p} | U(\vec{\theta})^\dagger H U(\vec{\theta}) | \Psi_{\text{odd},p} \rangle}{\langle \Psi_{\text{odd},p} | \Psi_{\text{odd},p} \rangle}.$$

Because $U(\vec{\theta})$ preserves momentum and parity, this optimization is confined to the (p, odd) block of H . By the Rayleigh–Ritz principle, decreasing \mathcal{E} increases the overlap with the lowest-energy eigenstate in that block; at the optimum $\vec{\theta}_*$ one has

$$U(\vec{\theta}_*) |\Psi_{\text{odd},p}\rangle \approx |1_p\rangle,$$

the interacting one-particle state at total momentum p . A practical confirmation is the smallness of the *energy variance* $\langle H^2 \rangle - \langle H \rangle^2$ on the cleaned state.

Measurements and shallow depth. Evaluating $\mathcal{E}(\vec{\theta})$ requires only translation-averaged few-body correlators because the generators in (16) are uniform sums. Gradients may be obtained by small finite differences or standard parameter-shift rules, but in practice a coarse grid over $\theta_{1,2,3}$ already suffices because the parameter space is low-dimensional. Each layer in (16) is a translation-invariant brickwork; on a ring it is implemented by identical two-qubit gates on alternating bonds, giving a total two-qubit depth of only a few layers.

A circuit sketch for one translation-invariant bond layer. The figure illustrates the uniform application of a two-qubit gate $e^{i\theta_2 \sigma^x \otimes \sigma^x}$ on every bond; staggering even and odd bonds yields constant depth. The ZZ layer has the same pattern.

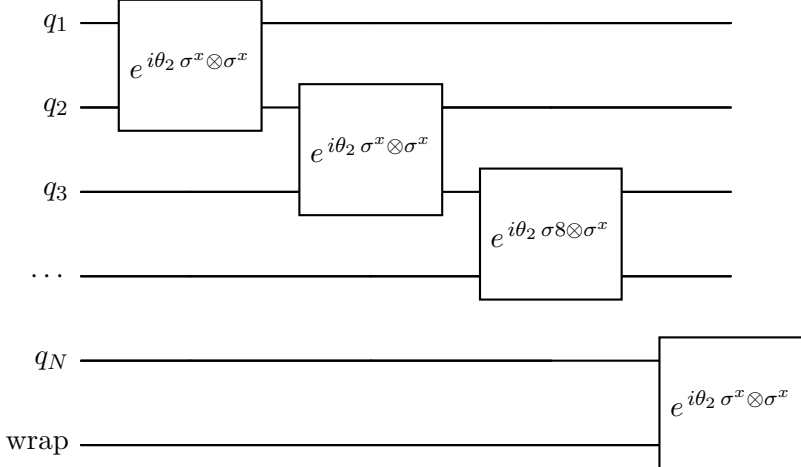


Figure 6: A translation-invariant two-qubit layer acting identically on every bond ($j, j+1$) around the ring. Staggering over even/odd bonds realizes constant two-qubit depth.

Outcome. Applying $U(\vec{\theta}_*)$ to the Step-3 state variationally projects it onto the lowest-energy state in the (p, odd) sector. The result is an interacting one-particle wave packet with the prescribed momentum and envelope, ready to be used (in duplicate, with $\pm p$ and well-separated supports) for real-time collision experiments and the extraction of phase shifts, Wigner time delays, and inelastic probabilities.

3.4 Choosing the cleaning angles $\vec{\theta}$

The cleaning unitary $U(\vec{\theta})$ in (16) is fixed by a tiny set of angles $\vec{\theta} = (\theta_1, \theta_2, \theta_3)$. The goal is to lower the Rayleigh quotient

$$\mathcal{E}(\vec{\theta}) = \frac{\langle \Psi_{\text{odd},p} | U(\vec{\theta})^\dagger H U(\vec{\theta}) | \Psi_{\text{odd},p} \rangle}{\langle \Psi_{\text{odd},p} | \Psi_{\text{odd},p} \rangle},$$

while staying inside the (p, odd) symmetry block. In practice one can choose $\vec{\theta}$ with very few measurements by exploiting the fact that \mathcal{E} is smooth and nearly quadratic in each angle near the optimum. Three equally simple routes are useful; any one of them suffices.

A parabolic line search with coordinate sweeps. Fix two angles and scan the third over three small values, fit a parabola, and jump to its minimum. Concretely, for a chosen step size s (e.g. $s = 0.05\text{--}0.2$ radians), measure $E_- = \mathcal{E}(\theta_i = -s)$, $E_0 = \mathcal{E}(0)$, $E_+ = \mathcal{E}(+s)$ with the other angles held fixed. The one-dimensional quadratic minimizer is

$$\theta_i^* = s \frac{E_- - E_+}{2(E_- - 2E_0 + E_+)}.$$

Update $\theta_i \leftarrow \theta_i^*$ and sweep $i = 1, 2, 3$ once or twice. Stop when the energy decrease per sweep is within noise and the energy variance $\langle H^2 \rangle - \langle H \rangle^2$ ceases to improve. In many cases θ_3 contributes little and may be omitted, leaving a two-angle search.

A parameter-shift gradient step. If the layers are implemented with Pauli generators (e.g. XX, ZZ, Z), the parameter-shift identity yields an exact derivative with two evaluations along each coordinate:

$$\frac{\partial \mathcal{E}}{\partial \theta_i} = \frac{1}{2} \left[\mathcal{E}(\theta_i + \frac{\pi}{2}) - \mathcal{E}(\theta_i - \frac{\pi}{2}) \right].$$

A single small update $\theta_i \leftarrow \theta_i - \eta \partial_{\theta_i} \mathcal{E}$ with $\eta \sim 0.1\text{--}0.3$ typically suffices; confirm with the variance proxy that the state sharpened toward an eigenstate.

A small-angle quadratic jump. Near $\vec{\theta} = \mathbf{0}$ one may write $\mathcal{E}(\vec{\theta}) \approx \mathcal{E}_0 + \vec{g} \cdot \vec{\theta} + \frac{1}{2} \vec{\theta}^\top H \vec{\theta}$. Estimate the gradient and diagonal Hessian by central and second differences at $\pm s$,

$$g_i \approx \frac{\mathcal{E}(+s) - \mathcal{E}(-s)}{2s}, \quad H_{ii} \approx \frac{\mathcal{E}(+s) - 2\mathcal{E}(0) + \mathcal{E}(-s)}{s^2},$$

neglect off-diagonal couplings on the first pass, and jump to $\theta_i^* \approx -g_i/H_{ii}$. A brief parabolic polish as above can follow.

What is actually measured. Because $U(\vec{\theta})$ and H are translation-invariant sums, $\mathcal{E}(\vec{\theta})$ reduces to a handful of translation-averaged few-body correlators, such as $\langle \sigma_j^z \sigma_{j+1}^z \rangle$, $\langle \sigma_j^x \rangle$, and $\langle \sigma_j^z \rangle$, which can be estimated with good signal-to-noise by averaging over all sites/bonds. As a convergence check, monitor the energy variance $\text{Var}(H) = \langle H^2 \rangle - \langle H \rangle^2$; it decreases as the state approaches the interacting one-particle eigenstate in the (p, odd) block and plateaus when further improvement is negligible.

Defaults that work out of the box. Initialize $\vec{\theta} = \mathbf{0}$ and perform a single coordinate sweep with the parabolic formula using $s = 0.1$ rad. Repeat once. If desired, apply one gradient step from the parameter-shift rule. In all cases the unitary $U(\vec{\theta})$ preserves momentum and Z -parity by construction, so the momentum profile set in Steps 1–3 remains intact while the residual $K \geq 3$ weight is variationally suppressed.

3.5 2-particle scattering

We are now in a position to discuss 2-particle scattering in this theory. We will set up initial states with momenta p and $-p$. The situation is depicted in the figure.

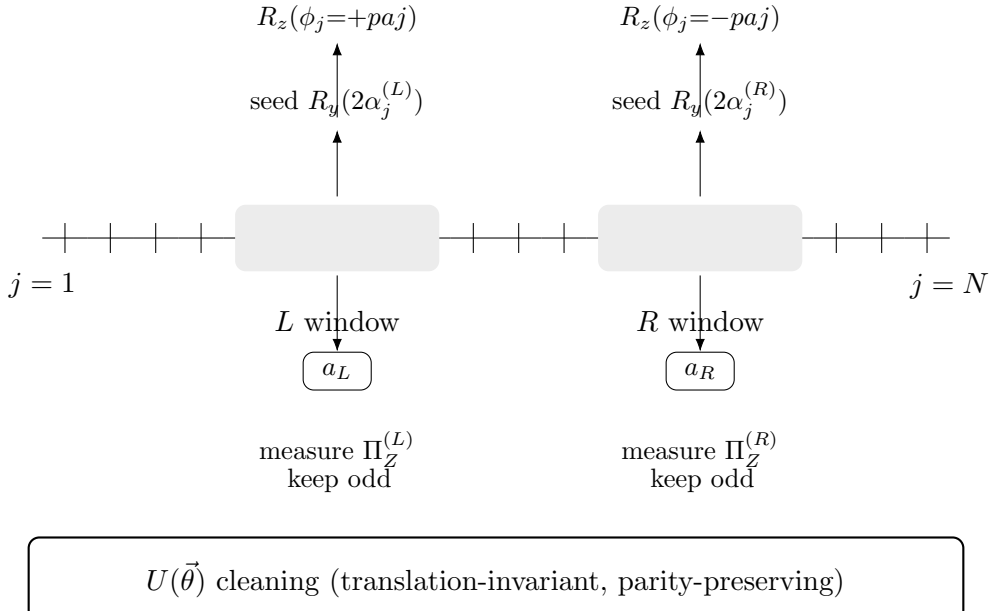


Figure 7: Two-particle center-of-mass state preparation. Seed small, shaped rotations only inside two disjoint windows L and R , imprint opposite momentum ramps ($+p$ on L , $-p$ on R), perform *block-wise* odd-parity measurements to herald one excitation in each block, then apply a shallow translation-invariant cleaner $U(\vec{\theta})$ to project onto the interacting one-particle in each block. Packets are well separated at $t=0$, so the total momentum is zero.

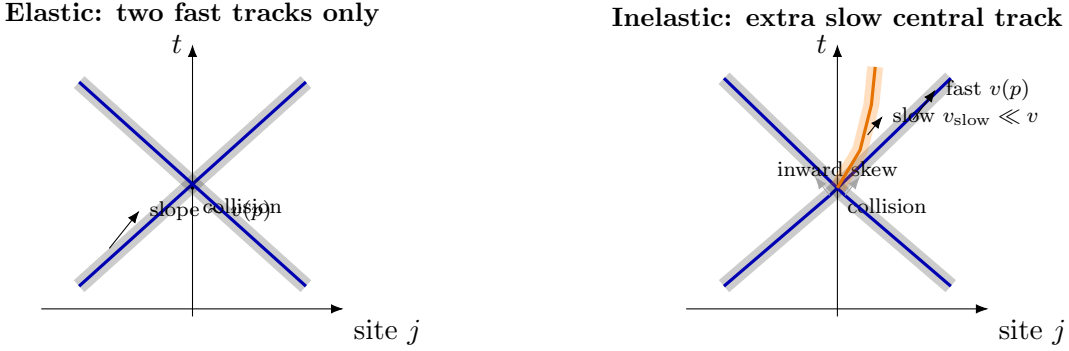


Figure 8: Schematic “energy-density tracks” (space–time ridges of vacuum-subtracted local energy) for two-packet scattering. **Left:** Below inelastic threshold, two clean outer ridges depart the collision with slopes set by the group velocity $v(p)$. **Right:** Above threshold, the outer ridges exhibit an inward skew after impact and a third, slow central ridge appears, signaling inelastic production of a heavier excitation. This is a qualitative cartoon, not data.

Vacuum–subtracted energy–density tracks as an inelasticity diagnostic

On the lattice Ising Hamiltonian

$$H(J, h_x, h_z) = -J \sum_j \sigma_j^z \sigma_{j+1}^z - h_x \sum_j \sigma_j^x - h_z \sum_j \sigma_j^z,$$

a convenient local energy density is built by assigning each bond term once and each on-site term to site j :

$$h_j \equiv -J \sigma_j^z \sigma_{j+1}^z - \frac{h_x}{2} (\sigma_j^x + \sigma_{j-1}^x) - \frac{h_z}{2} (\sigma_j^z + \sigma_{j-1}^z).$$

(Any symmetric partition of the on-site pieces is acceptable; the diagnostics below are insensitive to this choice.) Following Refs. [25, 26], we *vacuum–subtract* the expectation value to remove static backgrounds and visualize transport:

$$\Delta \varepsilon_j(t) \equiv \langle \psi(t) | h_j | \psi(t) \rangle - \langle 0 | h_j | 0 \rangle.$$

Space–time tracks. Plotting $\Delta \varepsilon_j(t)$ as a function of site j and time t yields a heatmap with bright, ballistic *tracks*. For two counter-propagating packets in the center-of-mass frame, purely elastic scattering produces two clean outer ridges which depart the collision region with slopes set by the group velocity $v(p)$. As the collision energy crosses the first inelastic threshold, Refs. [25, 26] report two robust signatures: (i) an *inward skew* of each outgoing bump shortly after impact (the outgoing one-particle packets are pulled toward the center by probability flux into additional channels); and, at later times, (ii) the emergence of a *slower central ridge* — a low-velocity energy–density track associated with the heavier product in $1+1 \rightarrow 1+2$ processes. On present hardware, the early-time skew is especially clear and noise-resilient [25].

Correlator “track finders”. The MPS companion study [26] sharpens these features by conditioning on the locations of the fast packets using energy–density correlators. Two-point functions $C_2(j, t; j', t) = \langle \Delta \varepsilon_j(t) \Delta \varepsilon_{j'}(t) \rangle$ already correlate opposite-moving tracks; three-point correlators $C_3(j_L, j_R, j_c; t)$ peak sharply when j_L, j_R sit on the outer ridges and j_c on the slow central track, enforcing the kinematics of the inelastic channel in the center-of-mass frame. This provides a quantitative, basis-independent way to identify multi-track final states in the post-collision wavefunction.

A scalar diagnostic (windowed central energy). For a compact number to plot versus center-of-mass energy, define a window of width w centered at the collision point n_0 and integrate

$$\Delta E_{\text{center}}(t; w) = \sum_{n=n_0-\lfloor w/2 \rfloor}^{n_0+\lfloor w/2 \rfloor} \Delta \varepsilon_n(t).$$

In the elastic regime $\Delta E_{\text{center}}(t)$ drops rapidly after the packets separate; when inelastic production occurs it exhibits a sustained tail (or a delayed peak) reflecting the slow central track [25, 26]. Averaging $\Delta E_{\text{center}}(t)$ over a late-time window (before ring wrap-around) yields a robust scalar that correlates closely with the inelastic probability extracted by sector projectors in numerics [26].

Practical notes. All required observables reduce to translation-averaged Pauli expectations $\langle \sigma_j^z \sigma_{j+1}^z \rangle_t$, $\langle \sigma_j^x \rangle_t$, and $\langle \sigma_j^z \rangle_t$, measured both for the scattering state and the prepared vacuum and then subtracted. The same readout supports (i) space-time heatmaps, (ii) two-/three-point correlator scans to localize tracks, and (iii) the scalar $\Delta E_{\text{center}}(t; w)$. On hardware, early-time snapshots already reveal the skewed outer bumps; longer evolutions make the central slow ridge visible and match tensor-network benchmarks [25, 26].

A Miscellaneous points

A.1 Rapidities, crossing, and the physical strip

The physical strip for θ is $0 \leq \Im \theta \leq \pi$. Crossing symmetry identifies s -channel and t -channel processes via $\theta \rightarrow i\pi - \theta$. Simple poles at $0 < \Im \theta < \pi$ correspond to bound states with residues proportional to the on-shell three-point couplings. Cuts associated with multiparticle thresholds start at real θ beyond kinematic onsets; in integrable theories these are absent in two-body amplitudes.

A.2 Minimal CFT recap for benchmarks

The Ising CFT is the minimal model $\mathcal{M}(4, 3)$ with $c = \frac{1}{2}$ and primaries $\{\psi, \sigma, \epsilon\}$ of weights $(0, 0)$, $(\frac{1}{16}, \frac{1}{16})$, and $(\frac{1}{2}, \frac{1}{2})$. On a cylinder of circumference L , energies are $E_n(L) = e_0 L + \frac{2\pi v}{L}(-\frac{c}{12} + \Delta_n + \bar{\Delta}_n)$. Measuring this spectrum at criticality fixes v and validates the normalization used away from criticality [1, 2]. This also sets the scale for comparing lattice and continuum quantities.

A.3 Truncated Conformal Space (TCSA) as a physics tool

Although our results later will not depend on any particular method, it is helpful to know that many quantitative checks in the literature use TCSA [11]: one truncates the Ising CFT Hilbert space on a circle and turns on τ and g , obtaining finite- L spectra and matrix elements directly comparable to the definitions in this chapter. This is often used to benchmark mass ratios along the E_8 line and to study confinement and inelasticity when $\tau g \neq 0$.

Reading guide

For an overview of integrable QFT and statistical models see [3]. E_8 scattering and mass ratios originate in [18]; form-factor technology is reviewed in [4, 5]. Finite-volume effects stem from [7, 8]. Confinement and meson spectra in the nonintegrable Ising regime are discussed in [9, 10]. CFT finite-size methods are in [1, 2]. Experimental signatures of E_8 in quasi-1D magnets provide useful physical context (see, e.g., Coldea *et al.* 2010).

B Classical vs. Quantum Ising Models

B.1 Classical Ising model (statistical)

Consider spins $s_i = \pm 1$ on a d -dimensional lattice with Hamiltonian

$$H_{\text{cl}}(s) = -J \sum_{\langle ij \rangle} s_i s_j - h \sum_i s_i, \quad (17)$$

and partition function $Z_{\text{cl}} = \sum_{\{s\}} e^{-\beta H_{\text{cl}}}$. Thermal fluctuations (controlled by $T = 1/\beta$) drive order-disorder transitions in $d \geq 2$; e.g. the 2D zero-field model has a finite- T critical point (Onsager).

B.2 Quantum Ising / TFIM (Hamiltonian)

The transverse-field Ising model (TFIM) replaces c -number spins by Pauli operators on a Hilbert space:

$$H_{\text{q}} = -J \sum_{\langle ij \rangle} \sigma_i^z \sigma_j^z - h_z \sum_i \sigma_i^z - \Gamma \sum_i \sigma_i^x, \quad (18)$$

with $[\sigma^x, \sigma^z] \neq 0$. Quantum fluctuations originate from the noncommuting transverse field Γ . At $T = 0$ this model exhibits a *quantum* phase transition tuned by Γ/J (for $h_z = 0$ in 1D, the critical point is at $\Gamma = J$).

B.3 Quantum \leftrightarrow Classical mapping (expanded derivation)

We derive the mapping of the d -dimensional transverse-field Ising model (TFIM)

$$H_{\text{q}} = -J \sum_{\langle ij \rangle} \sigma_i^z \sigma_j^z - h_z \sum_i \sigma_i^z - \Gamma \sum_i \sigma_i^x$$

to an anisotropic classical Ising model in $d+1$ dimensions by making all algebraic steps explicit.

Step 1: Lie–Trotter decomposition. Split $H_{\text{q}} = H_z + H_x$ with

$$H_z = -J \sum_{\langle ij \rangle} \sigma_i^z \sigma_j^z - h_z \sum_i \sigma_i^z, \quad H_x = -\Gamma \sum_i \sigma_i^x.$$

For inverse temperature β , write the partition function

$$Z = \text{Tr } e^{-\beta H_{\text{q}}} = \lim_{M \rightarrow \infty} \text{Tr} \left(e^{-\Delta\tau H_z} e^{-\Delta\tau H_x} \right)^M, \quad \Delta\tau \equiv \beta/M,$$

with Trotter error $\mathcal{O}((\Delta\tau)^2)$ that vanishes as $M \rightarrow \infty$. Note: all terms within H_z commute with each other, and all terms within H_x commute with each other, so no further Trotter breakup is needed inside those blocks.

Step 2: Insert complete sets in the σ^z basis. Let $\{|s(\tau)\rangle\}$ denote simultaneous eigenstates of all $\{\sigma_i^z\}$ with eigenvalues $s_i(\tau) = \pm 1$, one such basis at each time slice $\tau = 1, \dots, M$. Insert M resolutions of the identity:

$$\mathbf{1} = \sum_{\{s(\tau)\}} |s(\tau)\rangle \langle s(\tau)|, \quad \text{and use periodicity } s(M+1) \equiv s(1) \text{ (due to the trace).}$$

This gives

$$Z = \sum_{\{s(\tau)\}} \prod_{\tau=1}^M \langle s(\tau) | e^{-\Delta\tau H_z} e^{-\Delta\tau H_x} | s(\tau+1) \rangle.$$

Step 3: Evaluate the diagonal (spatial) factor. H_z is diagonal in the σ^z basis, hence

$$\langle s(\tau) | e^{-\Delta\tau H_z} | s(\tau) \rangle = \exp \left[\Delta\tau J \sum_{\langle ij \rangle} s_i(\tau) s_j(\tau) + \Delta\tau h_z \sum_i s_i(\tau) \right].$$

This yields a spatial Ising weight with coupling

$$K_s \equiv \Delta\tau J, \quad h_s \equiv \Delta\tau h_z.$$

Step 4: Evaluate the off-diagonal (temporal) factor one spin at a time. Because $H_x = -\Gamma \sum_i \sigma_i^x$ factorizes across sites,

$$\langle s(\tau) | e^{-\Delta\tau H_x} | s(\tau+1) \rangle = \prod_{i=1}^N \langle s_i(\tau) | e^{\Delta\tau \Gamma \sigma_i^x} | s_i(\tau+1) \rangle.$$

So it suffices to compute, for a single spin with $a \equiv \Delta\tau \Gamma$,

$$T_x(a) \equiv e^{a\sigma^x} = \cosh a \mathbf{1} + \sinh a \sigma^x.$$

In the σ^z eigenbasis $\{|+\rangle, |-\rangle\}$ (with $\sigma^z|\pm\rangle = \pm|\pm\rangle$ and $\sigma^x|\pm\rangle = |\mp\rangle$),

$$T_x(a) = \begin{pmatrix} \cosh a & \sinh a \\ \sinh a & \cosh a \end{pmatrix}_{\{\sigma^z\text{-basis}\}}.$$

We now parameterize the matrix element between $s, s' \in \{+1, -1\}$ as a nearest-neighbor Ising weight

$$\langle s | T_x(a) | s' \rangle = A(a) e^{K_\tau(a)s s'}.$$

Matching the two independent entries,

$$\cosh a = A e^{K_\tau}, \quad \sinh a = A e^{-K_\tau}.$$

Divide the equations to solve for K_τ and then back-substitute for A :

$$e^{2K_\tau} = \frac{\cosh a}{\sinh a} = \coth a \Rightarrow K_\tau(a) = \frac{1}{2} \ln \coth a, \quad A(a) = \sqrt{\sinh a \cosh a}.$$

Thus the single-spin temporal transfer factor is strictly positive (no sign problem) and can be written purely as an Ising coupling times a site-local normalization.

Step 5: Assemble the classical partition function. Collecting all slices and sites, we obtain

$$\begin{aligned} Z &= \sum_{\{s_i(\tau)=\pm 1\}} \left[\prod_{\tau,i} A(\Delta\tau \Gamma) \right] \exp \left[K_s \sum_{\tau} \sum_{\langle ij \rangle} s_i(\tau) s_j(\tau) + K_\tau \sum_i \sum_{\tau} s_i(\tau) s_i(\tau+1) + h_s \sum_{i,\tau} s_i(\tau) \right] \\ &\equiv \mathcal{N} Z_{\text{cl}}(K_s, K_\tau, h_s), \end{aligned}$$

with overall normalization

$$\mathcal{N} = \left[A(\Delta\tau \Gamma) \right]^{NM} = \left(\sqrt{\sinh(\Delta\tau \Gamma) \cosh(\Delta\tau \Gamma)} \right)^{NM}.$$

Therefore, the TFIM maps to an anisotropic classical Ising model in $d+1$ dimensions with couplings

$$K_s = \Delta\tau J, \quad K_\tau = \frac{1}{2} \ln \coth(\Delta\tau \Gamma), \quad h_s = \Delta\tau h_z.$$

The classical spins $s_i(\tau)$ live on a $(d+1)$ -dimensional space–(imaginary)–time lattice with periodic boundary condition $s_i(M+1) = s_i(1)$ in the time direction.

Asymptotics and anisotropy. In the Trotter limit $\Delta\tau \rightarrow 0$ (fixed Γ), $a = \Delta\tau\Gamma \rightarrow 0$ and

$$\coth a \sim \frac{1}{a} + \mathcal{O}(a), \quad K_\tau \sim \frac{1}{2} \ln \frac{1}{\Delta\tau\Gamma} \rightarrow \infty,$$

so time-like bonds are very strong compared to space-like bonds $K_s = \Delta\tau J \rightarrow 0$. Physical (isotropic) scaling emerges after rescaling the time lattice spacing so that correlation lengths in space and (imaginary) time scale with a common emergent velocity (dynamical exponent $z = 1$ for the TFIM).

Recovering the quantum critical point. For the $d=1$ TFIM (1+1D classical Ising), the exact classical critical line is

$$\sinh(2K_s) \sinh(2K_\tau) = 1.$$

Substituting $K_s = \Delta\tau J$ and $K_\tau = \frac{1}{2} \ln \coth(\Delta\tau\Gamma)$ and expanding for small $\Delta\tau$ reproduces $\Gamma = J$ in the continuum limit—i.e. the quantum critical point maps onto the classical critical manifold.

Stoquasticity (positivity of weights). In the σ^z basis, all factors are nonnegative:

$$\langle s(\tau) | e^{-\Delta\tau H_z} | s(\tau) \rangle > 0, \quad \langle s(\tau) | e^{-\Delta\tau H_x} | s(\tau+1) \rangle > 0,$$

so the resulting classical weight is positive definite. This is the content of “stoquasticity” for the TFIM and explains why worldline/path-integral QMC has no sign problem here.

Recipe (at a glance).

1. Choose M and $\Delta\tau = \beta/M$; write $Z = \text{Tr}(e^{-\Delta\tau H_z} e^{-\Delta\tau H_x})^M$.
2. Insert σ^z resolutions of identity between every factor.
3. Read off $K_s = \Delta\tau J$ and $h_s = \Delta\tau h_z$ from the H_z diagonal weight.
4. For each site, rewrite $\langle s | e^{\Delta\tau\Gamma\sigma^x} | s' \rangle = A e^{K_\tau ss'}$ with $K_\tau = \frac{1}{2} \ln \coth(\Delta\tau\Gamma)$.
5. Drop the overall constant \mathcal{N} if you only care about normalized observables; keep it if you want the absolute free energy.

Common pitfalls.

- *Forgetting periodicity in imaginary time:* the trace enforces $s_i(M+1) = s_i(1)$.
- *Mixing bases:* only insert σ^z identities; evaluating H_x in σ^x and H_z in σ^z simultaneously is inconsistent.
- *Over-Trotterizing H_z :* its terms already commute; unnecessary splitting just adds book-keeping.
- *Discarding \mathcal{N} prematurely:* thermodynamics depending on absolute free energy (e.g. specific heat) requires keeping track of \mathcal{N} , though it cancels in most normalized correlators.

Checks and limits.

- $\Gamma \rightarrow 0$ ($a \rightarrow 0$): $K_\tau \rightarrow \infty$ locks $s_i(\tau)$ constant in time; one recovers the classical d -dimensional Ising model with coupling $K_s = \beta J$ (since $\Delta\tau M = \beta$).
- $J \rightarrow 0$: $K_s \rightarrow 0$ decouples spatial neighbors; the model reduces to independent 1D classical chains in the time direction with coupling K_τ —i.e. paramagnet along x .

Summary box.

$$Z_{\text{TFIM}} = \mathcal{N} \sum_{\{s_i(\tau) = \pm 1\}} \exp \left[K_s \sum_{\tau, \langle ij \rangle} s_i(\tau) s_j(\tau) + K_\tau \sum_{i, \tau} s_i(\tau) s_i(\tau+1) + h_s \sum_{i, \tau} s_i(\tau) \right],$$

$$K_s = \Delta\tau J, \quad K_\tau = \frac{1}{2} \ln \coth(\Delta\tau\Gamma), \quad h_s = \Delta\tau h_z,$$

$$\mathcal{N} = (\sqrt{\sinh(\Delta\tau\Gamma)} \cosh(\Delta\tau\Gamma))^{NM}, \quad s_i(M+1) = s_i(1).$$

B.4 Exact solution of the 1D TFIM at $h_z = 0$ (outline)

Adopt periodic boundary conditions on N sites and set $a = \hbar = 1$. A Jordan–Wigner (JW) transformation maps spins to fermions,

$$\sigma_j^z = 1 - 2 c_j^\dagger c_j, \quad \sigma_j^x = (c_j^\dagger + c_j) \exp \left(i\pi \sum_{\ell < j} c_\ell^\dagger c_\ell \right), \quad (19)$$

which turns Eq. (18) (with $h_z = 0$) into a quadratic BCS-like Hamiltonian. After Fourier transform and a Bogoliubov rotation one obtains

$$H = \sum_{k \in \text{BZ}} \varepsilon_k \left(\gamma_k^\dagger \gamma_k - \frac{1}{2} \right), \quad \varepsilon_k = 2\sqrt{(\Gamma - J \cos k)^2 + (J \sin k)^2} = 2\sqrt{\Gamma^2 + J^2 - 2\Gamma J \cos k}. \quad (20)$$

The gap closes at $k = 0$ when $\Gamma = J$, identifying the quantum critical point. At criticality, low- k excitations are relativistic with velocity $v = 2J$:

$$\varepsilon_k \xrightarrow[\Gamma=J]{k \rightarrow 0} 2J|k|, \quad \Delta_L \sim \frac{\pi v}{L} \quad (L = N). \quad (21)$$

B.5 Phases, observables, and entanglement

For $h_z = 0$ in 1D:

$$\Gamma/J < 1 : \quad \text{ferromagnet, } m_z = \lim_{|i-j| \rightarrow \infty} \langle \sigma_i^z \sigma_j^z \rangle^{1/2} \neq 0, \text{ gapped,} \quad (22)$$

$$\Gamma/J > 1 : \quad \text{paramagnet polarized along } x, \text{ gapped,} \quad (23)$$

$$\Gamma/J = 1 : \quad \text{quantum critical (Ising CFT, } c = \frac{1}{2}). \quad (24)$$

Equal-time correlations cross over from exponential decay (gapped) to power-law at criticality. The bipartite entanglement entropy of a block of length ℓ obeys

$$S(\ell) = \begin{cases} \frac{c}{3} \ln \ell + \text{const}, & \text{critical } (c = \frac{1}{2}), \\ \text{area law (saturating)}, & \text{gapped phases,} \end{cases} \quad (25)$$

a sharp quantum signature with no classical counterpart.

B.6 Quick comparison table

Aspect	Classical Ising	Quantum Ising (TFIM)
Variables	$s_i = \pm 1$	Pauli operators $\sigma_i^{x,z}$
Fluctuations	Thermal (T)	Quantum (Γ noncommutes)
Dynamics	Added phenomenologically	Intrinsic unitary e^{-iHt}
Transitions	Thermal ($d \geq 2$)	Quantum at $T = 0$ (tuned by Γ/J)
Mapping	—	$dD \leftrightarrow (d+1)D$ classical (Trotter)
Simulation	Classical MC, exact results in 2D ($h = 0$)	JW/DMRG (1D), QMC (stoquastic), TN, QC

B.7 Notes for quantum computing

The 1D TFIM is exactly solvable (free fermions), enabling: (i) calibration/benchmarking of variational and Trotterized algorithms against exact spectra (20); (ii) quench dynamics with known light-cone velocity v (21); (iii) entanglement scaling tests (25). In higher d , stoquasticity permits sign-problem-free worldline QMC for equilibrium, while real-time dynamics remains a natural task for quantum circuits.

C Unitarity in 1+1D two-particle scattering: elastic vs. inelastic

Setup and normalization. Work in the center-of-mass (CM) basis of two-particle states

$$|p\rangle_2 \equiv |p, -p\rangle, \quad \langle p'|p\rangle_2 = (2\pi) 2E_p \delta(p' - p),$$

with $E_p = \sqrt{m^2 + p^2}$. Translation invariance implies momentum conservation, so two-to-two matrix elements in the CM basis are diagonal in p .

Start from operator unitarity. Unitarity is

$$SS^\dagger = \mathbf{1}.$$

Sandwiching between CM states and inserting a resolution of the identity over a complete set of out-states $\{|k\rangle_2\} \cup \{|X\rangle_{\neq 2}\}$ (two-particle and all multi-particle sectors):

$$\begin{aligned} \langle q|SS^\dagger|p\rangle_2 &= \sum_k \langle q|S|k\rangle_2 \langle k|S^\dagger|p\rangle + \sum_{X \neq 2} \langle q|S|X\rangle \langle X|S^\dagger|p\rangle \\ &= \langle q|p\rangle_2 = (2\pi) 2E_p \delta(q - p). \end{aligned} \tag{26}$$

Parameterizing the elastic matrix element. By CM momentum conservation the elastic $2 \rightarrow 2$ matrix element is diagonal:

$$2\langle q|S|p\rangle_2 = (2\pi) 2E_p \delta(q - p) S_2(p),$$

which defines the (single “partial wave” in 1+1D) two-body S -eigenvalue $S_2(p)$.

Purely elastic scattering

If no inelastic channels are kinematically open, the second sum in (26) vanishes:

$$\sum_{X \neq 2} \langle q|S|X\rangle \langle X|S^\dagger|p\rangle = 0,$$

and (26) reduces to ²

$$(2\pi) 2E_p \delta(q-p) |S_2(p)|^2 = (2\pi) 2E_p \delta(q-p).$$

Hence

$$|S_2(p)| = 1 \implies S_2(p) = e^{2i\delta(p)},$$

with a real phase shift $\delta(p)$ (time-reversal and real analyticity ensure $\delta \in \mathbb{R}$). Therefore,

$${}_2\langle q|S|p\rangle_2^{(\text{elastic})} = (2\pi) 2E_p \delta(q-p) e^{2i\delta(p)}$$

i.e. the two-body matrix element is a pure phase multiplying the momentum delta.

Inelastic scattering open

When channels with $n \geq 3$ final particles are open, the second term in (26) is nonzero. Using the elastic parameterization above, unitarity gives

$$(2\pi) 2E_p \delta(q-p) |S_2(p)|^2 + \sum_{X \neq 2} \langle q|S|X\rangle \langle X|S^\dagger|p\rangle = (2\pi) 2E_p \delta(q-p). \quad (27)$$

Rotational (here: parity) and translational invariance force the inelastic sum to be proportional to $(2\pi) 2E_p \delta(q-p)$. Defining the *inelasticity* (absorption) parameter $\eta(p) \in [0, 1]$ by

$$|S_2(p)| \equiv \eta(p), \quad 1 - \eta^2(p) = \frac{1}{(2\pi) 2E_p} \sum_{X \neq 2} \langle p|S^\dagger|X\rangle \langle X|S|p\rangle_2,$$

we may write the most general solution as

$$S_2(p) = \eta(p) e^{2i\delta(p)},$$

with $\delta(p) \in \mathbb{R}$. Consequently,

$${}_2\langle q|S|p\rangle_2^{(\text{inelastic})} = (2\pi) 2E_p \delta(q-p) \eta(p) e^{2i\delta(p)}, \quad 0 \leq \eta(p) \leq 1$$

and probability conservation becomes

$$1 - \eta^2(p) = \sum_{n \geq 3} \int d\Phi_n |\mathcal{M}_{2 \rightarrow n}(p \rightarrow \{k_i\})|^2,$$

i.e. the loss from the elastic amplitude equals the total inclusive probability into all inelastic channels (the 1+1D optical theorem in this single-channel setting).

Remarks.

- In 1+1D there is only one independent “partial wave” in the CM frame; the above $S_2(p)$ coincides with that single eigenvalue. For identical particles (bosons/fermions) the exchange symmetry is already baked into the definition of the two-body sector; the form $S_2 = \eta e^{2i\delta}$ still holds.
- In integrable models (e.g. massive Ising without a longitudinal field) $\eta(p) = 1$ exactly and scattering is purely elastic; relevant deformations that break integrability open channels, $\eta(p) < 1$, and encode inelasticity in the deficit $1 - \eta^2$.

²Obviously we need an identity like $\sum_k (2\pi)^2 (2E_p)^2 \delta(k-p) \delta(k-q) = (2\pi)(2E_p) \delta(p-q)$. Figure out where this comes from!

D State preparation in Qiskit and why we prefer the W-state route

D.1 What “state preparation” means

Given n qubits initially in $|0\rangle^{\otimes n}$, *state preparation* is the task of applying a circuit U such that

$$U|0\rangle^{\otimes n} = |\psi_{\text{target}}\rangle, \quad |\psi_{\text{target}}\rangle = \sum_{x=0}^{2^n-1} \alpha_x |x\rangle. \quad (28)$$

Depending on structure in $\{\alpha_x\}$, the circuit can be extremely shallow (product states) or exponentially large (generic amplitude encodings). Qiskit exposes several families of methods that cover this spectrum.

D.2 Cheap cases: basis and product states

Computational basis states. To prepare a basis state $|b_{n-1}\dots b_1 b_0\rangle$ with $b_j \in \{0, 1\}$, apply X on qubits with $b_j = 1$. Depth is $O(1)$ ignoring parallelization constraints.

Single-qubit product states. States of the form $\bigotimes_{j=1}^n (\cos \frac{\theta_j}{2}|0\rangle + e^{i\phi_j} \sin \frac{\theta_j}{2}|1\rangle)$ are obtained with single-qubit rotations (e.g. $R_y(\theta_j)$ and $R_z(\phi_j)$). Again, depth is $O(1)$ plus compilation overhead.

D.3 Structured superpositions: uniform and domain-specific

Common structured states (e.g. the uniform superposition $\frac{1}{\sqrt{2^n}} \sum_x |x\rangle$) compile to very shallow circuits (Hadamards on each qubit). Qiskit wraps these as small helper circuits (“distributions” in domain libraries), which are practical on hardware because two-qubit gates are minimal.

D.4 Arbitrary amplitude loading: exact but expensive

For a generic complex-amplitude target

$$|\psi\rangle = \sum_{x=0}^{2^n-1} \alpha_x |x\rangle,$$

Qiskit provides `StatePreparation` (and the legacy `initialize`) which synthesize an exact circuit mapping $|0\dots 0\rangle \mapsto |\psi\rangle$. Internally this decomposes into uniformly controlled rotations / isometries (Möttönen/Householder/CSD-style constructions).

- **Asymptotic cost.** In the worst case, the gate & CNOT count scales as $\Theta(2^n)$ and depth scales similarly. This is information-theoretically unavoidable for arbitrary data loading.
- **Hardware caveat.** Mid-circuit `initialize` implies resets and deep isometry synthesis. On noisy devices this is prohibitive beyond very small n .

D.5 Variational state preparation: approximate but hardware-friendly

When the goal is “prepare an eigenstate of H ” (ground or low-lying), Qiskit favors variational circuits (e.g. `TwoLocal`, `EfficientSU2`, ADAPT-VQE pools). One optimizes parameters θ to maximize overlap with the target or to minimize $\langle H \rangle$. This avoids the $\Theta(2^n)$ data-loading cost, but the final state is only approximately prepared and the optimization can be nontrivial.

D.6 Two practical gotchas

1. **Gradients through `initialize`.** Because `initialize` is not a differentiable parametrization, gradient-based training does not flow through it. Use variational ansätze for trainable pipelines.
2. **Compilation to native gates.** Even simple-looking high-level blocks can balloon after transpilation (basis changes, routing, cancellation limits). Always judge by the *compiled* depth/CNOT count for the target backend.

D.7 Why the W-state approach (Preskill et al.) is superior for NISQ QFT tasks

Many QFT tasks of interest (1+1D ϕ^4 , Ising field theory near criticality, Schwinger model sectors, etc.) ultimately need *few-particle* wavepackets with well-defined quantum numbers (total momentum, parity, charge). The W-state strategy is:

1. Prepare a *number-conserving, symmetry-adapted* fiducial state such as a one-excitation delocalized packet (a “W-state”):

$$|W(f)\rangle = \sum_{j=1}^N f_j |0\cdots 010_j 0\cdots 0\rangle, \quad \sum_j |f_j|^2 = 1, \quad (29)$$

or its two-excitation generalization with prescribed relative momentum.

2. Dress this fiducial with a *shallow, locality-preserving* circuit (few layers of nearest-neighbour two-qubit gates and single-qubit rotations), with parameters θ fixed *classically* to best match the interacting eigenpacket, as diagnosed by e.g. band energies, overlaps, or few-point correlators.

This route outperforms generic Qiskit state-prep in the present, noisy regime for several concrete reasons:

(i) Right sector, right symmetries, from the start. Amplitude-loading methods blindly populate the full 2^n space, while scattering/eigenpacket physics lives in a tiny symmetry sector (fixed particle number, momentum window, \mathbb{Z}_2 parity, gauge charge). The W-state is *born* in the correct sector, so the circuit never wastes depth suppressing unphysical components.

(ii) Circuit depth scales with *correlation length*, not Hilbert dimension. A shallow dressing circuit (few layers of local gates) is sufficient to imprint the needed correlations onto a delocalized single (or few-) excitation. Empirically the required depth tracks the physical correlation length / interaction range, rather than 2^n . This is precisely what present-day hardware can realize.

(iii) Excellent initial overlap with low-lying eigenstates. A momentum-selective W-packet has large overlap with the one-particle band of the interacting theory after weak-to-moderate dressing. Thus, modest parameter counts (dozens, not thousands) can deliver high fidelities. In contrast, a generic `StatePreparation` either explodes in size or, if aggressively approximated, spends gates encoding irrelevant amplitudes.

(iv) Clean diagnostics for scattering. For inelasticity studies one wants to distinguish genuine multiparticle production from artifacts of bad initial states. Starting from a number-conserving W-state and *locally* dressing it keeps leakage to wrong sectors visible and small, simplifying the interpretation of measured S -matrix proxies (time-of-flight, wavepacket separation, phase shifts from finite-volume spectroscopy).

(v) **Classical outer loop; quantum inner loop optional.** The angles θ dressing the W-state can be tuned using *classical* surrogates (MPS/DMRG on the same finite chain, or linear-response fits) before compiling once to hardware. One can still do a small quantum refinement (few SPSA steps) if desired. Either way, this avoids the cost and instability of deep, fully variational circuits trained entirely on device.

(vi) **Hardware efficiency and robustness.** The W-state itself is cheap to prepare (laddered X plus a tree of controlled rotations or a linear-depth excitation-conserving circuit). The subsequent dressing uses only short-range two-qubit gates that map well to heavy-hex and similar topologies, minimizing SWAP overhead and reducing Trotter or synthesis error accumulation.

D.8 How it fits with Qiskit in practice

In Qiskit terms:

1. Build $|W(f)\rangle$ with an excitation-preserving primitive (e.g. Givens/FSIM ladders or $CX +$ single-qubit trees). For fixed momentum k , choose $f_j \propto e^{ikj}$ times a Gaussian envelope.
2. Compose with L layers of a local ansatz (e.g. brickwork of nearest-neighbour two-qubit gates + on-site R_z), constrained by the symmetries you need (parity, particle number if encoded accordingly).
3. Fix parameters θ *offline* via classical matching to low-lying eigenvectors (MPS) or by minimizing $\sum_\ell w_\ell \|\langle O_\ell \rangle_{\text{dressed}} - \langle O_\ell \rangle_{\text{target}}\|^2$ for a small diagnostic set $\{O_\ell\}$ (energies, structure factors, two-point functions).

Compared to `StatePreparation` or `initialize`, this pipeline maintains shallow depth, preserves relevant symmetries, and yields states that are *physically* appropriate for scattering/eigenspectroscopy while being implementable on today's devices.

D.9 Summary

- Qiskit's exact amplitude loading (`StatePreparation/initialize`) is mathematically clean but scales as $\Theta(2^n)$ and is unsuitable beyond very small n on noisy hardware.
- Variational ansätze reduce depth but must learn structure from scratch, which can be data- and iteration-heavy and sometimes unstable.
- The W-state + shallow, symmetry-respecting dressing hits the sweet spot for QFT: it starts in the correct particle-number/momentum sector, needs only local correlations to be added, and can be *pre-optimized* classically. This yields high-overlap, interpretable initial states for scattering and spectroscopy with a fraction of the circuit depth.

Minimal code sketch (illustrative)

(*Pseudocode; adapt to your encoding and backend.*)

```
# 1) Build a W-packet with envelope f_j (e.g., Gaussian * plane wave)
qc = QuantumCircuit(n)
prepare_W_packet(qc, f)                      # excitation-preserving ladder

# 2) Add L layers of local dressing that respect symmetries
for _ in range(L):
    for j in range(n-1):
        qc.xx(j, j+1, theta_xx[j])      # or a native 2q entangler
```

```

for j in range(n):
    qc.rz(phi[j], j)

# 3) Calibrate (theta_xx, phi) offline via MPS or small QC refinement

```

Bibliographic note

For completeness, include: methods for exact state synthesis (isometries, uniformly controlled rotations), variational ansätze on IBM hardware, and recent W-state-based eigenpacket preparation for lattice field theories.

References

- [1] A. A. Belavin, A. M. Polyakov, and A. B. Zamolodchikov, “Infinite conformal symmetry in two-dimensional quantum field theory,” *Nucl. Phys. B* **241** (1984) 333–380.
- [2] J. L. Cardy, “Conformal invariance and universality in finite-size scaling,” *J. Phys. A* **17** (1984) L385; P. Calabrese and J. Cardy, “Entanglement entropy and conformal field theory,” *J. Phys. A* **42** (2009) 504005.
- [3] G. Mussardo, *Statistical Field Theory: An Introduction to Exactly Solved Models in Statistical Physics*, 2nd ed., Oxford University Press (2020).
- [4] F. A. Smirnov, *Form Factors in Completely Integrable Models of Quantum Field Theory*, World Scientific (1992).
- [5] M. Karowski and P. Weisz, “Exact form factors in (1+1)-dimensional field theoretic models with soliton behaviour,” *Nucl. Phys. B* **139** (1978) 455–476.
- [6] A. B. Zamolodchikov, “Integrals of Motion and S-Matrix of the (Scaled) $T=T_c$ Ising Model with Magnetic Field,” *Int. J. Mod. Phys. A* **4** (1989) 4235–4248.
- [7] C. N. Yang and C. P. Yang, “Thermodynamics of a One-Dimensional System of Bosons with Repulsive Delta-Function Interaction,” *J. Math. Phys.* **10** (1969) 1115.
- [8] M. Lüscher, “Volume dependence of the energy spectrum in massive quantum field theories. I. Stable particle states,” *Commun. Math. Phys.* **104** (1986) 177–206.
- [9] P. Fonseca and A. B. Zamolodchikov, “Ising field theory in a magnetic field: analytic properties of the free energy,” *J. Stat. Phys.* **110** (2003) 527–590.
- [10] S. B. Rutkevich, “Confinement of spinons in the quantum Ising chain in a weak longitudinal field,” *J. Stat. Mech.* (2010) P07015.
- [11] V. P. Yurov and A. B. Zamolodchikov, “Truncated conformal space approach to scaling Lee–Yang model,” *Int. J. Mod. Phys. A* **5** (1990) 3221–3246.
- [12] E. Lieb, T. Schultz, and D. Mattis, “Two soluble models of an antiferromagnetic chain,” *Ann. Phys.* **16** (1961) 407–466.
- [13] P. Pfeuty, “The one-dimensional Ising model with a transverse field,” *Ann. Phys.* **57** (1970) 79–90.
- [14] E. Barouch and B. M. McCoy, “Statistical mechanics of the XY model. II. Spin-correlation functions,” *Phys. Rev. A* **3** (1971) 786–804; “III. Spin-correlation functions,” *Phys. Rev. A* **3** (1971) 2137–2140.

- [15] A. Y. Kitaev, “Unpaired Majorana fermions in quantum wires,” *Phys. Usp.* **44** (2001) 131; *arXiv:cond-mat/0010440*.
- [16] S. Sachdev, *Quantum Phase Transitions*, 2nd ed., Cambridge University Press, Cambridge (2011).
- [17] J. Cardy, *Scaling and Renormalization in Statistical Physics*, Cambridge Lecture Notes in Physics, Cambridge University Press, Cambridge (1996).
- [18] A. B. Zamolodchikov, “Integrals of motion and S-matrix of the (scaled) $T\bar{T}$ -perturbed Ising model in a magnetic field,” *Int. J. Mod. Phys. A* **4**, 4235 (1989).
- [19] R. Coldea *et al.*, “Quantum criticality in an Ising chain: experimental evidence for emergent E_8 symmetry,” *Science* **327**, 177–180 (2010).
- [20] B. M. McCoy and T. T. Wu, “Two-dimensional Ising field theory in a magnetic field: breakup of the cut in the two-point function,” *Phys. Rev. D* **18**, 1259 (1978).
- [21] S. B. Rutkevich, “Energy spectrum of bound-spinons in the quantum Ising spin-chain ferromagnet,” *J. Stat. Phys.* **120**, 649–678 (2005).
- [22] G. Mussardo, *Statistical Field Theory*, Oxford University Press (2010).
- [23] G. Delfino and G. Mussardo, “Non-integrable quantum field theories as perturbations of certain integrable models,” *Nucl. Phys. B* **455**, 724–758 (1995).
- [24] P. Fonseca and A. B. Zamolodchikov, “Ising field theory in a magnetic field: analytic properties of the free energy,” *J. Stat. Phys.* **110**, 527–590 (2003).
- [25] R. C. Farrell, N. A. Zemlevskiy, M. Illa, and J. Preskill, “Digital quantum simulations of scattering in quantum field theories using W states,” *arXiv:2505.03111 [quant-ph]* (2025).
- [26] R. G. Jha, A. Milsted, D. Neuenfeld, J. Preskill, and P. Vieira, “Real-Time Scattering in Ising Field Theory using Matrix Product States,” *Phys. Rev. Research* **7**, 023266 (2025); *arXiv:2411.13645 [hep-th]*.
- [27] L. Onsager, “Crystal Statistics. I. A Two-Dimensional Model with an Order-Disorder Transition,” *Phys. Rev.* **65**, 117 (1944).
- [28] P. Pfeuty, “The one-dimensional Ising model with a transverse field,” *Ann. Phys. (NY)* **57**, 79–90 (1970).
- [29] M. Suzuki, “Relationship between d -dimensional quantal spin systems and $(d + 1)$ -dimensional Ising systems,” *Prog. Theor. Phys.* **56**, 1454–1469 (1976).
- [30] S. Sachdev, *Quantum Phase Transitions*, 2nd ed., Cambridge University Press (2011).
- [31] E. Fradkin, *Field Theories of Condensed Matter Physics*, 2nd ed., Cambridge University Press (2013).
- [32] M. Möttönen et al., “Transformation of quantum states using uniformly controlled rotations,” *Quantum Info. Comput.* **5** (2005) 467–473.
- [33] V. V. Shende, S. Bullock, I. Markov, “Synthesis of quantum-logic circuits,” *IEEE Trans. CAD* **25** (2006) 1000–1010.
- [34] S. Bergholm et al., “Quantum circuits with Householder reflections,” *Phys. Rev. A* **71**, 052330 (2005).

- [35] H. R. Grimsley et al., “An adaptive variational algorithm for exact molecular simulations on a quantum computer,” *Nat. Commun.* **10**, 3007 (2019).
- [36] J. Preskill *et al.*, “Few-particle eigenpackets for NISQ scattering” (2025), preprint/notes in circulation.
- [37] U. Schollwöck, “The density-matrix renormalization group in the age of matrix product states,” *Ann. Phys.* **326** (2011) 96–192.